The impact of altered haemodynamics on the development of the epicardium

Thesis submitted to the University of Nottingham for the degree of Doctor of Philosophy

Chrysostomos Perdios

February 2019

Abstract

During embryo development the heart is the first functioning organ. Although quiescent in the adult heart, the epicardium is essential during development to form a normal functioning heart. Epicardial derived cells contribute to the heart as it develops, including fibroblasts and vascular smooth muscle cells. Previous studies have shown that a heartbeat is required for epicardium formation. Further, preliminary studies from our laboratory have shown that the development of the epicardium is aberrant when the haemodynamics are altered.

This study aims to investigate how the epicardium and some of its derived cell lineages respond to altered haemodynamics in the developing embryo. Since the aetiology of many congenital heart diseases (CHDs) is unknown, we suggest that an alteration in the heart's haemodynamics might provide an explanatory basis for some of them. In order to change the heart's haemodynamics, outflow tract (OFT) banding using a double overhang knot was performed on Hamburger and Hamilton (HH) stage 21 chick embryos, with harvesting at different developmental stages.

Upon alteration of haemodynamics, the epicardium exhibited abnormal morphology and minor bleeding at HH29 using morphological analysis. This phenotype was exacerbated at HH35 with severe changes in the structure of the extracellular matrix (ECM) and the coronary vasculature. A number of genes tied to ECM production were also differentially expressed in HH29 and HH35 OTB hearts including, collagen I and collagen XII. At HH35, there was also downregulation in a number of vascular genes.

It is the first time that the importance of the epicardium is shown regarding CHDs that are caused by altered haemodynamics. In this study, the epicardium was found to be severely impacted by OFT banding. The altered phenotype also showed signs of becoming embryonically lethal as development ensued. More studies

should be conducted regarding the effects of haemodynamics on the epicardium with respect to ECM and coronary vessel maturation.

Acknowledgements

I would like to thank my supervisor, Dr. Siobhan Loughna, for her constant support and guidance, who I ended up seeing more as a friend rather than just my supervisor as my PhD progressed. I also want to thank my PhD colleagues for tolerating me, Dr. Kar Lai Pang and Dr. Mat Parnall, and hopefully soon to be Drs. Kawthar Alnahdi and Qazi Waheed Ullah and our lab technician Dr. Sophie Rochette.

I am grateful to Dr. Sally Wheatley and her PhD students, Amelia Townley, Dr. James Grey and Dr. Nicola Humphry for sharing their lab and office space with us and for the many intellectually stimulating conversations we had during our time together.

Thanks are also extended to Prof. David Brook and his lab team, for all the lab meeting we had together, as well as Prof. Fred Sablitzky, for his guidance and feedback over my PhD lab reports as well as being a great inspiration as my lecturer during my undergrad, and Prof. Margaret Pratten, for allowing me to attend the human anatomy and dissection medical school sessions.

Last but not least I would like to thank my parents and sister who although did not understand my PhD subject or its goals supported me during my decisions.

Declaration

Outflow tract banding was originally optimised by Dr. Kar Lai Pang. The apoptosis and proliferation experiment were carried out in association with Dr. Kar Lai Pang. RNA-Seq sample preparation was performed by Dr. Matt Parnall, sample readings

by Dr. Sunir Malla and initial bioinformatics were carried out by Dr. Fei Sang. All of the images taken by the Axioscan.Z1 slide scanner were done in association with Mrs. Joanne Marrison from the Technology Facility, Department of Biology at the University of York. All the DNA sequencing was performed by Mr. Matthew Carlile from the DNA sequencing facility at the University of Nottingham. Light sheet fluorescent imaging was carried out in the Wolfson Light Microscopy Facility, University of Sheffield, in association with Dr. Nick van Hateren. Transmission electron microscopy was done in association with Mrs. Denise Mclean from the advanced microscopic unit, University of Nottingham.

Table of Contents

Abbreviations

ANGPT	Angiopoietin
APES	3-aminopropyltriethoxysilane
AV	Atrioventricular
BCP	1-bromo-3-chloro-propane
bp	Base pairs
BSA	Bovine serum albumin
Bves	Blood vessel epicardial substance
BMP	Bone morphogenetic protein
CA	Coronary artery
CHD	Congenital Heart Disease
CHF	Congestive heart failure
CS	Carnegie stage
C_t	Threshold cycle
CV	Coronary vessel
dH_2O	Deionised water
DAB	3,3 diaminobenzidine
DIG	Digoxigenin
DiI	1,1'-dioctadecyl-3,3,3'3'-tetramethylindocarbocyanine perchlorate
DORV	Double outlet right ventricle
E	Embryonic day
EC	Endothelial cells
ECM	Extracellular matrix

EMT	Epithelial to mesenchymal transition
EPDC	Epicardial derived cells
EtOH	Ethanol
FACIT	Fibril associated collagen with interrupted triple helices
FC	Fold change
FGF	Fibroblast growth factor
GO	Gene ontology
GOI	Gene of interest
HH	Hamburger and Hamilton
hpf	Hours post fertilisation
HPS	His-Purkinje system
HRP	Horse radish peroxidase
HS	High salt
HT	Heart tube
IAS	Interatrial septum
ISH	In situ hybridisation
IV	Interventricular
IVS	Interventricular septum
LAD	Left anterior descending
LA	Left atrium
LAL	Left atrial ligation
LB	Lysogeny broth
LTR	LysoTracker Red

LV	Left ventricle
MABT	Maleic acid buffer with Tween20
MeOH	Methanol
MI	Myocardial infarction
MO	Morpholino oligonucleotide
n	Sample size
NaAc	Sodium Acetate
NRP	Neuropilin
OFT	Outflow tract
OTB	Outflow tract banding
PA	Pulmonary artery
PAA	pharyngeal arch artery
PBS	Phosphate buffer saline
PBST	Phosphate buffer saline with Tween 20
PCA	Principal component analysis
PCNA	Proliferating cell nuclear antigen
PCR	Polymerase chain reaction
PE	Proepicardium
PEO	Proepicardial organ
PFA	Paraformaldehyde
PHF	Primary heart field
PTA	Persistent truncus arteriosus
qPCR	Quantitative real time PCR

RA	Retinoic acid
RE	Restriction enzyme
ROI	Region of interest
RPKM	Reads per kilobase of transcript per million mapped reads
RPM	Reads per million
RT	Room temperature
RT-PCR	Reverse transcriptase PCR
RV	Right ventricle
SEM	Standard error of the mean
SHF	Secondary heart field
sih	*silent heart*
SLV	Semilunar valve
SMC	Smooth muscle cell
SSC	Saline-sodium citrate
ST	Septum transversum
SV	Sinus venosus
TAC	Transverse artery constriction
TBS	Tris-buffered saline
TBST	Tris-buffered saline with Tween 20
TdT	Terminal deoxynucleotidyl transferase
TEM	Transmission electron microscopy
TF	Transcription factor
TGF	Transforming growth factor

TJ	Tight junction
Tm	Melting temperature
TUNEL	dUTP nick end labelling
VAF	Void area fraction
VSD	Ventricular septal defect
VVL	Vitelline vein ligation
WM	Whole mount
WT	Wild type

List of figures

List of tables

1 Introduction

1.1 Heart formation

1.1.1 Heart tube formation and looping

During the development of the vertebrate embryo the heart is the first organ to become functional. During early gastrulation two bilateral cardiogenic plates, which consist of a collection of mesodermal cells, emerge to fuse and develop the cardiac tube (Fig. 1.1). Furthermore, two different populations of cardiac precursor cells, the primary and secondary heart field, will develop in different parts of the heart. For example the primary heart field forms the left ventricle (Brand, 2003).

The primary heart tube starts forming in chicks at Hamburger Hamilton stage (HH) 7 (Hamburger and Hamilton, 1992; Fig. 1.1A) and it starts beating at HH10, in which the heart starts to loop (Wittig and Münsterberg, 2016). After HH10 the primitive atrium forms (Fig. 1.1B) and at HH15 the heart forms an S-shape structure (Fig. 1.1C). By HH24 the heart has finished looping and it now has four chambers (Fig. 1.1D), resembling a human heart, although incomplete (Wittig and Münsterberg, 2016). At HH29 the heart has four chambers with the outflow tract (OFT) starting to septate (Fig. 1.1E). By HH35 the OFT has fully septated to the pulmonary artery and aorta (Fig. 1.1F, Wittig and Münsterberg, 2016).

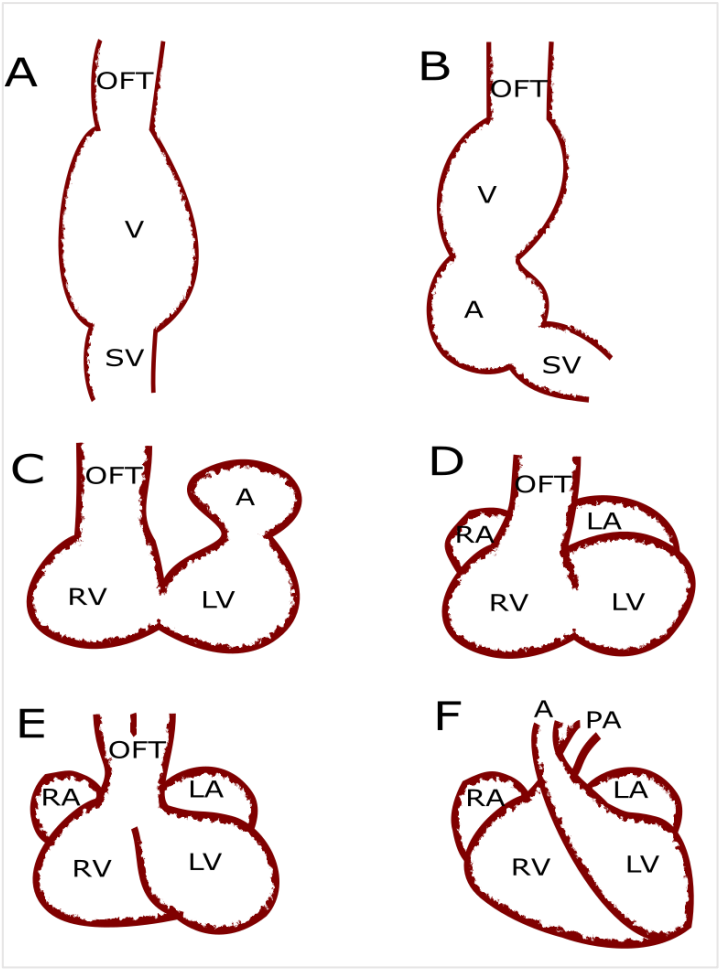

Figure 1.1: Chick heart development. (A) At HH10 the primitive heart tube consists of a primordial ventricle (V) and the arterial outflow tract (OFT), and the venous sinus venosus (SV). (B) Shortly after HH10 the primordial atrium (A) appears. (C) At HH15 the primordial ventricle separates into the left (LV) and right (RV) ventricles. (D) At HH24 the heart has four chambers, since the primordial atrium separates into the left (LA) and right (RA) atria. (E) At HH29 the heart now has four chambers with the OFT starting septation. (F) At HH35 OFT septation is now complete separating it into the pulmonary artery (PA) and aorta (A).

1.1.2 The primary and secondary heart fields

The cells destined to form the heart are among the first cell lineages formed in the vertebrate embryo (Wittig and Münsterberg, 2016). Cells from the splanchnic

mesoderm are committed to become cardiac cells by HH8 (Martinsen, 2005; Wittig and Münsterberg, 2016); these cells form the primary heart field (PHF) and secondary heart field (SHF) and are located bilaterally of the anterior primitive streak (Fig. 1.2A). Future endocardial cells migrate from the PHF to start the formation of the bilateral heart tubes, which merge in the midline to a single heart tube at HH9 (Fig. 1.2B; Brand, 2003; Martinsen, 2005; Wittig and Münsterberg, 2016). At HH13 there is formation of the early OFT and the right ventricle from the migrating cells of the SHF (Fig. 1.2C). At the same time, the cells from the PHF will develop to the sinus venosus (SV), left ventricle and the primary atrium (Fig. 1.2C), which will give rise to left and right atria (Martinsen, 2005; Wittig and Münsterberg, 2016).

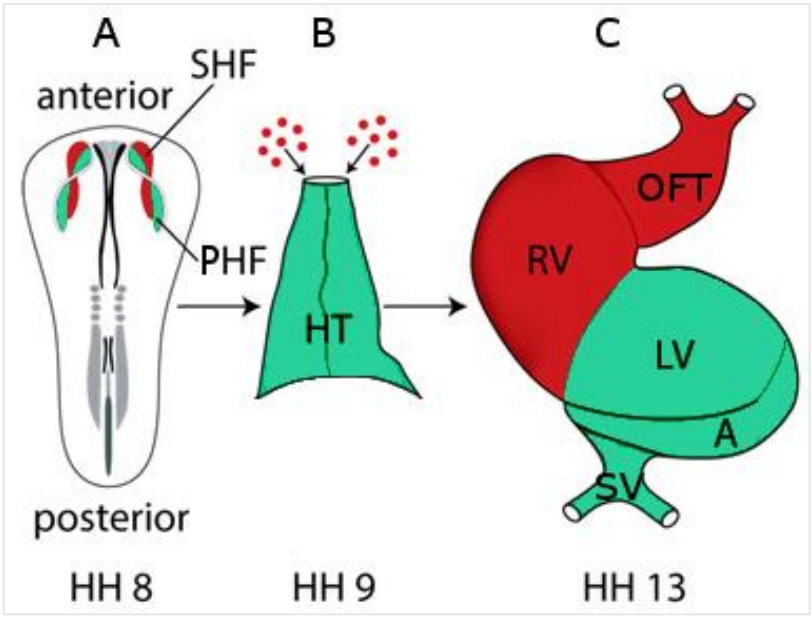

Figure 1.2: Primary and secondary heart fields contribution in early chick heart formation. (A) At HH8 the primary heart field (PHF; green) and secondary heart field (SHF; red) are formed bilaterally of the primitive streak (grey). (B) The PHF generates a primitive heart tube by HH9; secondarily added cell populations from the SHF have not yet contributed (red dots). (C) During dextral-looping, at HH13, the straight heart tube further matures and SHF-derived cells contribute to the heart. HT, heart tube; OFT, outflow tract; RV,

right ventricle; LV, left ventricle; A, primary atrium; SV, sinus venosus. Adapted from Ottaviani and Buja, 2016.

1.1.3 Formation of the interatrial and interventricular septum

The interatrial septum (IAS) is formed in several steps in higher vertebrates but in fewer steps in the chick. In humans the IAS is completed between the first and second month of foetal development. In higher vertebrates the primary atrial septum (septum primum) is initially formed at the roof between the two future atria (Fig. 1.23; Anderson, 2002, 2003). The septum primum moves towards the atrioventricular (AV) cushion (Fig. 1.3B) but by doing so part of it breaks down near the top of the atria forming a second foramen along with the one near the atrioventricular (AV) canal (Fig 1.3C). A second, more muscular, atrial septum (septum secundum) forms from the top of the atria along septum primum (Fig. 1.3D; Anderson, 2002, 2003). The septum secundum grows anteriorly closing the septum primum while leaving open the second foramen, which becomes the foramen ovale outlet (Fig. 1.3D, E). The foramen ovale outlet works as a valve for the foramen ovale (Fig. 1.3E, F; Anderson, 2002, 2003). The foramen ovale is important during foetal life since the lungs are non-functional and it is more efficient if they are bypassed, by circulation moving from the right to the left atrium. In the chick the septum primum transforms into the mature atrial septum; formation starts at HH16 and it is complete by HH24 (Fig. 1.3D; Chang, 1931). Complete septum maturation happens after birth in all vertebrates, when the right to left shunt stops due to the increased pressure in the left atrium.

The formation of the interventricular septum (IVS) is also different between humans and the chick. In humans the muscular part of the IVS derives from the ballooning of the right and left ventricle, forming from the base of the primitive ventricles towards the AV cushion, leaving an interventricular foramen (Fig. 1.3C; Anderson, 2003; Wenink, 1981). The membranous part of the IVS is formed by

the conotruncal septum (Fig. 1.4) and the fused AV cushions (Fig. 1.3F), closing the interventricular foramen. The IVS in human embryos is completed near the end of the second month (Anderson, 2003; Wenink, 1981). The IVS in the chick starts to form at HH19, and by HH29 (Fig. 1.1E) the septum has grown towards the AV cushions and started to fuse with them leaving only a small foramen between the left and right ventricles (Ben-Shachar et al., 1985; Martinsen, 2005). In the chick, the layered trabeculae in the heart compact by fusion creating an inferior muscularised IVS and the AV cushions muscularisation creates a superior muscular septum. Ventricular septation is complete by HH34 (Ben-Shachar et al., 1985; Martinsen, 2005).

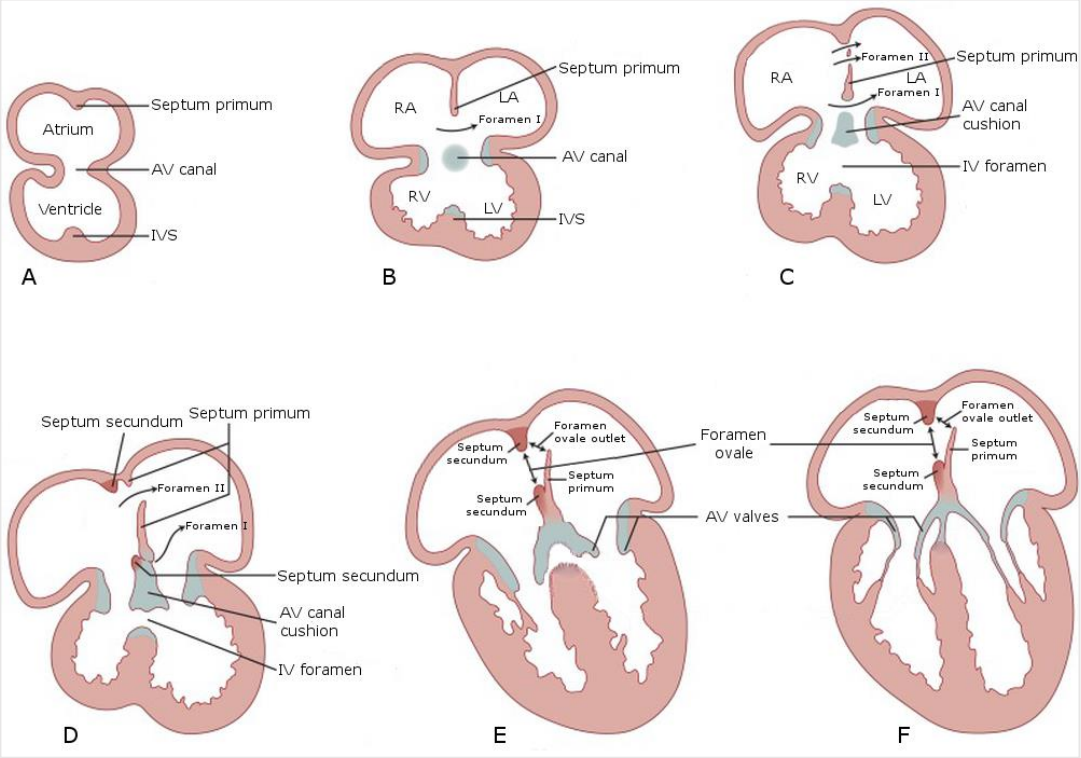

Figure 1.3: Interatrial and interventricular septation. (A) In human embryos atrial septation begins by day 28. (B) The septum primum grows towards the atrioventricular (AV) canal creating the first foramen (I), whilst cardiac jelly accumulates in the AV canal. (C) The second foramen (II) forms by the breakdown of the superior aspect of septum primum, while the interventricular septum (IVS) grows towards the AV canal cushions creating the

interventricular (IV) foramen. Cells from the endocardium populate the AV canal cushions. (D) The septum secundum develops closing foramen I. (E) Foramen II diminishes to an outlet for the foramen ovale with the septum primum functioning as a flap for the foramen ovale. The AV cushions are modified into the AV valves. (F) The IVS has fully closed. The AV valves further mature with papillary muscle attachments. Grey areas are the AV cushions, which are modified to the AV valves. Adapted from Ottaviani and Buja, 2016.

1.1.4 Atrioventricular and semilunar valve formation

The AV valves begin their formation around HH21 in the chick (Martinsen, 2005). In the AV canal the accumulation of cardiac jelly, made from extracellular matrix originating from in-between the endocardium and myocardium, creates a local tissue swelling (Fig. 1.3B; Lin et al., 2012). This tissue swelling further grows into endocardial cushions (Fig. 1.3C), which are populated by endocardial cells undergoing an epithelial to mesenchymal transformation (EMT; de Lange, 2004; Lin et al., 2012). Between HH28-36 the AV cushions are remodelled into the valve leaflets (Martinsen, 2005). As the heart chambers septate the AV cushions develop into the tricuspid (right) and bicuspid or mitral (left) valves (Fig.1.3E; Lin et al., 2012). The AV valves are further remodelled by the attachment of the papillary muscles via the chordae tendinae; together they make up the subvalvular apparatus (Fig. 1.3F). The subvalvular apparatus prevents the valves from prolapsing into the atria (Dal-Bianco and Levine, 2013).

The semilunar valves (SLVs) can be further subdivided to the aortic and pulmonary valve, located in the aorta and pulmonary artery respectively. These valves, in contrast to the AV valves, do not have a subvalvular apparatus (Anderson et al., 2003; Lin et al., 2012). SLV formation begins during HH29 with another pair of endocardial cushions forming in the OFT (Martinsen, 2005). Muscular tissue growth in the proximal OFT, a process called myocardilisation, also muscularises

the cushions. The cushions are further grown, remodelled and fused to create the valve cusps (Anderson et al., 2003). The SLVs are completely formed by HH34 (Martinsen, 2005).

1.1.5 Inflow and outflow tract formation and maturation

The inflow tract, also commonly known as the sinus venosus (SV), is a sinus for the systemic circulation allowing blood from the vitelline, umbilical and common cardinal veins to be returned to the heart (Christoffels, 2006; van den Berg and Moorman, 2011). The systemic veins will result in the vena cavae through extensive remodelling (Fig. 1.4). The fourth great vessel that becomes incorporated in the SV, during development, is the pulmonary vein. The relationship between pulmonary vein and the SV is still a controversial subject, since there is a debate as to whether the pulmonary veins develop an attachment to the left atria directly or attaches through the SV first (van den Berg and Moorman, 2011). The SV is only found during development as it is fused with the right atrium in the adult. The SV in the adult also forms the coronary sinus, for drainage of the myocardium, and the sinoatrial node, which is the heart's natural pacemaker (Christoffels, 2006).

The OFT is the arterial pole of the heart sending blood to the rest of the embryo (Anderson et al., 2003; Jain et al. , 2010). The OFT can be further separated to the proximal conus arteriosus and the distal truncus arteriosus. Although the OFT's external morphological appearance resembles a single vessel an "aorto-pulmonary" or conotruncal septum separates the future aorta from the pulmonary artery internally (Fig. 1.4; Anderson et al., 2003; Jain et al., 2010). The aortic and pulmonary channel twist around each other inside the OFT thus the two blood streams flow spirally. The conotruncal septum is formed from neural crest cells between the fourth and sixth pharyngeal arch artery, which will give rise to the future aorta and pulmonary artery respectively (Fig. 1.4). As development

progresses the OFT is fully partitioned to the aorta and pulmonary artery by the addition of fibroadipose tissue (Anderson et al., 2003; Jain et al., 2010).

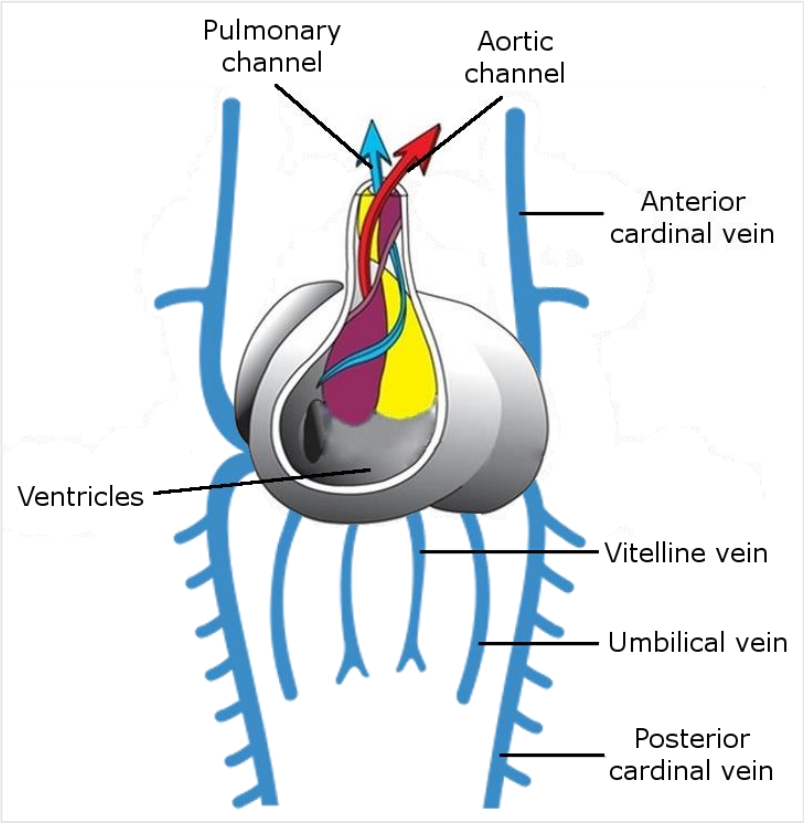

Figure 1.4: The heart's inflow and outflow tract. During chick development the heart has blood going in from the sinus venosus (through the various systemic veins), and blood coming out from the outflow tract which is internally splits in an aortic and pulmonary channel by the conotruncal septum. Adapted from Gray and Clemente, 1985; Sadler, 2006.

1.1.6 The pharyngeal arch arteries

The pharyngeal arches are precursors for a variety of anatomical structures during development (reviewed in Graham, 2001). The pharyngeal arches are vascularised by the pharyngeal arch arteries (PAAs) and are also of great importance in the adult. The PAAs are remodelled into the great arteries and the main arteries of the head and neck region, and their branches, delivering blood to the body. Although historically there are six PAAs only five are fully formed, the 1st to 4th pair and the

6th one, whereas the 5th pair is either never formed or only partially formed and then immediately regresses (Fig. 1.5; Gupta et al., 2015).

In the mouse embryo the PAAs are formed and undergo most of their remodelling in just 5 embryonic days (E), whereas in humans more than a month is needed (Hiruma et al., 2002; Rana et al., 2014). However, in context of total gestation time, humans develop their PAAs faster than mice as 5 days is 1/4 of mouse total gestation time, whereas 1 month is 1/9 for human. The first and second PAAs appear in mice around E9 with the third and fourth PAAs form during E9.5-10 and the sixth PAA forms at E10 (Hiruma et al., 2002). By E10.5 the first and second PAAs have either regressed or remodelled to other arteries, with PAAs still being bilaterally symmetrical. By E13 the symmetry completely disappears and the PAAs are remodelled into vessels found in the adult (Fig. 1.5; Hiruma et al., 2002).

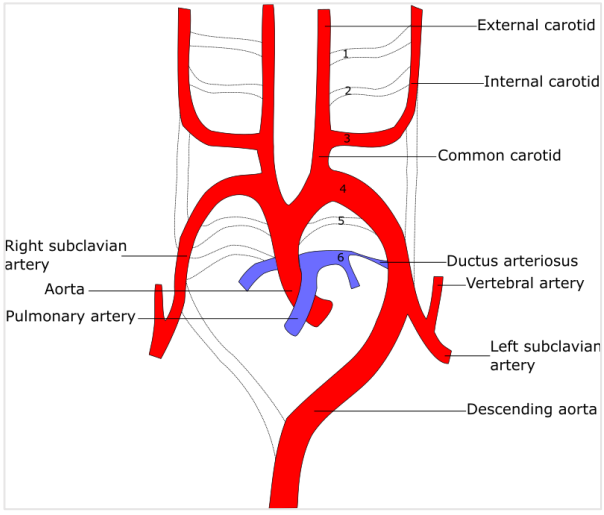

Figure 1.5: Remodelling of the pharyngeal aortic arches. During chick development the six pharyngeal aortic arches go through extensive remodelling to form some of the main arteries in the adult (white vessels have regressed). Adapted from Gray and Clemente, 1985.

1.2 Epicardial origins

1.2.1 The origins of the venous epicardium

The (venous) epicardium emerges from an aggregation of progenitor cells making the proepicardial organ (PEO), which is located inferior to the heart tube. The PEO is formed, around HH14, from the splanchnic mesoderm and is an outpouching from the septum transversum (Fig. 1.6A), a folding of mesodermal mesenchyme cells that gives rise to the thoracic and abdominal cavities (Cano et al., 2016). At HH17 (Fig. 1.6B) these proepicardial (PE) cells migrate to the myocardium, to cover it and form the epicardium (Hiruma and Hirakow, 1989). Studies in *Xenopus* suggest that the PEO attaches to the atrioventricular canal and then proceeds to form an epicardial sheet around the heart (Tandon et al., 2013). The epicardium is of great importance as a fraction of its cells migrate into the heart, termed epicardium derived cells (EPDC), and are crucial for the development of structures within the heart and coronary vessels (Gittenberger-de Groot et al., 1998).

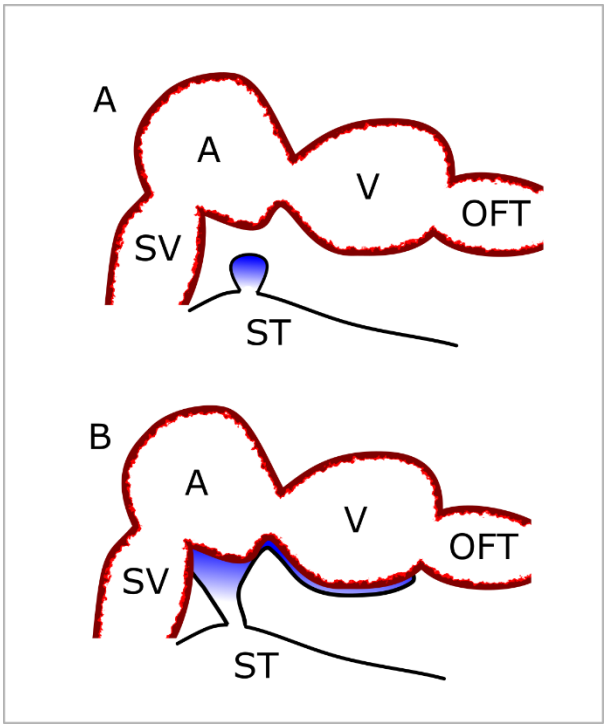

Figure 1.6: Proepicardium migration in the chick. (A) The heart tube, at HH14, showing the atria (A), ventricles (V), outflow tract (OFT) and sinus venosus (SV). The boundaries of the septum transversum (ST) can be seen with the proepicardial organ emerging (PEO; blue). (B) At HH17 proepicardial cells subsequently migrate from the PEO covering the heart.

Quail to chick PEO chimeras have shown that only the proximal section of the OFT is covered by epicardial cells of quail origin (PEO donor) in the chick embryo (host; (Pérez-Pomares et al., 2001). The distal part of the OFT was covered by epicardial cells that were originated by the host but only the proximal OFT epicardium, originated by the donor, was able to generate EPDC (Pérez-Pomares et al., 2001). This suggest that the distal OFT epicardium cell population is derived from the aortic sac. These results support that there are two populations of epicardial cells in the region of the OFT; PEO derived cells are located in the proximal region, whereas aortic sac derived cells, now called arterial epicardial cells, are found in the distal region. It is also possible that these two populations can differentially contribute to heart development (Pérez-Pomares et al., 2001, 2003).

1.2.2 The origins of the arterial epicardium

As discussed in section 1.2.1, there is a second epicardial population, called the arterial epicardium, which only covers the distal part of the OFT (Gittenberger-de Groot et al., 2000; Pérez-Pomares et al., 2003). The arterial epicardium originates from the pericardial coelom (Pérez-Pomares et al., 2003). The two epicardial populations, venous and arterial, do not make contact with each other until HH26. The arterial epicardium has a low expression of vimentin and RALDH2 making it molecularly distinct from the venous epicardium, which has a high expression of vimentin and RALDH2 (Pérez-Pomares et al., 2003). Both populations highly express cytokeratin. The arterial epicardium does not seem to undergo EMT (Pérez-Pomares et al., 2003).

Although, the arterial epicardium does not seem to make any contributions to the development of the heart, it might have a regulatory role in OFT development due to its position above the distal portion of the OFT (Pérez-Pomares et al., 2003). In the HH17 embryonic chick heart, where the venous epicardium has been mechanically inhibited from migrating, the arterial epicardium migrates further down in comparison to non-inhibited controls, touching the inner curvature

between the OFT and the atrium at HH29 (Gittenberger-de Groot et al., 2000). This shows that although the arterial epicardium has a quiescent phenotype it can be activated in response to insults on the venous epicardium, possibly as a compensatory mechanism. Due to the lack of data on the arterial epicardium, and the fact that it does not seem to contribute majorly in heart development, any further reference on the epicardium will only be for the venous epicardium unless stated otherwise.

1.3 PE cell migration in different model species

In avian embryos, the PEO forms in a bilaterally asymmetric fashion and the PE cells migrate, using villous protrusions, through an extracellular matrix bridge dorsally to the ventricular myocardium, near the atrioventricular (AV) junction on the inner curvature (Nahirney et al., 2003). In chicks, after the villous protrusions from the PEO contact the heart, at the AV junction, the epicardium starts to envelop the myocardium at HH17. The formation of the epicardium is complete by HH24 (Hiruma and Hirakow, 1989; Ishii et al., 2010).

In humans much is still not known about PE development, although the epicardium is believed to start to develop and envelop the heart at Carnegie stage (CS)11, which is equivalent to HH12-13 in chicks, and its complete formation over the heart is achieved by CS15, equivalent to HH20-21 (Risebro et al., 2015). In mice, in which PEO formation is symmetrical (Fig. 1.7), there is some controversy on how the PE cells migrate to the surface of the heart to form the epicardium, around E9. An early study suggested that the PEO sends cell aggregates that float towards the heart and attach to it (Komiyama et al., 1987). The cell aggregates then flatten on the heart's surface and merge together to form the epicardium (Komiyama et al., 1987). In a more recent study, the PE was found to contact the heart directly through villous protrusions, just like in the chick (Rodgers et al., 2008). Moreover, as cell aggregates were also observed, this suggest that is more than one mode of cell migration (Rodgers et al., 2008).

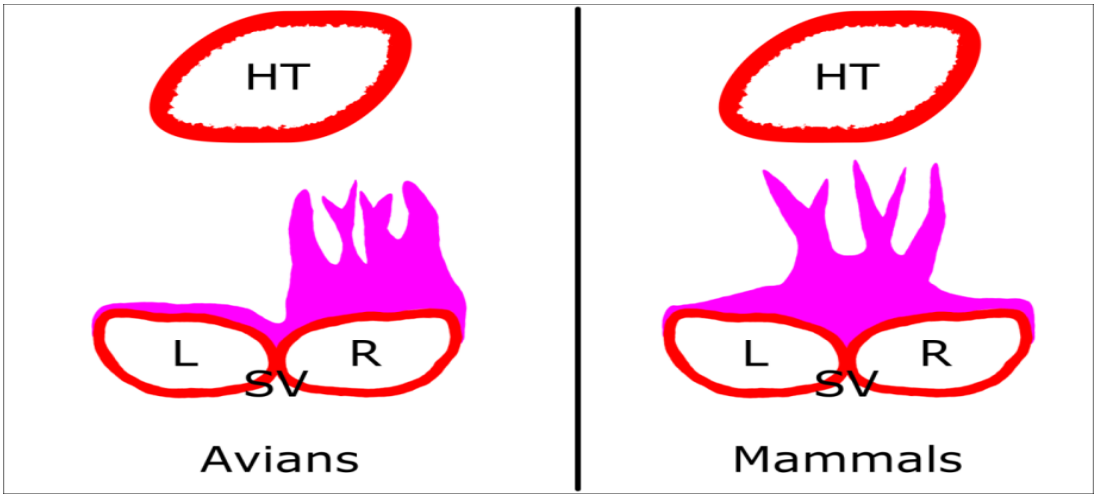

Figure 1.7: Proepicardium migration between species. Proepicardium (pink) migration from the sinus venosus (SV) to the heart tube (HT) in an asymmetrical, from the right (R), or symmetrical fashion, both left (L) and right (R), according to animal class.

1.4 The molecular genetics of PEO specification and migration

The liver bud was found to be able to induce the expression of the PEO and epicardial gene markers *TBX18* and *WT1* in the mesoderm through in vitro experiments. In these experiments *WT1* and *TBX18* expression could be induced in co-cultures with liver bud and lateral embryonic explant (Ishii et al., 2007). In addition, quail liver bud was found sufficient to induce expression of these marker genes in the mesothelium, in vivo, when implanted at the posterolateral region of a chick embryo. Endodermal tissues (e.g. lung bud) were found unable to be induced by the liver bud. Although the liver bud was shown to be sufficient to induce marker gene expression in the PE, it might not be necessary (Ishii et al., 2007). Although *TBX18* is expressed in the PEO, its loss does not seem to affect either the development of the epicardium or the migration of EPDC. This is possibly

due to other genes of the Tbx family having an overlapping function with *TBX18* (Braitsch and Yutzey, 2013).

The PEO possibly originates from a common, *TBX18* expressing, pool of progenitor cells, shared with the inflow myocardium, which originates from the secondary heart field. The separation of the PEO and myocardium populations was found to be dependent on fibroblast growth factor (FGF) 2 and bone morphogenetic proteins (BMP) 2, which transduce their signals via the SMAD and MEK-ERK pathway respectively (van Wijk et al., 2009). In chicken embryos, BMP treatment stimulated cells, from the common progenitor pool, to differentiate into myocardial cells, whereas FGF inhibited the effects of BMP and stimulate proepicardium differentiation in vivo and in vitro (van Wijk et al., 2009). A gene expression analysis revealed that FGF2 and BMP2 are expressed in the PEO, whereas the myocardium expresses BMP2 only, further supporting the notion that BMP2 promotes a myocardial fate and FGF2 blocks it (van Wijk et al., 2009).

TWIST1 is an important transcription factor (TF) for cell differentiation and mobilization. Between HH10 and HH14, *TWIST1* is expressed in the right lateral plate mesoderm. Knock down of *TWIST1*, before HH9, disrupted the formation of the PE villi and caused downregulation of the epicardial markers *WT1* and *TCF21* on the PEO's epithelial cells, but not the underlying mesenchyme (Schlueter and Brand, 2013). In addition, upon *TWIST1* knockdown, the PEO can suffer a volume reduction up to 50%, due to the loss of villous protrusions, showing the importance of TWIST1 in PE cell migration (Schlueter and Brand, 2013).

The villi protruding from the PEO, which target the heart, seem to be also dependent on BMP signalling. When chick PEO explants were cultured for 24 hours with BMP2 the explants had an increased radial expansion, which also spread about 50% faster than the control (Ishii et al., 2010). This expansion was found to be due to an alteration of the cells' behaviour rather than proliferation. Gene expression analysis has shown that the heart's AV junction expresses high levels

of *BMP2* and that the PE expresses BMP receptors (Ishii et al., 2010). Misexpression of Noggin, a BMP antagonist, in the myocardium caused PE cells to fail to attach to the heart or to have a delayed migration (Ishii et al., 2010). In addition, experimental misexpression of BMP in the myocardium led to aberrant attachment of the PE cells to the heart, further exhibiting how crucial BMP is for the PE cells to home to the right place (Ishii et al., 2010).

1.5 Epicardium derived cells migration

Epicardial derived cells (EPDC) undergo EMT, at HH19, invading the myocardium and the subendocardial region and giving rise to the subepicardial mesenchyme, or subepicardium (Fig. 1.8; Lie-Venema et al., 2005). Not every region of the myocardium is permissive to EPDC infiltration. At HH19-22 only the inner curvature is permissive to EPDC, but by HH23 the epicardial cells invade most regions of the myocardium except the OFT. Only at HH26 and onwards do EPDC invade the myocardium of the OFT (Lie-Venema et al., 2005).

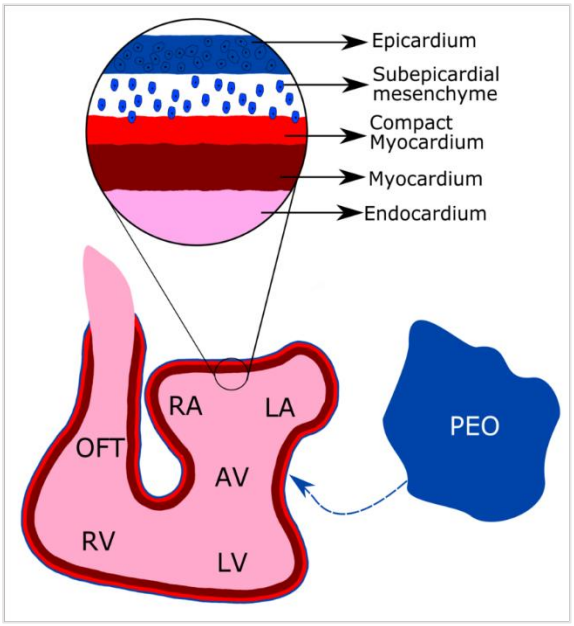

Figure 1.8: Epicardium derived cells migration. Cells migrate from the proepicardial organ (PEO) and cover the heart tube starting at the atrioventricular junction (AV). EPDC migrate from the epicardium into the myocardium creating the subepicardial mesenchyme. OFT: outflow tract. RV: right ventricle. LV: left ventricle. RA: right atrium. LA: left atrium.

EPDC can differentiate into a number of different cell types, which are important for the structural and functional integrity of the heart (Gittenberger-de Groot et al., 1998). For example, EPDC give rise to mural cells, which include smooth muscle cells (SMCs), found mainly in arteries and veins, and pericytes, found mainly in capillaries and venules. Mural cells become extremely important in the development of the coronary vessels (Gittenberger-de Groot et al., 1998). EPDC can also differentiate to fibroblasts, which are important for the formation of the heart's fibrous matrix. After HH32 EPDC can be detected in the AV cushions and in the AV valves suggesting a role in the maturation of the valves and cushions (Gittenberger-de Groot et al., 1998).

EMT in the epicardium is controlled by a number of signalling molecules, including transforming growth factor (TGF)-β and Wnt5a (von Gise et al., 2011; Olivey et al., 2006). TGFβ2 was found able to induce the production of hyaluronic acid, a major scaffolding constituent in the ECM, which in turn induces EPDC migration and differentiation (Craig et al., 2010). *WT1*, a zinc finger TF, expression is downregulated in heart migrating EPDC. WT1 promotes the expression of the zinc finger TFs *SNAIL1* and *SNAIL2 (SLUG*), genes that suppress the expression of adhesion proteins (e.g. E-cadherin). *SNAIL1* overexpression was found to promote migration of cultured avian epicardial cells (Martínez-Estrada et al., 2010; Takeichi et al., 2013). *Notch1* is expressed in EPDC in the subepicardium; since NOTCH1 also regulates EMT by regulating *Snail1* expression it is possible that it also promotes EMT for EPDC (del Monte et al., 2011). HAND2 also indirectly promotes epicardial EMT. Downregulation of *Hand2* in *Hand1* expressing cells, in mice, can lead to malformations in the epicardium and coronary vasculature (Barnes et al., 2011).

The movement of the migrating epicardial cells seems to be directed by the interaction of two proteins, blood vessel epicardial substance (Bves) and NDRG4 (Benesh et al., 2013). The interaction between Bves and NDRG4 is required for

the trafficking of the ECM glycoprotein fibronectin when it is internalized during the autocrine ECM fibronectin recycling pathway. Disruption of the interaction between these two proteins causes random cell migration (Benesh et al., 2013). Bves is also expressed in the cell junctions between the epicardium holding the cells together forming tight junctions (TJs; Wu et al., 2012). Evidence suggests that in zebrafish Bves can regulate the function of TJ and thus influence the barrier function of the epidermis. Bves possibly regulates TJ by anchoring atypical PKC on the plasma membrane, which phosphorylates claudins, a family of proteins that are key components in the paracellular barrier formation (Wu et al., 2012).

In vitro co-cultures involving zebrafish hearts with actively dividing epicardium, 84 hours post fertilisation (hpf), and hearts prior to epicardium formation, 60 hpf, have shown that the actively dividing epicardium of one heart goes on to cover the hearts without an epicardium (Yue et al., 2015). This migration assay was further tested using morpholino oligonucleotide (MO) for *silent heart* (*sih*) and *tbx5* in the epicardium recipient heart. Embryos with a *sih* knockdown have no heartbeat, due to ventricular acontractility, which was found to result in defective epicardial cell migration demonstrating *tbx5* is important for EPDC migration (Plavicki et al., 2014; Yue et al., 2015). There was minimal migration in the *sih* morphants and when migration did occur it was inhibited or significantly delayed. Similar defective migration was also found in *tbx5* morphants (Yue et al., 2015). These studies shows that *tbx5* expression in the myocardium is vital for the migration of epicardial cells, although *tbx5* expression in the epicardial cells was unaltered (Yue et al., 2015).

1.6 Genetics of EPDC development and differentiation

Retinoic acid (RA) signalling is required for cardiac development. RA is a product of the enzyme RALDH2, which expression is also regulated by WT1 (von Gise et al., 2011). TCF21 (capsuling/epicardin/Pod1) is a bHLH TF that is essential for EPDC differentiation into fibroblasts, while inhibiting their differentiation into

SMCs. This was demonstrated by studies in mice where *Tcf21* was deleted. In chicks RA signalling is required for the expression of *TCF21* (Braitsch et al., 2012).

In mice, Notch signalling was found to be significant in the development of the epicardium and EPDC function. The Notch ligands DELTA1/4 and JAGGED1 as well as the Notch receptors NOTCH2-4 were found to be active in the developing PEO. The epicardium and EPDC expressed *Notch2-4* from E11.5 (del Monte et al., 2011). The expression of *Notch2* in the PEO and epicardium suggests that it works as a differentiation suppressor while maintaining the epicardial features. Deletion of *Notch1* in the epicardium resulted in abnormal coronary vasculature, during E13.5, due do a reduction in the coronary arteries, and myocardial hypoplasia, possibly by a decrease in cell proliferation (del Monte et al., 2011). Notch overactivation was also found to cause myocardial hypoplasia and it also resulted in abnormal epicardium morphology and impaired differentiation (del Monte et al., 2011).

In mice the motility and contractility of the epicardial cells was found to be driven by the interaction between the TFs SRF and MRTF-A and B. MRTFs are upregulated in the epicardium before EMT and are required for the motility of EPDC that will become pericytes. Mice with knock downs for both *Mrtf*s in the epicardium have subepicardial haemorrhage and coronary plexus malformations (Trembley et al., 2015). In addition, the proteins YAP1 and TAZ, which are involved in Hippo signalling, can regulate the expression of WT1 and TBX18 (Singh et al., 2016). The ability of YAP1 and TAZ to regulate the expression of WT1 and TBX18 also means that they are involved in EMT and cell fate specification.

1.7 Epicardium related apoptosis and proliferation

Covering of the heart by the epicardium also seems to be correlated with an increase in programmed cell death, or apoptosis, in the underlying myocardium (Schaefer et al., 2004). Staining apoptotic cells with LysoTracker Red (LTR) and terminal deoxynucleotidyl transferase mediated dUTP nick end labelling (TUNEL)

have shown that apoptosis in the heart region follows a similar pattern with epicardial coverage. Apoptotic cells appear first in the inner curvature of the AV junction and then around the OFT region of the myocardium, during HH19-22. LTR staining revealed that apoptosis at the base of the OFT starts between stages HH22-23 (Schaefer et al., 2004).

The simultaneous peak in cell apoptosis together with the epicardial covering over the apoptotic areas leads to a number of speculations. There is the possibility that epicardial cells secrete pro-apoptotic factor or induce apoptosis by hypoxia. There is also the possibility that there is no connection between epicardial coverage and cell death (Schaefer et al., 2004). Epicardial cells and EPDC did not secret pro-apoptotic factors but hypoxia can lead to apoptosis and vascular development, thus connecting it with coronary vasculature development. Apoptosis in the OFT region also leads to the remodelling of the OFT, leading to the separation of the aorta and pulmonary artery (Schaefer et al., 2004). In addition, apoptotic multinucleated epicardial cells have been observed during regeneration (Cao et al., 2017).

The epicardium not only affects the apoptosis of the myocardium, through hypoxia, but also its proliferation. *Igf2*, which encodes for a protein growth factor with mitogenic activities, was found to be the most active mitogen in the epicardium of mice during midgestation of heart development (Li et al., 2011). Cardiomyocyte cultures were found to have a high cell proliferation index when co-cultured with epicardial cells, whereas a low proliferation index was found in cultures with only cardiomyocytes. Inhibition of the IGF2 receptors during the co-cultures eliminated the high proliferation effect, suggesting that the epicardium is needed for the proliferation of cardiomyocytes (Li et al., 2011). Further in vivo experiments showed that IGF2 affects predominately the proliferation of the ventricular myocardium. In mice the proliferation of compact zone cardiomyocytes was found to be dependent on IGF only during E10.5-14.5. After E14.5 the

proliferative index was comparable with the controls. The fact that by E14.5 coronary circulation is active might be responsible for the change in proliferative index since mitogenic factors can be transferred through the bloodstream (Li et al., 2011).

The growth factor *Fgf9* is also expressed in the epicardium and endocardium of the midgestation mouse heart (Lavine et al., 2005). FGF9 was found able to induce proliferation in the ventricular myocardium in vivo and in vitro. FGF9 exerts its effects on the myocardium by binding to FGFR1c and FGFR2c (Lavine et al., 2005). *Fgf9* and *Fgfr1c/2c* knock down mice have a hypoplastic compact myocardium, just like mice that are unresponsive to IGF2 (Lavine et al., 2005).

1.8 Epicardial fibroblasts and their contribution to the ECM

As stated previously, one of the major cell types that develops from the migrating EPDC are fibroblasts. As the heart develops in the embryo the number of fibroblasts increase and so does the amount of collagen they deposit (Camelliti et al., 2005). The study of fibroblasts is challenging due to the lack of a clear marker (Goldsmith et al., 2004). DDR2 is a receptor that binds to fibrillar collagen; although it is found in a number of cells it is absent from cardiac endothelial cells (EC), cardiomyocytes and SMCs. The absence of DDR2 expression in most of the heart makes it a very specific fibroblast marker, with the only other cells expressing it being certain white blood cells, which appear later in development (Goldsmith et al., 2004). *DDR2* null mice were found to have smaller heart and a lower collagen density, due to slower collagen deposition, compared to the wild type (WT; Cowling et al., 2014).

The transcription factor TCF21 was found to be indispensable for the development of cardiac fibroblasts (Acharya et al., 2012). Early during epicardial migration EPDCs expressing *TCF21* are multipotent, but as development progresses only fibroblasts express *TCF21* (Acharya et al., 2012). Mice with a *TCF21* knockout lack

epicardial derived cardiac fibroblasts; have lower collagen levels and a defective EPDC migration. Although *TCF21* null mice have a defective heart, epicardial apoptosis, proliferation and vessel formation seems to be normal (Acharya et al., 2012). In chicks, EPDC destined to become fibroblasts start invading the myocardium and the subendocardial region at HH25 and at HH32 they invade the AV cushions as well (Gittenberger-de Groot et al., 1998).

One of the features of heart failure is the accumulation of fibroblasts and the subsequent deposition of ECM (Segura et al., 2014). This makes the heart more rigid, harder to contract, and can lead to ischaemia. Mice with altered haemodynamics, due to a transverse artery constriction (TAC) causing pressure overload, were found to have increased fibrosis (Moore-Morris et al., 2014). This fibrosis did not come directly from the epicardium but from cardiac fibroblasts that originated from EPDC. The cardiac fibroblasts had increased proliferation leading to fibrosis (Moore-Morris et al., 2014). Ischaemic mouse models and humans with congestive heart failure (CHF), a disease where the blood is pumped inadequately from the ventricles, had epicardial fibrosis and an increased expression of all three main epicardial markers, *WT1, TBX18* and *TCF21*, in their subepicardial cells (Braitsch et al., 2013). In contrast, TAC mouse models and humans with cardiovascular disease had a greater increase of perivascular fibrosis and an increased expression of *TCF21*, without an increase in the other epicardial markers, *TBX18* and *WT1*, in the subepicardial cells (Braitsch et al., 2013).

Epicardial fibroblasts are in part responsible for the production of collagen XII, a fibril associated collagen with interrupted triple helices (FACIT), which forms complexes with collagen I (Marro et al., 2016). Collagen XII was found in the epicardium and subepicardium of early zebrafish embryos, outlining the ventricles, and its expression increased with development to the point where it fully encased the heart and penetrated into the compact myocardium. Although it is not known if collagen XII is expressed in the hearts of other animals, it is expressed in their

bone and muscle tissue and it can modify the stiffness of the tissue in response to shear stress (Chiquet et al., 2014; Marro et al., 2016).

1.9 The coronary vessels

1.9.1 Formation of coronary vessels

At HH18 the first vascular ECs can be detected near the sinus venosus (Poelmann et al., 1993). Around HH25 the early coronary vasculature is formed; these early vessels are endothelium lined without any SMC support and are connected to the sinus venosus but not to the aorta (Vrancken Peeters et al., 1999). The coronary vessels populate only the subepicardium and start invading the myocardium at HH26. From HH26 to HH31 the vessels extend into the heart arranging themselves in an equal distanced pattern (Vrancken Peeters et al., 1999).

The epicardial coronary system consists of a left and right artery, which arise from the coronary ostia of the aorta; although a range of normal phenotypes exist with up to five smaller coronary ostia (Waller et al., 1992). The main coronary arteries (CAs) are primarily located subepicardially but can also have sections into the myocardium. CAs have three layers, the inner layer (tunica) intima, the middle layer (tunica) media and the outer layer (tunica) adventitia (Waller et al., 1992). The intima consists of endothelial cells and a subendothelial layer of connective tissue and SMCs. The intimal layer is separated from the medial layer by an (internal) elastic membrane (Waller et al., 1992). The medial layer consist of multiple layers of SMCs and connective tissue. The medial layer is also separated from the adventitial layer by an (external) elastic membrane. The adventitial layer consists of fibrous tissue (Waller et al., 1992).

EPDC migration is required for the formation of mature coronary vessels and is important for blood circulation in the myocardium. The maturing coronary vessels attach to the aorta at HH33 but are not patent (Fig. 1.9). At that stage, apoptotic clusters appear at the interface between the coronary vessels and the aorta.

Eventually by HH35 the coronary vessels are patent (Fig. 1.9) and blood flows from the aorta to the rest of the heart (Bernanke and Velkey, 2002; Eralp, 2005).

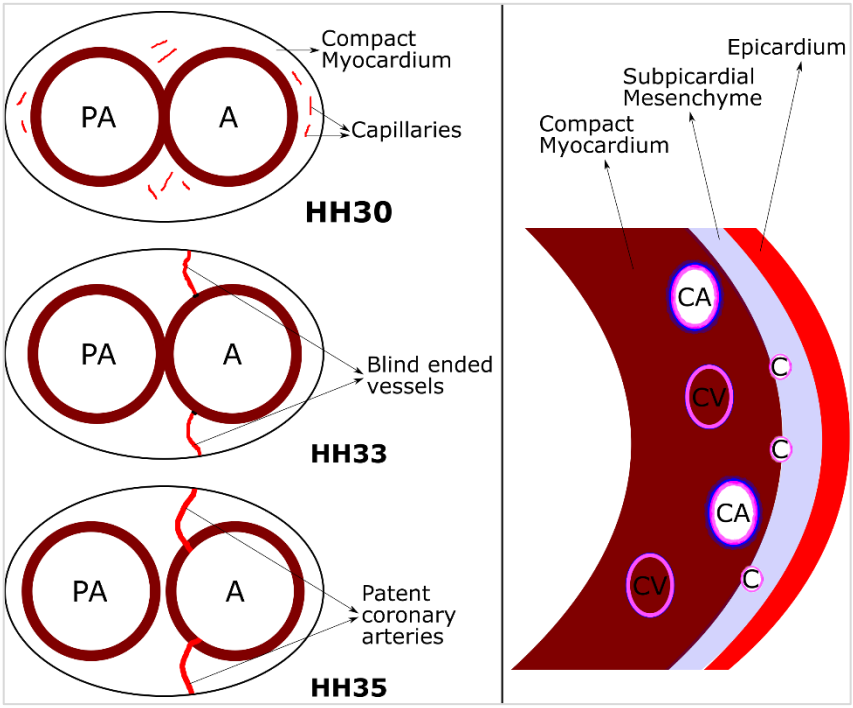

Figure 1.9: Normal formation of coronary arteries in different chick developmental stages. Healthy coronary arteries (CAs) have endothelial cells (pink) and smooth muscle cells (SMCs; blue). Coronary veins (CV) have less SMCs. Capillaries (C) do not have any SMCs. A: aorta. PA: pulmonary artery.

While it is clear that the epicardium has SMC precursors (Braitsch and Yutzey, 2013) that form the smooth muscles of the coronary vessels (Fig. 1.9), the origins of the ECs are not so apparent. Experiments on quail embryos suggest that endothelial precursor cells originate from the liver and migrate with the PEO to the heart, where they form the first capillaries in the subepicardium (Lie-Venema et al., 2005). Studies in mice, conducted by Katz et al. (2012), contradicted the conclusions drawn by Lie-Venema et al. (2005) by showing that specialised compartments of the epicardium, which do not express *Tbx18* or *Wt1*, are capable of giving rise to epithelial cells. In mice, *Scx* and *Sema3D* expressing cells in the

PEO are competent to give rise to ECs in vivo, when transplanted to chick embryos, and in vitro, during cell culture assays (Katz et al., 2012).

1.9.2 Coronary vessels and the epicardium

In chicks, complete mechanical inhibition of epicardial outgrowth, during HH15-17, results not only in embryonic death but also in a thin compact myocardium without coronary vasculature (Eralp, 2005). If the epicardial outgrowth is delayed, by approximately one day, the phenotype is less severe with surviving embryos having an abnormal coronary development and reduced myocardial volume. Coronary vessels in HH30 and HH35 embryos, with delayed epicardial outgrowth, had poor or absent development of the orifices that should connect to the aorta (Eralp, 2005). Apoptosis was also significantly reduced. Clusters of apoptotic cells, which are found where the CAs merge with the aorta, were greatly reduced and randomly scattered in the embryos with epicardial growth delay. The results suggested that the correct temporal development of the epicardium over the heart is crucial for coronary development (Eralp, 2005). *Wt1* null mice also have an absent coronary vasculature and epicardial defects. One of the genes that is regulated by WT1 is *Ntrk2*, which encodes for the receptor kinase TrkB. *Ntrk2* null mice do not have any epicardial defects but they were found to have diminished coronary vasculature. It is possible that TrkB interacts with the neurotrophic factor BDNF to promote blood vessel formation (Wagner, 2005).

1.9.3 The molecular genetics of coronary vessel development

Neuropilin 1 (NRP1) and neuropilin 2 (NRP2) are receptor proteins for a range of VEGF proteins and class-3 semaphorins (Herzog et al., 2001). In more detail, NRP1 can form a complex with VEFGR2, which results in the enrichment of VEGF signals received by the EC. Mutations inhibiting the ability of NRP1 to form a complex with VEGFR2 result in an increase in mortality and a decrease in myocardial vascularization (Fantin et al., 2014). *NRP1* is expressed in the ECs of nascent

arteries in a fashion similar to the arterial marker ephrin-B2. *NRP2* is expressed in vessels with low or no NRP1 expression making it a venous marker (Herzog et al., 2001).

In the mouse embryo, hematopoietic cells were found to already exist in the myocardium even before the coronary vessels mature and connect to the rest of the systemic circulation (Jankowska-Steifer et al., 2015). Further studies, using haematopoietic ablation in mouse models, suggest that haematopoietic progenitor cells are crucial for epicardial EMT and development of the coronary vasculature. *Runx1* is a TF that regulates differentiation of haematopoietic stem cells, and *Vav1* is a GTPase important in haematopoiesis. *Runx1* and *Vav1* null embryos had a hypoplastic coronary vasculature and underexpression of the TFs *Snail2* and *Twist1* (Lluri et al., 2015).

In the last two decades, there has been an increase in the research for early markers of ECs and SMCs, as well as genes that can affect the pattering of coronary vessels. For example, Bves was discovered to be an early marker of SMCs in the coronary vessels (Reese et al., 1999). FOG-2 is a cofactor that interacts with the GATA TFs. Mice with no *Fog-2* expression in their myocardium were found to have low *Icam-2* and *Flk-1* expression in the ECs and absence of coronary vasculature, although epicardial development was normal. Re-expression of *Fog-2* in these mice resulted in a WT phenotype (Tevosian et al., 2000). ECs secrete the growth factor PDGFB, which promotes the migration and maturation of mural cells. The now proliferating mural cells expand on the endothelium and reciprocate by secreting Angiopoietin 1 (ANGPT1), promoting the maturation of the vessel and tightening the junctions between the cells, preventing blood leakage (Udan et al., 2013). Myocardial specific overexpression of *Angpt1* was also found to disturb coronary vessel formation in mice. The transgenic mice's hearts had no coronary vessels but there was haemorrhaging and increased cell death (Ward et al., 2004).

These results show the importance of crosstalk between the myocardium and epicardium for the development of coronary vessels.

Experiments in *Tbx18* null mouse embryos also show no effect during the initial development of the PE and epicardium. As development progresses, the mutant mice demonstrate subsequent defects in their epicardial morphology and coronary vessel development (Wu et al., 2013). Furthermore, gene expression profiling of the *Tbx18* null mice revealed altered expression of a number of genes, including those that affect the development of the vascular system (e.g. *Vegf-A* and *Angiopoietin-1*). The coronary vessels in *Tbx18* null hearts had a poorly structured network with reduced branching and an overall smaller lumen diameter (Wu et al., 2013). The CAs had a smaller number of SMCs, possibly due to TBX18 being a premature SMC differentiation suppressor. The subepicardium of mutant mice contained dense clusters of erythroid cells, which are rarely seen in a normal subepicardium (Wu et al., 2013).

1.10 The epicardium in the adult

1.10.1 The epicardium as a part of the visceral pericardium

The pericardium in the adult is divided into two layers, the parietal layer and the visceral layer (Rodriguez and Tan, 2017). The parietal layer can be divided into a fibrous layer on the outside and a serous layer in the inside, both being fused together (Fig. 1.10). The visceral layer is also a serous layer, forming a mesothelium of loose connective tissue and epithelial cells (Rodriguez and Tan, 2017). The pericardial cavity separates the parietal layer from the visceral layer (Fig 1.10). The pericardial cavity is a space between the two layers containing serous fluid (plasma ultrafiltrate), which helps in the lubrication of the two layers resulting in diminished friction during heart movement (Jaworska-Wilczynska et al., 2016; Rodriguez and Tan, 2017).

The fibrous parietal layer, which is made from fibrous tissue with dense collagen, is attached to the mediastinum at various points. The serous undercoat of the parietal layer is a mesothelial tissue important for the deposition and absorption of pericardial fluid (Jaworska-Wilczynska et al., 2016; Rodriguez and Tan, 2017). The visceral layer becomes the quiescent epicardium in the adult and hence its importance is greatly diminished in relation to the epicardium during development. Although the epicardium has lost its high proliferating and cell differentiating properties the subepicardium can have fat pads and a number of nerves and blood and lymphatic vessels passing through it (Rodriguez and Tan, 2017).

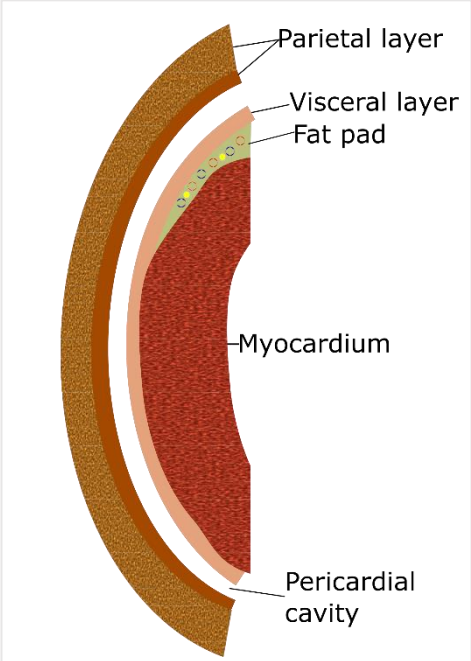

Figure 1.10: The pericardium in the adult. The parietal layer with its fibrous and serous components separated by the pericardial cavity from the visceral layer (epicardium). The sub epicardial space can have epicardial fat in its sub epicardium and also a great number of blood vessels (red for arteries, blue for veins) and nerves (yellow).

1.10.2 The regenerative potential of the adult epicardium

A myocardial infarction (MI) is caused by restricted blood flow to the heart with the most common cause being the blockage of a CA (e.g. atherosclerosis; Buja, 2005). The aftermath of an MI is mass cardiomyocyte death, in the area where the blood flow was restricted, through necrosis due to hypoxia. Formation of scar tissue then takes place reducing the contractility of the heart (Buja, 2005).

In adult zebrafish, a MI was found to increase the amount of *WT1* positive cells in the epicardium from 25% to 75% as well as causing an increase in other epicardial markers, including *Raldh* (Zhou et al., 2011). This increase of epicardial markers was also coincided with thickening of the epicardium from one cell layer to several. Increased proliferation of the quiescent WT1 cells was also observed not only in zebrafish but also in dogs and mice after a MI (Zhou et al., 2011). EMT in mice is normally absent in the adult epicardium, but it was also observed after a MI. EMT markers such as *SLUG* and *SNAIL* were upregulated in the *WT1*+ epicardial cells (Zhou et al., 2011). The adult human and mouse cells that had undergone EMT had a mesenchymal morphology, making them EPDC; these cells could also differentiate to SMC and fibroblast in vivo and in vitro (Moerkamp et al., 2016; Zhou et al., 2011). Although EPDC did not take an ECs fate after a MI, it was shown that they promote ECs growth through paracrine factors, further promoting vessel growth in the damaged area (Zhou et al., 2011). Using adult EPDC, taken after a MI and grown in conditioned media, and subsequently injecting them into a different mice group directly after a MI was induced, was proven to improve systolic function and contractility, in relation to untreated (Zhou et al., 2011).

1.11 Haemodynamics and development

1.11.1 The importance of haemodynamics during heart development

Haemodynamics is the dynamics of blood flow (Culver and Dickinson, 2010). Changes in the blood flow are mainly perceived by vascular ECs, in the form of shear stress, since they are in direct contact with the blood flow. ECs are able to detect haemodynamic changes via their mechanoreceptors, which are able to cause downstream effects in the cells (Culver and Dickinson, 2010). Differences in shear stress can cause changes in the methylation and acetylation of histones resulting in chromatin alteration and thus changes in gene expression (Illi, 2003).

In addition, an increase in shear stress causes endothelial progenitor cells to adopt an arterial fate (Obi et al., 2008).

There are three main mechanical forces that affect the heart, pressure, shear stress and stretch (Fig. 1.11). Blood flow induces shear stress, which is a force parallel to the endocardium (Andrés-Delgado and Mercader, 2016). Blood also creates a pressure force, which is applied perpendicular to the heart wall. Any changes in blood flow during contraction-relaxation as well as differences in blood viscosity can create a cyclic strain (Andrés-Delgado and Mercader, 2016). Strain can cause stretch to the myocardium; the factor that defines the ratio between stress and strain is the stiffness of the material. These forces can disturb normal homeostasis and result in extensive tissue remodelling (Andrés-Delgado and Mercader, 2016).

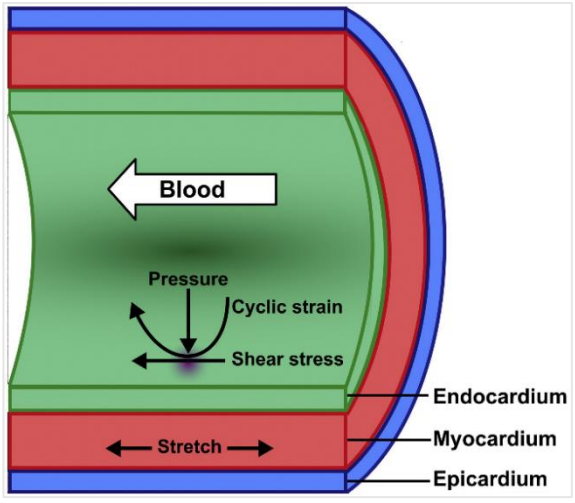

Figure 1.11: The main mechanical forces influencing cardiac development. Inside the heart, the blood and its flow apply pressure and shear stress to the endocardium as well as cyclic strain on the three heart layers. The underlying myocardium stretches as a response to the shear stress. Adapted from Andrés-Delgado and Mercader, 2016.

In the heart, mechanical forces seem to play an important role even before the need for an established circulation. Although the heart starts to beat by HH10 there is no laminar blood flow until HH12 (Hogers et al., 1995). In addition, although a primary circulation is established early on, no haemoglobin-mediated

transport of oxygen is observed until HH18 (Cirotto and Arangi, 1989). Furthermore, complete ligation of the OFT in HH20 chicken embryos showed that body growth and oxygen consumption was independent of cardiac output (Burggren et al., 2000).

By targeting α-myosin heavy chain (*MYH6*), which is important for the contraction of myocytes, using morpholino knock downs in the chick at HH12, HH14 and HH16, abnormal atrial septal development was seen (Rutland et al., 2009). Furthermore, mutations in the gene *MYH6* have been associated with atrial septal defects in humans (Ching et al., 2005). Furthermore, mice deficient in myosin light chain 2 (*MYL2*), which is important for atrial contraction, have looping and chamber morphology abnormalities due to diminished atrial function (Huang et al., 2003). In addition, mutations in zebrafish's sarcomeric proteins, cardiac troponin T (*tnnt2*) and a sarcomeric actin (*cfk*), result in endocardial cushion and valve defects due to a reduction in the myocardial function (Bartman et al., 2004). These factors suggest that haemodynamic forces and heart contractions play an important role in early heart morphogenesis, before they serve a functional role in oxygen transport.

1.11.2 Altering the haemodynamics in the adult

In adult animals, usually mice and rats, there are two main ways in which the haemodynamics can be altered; these involve constriction of the aorta or the left anterior descending (LAD) coronary artery (deAlmeida et al., 2010). Constriction of the aorta can be performed on its ascending, transverse (aortic arch) or abdominal (descending) section (Gs et al., 2014; Dai et al., 2016; deAlmeida, van Oort and Wehrens, 2010). All aortic constrictions produce a volume overload model with cardiac hypertrophy and heart failure.

Transverse artery constriction (TAC; i.e. constriction of the aortic arch) is the most common experimental pressure overload model; it initially induces cardiac hypertrophy but long term constriction leads to cardiac dilation and heart failure

(deAlmeida et al., 2010). Abdominal aortic constriction more specifically causes left ventricular hypertrophy, instead of generalised cardiac hypertrophy, and it can also lead to left ventricular dilation and heart failure (Dai et al., 2016). Ascending aorta constriction also causes left ventricular hypertrophy (Gs et al., 2014). LAD artery constriction is used to model MI and ischaemia and is associated with all the pathophysiological aspects of a MI (Kolk et al., 2009).

1.11.3 The chick as a model for altered haemodynamics

Animal embryo models with haemodynamics alterations develop phenotypes similar to human CHDs. Although a number of animal models have been used to study the alteration of haemodynamics on the cardiovascular system, including the zebrafish and mouse, the chick is the most widely used organism to study haemodynamic alterations during development (Bakkers, 2011; Kirby and Sahn, 2010). Some of the main reasons as to why the chicken (*Gallus gallus*) is one of the preferred models are, a four chambered heart similar to humans, development outside the mother offering ease of access, short developmental period (21 days) and the development of a variety of genomic resources making the analysis of vertebrate gene functions of the cardiovascular system possible (Brown et al., 2003; Ruijtenbeek, De Mey and Blanco, 2002).

1.11.4 Altering the haemodynamics during development

The three most common surgical alterations, which result in haemodynamically altered models, in chicken embryos are vitelline vein ligation (VVL), left atrial ligation (LAL) and outflow tract banding (OTB; Midgett and Rugonyi, 2014). VVL works by reducing the venous inflow and thus the haemodynamic load of the heart (Midgett and Rugonyi, 2014). VVL can cause ventricular septal defects, semilunar valve anomalies and PAA malformations (Hogers et al., 1999). LAL results in left heart hypoplasia via reduction of blood flow into the primitive ventricle (Midgett and Rugonyi, 2014). The reduced load on the ventricle results in differential

development of the left and right ventricle, with left ventricle hypoplasia as the main effect (Tobita and Keller, 2000).

VVL and LAL are beyond the scope of this thesis so we will only focus in OTB. OTB involves a ligature being made around the OFT (Fig. 1.12) resulting in its constriction and increasing the blood pressure in the heart's ventricle, thus increasing shear stress (Midgett and Rugonyi, 2014). Some of the most well described defects after OTB are ventricular septal defects and a range of pharyngeal arch artery malformations, with persistent truncus arteriosus being the most severe (Sedmera et al., 1999).

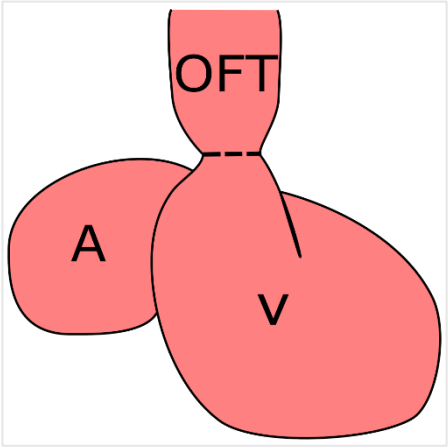

Figure 1.12: Outflow tract banding. The dotted lines show the position of the ligature around the outflow tract (OFT) during outflow tract banding. V, ventricles; A, atrium.

1.11.5 The mechanistic effects of outflow tract banding

Blood is a non-Newtonian fluid, a fluid of which the viscosity can be altered based on shear strain, the deformation due to shear stress (Cherry and Eaton, 2013). Furthermore, blood is a shear thinning non-Newtonian fluid, which means that its viscosity decreases as shear stress increases (Fig. 1.13). A higher shear stress will result in a higher shear strain on the blood and the surrounding tissue wall (Cherry and Eaton, 2013). This means that blood during systole, where the blood is forced out of the ventricles through the aorta and pulmonary artery (or OFT during

development), has a lower viscosity. On the other hand, at diastole, where the ventricles are filled with blood, blood's viscosity is higher.

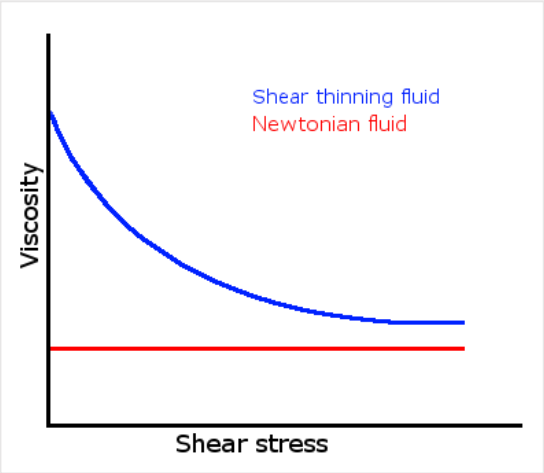

Figure 1.13: Viscosity of shear thinning and Newtonian fluids due to shear stress. Shear thinning fluids, like blood, have a lower viscosity when the shear stress is higher whereas Newtonian fluids maintain the same viscosity. Adapted from Çengel and Cimbala, 2006.

Blood flow in the ventricles and the outflow vessels is primarily laminar (Markl et al., 2011), which means a higher shear stress will be found near the walls of the ventricles and vessels rather than the inside. Thus, the viscosity will be lower in the middle of the cardiovascular system channels and higher at the sides near the walls. Under laminar flow, the reverse is true for blood velocity, which has a near parabolic profile, in the cardiovascular system channels, the velocity is lower near the wall of the channel and higher near the middle (Fig. 1.14A). Pipe models of turbulence in sheer thinning fluids have proven that although the velocity and viscosity patterns are similar to the laminar flow models, with a flatter velocity profile that plummets near the pipe wall (Fig. 1.14B), the wall shear stress is higher (Rudman et al., 2004). Turbulence also results in an increase of friction, resulting in the loss of energy in the form of heat (Smith, 1966). Thus, switching from a laminar to a turbulent blood flow, as happens with OTB, will require the heart to use more energy to drive the blood flow.

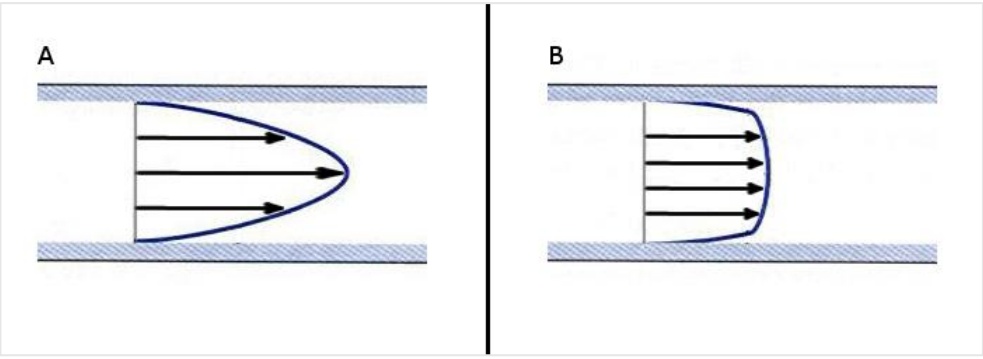

Figure 1.14: Laminar and turbulent flow velocity profiles. A laminar flow (A) is more energy efficient than a turbulent flow (B), which has a flatter velocity profile and a sharp decrease of velocity near the wall. Adapted from Çengel and Cimbala, 2006.

Within the literature OTB is predominately done between stages HH18 to HH21 (Sedmera et al., 1999; Stovall et al., 2016; Midgett et al., 2014). The ligature around the OFT causes a number of mechanistic effects at the OFT and the heart even before any major structural or genetic biological changes are evident. The changes seen in OTB cannot only be due to the physical restriction imposed by the ligature since the tissues above and below the band exhibit different mechanical aberrations. These mechanical responses can be observed in a matter of hours, while the embryo is still at the same HH stage, showing the adaptability of the heart (Shi et al., 2013; Stovall et al., 2016; Tobita et al., 2002). Although the motion of the ventricular wall was found to be identical between OTB and controls at HH18, the wall motion of the OFT wall undergoes faster expansion and contraction movements, rather than the peristaltic like movements seen in controls (Stovall et al., 2016). Blood pressure, wall shear stress and pulse wave velocity, the speed of the arterial pulse in the cardiovascular system, was also found to increase in the OFT of HH18 OTB embryos (Shi et al., 2013). In the ventricle of HH18 and HH21 OTB hearts, there is an increase in end-diastolic blood pressure and pressure amplitude (Shi et al., 2013; Tobita et al., 2002). Moreover, this increase was dependent on the tightness of the ligature (Shi et al., 2013).

Focusing in more detail on the tightness of the ligature and its mechanistic effects, it was found that the peak blood flow velocity (during systole) increases with band tightness, but if the ligature is made too tight peak blood flow velocity decreases (Midgett et al., 2014).

1.12 Preload and afterload changes in heart disease

1.12.1 Definition of preload and afterload

In its simplest form preload can be defined as the sum of factors, be it heart chamber pressure, radius or wall thickness, that affect the myocardial wall stress or tension at the end of diastole (Norton, 2001; Rothe, 2003). Likewise, afterload are all the factors that affect myocardial tension during systolic ejection. Systolic ejection is the pressure needed to be applied by the myocardium to eject blood during systole, where the ventricular chambers contract (Norton, 2001; Rothe, 2003). The preload and afterload definitions can be expressed mathematically using the Law of Laplace, which states that the wall stress (σ) is proportional to the chamber pressure (P) and radius (R) but inversely proportional to the wall thickness (w), giving the equation $\sigma=PR/2w$ (Norton, 2001; Rothe, 2003).

1.12.2 Changes in preload and afterload during heart disease

Change in one of the variables stated in the Law of Laplace, resulting in an increase in afterload, will result in a greater demand for oxygen by the myocardium (Norton, 2001). During heart disease, heart remodelling will commence to compensate for the changed factor in an attempt to decrease the wall stress back to normal. For example, in systemic hypertension, where the blood pressure is elevated, there is an increase in the afterload of the left ventricle (LV) since the chamber pressure is increased in order to eject blood into the aorta (Kimball et al., 1993). Heart remodelling will commence to decrease the afterload, by increasing the LV wall thickness, resulting in hypertrophy (Kimball et al., 1993).

Heart remodelling can also bring new problems instead of helping to alleviate heart disease. For example, aortic valve stenosis results in an increased LV afterload, which results in LV hypertrophy; hypertrophy results in a "stiffer" LV, increasing end diastolic pressure resulting in an increase in preload (Hachicha et al., 2007). The situation can get even worse with the high LV end diastolic pressure forcing blood back into the left atrium (LA), increasing the LA afterload, resulting in LA hypertrophy (Sanada et al., 1991).

1.13 Congenital heart diseases

1.13.1 Epidemiology of congenital heart diseases

In humans 0.9% of all the live born infants have a congenital heart disease (CHD; van der Linde et al., 2011). Prenatal fatal CHDs have been reported to be even higher reaching 5-10% (Hoffman, 1995). The epicardium is an extremely important factor in these diseases. The aetiology of CHD is largely unknown, with only 15% having a known genetic cause (Yuan et al., 2013). Most CHD with a genetic cause come from de novo mutations since only 2.2-4.2% of CHD in the population can be attributed to first degree relatives, with a CHD (Oyen et al., 2009).

A number of environmental factors have been documented to cause a CHD. CHDs were confirmed in 3.6% of babies born by diabetic mothers in contrast to 0.74% in babies of non-diabetic mothers (Wren et al., 2003). The most common malformations were transposition of great arteries and truncus arteriosus. Pre-existing maternal diabetes increases the risk of the offspring being born with a CHD by five-fold (Wren et al., 2003). Maternal rubella infections during pregnancy can result in offspring with pulmonary valve abnormalities and VSDs (Jenkins et al., 2007). In addition, other febrile illnesses during the first trimester of pregnancy increase the risk of CHD in the offspring by two-fold. Maternal HIV infection can be transmitted vertically to the baby and result in CHDs such as

dilated cardiomyopathy (Jenkins et al., 2007). A number of teratogens can also cause CHD; some of them are thalidomide, alcohol and cigarette smoking (Jenkins et al., 2007). Epigenetics also play a role in the development of CHDs. Patients with tetralogy of Fallot have increased methylation levels in certain DNA parts of the genes NKX2.5 and HAND1 (Sheng et al., 2013). An increase in methylation was found to correlate with a decrease in mRNA levels of the methylated genes in cardiac tissue (Sheng et al., 2013).

1.13.2 Ventricular septal defect

A ventricular septal defect (VSD) is the most common CHD making up to 42% of all the CHDs (Hoffman and Kaplan, 2002). A VSD is commonly associated with other CHD malformations and it can have different diameters ranging from small, requiring no operation, to dangerously large, which will result in further problems and eventual heart failure (Ottaviani and Buja, 2016). In cases where an individual has multiple holes in the IVS, other CHDs are commonly associated such as a double outlet right ventricle (Ottaviani and Buja, 2016).

The amount of flow between the ventricles with a VSD is affected by the size of the defect and the resistance of the vascular and systemic vessels (Penny and Vick, 2011). A VSD can result in a left to right shunt, where most blood is ejected from the LV to the RV due to the high pressure of the LV. In patients with a large VSD a right to left shunt might develop due to a high blood volume returning from the pulmonary circulation and pulmonary hypertension (Penny and Vick, 2011). In patients with a large VSD and no pulmonary hypertension LV dilation can occur (Kleinman et al., 2007).

1.13.3 Outflow tract anomalies

A double outlet right ventricle (DORV; Fig. 1.15B) accounts for 0.9% of all CHDs (Go et al., 2014). DORV is a condition where both great arteries, the aorta and pulmonary artery, arise from the right ventricle, although they could arise from

the left one in a condition called double outlet left ventricle (Neeb et al., 2013; Ottaviani and Buja, 2016; Thiene and Frescura, 2010). DORV is accompanied with a VSD since there is no other way for the returning blood of the left ventricle to pass through the rest of the cardiovascular system (Neeb et al., 2013; Ottaviani and Buja, 2016).

A persistent truncus arteriosus (PTA; Fig. 1.15A) is the consequence of the OFT's failure to septate, resulting in one common arterial trunk, making up to 1% of all CHDs (Neeb et al., 2013; Ottaviani and Buja, 2016). The arterial trunk can be found exiting the right or left ventricle and this can also be associated with the size of the VSD, which accompanies a PTA (Adachi et al., 2009). Both PTA and DORV cause cyanosis in the new-born due to mixing of oxygenated and unoxygenated blood resulting in a blue skin discolouration. In addition both can result in a right to left shunt through the VSD, instead of the most prevalent left to right (Ottaviani and Buja, 2016).

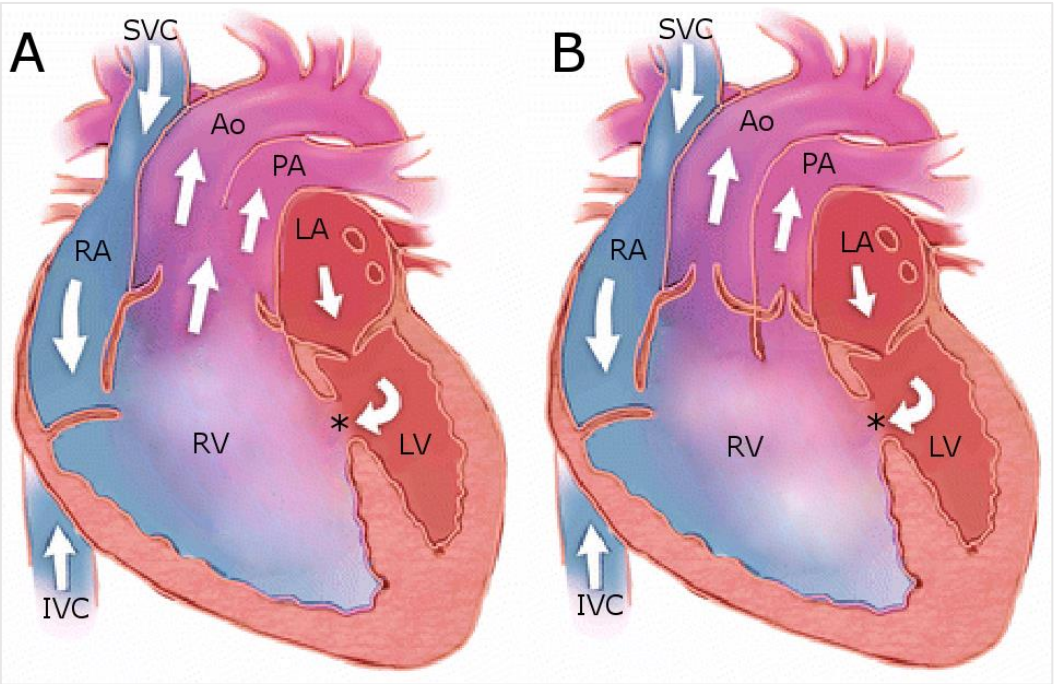

Figure 1.15: Outflow tract anomalies accompanied by a ventricular septal defect. (A) A persistent truncus arteriosus causing blood from the right ventricle (RV) to go in both the aorta (Ao) and pulmonary artery (PA). A

ventricular septal defect (VSD; asterisk) also causes blood from the left ventricle to go in both great arteries. (B) A double outlet right ventricle with an overriding VSD (asterisk) on the PA. Key: RA, right atria; LA, left atria; SVC, superior vena cava; IVC, inferior vena cava. Adapted from Giannopoulos et al., 2015.

1.13.4 An aberrant epicardium could cause congenital heart diseases

Without the epicardium being able to contribute cells to the developing heart, structural malformations occur, including malformation of valve cushion and CAs (Wessels et al., 2012; Eralp, 2005). Since the migration of the PEO and the expansion of the epicardium along the heart is a complex process, any deviations from its regular development could potentially not only cause an aberrant epicardium and its cell lineages, but also have downstream effects on the remodelling of the rest of the heart. Since in the adult the epicardium is quiescent, any minor epicardial aberrations that could cause a CHD during development might not be visible in the adult, whereas any major aberrations could lead to a fatal prenatal CHD, which have not been looked at in detail (Gittenberger-de Groot et al., 2000; Rodriguez and Tan, 2017). These reasons make the epicardium a major candidate for the development of CHDs, which could include aberrant CV development.

There are studies that support the link between epicardium development and CHDs. There is an association between CHDs and CA anomalies, with 1.5% of patients with a CHD having a CA anomaly (Tuzcu et al., 1990). Later research shows that patients with a complex CHD (e.g. tetralogy of Fallot) have a higher prevalence of congenital heart diseases (Yu et al., 2013). Both, abnormal differentiation of SMC progenitors and aberrant epicardial EMT can affect coronary progenitors cell numbers or their maturation. In addition, epicardial EMT takes place in the AV groove, which results in an epicardially-derived mesenchyme in the AV cushions (Wessels et al., 2012). Epicardially-derived fibroblasts

differentially contribute to the different developing leaflets of the AV valves. The unequal contribution of epicardial and endocardial cells in the leaflets of the AV valves could explain aberrations that affect individual components of valve development (Wessels et al., 2012).

1.14 Project's aims

Preliminary studies from the Loughna laboratory have shown that a morphologically abnormal epicardium was present in OTB chick hearts at HH29 (Fig. 1.16; Pang, 2016). In OTB hearts, the left ventricle had an increased lumen volume of 43.6% as well as a 40.7% thinner myocardium, compared to shams. The left atrium also had an increased lumen volume of 47.4% as well as a 40.7% thinner myocardium (Pang, 2016). There was no significant difference in the right ventricle or the right atria. The epicardium also had an abnormal morphology and an increased volume of 60.1%. The thickened epicardium phenotype had a 43% penetrance (Pang, 2016). Although an aberrant or absent epicardium was reported in experiments where proepicardial migration or heartbeat was inhibited (Gittenberger-de Groot et al., 2000; Plavicki et al., 2014), there is no literature on the effects of OTB on epicardial development.

This project is separated into three parts, all using the OTB model. One part looks at the abnormal morphology of the epicardium at HH29. A second part investigates the development of the SMCs and the coronary vasculature at HH35 and the last one at the development of fibroblasts and changes in the structure of the ECM, at HH35. The null hypothesis (H_0) is that although the epicardial morphology was aberrant, the epicardium and its cell lineages, SMCs and fibroblasts, will have no functional effect in the heart. The alternative hypothesis (H_a) is that there will be a functional effect on either the epicardium itself or its cell lineages.

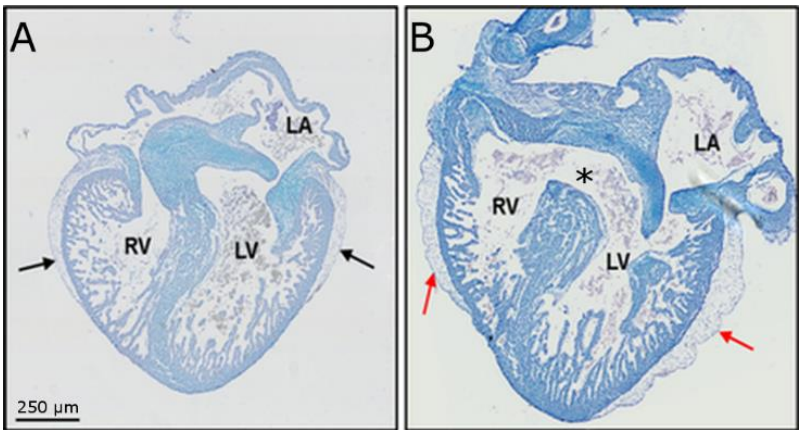

Figure 1.16: Gross morphology of an outflow tract banded and control hearts. Compared to sham **(A)** outflow tract banded hearts **(B)** were found to be larger with an increased lumen volume, but a thinner myocardium, in left ventricle (LV) and left atria (LA). There was no significant difference in the right ventricle (RV) or the right atria. The epicardium (red arrows) also had an abnormal morphology and an increased volume in comparison to the epicardium of the shams (black arrows). Banded hearts also had a ventricular septal defect (asterisk). Image taken from Pang, 2016.

2 Methods

2.1 Outflow tract banding and tissue isolation

2.1.1 Ethical approval and the banding procedure

All works in this study are Schedule 1 procedures and have been ethically reviewed at the University of Nottingham and all procedures and facilities are compliant with local and institutional guidelines. *Gallus gallus* fertilised eggs (Henry Stewart & Co, UK), of the white leghorn variety, were placed at 38 ^{o}C in a humidified rotating incubator. At HH21, the eggs were fenestrated. The OTB embryos had their OFT constricted with a transverse, double overhang knot using an ETHILON® Nylon Suture (Ethicon; W1770), which had a 3/8 circle needle attached to a 10-0 suture. The needle was passed below the proximal OFT using surgical forceps. A double overhang knot was made near the end of the suture. The knot was tightened around the OFT, with the loop's diameter matching the diameter of the eye of the chick embryo, and then the suture's ends were trimmed to match the radius of the fenestration. The "shams" had the suture passed below the OFT but no ligature was made. Any embryos that showed haemorrhage during the banding procedure or had phenotypic malformations were excluded from the studies. The banding procedure was carried out using a Stemi SV 11 stereomicroscope (Carl Zeiss). In both groups the fenestration was covered with microporous masking tape and the eggs were reincubated at 38 ^{o}C in a humidified incubator without rotation. The eggs were incubated until they reached the required stage, depending on the study's requirements. Incubation times as well as the staging criteria were according to Hamburger Hamilton stages (Hamburger and Hamilton, 1992).

2.1.2 Qualitative assessment of the procedures and tissue isolation

Upon reaching the required developmental stage, the embryos were severed from the chorion and vitelline membranes and if they were older than HH26 they were also decapitated. The embryos were then transferred to 1X phosphate buffer saline

(PBS) and morphologically assessed for their phenotype. The OTB hearts were only harvested if the suture was still attached around the OFT with the knot intact. Both OTB and shams were assessed for any other visible morphological abnormalities not associated with their respective phenotype. Any embryos with structural deformities or developmental delays were excluded from further studies. Hearts were isolated for all described studies except whole mount in situ hybridisation, where whole embryos were used. Whole embryos or heart tissue were further isolated from any membranes in 1X PBS (Thermo Scientific) after decapitation, and were transferred to 4% paraformaldehyde (PFA), diluted in PBS, for fixation overnight or were snap frozen in liquid nitrogen and kept at -80 ^{o}C.

2.2 Tissue processing and sectioning

Fixed HH29 and HH35 hearts were dehydrated in increasing concentrations of ethanol (EtOH; Table 2.1) diluted in deionised water (dH_2O). The processed hearts were placed in paraffin wax blocks for longitudinal sectioning in an anterior to posterior fashion. Hearts were sectioned on a DSC1 microtome (Leica). Sections were floated onto a 42 ^{o}C water bath (Leica) and were then collected onto 3-aminopropyltriethoxysilane (APES)-treated glass slides (Sigma Aldrich), unless stated otherwise. Slides were then left to dry at 40 ^{o}C on a hot plate (Leica) overnight.

	HH29		HH35	
Placed in:	**Time (minutes)**	**Repeats**	**Time (minutes)**	**Repeats**
PBS	30	3	50	3
dH_2O	30	3	50	3
50% EtOH (with dH_2O)	30	3	50	2*
75% EtOH (with dH_2O)	45	2	50	3
95% EtOH (with dH_2O)	45	2	50	3
100% EtOH	45	2*	50	2*
Xylene	60	3	100	3
Xylene:wax (1:1)	60	1	60	1
Wax	60	2	60	3

Table 2.1: The processing of HH35 hearts in order to be embedded in paraffin blocks, after the PFA step. *Overnight wash was performed after the second repeat.

2.3 Apoptosis and proliferation study

HH29 hearts (n=3 per treatment group) were serially sectioned into five slide groups, with each section of tissue going to the next slide group (from the 1st to the 5th) and restarting from the 5th to the 1st again. One of these groups was used for the apoptosis study and another group for the proliferation study. All sections had a thickness of 5 μm and were collected on superfrost plus slides (Thermo Fisher Scientific). This study was done in collaboration with Dr. Kar Lai Pang. All the stained sections were digitally captured using the University of York Imaging and cytometry facility's AxioScan.Z1 slide scanner (Carl Zeiss). Visual analysis was performed using the ZEN 2 (blue edition; Carl Zeiss) software. DAB and DAPI positive cells were counted manually in the epicardium of alternating sections. A *t*-test was used to assess statistical significance.

2.3.1 Apoptosis study

For the apoptosis study, the sections were deparaffinised in xylene and rehydrated in decreasing concentrations of alcohol. The ApopTag® Peroxidase In Situ Apoptosis Detection (S7100; Millipore) kit and protocol was used for the apoptosis study. The manufacturer's instructions were followed with the following variations.

Proteinase K (20 µg/ml; Sigma Aldrich) was applied to the sections for 15 minutes at RT and then washed with dH_2O. Endogenous peroxidase activity was quenched using 3% hydrogen peroxide in 1X PBS for 10 minutes. Equilibration buffer was applied to the sections for 15 minutes. Working terminal deoxynucleotidyl transferase (TdT) enzyme was applied on the sections, which were incubated at 37 ^{o}C for one hour. Stop/wash buffer was applied on the sections for 10 minutes at RT. Sections were then washed with PBS and goat anti-digoxigenin conjugated antibody was applied for 30 minutes in a humidified incubator at RT. Sections were rinsed with PBS and 200 µl 0.05% 3,3 diaminobenzidine (DAB) with 0.03% hydrogen peroxide in PBS was applied. DAB colour development was monitored under a microscope until an acceptable colour intensity was reached. The sections were then washed in dH_2O. For counter staining, sections were treated with DAPI diluted in dH_2O (1:500, Sigma Aldrich) for 15 minutes and washed with dH_2O. Aqueous mounting medium was applied and the slides were sealed with a coverslip using nail varnish. For a positive control, heart sections were pre-treated with DNase I before incubating them with the equilibration buffer. For a negative control, working strength TdT enzyme was substituted with PBS, with all other steps remaining identical.

2.3.2 Proliferation study

For the proliferation study, the sections were deparaffinised in xylene and rehydrated in decreasing concentrations of alcohol. The proliferating cell nuclear antigen (PCNA) Staining (Invitrogen) kit and protocol was used for the proliferation study. The manufacturer's instructions were followed with the following variations.

The sections were treated with 3% H_2O_2, diluted in methanol, for 30 minutes and then washed with 1X PBS at RT. Then they were treated with blocking solution for 20 minutes followed by mouse biotinylated anti-PCNA primary antibody for one hour. The sections were washed in PBS, treated with streptavidin peroxidase for 15 minutes and then washed in PBS again. The sections were then treated with DAB chromogen and washed in dH_2O; followed by DAPI diluted in dH_2O (1:500, Sigma Aldrich) for 15 minutes and washed with dH_2O. Aqueous mounting medium was applied to the slides and then they were sealed with a coverslip using nail varnish. For a negative control, the primary antibody solution was substituted with PBS.

2.4 HH35 fluorescent immunohistochemistry

HH35 hearts (n=3 per treatment group) were serially sectioned into five groups, as previously described. One of these groups used for the coronary vessels study and another group for the fibroblast and extracellular matrix study. All sections had a thickness of 5 μm.

2.4.1 Coronary vessels

The sections were deparaffinised and hydrated in decreasing concentrations of ethanol and permeabilized with 0.1% Triton X-100 (Fisher) for 20 minutes. The slides were washed in PBS three times for five minutes each. The sections were blocked with a mixture of 10% normal goat serum (Invitrogen), 1% bovine serum albumin (BSA) and PBS for two hours.

The sections were incubated overnight at 4 ^oC with mouse α-smooth muscle actin antibody (A2547; Sigma-Aldrich), diluted 1:400 in 1% BSA/PBS. Then the sections were washed in PBS three times, five minutes each. The sections were incubated for one hour at RT with Alexa Fluor 594 goat anti-mouse antibody (R37121; Life Technologies), diluted 1:500 in 1% BSA/PBS. Then the sections were washed in PBS three times, five minutes each. DAPI, diluted in PBS (1:500, Sigma Aldrich),

was added for 15 minutes and washed with PBS three times, five minutes each. Mowiol 40-88 (Sigma-Aldrich) was used as mounting medium and No. 1.5 coverslips were added to the slides, sealed with nail varnish.

Images were taken, using Zeiss Axiovert 200M (Carl Zeiss) inverted microscope, in a tiled fashion to be used for stitching. Stitching was achieved in ImageJ using the Grid/Collection Stitching method (Preibisch et al., 2009). The average number of vessels, smooth muscle cell (SMC) area (μm^2), lumen area (μm^2) and wall (SMC) area to lumen area ratio was measured using ZEN 2 (blue edition; Carl Zeiss). Statistical significance between groups was assessed using Hotelling's T^2 test and a *t*-test for each dependent variable.

2.4.2 Fibroblasts and extracellular matrix

The sections were deparaffinised and hydrated in decreasing concentrations of ethanol and permeabilized with 0.1% Triton X-100 (Fisher) for 20 minutes. The slides were then washed in tris-buffered saline (TBS; Sigma Aldrich) with 0.1% Tween 20 (TBST; Sigma Aldrich) three times for five minutes each. The sections were blocked with a mixture of 10% normal goat serum (Invitrogen), 1% bovine serum albumin (BSA) and TBST for two hours.

The sections were incubated overnight at 4 ^{o}C with mouse anti-TCF21 (sc377225; Santa Cruz) and rabbit anti-collagen I (PA1-26147; Fisher) antibodies, diluted 1:200 in 1% BSA/TBST. Then the sections were washed in TBST three times, five minutes each. The sections were incubated for one hour at RT with Alexa Fluor 568 goat anti-rabbit (ab175471; Abcam) and 488 goat anti-mouse antibody (ab150113; Abcam), diluted 1:400 in 1% BSA/TBST. Then the sections were washed in TBST three times, five minutes each. DAPI, diluted in PBS (1:500, Sigma Aldrich), was added for 15 minutes and washed with PBS three times, five minutes each. Mowiol 40-88 (Sigma-Aldrich) was used as mounting medium and No. 1.5 coverslips were added to the slides, sealed with nail varnish.

Sections were digitally captured using the University of York Imaging facility's AxioScan.Z1 slide scanner (Carl Zeiss). TCF21 analysis was performed on alternating sections using the ZEN 2 (blue edition; Carl Zeiss) software, by counting the cells manually in the myocardium, epicardium and atrioventricular canal and using a *t*-test to assess statistical significance.

Twelve alternating sections from each sample, with both the epicardium and the AV canal present on each section, were chosen for further analysis. Fiji (Schindelin et al., 2012) was used to quantify the void to area fraction (VAF) of collagen I and count TCF21+ and TCF21- cells in a region of interest (ROI). The ROI was kept at a constant area of 0.06 mm^2 for the epicardium and 0.015 mm^2 for the AV canal. The ROI's width and height changed to accommodate the size of the epicardium. The major and minor axes of the ROI were also measured using Fiji. Correlation and regression statistics were used between the VAF and TCF21+cell number. The ratio of the minor and major axes, between groups, was also assessed using a t-test.

2.5 HH29 fluorescent immunohistochemistry

HH29 hearts (n=4 per treatment group) were serially sectioned into three slide groups, with each section of tissue going to the next slide group (from the 1st to the 3rd) and restarting from the 3rd to the 1st again. One of these groups used for the myocardium and extracellular matrix study. All sections had a thickness of 5 µm.

2.5.1 Myocardium and extracellular matrix

The sections were deparaffinised and hydrated in decreasing concentrations of ethanol and permeabilized with 0.1% Triton X-100 (Fisher) for 20 minutes. The slides were then washed in TBS (Sigma Aldrich) with 0.1% Tween 20 (TBST; Sigma Aldrich) three times for five minutes each. The sections were blocked with

a mixture of 10% normal goat serum (Invitrogen), 1% bovine serum albumin (BSA) and TBST for two hours.

The sections were incubated overnight at 4 °C with mouse anti-MYH1E (MF20; DSHB), which detects sarcomeric myosin, diluted 1:50 in 1% BSA/TBST, and anti-collagen I (PA1-26147; Fisher) antibodies, diluted 1:200 in 1% BSA/TBST. Then the sections were washed in TBST three times, five minutes each. The sections were incubated for one hour at RT with Alexa Fluor 568 anti-rabbit (ab175471; Abcam) and 488 anti-mouse antibody (ab150113; Abcam), diluted 1:400 in 1% BSA/TBST. Then the sections were washed in TBST three times, five minutes each. DAPI, diluted in PBS (1:500, Sigma Aldrich), was added for 15 minutes and washed with PBS three times, five minutes each. Mowiol 40-88 (Sigma-Aldrich) was used as mounting medium and No. 1.5 coverslips were added to the slides, sealed with nail varnish.

Twelve alternating sections from each sample, with both the epicardium and the AV canal present on each section, were chosen for further analysis. Fiji (Schindelin et al., 2012) was use to quantify the VAF of collagen I and count the total number of cells in a ROI. The ROI was kept at a constant area of 0.06 mm^2 for the epicardium and 0.015 mm^2 for the AV canal. The ROI's width and height changed to accommodate the size of the epicardium. The major and minor axes of the ROI were also measured using Fiji. The ratio of the minor and major axes and cell numbers between groups was assessed using a t-test.

2.6 Immunoblotting

2.6.1 Sample preparation

HH29 and HH35 snap frozen hearts (n=6 per treatment groups, for both stage studies) were thawed at 4 °C and centrifuged at 94 x g for one minute. Any excess PBS was removed and the tissue was rinsed with ice cold PBS and centrifuged again. Any excess PBS was removed and 200 µl of lysis buffer (recipe in Table 2.2)

was added. The tissue was homogenised by passing them through a 21G and 23G needle multiple times and then sonicated. The homogenised sample was centrifuged at 94 x g for one minute and left in ice for 10 minutes. The samples were centrifuged at 10,000 x g for 20 minutes and the supernatant was stored at -20 °C. Protein concentration was determined by Bradford protein assay (Sigma). Then the samples were mixed with 5X SDS sample buffer (5:1; recipe in Table 2.3) and heated at 95 °C for five minutes. The samples were then centrifuged at 16,200 x g for one minute and stored at -20 °C.

Reagent	Working Conc.
Tris (pH 7.6)	50 mM
Sucrose	250 mM
Sodium Dodecyl Sulphate	2%
Sodium deoxycholate	0.5%
cOmplete™, Mini Protease Inhibitor Cocktail (Sigma-Aldrich)	1 tablet/10 ml

Table 2.2: The recipe for the lysis buffer.

Reagent	Working Conc.
Tris (pH 6.8)	250 mM
Glycerol	50%
SDS	5%
Bromophenol blue	0.05%
β-mercaptoethanol	25 mM

Table 2.3: The recipe for 5X SDS sample buffer.

2.6.2 Western blotting

The samples were run on an SDS-PAGE gel (recipe in Table 2.4) in 1X running buffer (recipe in Table 2.5) at 200 V, with precision plus protein dual colour

standards ladders (Bio-Rad) at both ends of the gel. The gel was run until the dye front reached the bottom of the gel, and then it was transferred to a nitrocellulose membrane (Pall Corporation) at 350 mA for 90 minutes with 1X transfer buffer (recipe in Table 2.6). The membrane was then covered with Ponceau S stain (Sigma) for a reversible detection of protein bands and it was subsequently washed with dH_2O. After the transfer the membrane was blocked using 5% BSA in TBST for one hour at RT. Immunoblotting was performed using the following primary antibodies, in 5% BSA-TBST, mouse anti-TCF21 (sc377225; Santa Cruz) at 1:750, rabbit anti-GAPDH (ab9485; Abcam) at 1:500, mouse anti-N-cadherin (6B3; DSHB) at 1:100 and mouse anti-E-cadherin (8C2; DSHB) at 1:25 dilutions. The secondary antibodies used were horseradish peroxidase (HRP) conjugated rabbit anti-mouse (P0260; Dako) at 1:2,000 and swine anti-rabbit (P0217; Dako) at 1:2,000, also diluted in 5% BSA-TBST. Development was carried out using the Amersham ECL Western Blotting Detection Reagents (GE Healthcare) for chemiluminescence and detected using photographic film (GE Healthcare).

Reagent	Working Conc.
dH_2O	-
30% acrylamide/bisacrylamide	10%
1.5 M Tris (pH 8.8)	0.39 M
SDS	0.1%
TEMED	0.04%
10% APS	0.1%

Table 2.4: The recipe for a 10% SDS-PAGE gel.

Reagent	Working Conc.
dH_2O	-
Tris-base	25 mM
Glycine	0.192 M
SDS	1%

Table 2.5: The recipe for 1X running buffer.

Reagent	Working Conc.
dH_2O	-
Tris-base	25 mM
Glycine	0.192 M
SDS	1%
Methanol	10%

Table 2.6: The recipe for 1X transfer buffer.

The photographic film was electronically scanned in TIF format. Both studies at HH29 and HH35 were repeated in triplicates. The analysis was carried out in Fiji using the relative density of the pixels in each protein band, which was then normalised against GAPDH. The average relative expression of each protein for each treatment group was then statistically assessed with a t-test.

2.7 RNA isolation

Snap frozen hearts were homogenized in TRI Reagent® (Sigma-Aldrich; 1ml for 50-100 mg of tissue), using a needle and syringe. Then 1-bromo-3-chloro-propane (BCP; Sigma-Aldrich) was added in a 1:5 (BCP:TRI Reagent®) ratio. The mixture was shaken and centrifuged at 10,000 x *g* for 15 minutes at 4 °C. The upper aqueous phase was transferred to a new Eppendorf tube where 2 M pH 4 Sodium Acetate (NaAc; Fisher Scientific) and isopropanol were added in a 1:4 (NaAc:TRI Reagent®) and 7:10 (Isopropanol:TRI Reagent®) ratio. The mixture was incubated overnight at -20 °C.

The overnight mixture was put in the centrifuge at max speed (17,200 x *g*) for 15 minutes at 4 °C. The supernatant was discarded and the pellet was washed with 1 ml 70% ethanol and then centrifuged again. The supernatant was discarded and the pellet was washed with 300 µl 70% ethanol and centrifuged again. The ethanol was removed/left to evaporate and 87.5 µl of DEPC treated H_2O was added. The pellet was dissolved and 10 µl of RDD buffer and 2.5 µl of DNaseI (Qiagen) were added. The mixture was incubated at RT for 15 minutes. Subsequently, 400 µl of DEPC treated H_2O and 500 µl of phenol:chloroform was added, mixed and

centrifuged at 11,000 x *g* for 9 minutes at 12 °C. Then 500 µl of supernatant were removed, mixed with 500 µl of chloroform and centrifuged again. The supernatant was removed and mixed with 3 M NaAc pH 5.2 and 100% ethanol in a 10:1 (RNA:NaAc) and 1:2 (RNA:EtOH) ratio and left overnight at -20 °C.

The overnight mixture was centrifuged at 17,200 x *g* for 13 minutes at 4 °C. The supernatant was discarded and the pellet was washed with 1 ml 70% ethanol and then centrifuged again. The supernatant was discarded and the pellet was washed with 300 µl 70% ethanol and centrifuged again. The ethanol was removed/left to evaporate and 52 µl of DEPC treated H_2O was added. Purity of RNA was checked using NanoDrop 2000 (Thermo Scientific) and the samples were stored at -80 °C.

2.8 RNA-Sequencing

RNA-sequencing at HH29 (n=3 per treatment group) was performed by Dr. Kar Lai Pang and Dr. Matt Parnall in collaboration with the University of Nottingham Deep Seq department using an Illumina NextSeq500. The samples were globin depleted by Dr. Matt Parnall (for more information see Parnall, 2017). After trimming of low-quality reads and adaptor sequences, the sequence reads were mapped onto the reference chicken genome galGal4 (UCSC). The mapping quality was scored and the read counts for each gene were calculated using unique and correctly aligned reads. The reads per kilobase of transcript per million mapped reads (RPKM) for each gene was normalised against the total number of mapped reads (Mortazavi et al., 2008). Differential gene expression was analysed using the R package DESeq (Anders and Huber, 2010). A $p<0.5$ and fold-change>2 were used as the DESeq thresholds.

2.9 cDNA synthesis

cDNA synthesis was performed according to the SuperScript™ II Reverse Transcriptase (Invitrogen) protocol. Reagents and concentrations can be found in Table 2.7. Hexamers, dNTPs and 13 µl dH_2O were added to the RNA samples. The

mixture was incubated at 65 °C for 5 minutes and then was placed on ice. The reverse transcriptase (RT) buffer, DTT and RNaseOUT was also added to the mixture. RT+ samples had SuperScript II RT added to them, in RT- samples SuperScript II RT was replaced with dH_2O. The final volume was 20 µl. The mixture was incubated at 25 °C for 5 minutes and then at 50 °C for one hour. The reaction finally reached 70 °C for 15 minutes. The samples were stored at -20 °C.

Reagents	Working Conc.
DEPC treated H_20	N/A
RNA	50 ng/µl
dNTPs (Promega)	0.5 mM
Hexamers	2.5 ng/µl
RT Buffer	1X
DTT	10 mM
RNaseOUT™	1 unit/µl
SuperScript™ II RT (for RT+ only)	10 units/µl

Table 2.7: Reagent and concentrations used for the cDNA synthesis reaction.

2.6 Primer design

All primers were designed using Primer-BLAST (Ye et al., 2012), except two which were taken from the literature or from in house (Table 2.8). Primers designed for in situ hybridization (ISH) had a product size of 450-850bp with various melting temperatures. Primers for qPCR had a product size of 100-230bp and their optimal melting temperature was 62 °C.

Genes	Orientation	Sequence (5'-3')	Tm (°C)
WT1*	Forward	TCTAGGGGACCAGCAGTACTC	59
(ISH)	Reverse	GATATGGTTTTTCACCAGTGTGC	
TCF21	Forward	GTGCGATGGCCTGAAAATGG	60
(ISH)	Reverse	CGCGTGGTAGGTTTTGTTTGA	
TBP*	Forward	TGGTCAAACTCCCCAGCTCTTC	62
(qPCR)	Reverse	TTCGGGCACGAAGTGCAATG	

EEF1A1	Forward	GCTCTAACATGCCCTGGTTCAAG	62
(qPCR)	Reverse	TGGCTTCAGGACACCAGTTTC	
COL1A2	Forward	CCTGGAGCAGATGGTAGGGT	62
(qPCR)	Reverse	GCACCTTGGTTGCCAGTGAC	
COL12A1	Forward	TGTCATGGAAAAGGCCACCAGA	62
(qPCR)	Reverse	TGGGTTGTGCTAGGTGAAAGAGT	
GAPDH	Forward	AGACGGTGGATGGCCCCTCT	62
(qPCR)	Reverse	ACGGCAGGTCAGGTCAACAACA	
ANGPT1	Forward	AGGTGAACACTGGCTGGGAAA	62
(qPCR)	Reverse	TGCAGGATCAGGCTACTCTGT	
BDNF	Forward	GGGGAACTGAGCGTCTGTGA	62
(qPCR)	Reverse	CCTTGGGGTTGCATTTGGTCTC	
SNAI2	Forward	CAAAATGCCACGCTCCTTCCT	62
(qPCR)	Reverse	GGATCTCTGGCTGCGGTATGAT	
TAZ	Forward	TGTGGGAAAGCGGATCACAGT	62
(qPCR)	Reverse	TGGTTGGGTGTAAGGTCCGT	
YAP1	Forward	AGAGTCCCCAAGGTGGTGTC	62
(qPCR)	Reverse	GTTGGAAGCTGGCTACGGAGA	
WT1	Forward	GCCCCTTCATGTGTGCCTAC	62
(qPCR)	Reverse	GTGTCGTCTTTGGTGCCGTTT	
PDGFRB	Forward	TCATCTGCGAGGGGAAGCTG	62
(qPCR)	Reverse	CTCTCTGGGGCCATCCACTT	
SMAD2	Forward	GGGCAAGAGGAGAAGTGGTG	62
(qPCR)	Reverse	TCTGGTTTGTTCAGAGAAGCTGTAA	
SNAI1	Forward	GTACTGCGAGAAGGAGTATGTGAG	62
(qPCR)	Reverse	GCAGATTAGAACGGTCAGCAAAG	
Bves	Forward	CGAGGTTTGCTCACCGTAGGAT	62
(qPCR)	Reverse	CTGGAGGCACATGGAGTGGTT	
CSPG4	Forward	CCCTACTTTGCGGCCCTTGAT	62
(qPCR)	Reverse	GGTACTGGATTTGCTGGCTCTGA	
DDR2	Forward	CAGTGCCATCAAGTGCCAGT	62
(qPCR)	Reverse	GCGTGTGTTGCTATCGTCCA	
GJA1	Forward	TCCGTTTTCCCTTAACCCTCCAG	62
(qPCR)	Reverse	AGACAGCCACACTTTTCCTCCT	

NRP1	Forward	GCAGCCCTCACCTTCACTCT	62
(qPCR)	Reverse	TCAGCCACTCGCACTTCTGG	
NRP2	Forward	TGGAACCCATCACAGCTTTCCC	62
(qPCR)	Reverse	GTTAGTAGAGAACAGGGTGTCGTTC	
TJP1	Forward	TTGCTCTAAAATCCTCTGACTCCTC	62
(qPCR)	Reverse	AGACACAGTTTGCTCCAACAAGAT	
NTRK2	Forward	GTCAGTGCCTGGAGATGGTAGT	62
(qPCR)	Reverse	TCCCACCACAACGTACACAGT	

Table 2.8: Primers designed for RT- and q- PCR, their sequence and melting temperature (Tm). * Primers taken from Ishii et al. (2007). ** Primers taken from Parnall (2017). For more information see Appendix Table 8.1.

2.7 RT-PCR

The cDNA was amplified using the T100™ Thermal Cycler (BIO-RAD). The PCR had a final volume of 20 µl (Table 2.9) and was run for 34 cycles (Table 2.10). Agarose gels were made with 100ml TAE containing 1-1.2% agarose (Fisher Scientific) and 10 µl of Ethidium Bromide. A 1kb Plus DNA Ladder (Invitrogen) was also added in one of the wells. The gels were run at 100 V for 35 minutes.

Reagent	**Working Conc.**
REDTaq PCR Reaction Buffer (Sigma-Aldrich)	1X
dNTPs (Promega)	0.25 mM
dH_2O	N/A
PR-F (Sigma-Aldrich)	0.25 µM
PR-R (Sigma-Aldrich)	0.25 µM
REDTaq DNA Polymerase (Sigma-Aldrich)	0.05 unit/ml
RT+ (cDNA)	625 pg/µl
RT- (RNA)	625 pg/µl
Blank (dH_2O)	N/A

Table 2.9: Reagents and concentrations used for the RT-PCR reaction.

PCR Steps	Temp. (°C)	Time (minutes)
1	95	3
2 (34 cycles)	95	0.5
	Tm*	0.5
	72	1
3	72	5

Table 2.10: The thermal cycler specifications used for RT-PCR. *Melting temperature.

2.8 qPCR standard curve and relative quantification

The standard curve was performed for each pair of primers to be used for qPCR. A duplicated, six point, 1:3 dilution series was used starting from an undiluted RT+, which was diluted in water control. In addition, one undiluted duplicate was used for RT- and one for the water control. The concentrations for undiluted reactions can be found in Table 2.11.

Reagent	Working Conc. for RT+/-	Working Conc. for water control
SYBR® Green Supermix (BIO-RAD)	1X	1X
DEPC treated H_2O	N/A	N/A
Primers (Sigma)	0.375 µM	0.375 µM
RT (+ or -)	1.66 ng/µl	---

Table 2.11: Reagents and concentrations used for the qPCR standard curve.

Relative quantification was performed (Table 2.12) with three technical repeats for each biological sample. Two stage groups were used, one at HH29 and one at HH35 (n=3 per treatment group, for both studies). A water control was added for each gene of interest tested. An RT- control was added only if the introns between the primers had a sum of less than 1kb.

Reagent	Working Conc. for RT+/-	Working Conc. for water control
SYBR® Green Supermix (BIO-RAD)	1X	1X
DEPC treated H_2O	N/A	N/A
Primers (Sigma)	0.375 μM	0.375 μM
RT (+ or -)	0.17 ng/μl	---

Table 2.12: Reagents and concentrations used for the qPCR relative quantification.

A MicroAmp® Optical 96-Well Reaction Plate (Applied Biosystems) was used to load 20 μl of each sample. The plate was sealed with optical adhesive film (Applied Biosystems) and the readings were taken using the 7500 Fast Real-Time PCR System (Applied Biosystems). The cycles' setup can be found in Table 2.13. Analysis of the readings was done using the Pfaffl method (Pfaffl, 2001) and statistical analysis was done in REST (software; Pfaffl, 2002).

Steps	Temp. (°C)	Time (s)
1	95	25
2 (40 cycles)	95	15
	62	30
3 (Melt Curve)	95	15
	60	60
	95	30

Table 2.13: The thermal cycler specifications used for qPCR.

2.9 In situ hybridisation

2.9.1 PCR clean-up

The GenElute™ PCR Clean-Up (Sigma-Aldrich) kit and protocol was used for PCR clean-up of genes of interest (GOI) fragments, obtained by RT-PCR. After the products had been purified their concentration was measured with NanoDrop (Thermo Scientific) and then they were stored at -20 °C.

2.9.2 Ligation and transformation

Ligation of the GOI fragments and transformation was done using the pGEM®-T Easy Vector (Fig. 2.1) Systems (Promega) kit and protocol. The final volume of the reaction was 10 μl (Table 2.14). The reaction was placed overnight at 16 °C.

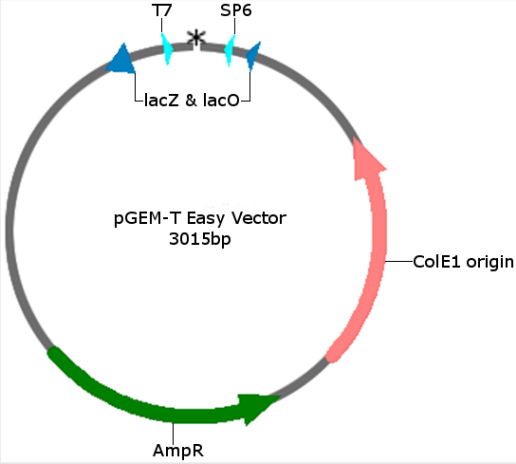

Figure 2.1: The pGEM-T easy vector used to transform bacteria. Insertion of the PCR product (*) causes disruption of lacZ transcription. Features: lactose operator (lacO), β-galactosidase (lacZ), ampicillin resistance (AmpR), origin of replication (ColE1), SP6 and T7 RNA polymerase promoters.

Reagent	Stock Conc.	Working Conc.
Rapid Ligation Buffer	2X	1X
pGEM®-T Easy Vector	50 ng/μl	5 ng/μl
PCR product	*	*
T4 DNA Ligase	3 Weiss units/μl	0.3 Weiss units/μl
dH_2O	N/A	N/A

Table 2.14: Reagents and concentrations used for the ligation reaction. *PCR product concentrations were variable.

For the transformation 30 μl of DH5α competent cells (in house) were mixed with 2 μl of the ligation reaction and they were incubated on ice for 20 minutes. Subsequently, they were heat shocked at 42 °C for 50 seconds and then incubated on ice for 2 more minutes. The cells were mixed with 950 μl of SOC medium and then they were incubated at 37 °C for 1.5 hours. After the incubation 100 μl were taken from the cell mixture and spread to a plate containing MacConkey agar

(Oxoid) and 0.1 mg/ml ampicillin (Sigma Aldrich). The plates were incubated at 37 °C. Colonies with an insert had a white/pink colour; in contrast colonies without an insert were red. To validate if the transformants had taken up the right insert a PCR was set up with the same conditions it took to clone each gene with some exceptions. The first step had its time increased to 18 minutes at 95 °C. Part of each bacterial colony of interest was transferred to a 19 µl of PCR reaction, instead of a template. The agarose gel was made as previously described. What was left from the bacterial colony of interest was added to a glass tube containing 4 ml Lysogeny broth (LB) high salt (HS) broth (in house) with 0.1 mg/ml ampicillin. The colonies were incubated at 37 °C for 6 hours at 200 rpm.

2.9.3 Midiprep

Colonies with the right insert had 800 µl taken from their LB HS broth and added to a 100 ml conical flask containing LB HS and 0.1 mg Ampicillin per ml. The flask was incubated overnight at 37 °C at 200 rpm. The spectrophotometer SmartSpec™ 3000 (BIO-RAD) was used to calculate the density of the culture. Midiprep was done using the GenElute® Plasmid Midiprep (Sigma-Aldrich) kit and protocol.

A cell mass of 80 (reading at OD_{600} x ml of culture) was inserted into Oak Ridge centrifuge tubes. The tubes were centrifuged at 5000 x *g* for 10 minutes and the supernatant was discarded. The remaining pellet was resuspended using 1.2 ml of resuspension solution. Then 1.2 ml of lysis solution was mixed in the tubes. A further 1.6 ml of neutralising solution were added and mixed in the reaction. The tubes were centrifuged at 15,000 x *g* for 15 minutes.

The binding column was prepared by placing it in a 15 ml Falcon tube and adding 3 ml of column preparation solution. The column was centrifuged at 5000 x *g* for 2 minutes. The lysate from the previous reaction was added to the column and centrifuged 5000 x *g* for 2 minutes. The flow through was discarded and 3ml of wash solution were added to the column. The column was centrifuged at 5000 x *g* for 5 minutes and then centrifuged again for 2 more minutes. The column was

transferred to a new 15 ml Falcon tube and 600 µl of dH_2O were added to it. The column was left in RT for 10 minutes and then centrifuged at 4000 x *g* for 5 minutes. The plasmid, in the eluate, had its concentration measured using NanoDrop and was stored at -20 °C.

2.9.4 Plasmid sequencing and linearisation

The plasmids from the midiprep were sequenced using a T7 promoter forward primer by the University of Nottingham DNA sequencing facility's 3130xl ABI PRISM Genetic Analyzer (Life Technologies). Restriction enzyme (RE; NEB) selection was made based on their ability to isolate the probe from the sense or antisense RNA transcription promoter, without cutting the inserter GOI fragment (Table 2.15). The linearisation reaction had a final volume of 50 µl (Table 2.16) and was incubated at 37 °C for three hours.

Plasmid with:	Sense RE	Antisense RE
WT1	SacII	NdeI
TBX18*	EcorVI	SpeI
TCF21	NcoI	NdeI

Table 2.15: The restriction enzymes used for linearisation. *TBX18 plasmid was donated by Dr. Kispert (Haenig and Kispert (2004).

Reagents	Working Conc.
DEPC treated dH_2O	N/A
Cut smart buffer (NEB)	1X
Plasmid DNA	300 ng/µl
RE (NEB)	0.8 units/µl

Table 2.16: Reagents and concentrations used for the linearisation reaction.

Then 425 µl of DEPC treated dH_2O and 500 µl of phenol:chloroform was added, mixed and centrifuged at 11,000 x *g* for 9 minutes. The supernatant was removed and mixed with 3 M NaAc pH 5.2 and 100% ethanol in a 10:1 (DNA:NaAc) and 1:2 (DNA:EtOH) ratio and left overnight at -20 °C.

The overnight mixture was centrifuged at 17,200 x *g* for 10 minutes at 4 °C. The supernatant was discarded and the pellet was washed with 300 µl 70% ethanol and centrifuged at 17,200 x *g* for 15 minutes at 4 °C. The ethanol was removed/left to evaporate and 11 µl of DEPC treated H_2O were added. The samples had their concentration checked using NanoDrop and then they were stored at -20 °C.

2.9.5 Riboprobe synthesis and purification

The linearised plasmid was used as a template to synthesize digoxigenin (DIG)-labelled RNA probes using in vitro transcription with SP6, T7 or T3 RNA polymerases (Table 2.17). The reaction (Table 2.18) was set up using Riboprobe® in vitro Transcription Systems (Promega) reagents and had a final volume of 33.6 µl. The reaction was incubated at 37 °C for 2.5 hours.

Plasmid with:	Sense polymerase	Antisense polymerase
WT1	SP6	T7
TBX18*	T7	T3
TCF21	SP6	T7

Table 2.17: The RNA polymerases used for riboprobe synthesis. *TBX18 plasmid was donated by Dr. Kispert (Haenig and Kispert (2004).

Reagents	Stock Conc.	Working Conc.
Trans Buffer	5X	1.12X
DEPC treated dH_2O	N/A	N/A
DTT	100 nM	0.112 nM
rRNasin	40 U/µl	0.84 U/µl
DIG Mix	10X	1.12X
3 µg Plasmid DNA	*	0.09 µg/µl
RNA polymerase	20 U/µl	1.68 U/µl

Table 2.18: The riboprobe synthesis reaction. *The concentration was variable.

Riboprobes were purified using the ProbeQuant G-50 micro columns (Illustra) kit and protocol. Firstly, column preparation was performed by resuspension of the resin by vortexing, loosening of the cap by one quarter turn and removal of the bottom closure. The column was placed in a collection tube and was centrifuged for 1 minute at 735 x g. The column was placed in a new collection tube and the riboprobe mixture was carefully applied to the top centre of the resin. The column was centrifuged at 735 x g for 2 minutes for elution. After centrifugation 20 µl of prehybe buffer (Table 2.20) were added to the eluate. Purified riboprobes were stored at -80 ºC.

In order to check the purified product a sample of 2.5 µl riboprobe-prehybe was mixed with 7.5 µl RNA denaturing buffer (in house) and 2 µl 6X Gel loading dye (NEB). The samples were incubated at 67 ºC for 8 minutes and were loaded in 1% agarose gel, cooled at 4 ºC with 1X TAE running buffer. A pGEM-T express positive control (Promega) was used as a positive control and ladder. The gel was run at 70 V for 1.5 hours.

2.9.6 Tissue processing for whole mount ISH

Fixed HH24, HH26 and HH28 embryos (n=8 per treatment group, for all stages) were dehydrated in increasing concentrations of methanol (MeOH). The time and repeats of the washes are given in Table 2.19. The processed embryos were placed at -20 ºC for a maximum storage period of two weeks.

	HH24-26		HH28	
Placed in:	**Time (minutes)**	**Repeats**	**Time (minutes)**	**Repeats**
RNase free PBS	30	2	45	2
25% MeOH (with RNase free PBS)	30	2	45	2
50% MeOH (with RNase free PBS)	30	2	45	2
75% MeOH (with RNase free PBS)	30	2	45	2
95% MeOH (with RNase free PBS)	30	2	45	2
100% MeOH	30	2	45	2

Table 2.19: The processing of whole mount embryos after the PFA step.

2.9.7 Whole mount ISH

Embryos were hydrated in decreasing concentrations of methanol. The embryos were placed in pairs in each well of a 24-well plate. The embryos were treated with Proteinase K (0.02 mg/ml) for 30 min. The digestion was stopped with two 10 minute washes of glycine (2 mg/ml) and then for the same amount of time using PBS with Tween 20 (PBST). The embryos were refixed in 4% PFA, diluted in PBS, for 30 minutes and then washed in three 10 minutes PBST washes. Subsequently, the embryos were treated with 75% posthybe solution (Table 2.20) for 30 minutes and then in prehybe solution (Table 2.20) for three hours at 65 ^{o}C. The ISH probe, *WT1* (in house), *TCF21* (in house) and *TBX18* (Haenig and Kispert, 2004), was added to the prehybe in a concentration of 530 ng/µl and left for 24 hours at 65 ^{o}C.

Reagents	Stock Conc.	Working Conc.
Deionized formamide	100%	50%
SSC 20X	20X	5X
Citric acid	1 M	9.2 mM
EDTA	0.5 M	5 mM
CHAPS	10%	0.1%
tRNA*	100 mg/ml	1 mg/ml
Heparin*	100 mg/ml	50 µg/ml
Tween20	20%	0.1%
DEPC treated dH_2O	**	**

Table 2.20: In house post- and pre- hybe reagents made for ISH. *Remove reagents with asterisk to make posthybe solution, include to make prehybe solution. **Water was added accordingly.

After hybridisation, the embryos were washed two times with 50% posthybe solution, three times with saline-sodium citrate (SSC) X2 and four times with SSC X0.2; all washes lasted 20 minutes each at 65 °C. The embryos were then washed for 20 minutes in SSC X2:maleic acid buffer with Tween20 (MABT; 1:1) and MABT at RT. Background was reduced with a 30 minutes wash of RNase (100 µg/ml) and three 10 minutes washes of MABT at 37 °C. The embryos were washed with 2% Boehringer blocking reagent (Roche) and 20% sheep serum (Sigma) for three hours at RT. Sheep anti-Digoxigenin antibody (Roche) was added in a dilution of 1:5,000 and left overnight at 4 °C. Unbound antibody was removed with five washes of MABT for one hour and one overnight.

The embryos were washed in BCL III buffer (Table 2.21) three times for five minutes each. Then colour development was carried out with 50% BM purple (Roche) for six hours. After colour development, the embryos were washed three times in PBST for 15 minutes each. If it was deemed necessary, the BCL III and BM purple steps were repeated for better staining; if not the embryos were washed

in 50% glycerol after the PBST washes. Finally, the embryos were left overnight at 100% glycerol before taking photographs for the expression analysis.

Reagents	Stock Conc.	Working Conc.
Tris-HCl (pH 9.5)	1 M	0.1 M
NaCl	5 M	0.1 M
$MgCl_2$	0.5 M	0.05 M
Tween20	20%	0.1%
dH_2O	*	*

Table 2.21: In house BCL III reagent made for ISH. *Water was added accordingly.

2.10 Fluorescent light sheet microscopy

2.10.1 DiI injection

A 25G winged infusion set (BD) was used to pierce the apex of HH35 hearts (n=4 per treatment), while still attached to the chick embryo, and to inject a series of solutions in the right ventricle. The first solution was 1X PBS, subsequently 0.012% 1,1'-dioctadecyl-3,3,3'3'-tetramethylindocarbocyanine perchlorate (DiI; 42364, Sigma-Aldrich) with 1.25% glucose (Fisher), diluted in PBS, was injected into the hearts. Finally, 4% PFA, diluted in PBS, was injected into the hearts and the hearts were subsequently harvested and stored in 4% PFA, diluted in PBS, overnight. A total volume of 2 ml for each solution was injected in each heart in a rate of 1 ml/minute.

2.10.2 Whole mount immunohistochemistry

The fixed hearts were washed three times for 45 minutes in 1% Triton X-100 (Fisher) with PBS. Then they were incubated in 1% Triton/10% BSA diluted in 1X PBS for 3 hours. Subsequently the hearts were incubated overnight at 4 ^{o}C with mouse anti-α-smooth muscle actin antibody (A2547; Sigma-Aldrich), diluted 1:300 in 1% Triton/10% BSA/1X PBS.

The next day the hearts were washed three times for 20 minutes in 1% Triton/1X PBS. Then they were incubated in 1% Triton/10% BSA/1X PBS for 3 hours. Subsequently the hearts were incubated overnight at 4 °C with rabbit anti-mouse IgG (H+L) Alexa Fluor 488 antibody (A-11059; Thermo Fisher Scientific), diluted 1:300 in 1% Triton/10% BSA/1X PBS.

Finally, the hearts were washed three times for 20 minutes in 1% Triton/1X PBS and then three times for 20 minutes in 1X PBS. High gelling point (~36 °C) agarose (Fisher Scientific) was diluted down to 1% with PBS and then 2 μm fluorescent yellow-green latex beads (L4530, Merck) were added into the agarose in a concentration of 1:1,500. The hearts were embedded in the agarose inside a 1 ml syringe (Omnifix-F) and stored in the dark at 4 °C.

2.10.3 Light sheet microscopy and image processing

Imaging was carried out in the Wolfson Light Microscopy Facility (University of Sheffield), supported by a BBSRC ALERT14 award for light-sheet microscopy (BB/M012522/1), in collaboration with Dr. Nick Van Hateren. A lightsheet Z.1 (Zeiss) microscope was used to image the hearts using a 5X lens and 0.38 zooming. Six opposing angles were imaged for the top half of the hearts and the bottom half. Maximum projections were made using ZEN black (Zeiss) and stitched together in Fiji. The alignment of the different angles in the raw dataset as well as the stitching of the hearts was carried out using the BigStitcher plugin (Hörl et al., 2018) in Fiji.

2.11 Transmission electron microscopy

2.11.1 Fixing and processing

All the solutions listed were prepared by the University of Nottingham Advanced Microscopy Unit. HH35 hearts (n=4 per group) were harvested and fixed in 3.4% glutaraldehyde diluted in 0.1 M cacodylate buffer overnight at 4 °C. The hearts

where then washed two times with 0.1 M cacodylate buffer for 40 minutes and then stored in it at 4 °C until further processing.

Subsequently, the hearts were post fixed in 1% osmium tetroxide (Agar Scientific) diluted in 0.1 M cacodylate buffer for 2 hours and washed two times in dH_2O for 5 minutes. The tissue was dehydrated in graded ethanol (Sigma-Aldrich) series until it was incubated in propylene oxide (TAAB; Table 2.22). Fresh resin was made on the day (Table 2.23) and hearts were infiltrated with a mixture of propanol oxide and resin 3:1 (propanol oxide:resin) for four hours and then 1:1 (propanol oxide:resin) overnight. The following day the hearts were infiltrated with resin three times for two and a half hours and then left to polymerise for 48 hours at 60 °C.

Placed in:	Time (minutes)	Repeats
50% EtOH (with dH_2O)	15	2
70% EtOH (with dH_2O)	15	2
90% EtOH (with dH_2O)	15	2
100% EtOH	20	3
Propylene oxide	15	2

Table 2.22: The processing of hearts for transmission electron microscopy.

Reagents:	Working Conc.
Araldite CY212 resin (TAAB)	25.4%
Agar 100 resin (Agar Scientific)	15.3%
Dodecenylsuccinic anhydrate (TAAB)	55.8%
Dibutyl phthalate (Agar Scientific)	2%
DMP 30 (TAAB)	1.5%

Table 2.23: The reagents used to make the resin.

2.11.2 Sectioning, staining and imaging

Trimming and sectioning took place using an EM UC6 (Leica) ultramicrotome. The hearts were trimmed at a thickness of 1-0.5 µm using a glass knife until the ROI

was reached. To verify the ROI sections acquired from trimming were collected on a glass slide and allowed to dry on a 100 ^{o}C hot plate. The sections were stained with 1% toluidine blue for 1 minute and then washed with dH_2O. Once the ROI was verified samples were sectioned at a thickness of 90 nm using a diamond knife (DiATOME, TAAB). Two sections from each heart were collected on a 3.05 mm diameter copper grid (G200HH, Gilder).

The sections were further stained by incubating them in 50% methanolic uracyl acetate for 5 minutes. The sections where then washed briefly in 50% methanol followed by dH_2O. Subsequently, the sections were incubated in Reynold's lead citrate solution for 5 minutes and then briefly washed in dH_2O. Sections were visualised using Tecnai G2 T12 BioTwin (FEI) with an accelerating voltage of 100 kV and a MegaView II (Olympus) camera system.

2.12 Statistics and graphs

Statistics were carried using the statistical language R and its packages R commander (Fox, 2005) for the statistical tests and GrapheR for the generation of most graphs (Hervé, 2011). All the other graphs were generated in Excel. All statistical tests were two-tailed and had a cut off value of $p<0.05$. The statistical tests used were Shapiro-Wil normality test, Levene's test of homogeneity of variance, independent samples t-test, Hotelling's T^2 test, multivariate analysis of variance (MANOVA), Tuckey post-hoc test, Spearman's and Pearson's correlation and regression analysis. The tests were picked based on the number of dependent variables and the nature of the independent and dependent variables.

3 Characterisation of the epicardial phenotype at HH29

3.1 Overview and aims

Although two out of the three heart layers, the endocardium and myocardium, are formed in chick early in development, before HH10, the epicardium joins them later in development (Martinsen, 2005). The epicardium comes from the proepicardial organ (PEO), which is formed at HH14 (Cano et al., 2016), and it starts to migrate on the hearts surface at HH17 (Hiruma and Hirakow, 1989). The epicardium completely envelops the heart by HH24 (Ishii et al., 2010) and sends epicardial derived cells (EPDCs) into the rest of the heart, starting at HH19 (Lie-Venema et al., 2005). EPDCs differentiate to a number of different cells; two of the best described and least controversial examples are fibroblasts and smooth muscle cells (SMCs; Gittenberger-de Groot et al., 1998).

Different subsets of cells in the epicardium express the markers TCF21, WT1 and TBX18 (Braitsch et al., 2012; Ishii et al., 2007). All three markers are transcription factors (TFs). Not much is known about their function in the epicardium. What is known so far is that WT1 and TBX18 are able to regulate the migration of EPDCs through the migration markers SNAI1 and SNAI2, which are also TFs (Singh et al., 2016). Knockdown of TBX18 does not seem to have an impact on EPDC migration, possibly due to functional overlap with other proteins, but it affects coronary vessel (CV) development (Wu et al., 2013). TCF21 was found to be of critical importance in promoting the fibroblast fate in EPDCs and at the same time blocking the SMCs fate (Braitsch et al., 2012; Acharya et al., 2012).

The adhesion proteins N- and E- cadherin are expressed in the cells of the epicardial epithelium (Martínez-Estrada et al., 2010; Wu et al., 2010). Cadherins are transmembrane cell adhesion molecules (Maître and Heisenberg, 2013). They are responsible for cell to cell adhesion but can also function as cell signalling

molecules. The formation of the cadherin mediated adhesion complex also requires the recruitment of β-catenin, which can further trigger signals affecting the actomyosin cytoskeleton (Maître and Heisenberg, 2013). The maturation of the cell to cell adhesion is further facilitated by the establishment of cell polarity and tight junctions. Cell to cell adhesion can then be disrupted by the transcriptional downregulation of cadherin mRNA and cleavage of the existing cadherin proteins (Maître and Heisenberg, 2013).

TGFβ signalling was found to be of great importance for EPDCs migration (Craig et al., 2010). TGFβ signalling works through SMADs in the cytoplasm and induces epicardial cells to undergo EMT (Takeichi et al., 2013). EPDCs migrate from the epicardium, which is an epithelial tissue; this suggests that there is also cadherin switching involved, where E-cadherin is downregulated and N-cadherin is upregulated (Wheelock et al., 2008). EPDCs that have differentiated into fibroblasts are responsible for most collagen produced in the heart and also express other genes commonly found in fibroblasts (e.g. DDR2; Goldsmith et al., 2004).

There are a number of potential explanations for the aberrant epicardial morphology seen in OTB hearts at HH29 (Pang, 2016), which was mentioned in section 1.14 (Fig. 1.16). These include an incorrect migration of the PEO over the heart, or the EPDC fail to migrate correctly and are populating the subepicardial space instead. Other explanations are too many ECM related molecules (e.g. collagen I) are being produced by the fibroblasts causing a swelling due to the increase in the connective tissue, or there is a change in the apoptosis or proliferation rates of epicardial cells.

Therefore, in order to determine the potential causes of the aberrant epicardial phenotype a set of specific experimental aims was established:

- To assess the complete epicardial migration and coverage along the heart's surface at HH24, HH26 and HH28 through whole mount (WM)-in situ hybridisation (ISH).
- Measure the expression levels of the three epicardial markers WT1, TBX18 and TCF21 using semiquantitative and quantitative methods.
- Measure the expression levels of other genes or proteins relevant to EPDC migration and function of fibroblasts using semiquantitative and quantitative methods.
- Measure the number of apoptotic and proliferating cells in the epicardium.
- Measure the density of collagen I and assess its morphology in the epicardium.
- Morphological characterisation of the myocardium and the OFT.

3.2 Epicardial migration along the heart

3.2.1 Isolation of cDNA fragments using RT-PCR

Wild type HH29 hearts were isolated and had their RNA purified from the tissue. The RNA was converted to cDNA by in vitro reverse transcription (RT). Certain cDNA fragments encoding for genes of interest (GOI) were needed to elucidate the epicardial migration in the OTB hearts. An RT-PCR reaction was set up for each GOI. The RT-PCR product was visualised by gel electrophoresis. The agarose gel had three lanes for each GOI fragment. There was an RT+, where cDNA was used as a template for the RT-PCR reaction, an RT-, where RNA was used as a template, and a water control (blank) with just deionised water (dH_2O).

The blank lane would be expected to have no bands denoting no external contamination of the RT-PCR reaction. The RT- would also be expected to have no bands denoting no genomic DNA (gDNA) contamination of the RNA samples. A gDNA contamination could display two bands on the RT+ lane although this depends on the intron size of the amplicon. The WT1 band in the RT+ lane had

the expected size of 455 bp (Fig. 3.1A). The TCF21 band in the RT+ lane had the expected size of 769 bp (Fig. 3.1B). Although there was gDNA contamination in the RT- sample the vast genomic size of WT1 (14,931 bp) and TCF21 (1,792 bp), made their amplification inefficient (for more information on amplicon sizes for all primers used see Appendix Table 8.1). In contrast, genomic contamination can be seen in the GAPDH RT- lane, with a band of 317 bp in comparison to the 188 bp fragment in the RT+ lane (Fig. 3.1).

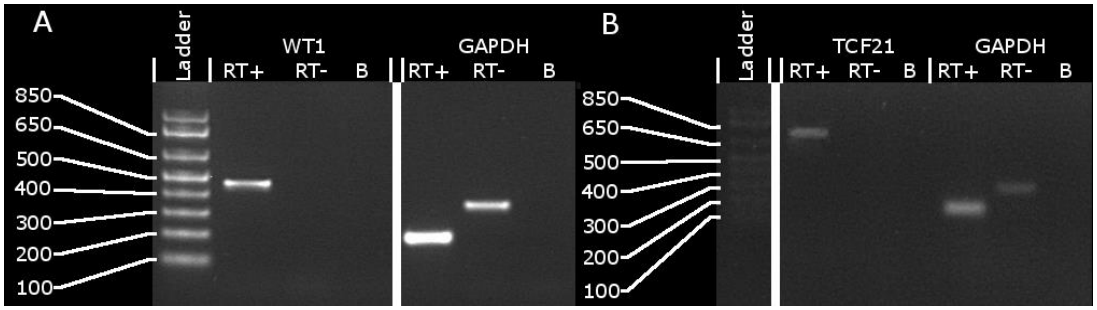

Figure 3.1: RT-PCR on WT1 and TCF21 cDNA fragment. The agarose gel had a ladder with band sizes in bp. (A) The WT1 fragment had the correct size of 455 bp. (B) The TCF21 fragment had the correct size of 769 bp. A GAPDH fragment, 188 bp, was used for positive control and since it had a small intron gDNA contamination can also be seen in the RT- lane, 317 bp. Irrelevant lanes have been excluded. Key: RT+, cDNA template; RT-, RNA template; B, water control.

3.2.2 Bacterial transformation and plasmid isolation

The RT-PCR products were purified and then successfully ligated in the plasmid pGEM-T easy. After the plasmid was used to transform competent bacteria, the bacteria were plated on agar containing petri dishes.

PCR was used, using bacterial colonies in the PCR reaction as templates, to prove that the plasmid had the correct insert. Three bacterial colonies were randomly chosen for PCR using the same primers used in the RT-PCR. For simplicity, WT1

will be used as representative example. The PCR products were visualised by gel electrophoresis (Fig. 3.2). Some of the colonies had no insert suggesting that the plasmid had self-ligated.

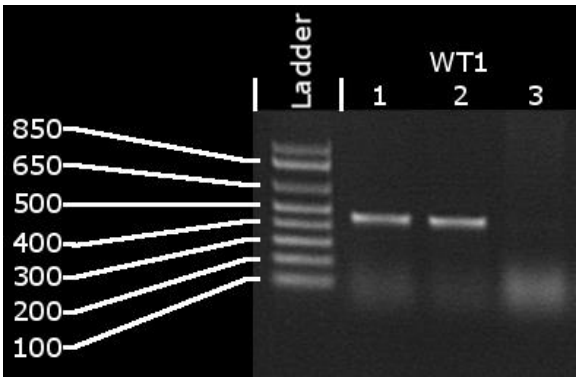

Figure 3.2: PCR on three bacterial colonies. The agarose gel had a ladder with band sizes in bp. The WT1 fragment had the correct size of 455 bp in the first (1) and second (2) bacterial colonies. The third one (3) had no band.

Only one colony with the correct insert was chosen every time for plasmid purification using a midiprep. Following plasmid isolation the plasmids were sent for sequencing using a T7 promoter forward primer (performed by Dr. Matthew Carlile of the university's sequencing facility) in order to reveal the inserts orientation in the plasmid. The orientation of the plasmid could be either 5' to 3' or 3' to 5'. The sequence of the insert was also examined for any major deviations from the one in the NCBI database (Fig. 3.3).

```
WT1-NCBI
cagtactcggtgccccctccggtgtacggctgtcacacccccacggacacgtgcacgggc
WT1-Seq
cagtactcggtgccccctccggtgtacggctgtcacacccccacggacagctgcacgggc


WT1-NCBI
agccaggccctgctcctgcggacccccctacaacagtgacaatttgtaccaaatgacgtca
WT1-Seq
agccaggccctgctcctgcggacccccctacaacagtgacaatttgtaccaaatgacgtca


WT1-NCBI
cgactggaatgcatgacatggaaccaaatgaacctgggatccacgctgaagggccatacg
```

```
WT1-Seq
cagctggaatgcatgacatggaaccaaatgaacctgggatccacgctgaagggccatacg


WT1-NCBI
acaggatatgaaaatgagaaccacagtgctcccatgttatacagctgtggggcccaatac
WT1-Seq
acaggatatgaaaatgagaaccacagtgctcccatgttatacagctgtggggcccaatac


WT1-NCBI
agaatacacacccatggagtctttagaggcatacaagatgtccgacgagtgccaggagta
WT1-Seq
agaatacacacccatggagtctttagaggcatacaagatgtccgacgagtgccaggagta


WT1-NCBI
gctccgactattgtccgatcagcaagtgagacaaatgaaaaacgccccttcatgtgtgcc
WT1-Seq
gctccgactattgtccgatcagcaagtgagacaaatgaaaaacgccccttcatgtgtgcc


WT1-NCBI
taccccggctgcaacaagcgatacttcaagctgtcccatctacagatgcacagcagaaag
WT1-Seq
taccccggctgcaacaagcgatacttcaagctgtcccatctacagatgcacagcagaaag
```

Figure 3.3: Comparing the cDNA sequence in NCBI with our own. The WT1 sequence from NCBI (WT1-NCBI) compared to the one from the DNA sequencing facility (WT1-Seq). There was a two nucleotides change (red) in our sequence.

3.2.3 Plasmid linearisation and riboprobe synthesis

The pGEM®-T Easy plasmid with the WT1 insert was linearised in order to stop the T7 or SP6 RNA polymerase for transcribing anything more than the insert. The orientation of the insert indicated that an RNA transcription reaction with SP6 RNA polymerase would result in the sense riboprobe. Alternatively, an RNA transcription reaction with T7 RNA polymerase would result in the antisense riboprobe (Fig. 3.4).

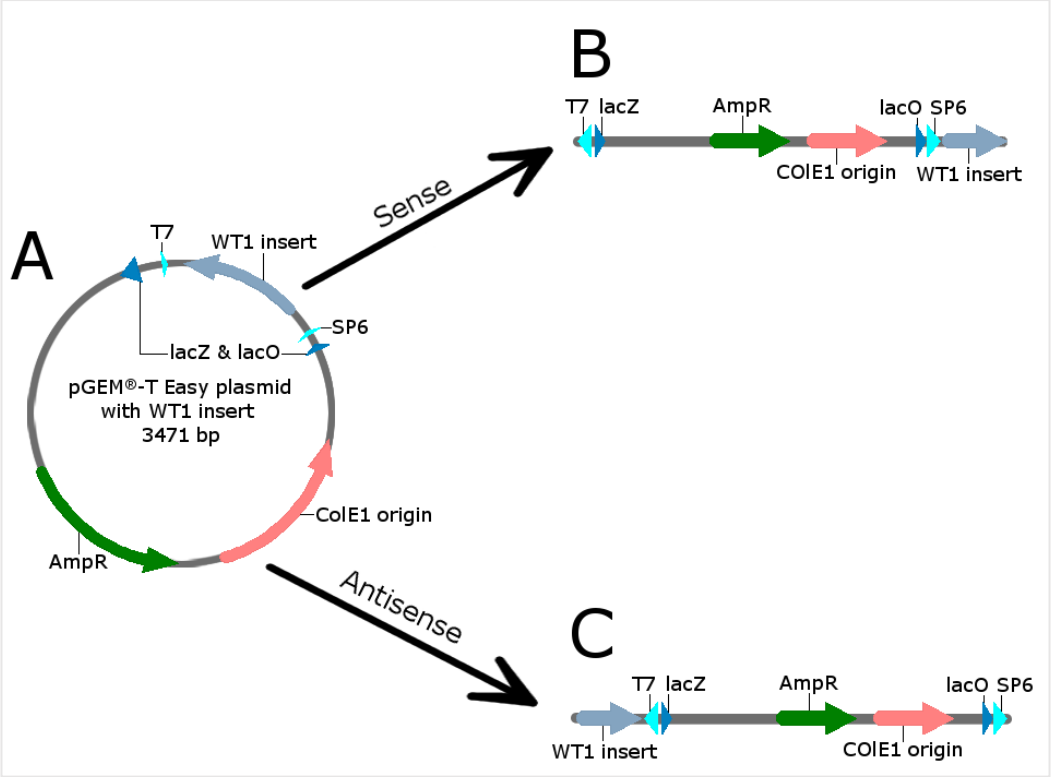

Figure 3.4: Schematic showing the linearisation of plasmid with the WT1 insert. (A) The pGEM®-T Easy plasmid with the WT1 insert. (B) The linearised plasmid to be used for the sense riboprobe by SP6 transcription. (C) The linearised plasmid to be used for the antisense riboprobe by T7 transcription. Features: lactose operator (lacO), β-galactosidase (lacZ), ampicillin resistance (AmpR), origin of replication (ColE1), SP6 and T7 RNA polymerase promoters.

The linearised plasmid was visualised by gel electrophoresis (Fig. 3.5). If no other major bands were seen in the linearised plasmid lanes, linearisation was deemed successful. After the riboprobe was synthesized and purified a sample of it was run in a gel in order to visualise its integrity (Fig. 3.6). A pGEM-T express positive control (Promega; riboprobe) was used as a positive control and a ladder, was used to verify band size.

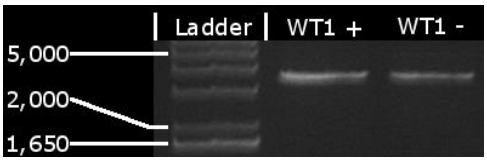

Figure 3.5: Linearisation of the plasmid with the WT1 insert. The agarose gel had a ladder with band sizes in bp. The linearised plasmids destined to be the sense (+) and antisense (-) template for the riboprobe had the correct size of 3471 bp. No other band can clearly be seen meaning that almost all of the plasmid was linearised in both + and - reactions.

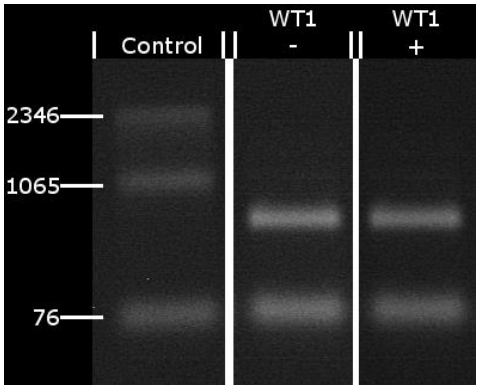

Figure 3.6: Integrity of WT1 riboprobe. The agarose gel had a pGEM-T express positive control (Control) loaded, with two bands that can be used as a ladder, 2346 bp and 1065 bp. The bands at 76 bp are tRNA, found in prehybe. The antisense probe (-) and the sense probe (+) had the expected size, around 505 bp. Irrelevant lanes have been excluded.

3.2.4 Differential expression of epicardial markers seen at HH28

Whole mount embryos were harvested at HH24, HH26 and HH28. Sixteen embryos were harvested for each developmental stage (n=8 per treatment group; for all studies). *WT1*, *TCF21* and *TBX18* riboprobes were used for hybridisation with the embryos' mRNA. Since the riboprobe's uracil (U) nucleotide was conjugated with digoxigenin (DIG), a semiquantitative visualisation of the mRNA levels was possible using an anti-DIG antibody and chromogenic substrate, BM Purple.

The developmental stages were chosen based on the fact that OFT banding is performed at HH21, and preliminary data from our lab has shown that the

epicardium was already abnormal by HH29. If it is migratory abnormalities, during the formation of the epicardium, that cause the aberrant phenotype seen at HH29, then they should happen between HH22-28. HH24 was chosen as the earliest stage to give enough time for any effects banding has on gene expression to be manifested. In addition, epicardial migration is complete by HH24, which would allow for an early examination of the heart's coverage by the epicardium. HH26 and HH28 stages were selected in the prospect of a clearer spatial and temporal gene expression difference, over the course of the developing epicardium. The sense control for the ISH experiments can be found in Appendix Figure 2.

To ensure a robust gene expression study, which would account for any potential difference in phenotypic penetrance, eight embryos were used for each treatment group for each GOI and this resulted in 48 embryos being used per HH stage. Attention was given at any difference in gene expression in the epicardium covering the atria, ventricles and the OFT. The morphology of the heart was found to be similar between sham and OTB at HH24 with normal development of the ventricle, atria and the OFT (Fig. 3.7-9). In contrast, at HH26 the shape of the OFT in the OTB hearts was aberrant. The OFT was more noticeable in the OTB hearts as it appeared anatomically distal from the ventricles, whereas in the shams it was adjacent to them (Fig. 3.7-9). This aberration was even more prominent at HH28 with the OFT clearly more convex and more distally superior from the ventricles (Fig. 3.7-9). In addition, in HH28 OTB hearts, the OFT is not positioned centrally between the atria, as in shams, but is right shifted (Fig. 3.7-9).

There was no apparent difference in the staining of HH24 hearts using all three epicardial markers, *WT1*, *TCF21* and *TBX18* (Fig. 3.7-9). At HH26 there was a ring of ectopic *WT1* expression around the OFT in 87.5% (7/8) of the banded hearts, which was absent in 100% (8/8) of the shams (Fig. 3.7). However, the other two markers showed no apparent difference in their expression in the HH26 heart (Fig. 3.8-9). At HH28 *WT1* was strongly expressed around the ventricles, atria and OFT

(Fig. 3.7 & 3.10). *WT1* was also uniformly expressed at the OFT of both sham and OTB hearts at HH28 (Fig. 3.10).

In both shams and OTB hearts, *TBX18* had a low starting expression at HH24, which became stronger at HH26 and HH28 (Fig. 3.8). *TBX18* was expressed in the atria and ventricles but was absent throughout the OFT of shams (8/8; Fig. 3.8 & 3.10). In contrast, at HH28 75% (6/8) of the OTB hearts had an increased expression of TBX18 in the epicardium covering the right ventricle of the heart in comparison to shams (8/8; Fig. 3.8); the other markers showed no apparent difference in their expression in that area. The OFT of OTB embryos at HH28 showed increased expression of *TBX18* at the proximal region (base) of the OFT in 100% (8/8) of the embryos in comparison to shams (Fig. 3.8 & 3.10). Furthermore, in shams, at HH28 there was triangle of *TBX18* expression at the interface between the superior heart boundary and the proximal OFT (8/8; Fig. 3.10). This triangle of expression was missing from all (8/8) the OTB hearts as the gene expression of *TBX18* was uniform along the length of the OFT (Fig. 3.10).

In both shams and OTB hearts, *TCF21* expression increased with development and it was remarkably strong at HH28 (Fig. 3.9). *TCF21* was not found to be strongly expressed in the OFT of shams (Fig. 3.10). In contrast, a closer examination of the OFT at HH28 showed increased expression of *TCF21* at the proximal region (base) of the OFT in 100% (8/8) of the OTB hearts (Fig. 3.9 & 3.10). Furthermore, in shams, at HH28 there was a triangle of *TCF21* expression (8/8; Fig. 3.10) in a similar fashion to *TBX18*. This triangle of expression was missing from all (8/8) of the OTB hearts as the gene expression of *TCF21* was uniform along the length of the OFT (Fig. 3.10).

In conclusion, there is an aberrant ring of *WT1* expression found around the OFT of the HH26 OTB hearts. At HH28 we have expression of *TCF21* and *TBX18* in the OFT of the OTB hearts but low or no expression in shams. *TBX18* expression was

also aberrant on the epicardium of HH28 OTB hearts, with an increased expression on the right side of the heart, in comparison to the left.

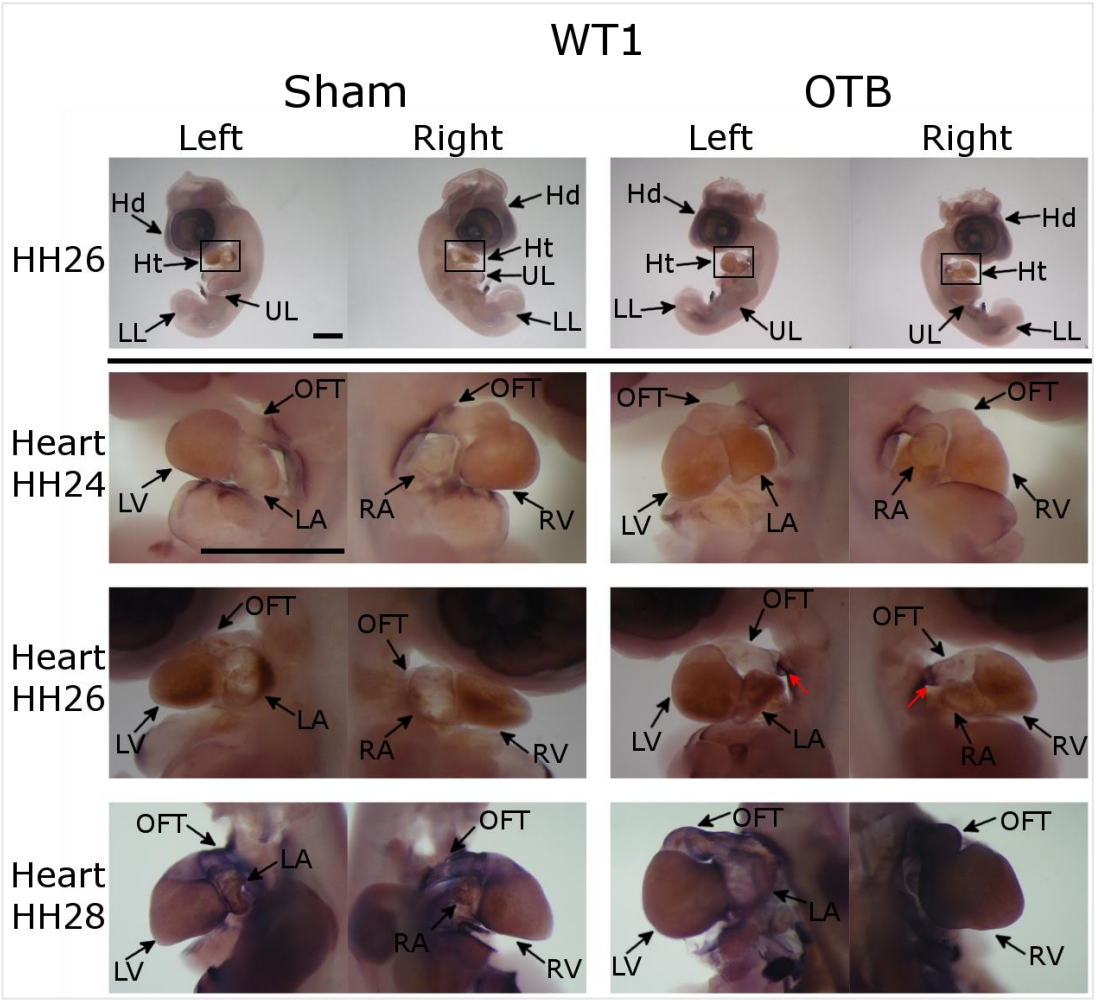

Figure 3.7: WT1 ISH on whole mount chicken embryos. The same embryo is shown on its left and right sides. Each heart (HH24, HH26 and HH28) is a 4X magnification of the HH26 representative whole embryo (top row). A ring of increase in expression was found around the OFT at HH26 (red arrow). Scale bar: 2 mm; for each image. Key: Hd, head; Ht, heart; UL, upper limb; LL, lower limb; OFT, outflow tract; LA, left atria; RA, right atria; LV, left ventricle; RV, right ventricle; A, atria.

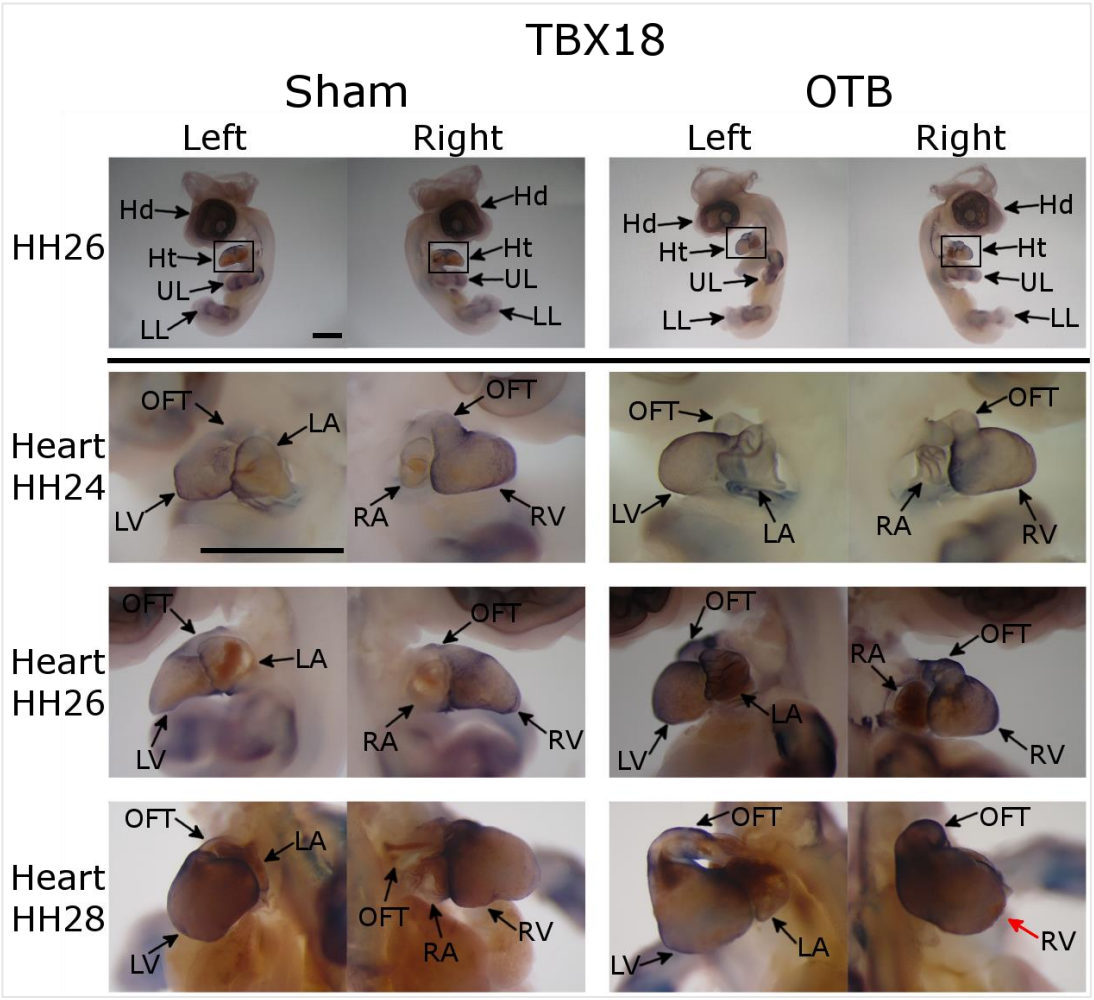

Figure 3.8: TBX18 ISH on whole mount chicken embryos. The same embryo is shown on its left and right sides. Each heart (HH24, HH26 and HH28) is a 4X magnification of the HH26 representative whole embryo (top row). There was an increased expression at HH28 (red arrow) on the RV of the heart. Scale bar: 2 mm; for each image. Key: Hd, head; Ht, heart; UL, upper limb; LL, lower limb; OFT, outflow tract; LA, left atria; RA, right atria; LV, left ventricle; RV, right ventricle; A, atria.

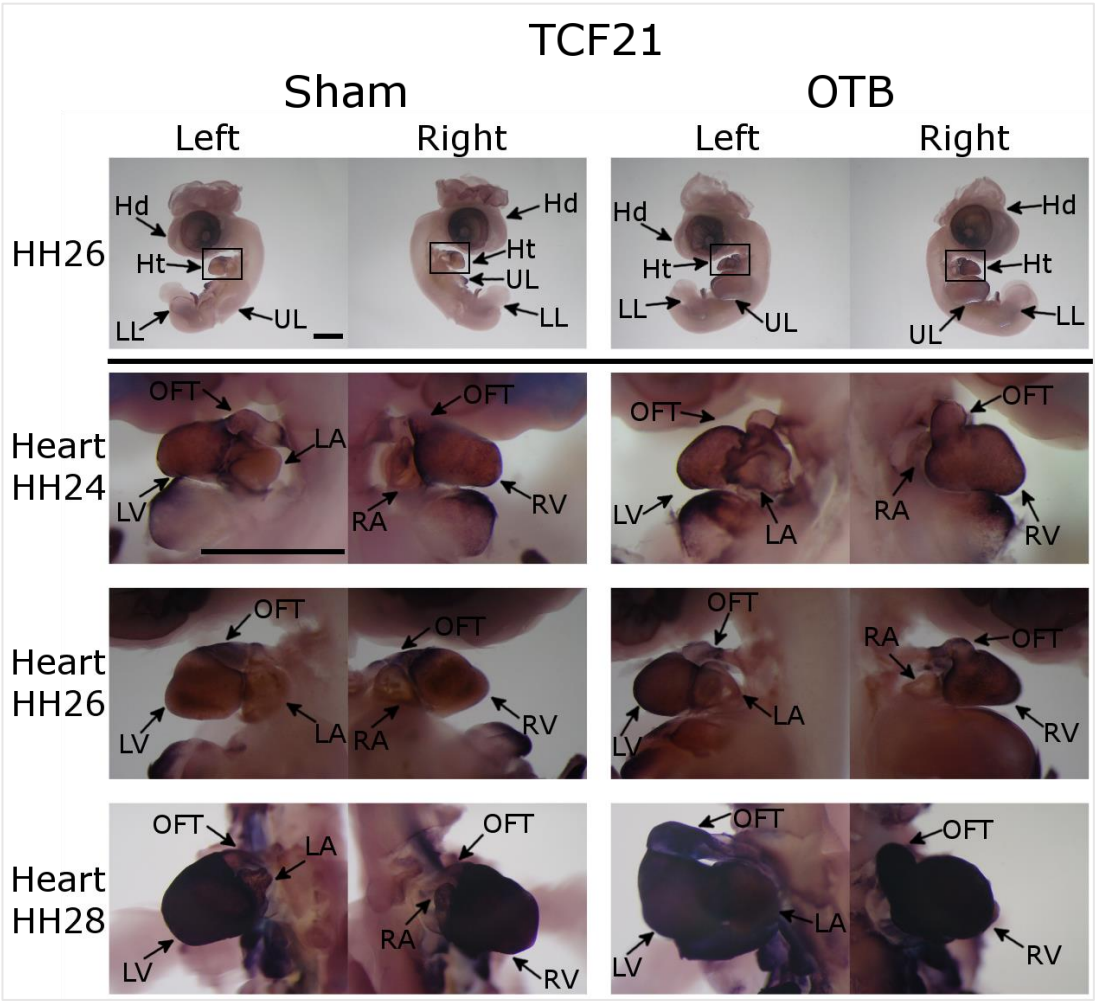

Figure 3.9: TCF21 ISH on whole mount chicken embryos. The same embryo is shown on its left and right sides. Each heart (HH24, HH26 and HH28) is a 4X magnification of the HH26 representative whole embryo (top row). No expression difference was apparent along the surface of the heart. Scale bar: 2 mm; for each image. Key: Hd, head; Ht, heart; UL, upper limb; LL, lower limb; OFT, outflow tract; LA, left atria; RA, right atria; LV, left ventricle; RV, right ventricle; A, atria.

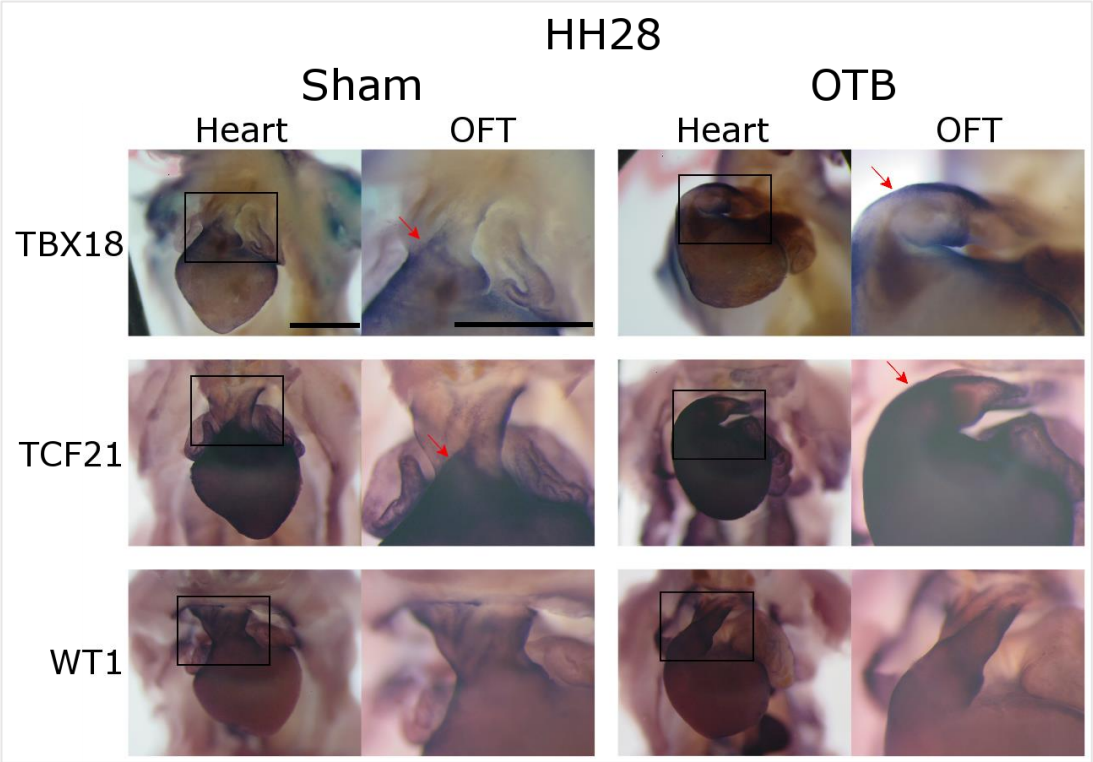

Figure 3.10: ISH on whole mount HH28 chicken embryos. Each OFT is a 2X magnification of the boxed region. In the shams the red arrow shows the triangle of *TBX18* and *TCF21* expression that was found in the interface between the heart and OFT. In the OTB hearts there was an increased *TBX18* and *TCF21* expression at the OFT (red arrow). Scale bar: 1 mm; for each image.

3.3 RNA-sequencing on whole hearts

3.3.1 General RNA-sequencing results

RNA from six (n=3 per treatment group) HH29 hearts were isolated by Dr. Kar Lai Pang. The hearts were codenamed OTB 1-3 for the OTB hearts and sham 1-3 for the sham hearts. The samples were globin depleted (globin mRNA reduced) by Dr. Matt Parnall. RNA-Seq was conducted by Dr. Sunir Malla, Dr. Matt Parnall and Dr. Fai Sang. RNA-Seq is used for sequencing large numbers of fragmented cDNA and enables a quantitative analysis of the transcriptome.

HH29 was chosen as the stage of interest since the aberrant epicardial phenotype was described at HH29 and the epicardium has fully enveloped the heart by that

stage. This means that any potential significant difference on migratory gene markers would have to do with EPDC migration rather than epicardial migration. In addition, any significant difference in fibroblast and ECM markers would potentially come from aberrant, EPDC derived, fibroblasts fate specification or function.

Briefly, the total gene read counts in a sample were counted and divided by 1,000,000. The resulting number is called the scaling factor. The read counts were divided by the scaling factor, for each gene. This normalises for sequencing depth, giving reads per million (RPM). The RPM values are divided by the length of the gene, in kilobases, resulting in reads per kilobase of transcript per million (RPKM; Fig. 3.11). The sequence was also aligned and mapped to the galGal4 (UCSC) reference genome, from red junglefowl.

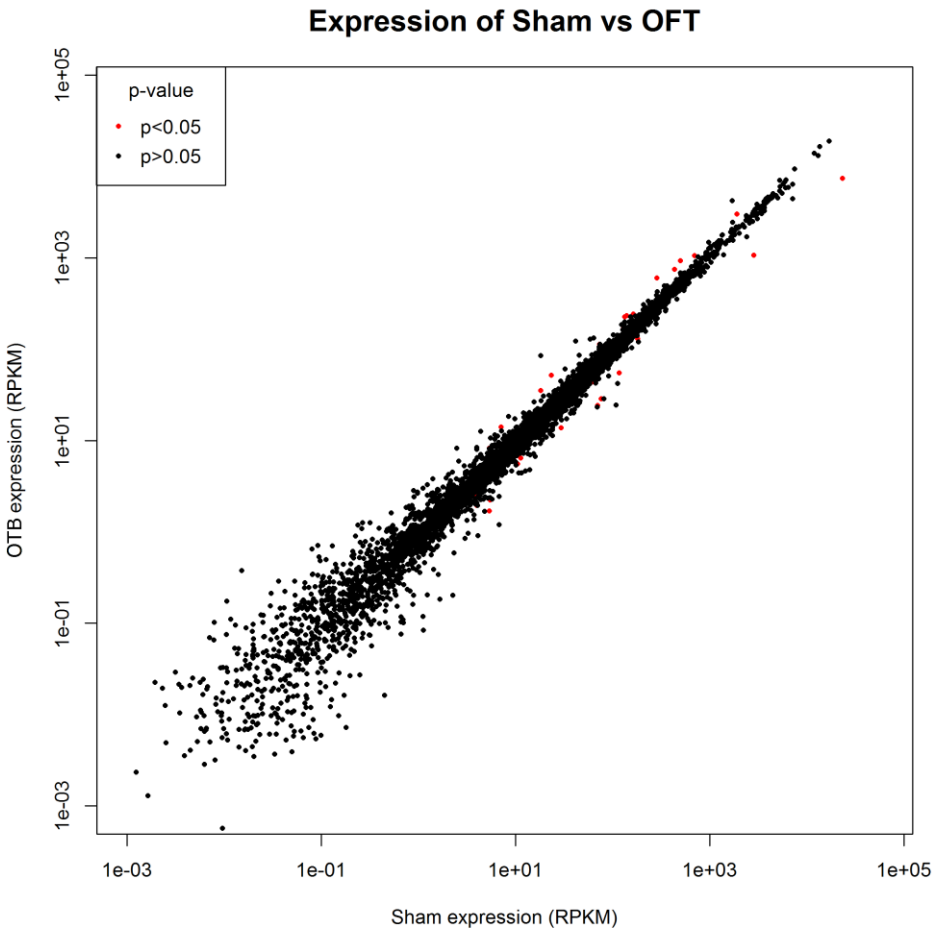

Figure 3.11: The RPKM expression of the sham samples against OTB. The genes marked in red had a statistically significant differential expression.

Only 30 genes were found to be differentially expressed, using a $p<0.05$ cut off; statistics were carried out Dr. Fei Sang and Dr. Matt Parnall, in OTB compared to sham (Fig. 3.11; Table 3.1). A Gene ontology (GO) term enrichment analysis, used for retrieving a functional profile of differentially expressed gene sets in order to distinguish any underlying biological processes, was not performed due to the low number of differentially expressed genes. None of the differentially expressed genes was found to have any strong connection with the epicardium or its cell lineages, after doing a literature survey.

Gene ID	Gene Name	Log_2 fold change	SEM	p-values
NM_205068	*GBX2*	0.83	0.17	8.27E-04
NM_205450	*TNNC2*	0.75	0.16	1.34E-03
NM_001302201	*TIMM10*	0.72	0.13	2.98E-05
NM_001159315	*PVALB*	0.7	0.17	1.91E-02
NM_001097526	*MYL10*	0.67	0.18	4.37E-02
NM_204177	*LDHB*	0.64	0.13	1.23E-03
NM_205495	*LGALS1*	0.64	0.18	4.88E-02
NM_001031038	*LBH*	0.6	0.17	4.86E-02
NM_001079490	*PNO1*	0.59	0.13	3.62E-03
NM_001079501	*LLPH*	0.58	0.16	4.97E-02
NM_001130387	*IFNGR1*	0.55	0.15	4.46E-02
NM_001044632	*MYL1*	0.54	0.15	4.46E-02
NM_205166	*S100A11*	0.52	0.14	4.46E-02
NM_001080873	*ENS-1*	-0.91	0.16	2.98E-05
NM_001081704	*HBE*	-0.8	0.18	5.64E-03
NM_001080874	*ERNI*	-0.76	0.15	4.79E-04
NM_205087	*ADORA2B*	-0.74	0.18	2.08E-02
NM_205160	*GLRX*	-0.71	0.18	3.33E-02

NM_001012588	*ITPK1*	-0.68	0.17	2.34E-02
NM_001004390	*HBG1*	-0.68	0.18	4.37E-02
NM_204818	*GSTA4*	-0.65	0.18	4.88E-02
NM_001044673	*H1F0*	-0.64	0.18	4.46E-02
NM_001100289	*CDH8*	-0.6	0.16	4.86E-02
NM_001031478	*RAP1GAP2*	-0.57	0.15	4.46E-02
NM_001177415	*DNAJC6*	-0.48	0.13	4.40E-02
NM_001030857	*ARFGAP1*	-0.47	0.13	4.46E-02
NM_204304	*PDCD4*	-0.41	0.11	3.52E-02
NM_205448	*TGM2*	-0.38	0.1	4.37E-02
NM_001030626	*PIAS2*	-0.36	0.1	4.37E-02

Table 3.1: Significant differential expression of genes in OTB hearts. The NCBI gene ID and gene name are shown. A negative fold change indicates downregulation and a positive upregulation. The standard error of the mean (SEM) is also shown. The p-values were adjusted.

A principal component analysis (PCA) plot was used to determine how the biological replicates were inter- and intra-comparable between groups (Fig. 3.12). The separation between the OTB and sham treatment groups was by the PC2 and less so by PC1, indicating a small number of differentially expressed genes, as it was seen by the statistical results. Both OTB 3 and Sham 3 were not considered outliers as they were separated from the biological replicates of their respective treatment groups by a similar distance.

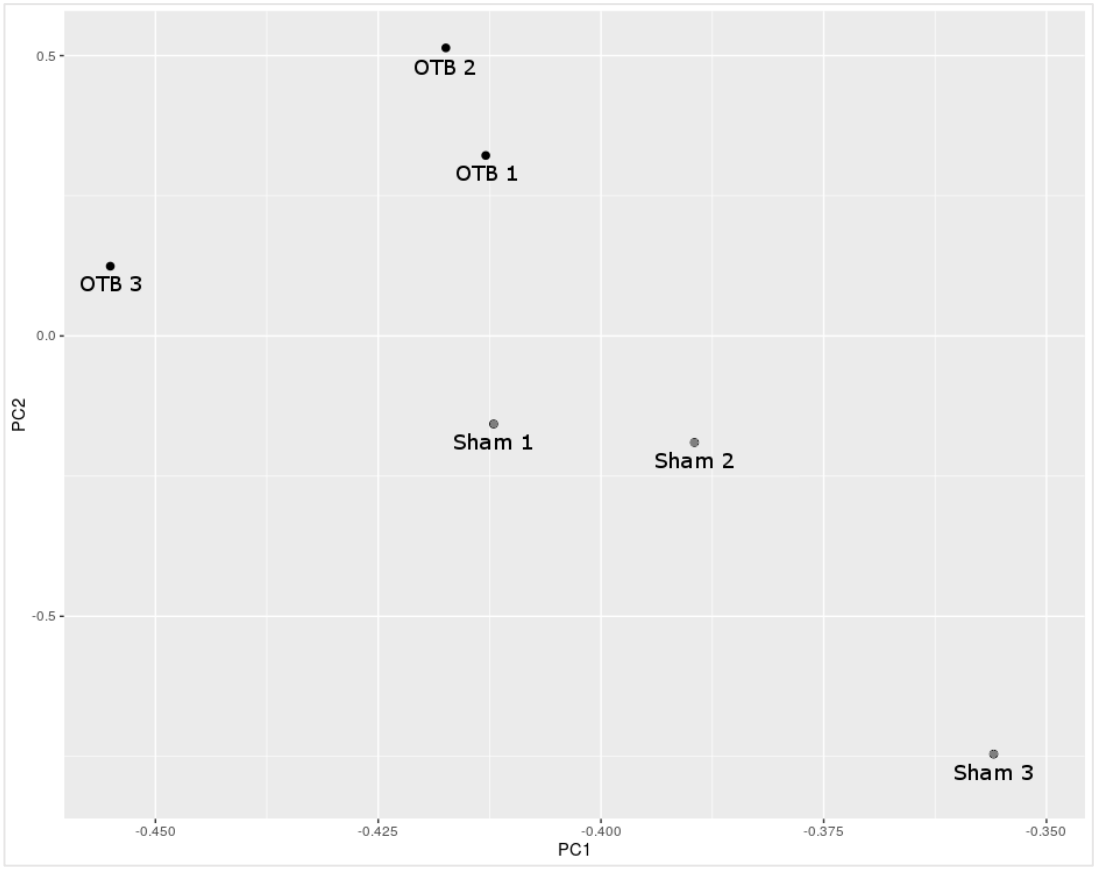

Figure 3.12: Principal component analysis (PCA) of OTB hearts and shams. The PCA plot was used to evaluate the inter- and intra-group variation of the biological replicates. Biological replicates of the same treatment group were widely spread. The separation between two groups was by the second principal component (PC2) but less so by the first principal component (PC1).

3.3.2 Finding potential qPCR targets from the RNA-sequencing dataset

Since none of the 30 differentially expressed genes had any strong ties with the epicardium or any of the cell lineages coming from EPDC differentiation, the data was manually scanned for any genes with high differential expression that just did not make the p-value cut. Those genes would initially be validated by quantitative real time PCR (qPCR) and also tested at later developmental stages (e.g. HH35). Any mRNA transcript labelled as predicted in NCBI were found to be excluded by the RNA-sequencing dataset. This prompted a literature search of genes found to

cause aberrant epicardial phenotypes that were not included in the RNA-sequencing dataset. Any predicted gene fragments that were acquired by PCR using cDNA were confirmed by gene sequencing.

SMAD2, of the SMAD superfamily, and *COL12A1* (collagen XII) were found to have a $\log_2$ fold change of -0.41 and 0.49, respectively. This fold change was deemed high enough for these genes to be selected for qPCR validation. *SNAI2*, migratory marker, and *DDR2*, cardiac fibroblast receptor, were predicted mRNA transcripts and so they were excluded by the RNA-sequencing dataset. Both genes were also selected for qPCR.

3.4 qPCR on genes with strong ties to the epicardium and its cell lineages

3.4.1 qPCR primer efficiency optimisation

Eight genes were selected for qPCR. *SMAD2* and *COL12A1* due to their fold change from RNA-sequencing. *SNAI2* and *DDR2* due to their importance in EPDC migration and differentiation and because they were excluded from the RNA-sequencing dataset due to having a predicted mRNA sequence. *TBX18* and *WT1* were chosen because they are two of the three main epicardial markers, the other being *TCF21*. Even though *SNAI1* was found to be normally expressed in the RNA-sequencing it was chosen because it is an important migratory marker with *SNAI2*. Finally, although *COL1A2* (collagen I) was also found to be normally expressed in the RNA-sequencing it was chosen because it is thought to be associated with collagen XII.

For primer optimisation, a wild type HH29 heart was isolated and had its RNA purified from the tissue. The RNA was converted to cDNA by in vitro reverse transcription (RT). The cDNA was used to test if the primers annealed at the designated temperature (62 ^{o}C) and to test their amplification efficiency. Again,

for simplicity reasons the workflow for one gene will be shown, using WT1 as an example, but the same process was done for all the genes shown in the end comparative qPCR result.

The primers were used for a normal RT-PCR with a primer annealing temperature of 60 °C, 62 °C and 64 °C. This was done to assess the quality of the primer design and their ability to anneal to the qPCR annealing temperature of 62 °C with no unspecific bands. If unspecific bands were present or no band was present using a 62 °C annealing temperature new primers would be designed. The RT-PCR products were visualised by gel electrophoresis (Fig. 3.13). Again, there were three different primer templates. RT+, where cDNA was used as a template, an RT-, where RNA was used as a template, and water control (blank) with just dH_2O being used as a template.

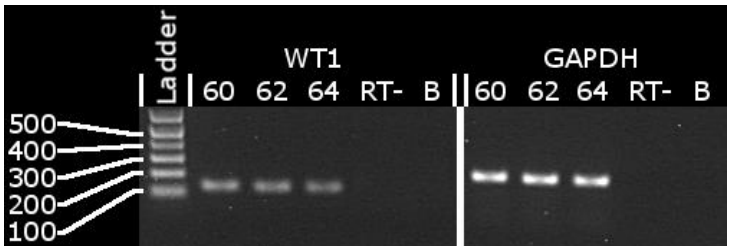

Figure 3.13: Assessing the annealing temperature and specificity of qPCR primers. The agarose gel had a ladder with band sizes in bp. The WT1 fragment had the correct size of 170 bp. GAPDH primers were used as positive control giving an amplicon of 188 bp. The numbers 60, 62 and 64 denote the three different temperatures (°C), where primer annealing was tested, using a cDNA template. Irrelevant lanes have been excluded Key: RT-, RNA template; B, water control.

A six point, three fold, dilution of the cDNA template was then set up for primer efficiency. Two technical replicates were performed for each dilution, along with an RT- and water control. The standard curve (Fig. 3.14A) had a primer efficiency (= $(10^{(-1/\text{gradient})}-1) \times 100$) cut off between 90% and 110% with an r^2 of 0.990 or

higher. The melting curve should have one, overlapping peak for each dilution sample (Fig.3.14B). A small peak at a lower temperature in relation to the major peak denoted primer dimers and it was considered acceptable as long as the efficiency and r^2 values met the designated standards. A peak at higher temperature denoted gDNA contamination, which was deemed unacceptable. The qPCR optimisation for all primers can be found in Appendix Figure 8.2. The primer efficiency and r^2 for each primer pair can be found at Table 3.2.

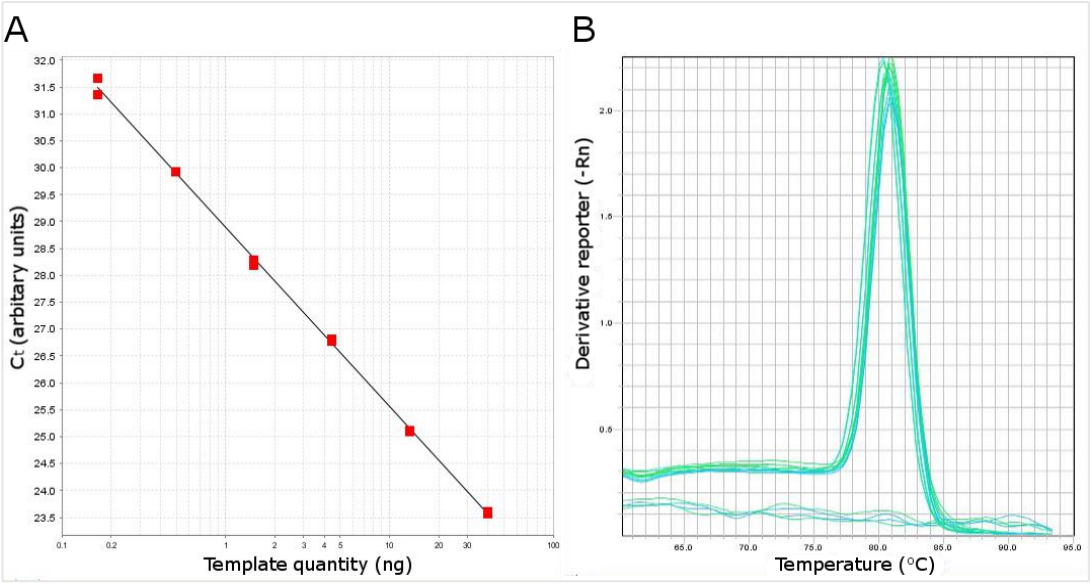

Figure 3.14: qPCR primer optimisation using WT1 primers. (A) The standard curve graph. The threshold cycle (C_t) is plotted against the total amount of cDNA template for each dilution. Note that the standard curve is generated only by readings taken from the cDNA template. (B) The melting curve graph. The derivative reporter (negative derivative of the function of fluorescent intensity vs. melting temperature) is plotted against the melting temperature. cDNA samples had a single, overlapping peak whereas RNA and water controls had no peak.

Primer pairs	Efficiency (%)	r^2
GAPDH*	99.6	1
TBP*	95.3	0.993
SNAI1	90.4	0.999
SNAI2	103.5	0.998
DDR2	93.3	0.999
SMAD2	108.1	0.998
COL1A2	95.3	0.999
COL12A1	93.2	0.999
TBX18*	109.7	0.998
WT1	100.1	0.999

Table 3.2: The efficiency and r2 values of the primer pairs used for qPCR at HH29. The primer pairs were named after their target amplicon. *Primer pairs were optimised by Dr. Matt Parnall.

3.4.2 Comparative qPCR

RNA from six HH29 hearts was isolated (n=3 per treatment group). The RNA was converted to cDNA by reverse transcription to be used as the template for qPCR. The genes GAPDH and TBP were used as reference genes for normalisation in order to measure the fold change (FC). The genes *DDR2* (FC=1.189; p=0.005), *COL12A1* (FC=1.390; p=0.002) and *TBX18* (FC=1.350; p<0.001) were found to be significantly upregulated (Fig. 3.15). *SNAI1* (FC=1.125; p=0.158), *SNAI2* (FC=1.057; p=0.523), *SMAD2* (FC=1.073; p=0.513), *COL1A2* (FC=1.062; p=0.539) and *WT1* (FC=1.133; p=0.066) had no significant difference (Fig. 3.15). Statistics were carried out automatically by the REST software. In conclusion, the qPCR data has shown upregulation of *DDR2*, *COL12A1* and *TBX18* in OTB hearts at HH29, in comparison to shams (Fig. 3.15).

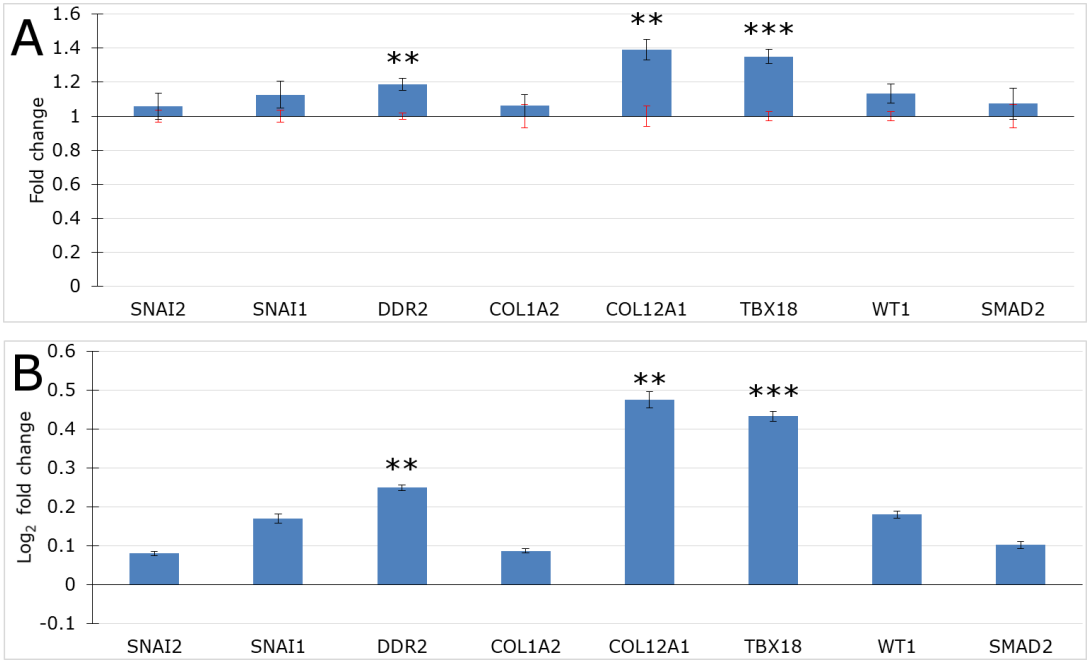

Figure 3.15: Relative expression differences between OTB and sham hearts at HH29. The fold change (A) and log_2 fold change (B) in OTB gene expression (bars) in comparison to shams (baseline). The error bars represent SEM (OTB, black; sham, red). Note that by definition shams have no error bars when log_2 transformed (n=3 per group). **p<0.01; ***p<0.001.

3.5 Immunoblot on cell adhesion molecules and TCF21 at HH29

Immunoblot analysis was used to quantify expression of proteins that could potentially give a more useful insight on the OTB model on the protein expression level, rather than the gene expression level. Protein from 12 HH29 hearts (n=6 per treatment group) was isolated. GAPDH expression was used for normalisation. The relative protein expression levels of N-cadherin, E-cadherin and TCF21 were measured (Fig. 3.16; three dependent variables). In comparison to shams, whose protein expression was assumed to be 100%, OTB hearts had an expression 103.227% for N-cadherin, 102.663% for E-cadherin and 98.722% for TCF21 (Fig. 3.16B).

The assumption of normality was tested in all dependent variables using a Shapiro-Wilk normality test. N-cadherin (W=0.886, p=0.106) and TCF21 (W=0.955, p=0.708), were normally distributed, whereas E-cadherin (W= 0.854, p=0.0411) was not. The assumption of variance was only tested on normally distributed dependent variables, using a Levene's test for homogeneity of variance. Both, N-cadherin ($F_{(DF)}=0.021_{(1,10)}$, p=0.887) and TCF21 ($F_{(DF)}=0.192_{(1,10)}$, p=0.671), had equal variances. An independent samples t-test was used to assess statistical significance, for N-cadherin and TCF21, and a two-sample Wilcoxon test, for E-cadherin, between the two treatment groups. The cell adhesion molecules N-cadherin (t=0.511, d.f.=10, p=0.620) and E-cadherin (W=12, p=0.393) showed no significant difference (Fig. 3.16B). The transcription factor and epicardial marker TCF21 (t=0.506, d.f.=10, p=0.624) also showed no significant difference (Fig. 3.16B). In conclusion, HH29 OTB hearts have shown no difference in the protein expression of E-cadherin, N-cadherin and TCF21, in comparison to shams (Fig. 3.16).

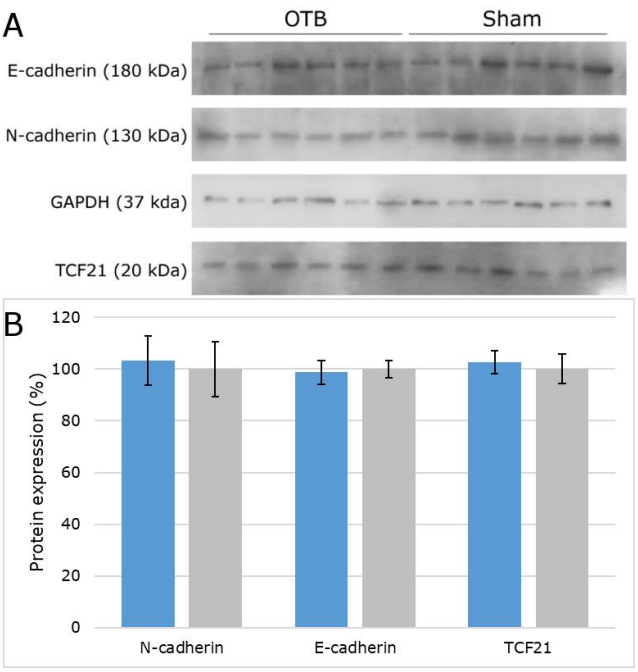

Figure 3.16: HH29 immunoblot. (A) The immunoblot showing the protein band for each protein used. (B) The protein expression of OTB (blue) proteins in comparison to shams (grey). Error bars represent SEM (n=6 per group).

3.6 Numbers of apoptotic, proliferating and total cells in the epicardium

From serially sectioned stained hearts, one group was stained using a marker for apoptotic cells (Fig. 3.17) and the other for proliferating cells. Counterstaining was achieved by DAPI. In total six HH29 hearts were analysed (n=3 per treatment group) with an average of 39 sections analysed per heart. The number of proliferating, apoptotic and DAPI stained cells, in the epicardium, was manually counted for all hearts. The apoptosis positive control can be found in Appendix Figure 3.

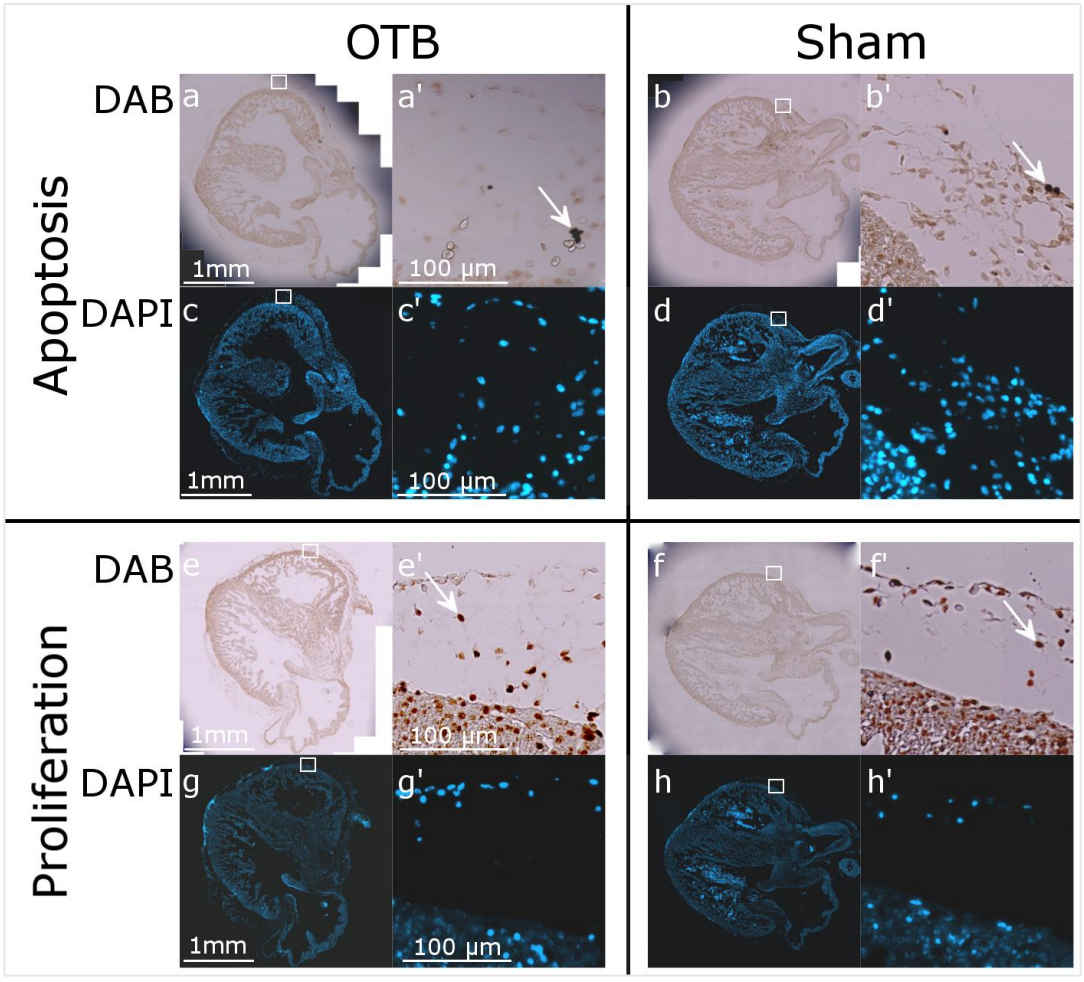

Figure 3.17: Immunostaining for apoptotic and proliferating cells. Immunostaining was achieved using TdT enzyme and anti-digoxigenin conjugated antibody for apoptotic cells and anti-PCNA antibody for proliferating

cells. The addition of DAB chromogen resulted in the cells being stained black-brown (arrows; a-b, e-f). DAPI was used to counterstain all the other cells (c-d, g-h). DAB positive cells were DAPI negative. Boxed areas in a-h are shown in a'-h'. The scale bar is the same for all panels.

Three dependent variables were measured; apoptotic cell ratio, proliferating cells ratio (=apoptotic or proliferating cells/total cell number) and total cell number (apoptotic cells, proliferating cells and DAPI+ cells), in the epicardium. Sham hearts had an average of 1098.3 apoptotic cells, 7870 proliferating cells and 32058.3 total cells. In contrast, OTB hearts had an average of 1530.3 apoptotic cells, 7392.3 proliferating cells and 57265.2 total cells.

The assumption of normality was tested in all dependent variables using a Shapiro-Wilk normality test. All dependent variables, apoptosis ratio ($W=0.951$, $p=0.747$), proliferation ratio ($W= 0.987$, $p=0.980$) and total cell number ($W=0.967$, $p=0.873$), were normally distributed. The assumption of variance was also tested, in all dependent variables, using a Levene's test for homogeneity of variance. All dependent variables, apoptosis ratio ($F_{(DF)}=0.035_{(1,4)}$, $p=0.956$), proliferation ratio ($F_{(DF)}=0.001_{(1,4)}$, $p=0.983$) and total cell number ($F_{(DF)}=0.043_{(1,4)}$, $p=0.846$), had equal variances. An independent samples t-test was used to assess statistical significance in the dependent variable between the two treatment groups. No significant difference was found in the ratio of apoptotic ($t=-1.136$, $d.f.=4$, $p=0.319$) or proliferating cells ($t=-2.195$, $d.f.=4$, $p=0.093$), between the two treatment groups (Fig. 3.18A, B). In addition, the total number of cells in the epicardium ($t= 2.224$, $d.f.=4$, $p=0.090$) was also insignificantly different (Fig. 3.18C). The epicardium of OTB hearts had a 23.2% decrease in apoptosis, 39.1% decrease in proliferation and 78.6% increase in the number of total cells compared to shams. In conclusion, there was no significance increase in the number of apoptotic, proliferating or total cells.

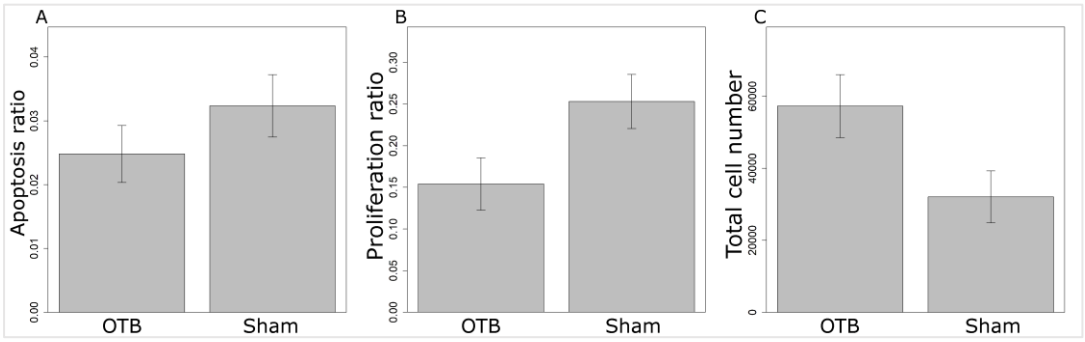

Figure 3.18: Rates of apoptosis and proliferation in the epicardium between OTB and shams. (A) The ratio of apoptotic cells vs the total number of cells. (B) The ratio of proliferating cells vs the total number of cells. (C) The total number of cells in the epicardium of OTB and sham hearts. Error bars represent SEM (n=3 per group).

3.7 Myocardial and collagen immunohistochemistry

A fixed area of 0.06 mm^2, for the epicardium on top of the right ventricle, and 0.015 mm^2, for the epicardium in the AV canal, was defined (Fig. 3.19A, E). The number of epicardial and blood cells could be measured as well as the void area fraction (VAF=empty space/total area) of the collagen I channel. Each heart was stained for collagen I, myocardium, using sarcomeric myosin heavy chain (MYH1E), and counterstained with DAPI (n=4 per treatment group). An average of 12 sections were analysed per heart. The epicardium of all four OTB hearts had ruffles on its surface (Fig. 3.19A-D; 3.20b/b'), as previously described in the introduction (Fig. 1.16; Pang, 2016). In contrast, the epicardium of all four shams appeared normal (Fig. 3.19E-H; 3.20a/a'). Any blood cells that were present in the sections fluoresced in all channels.

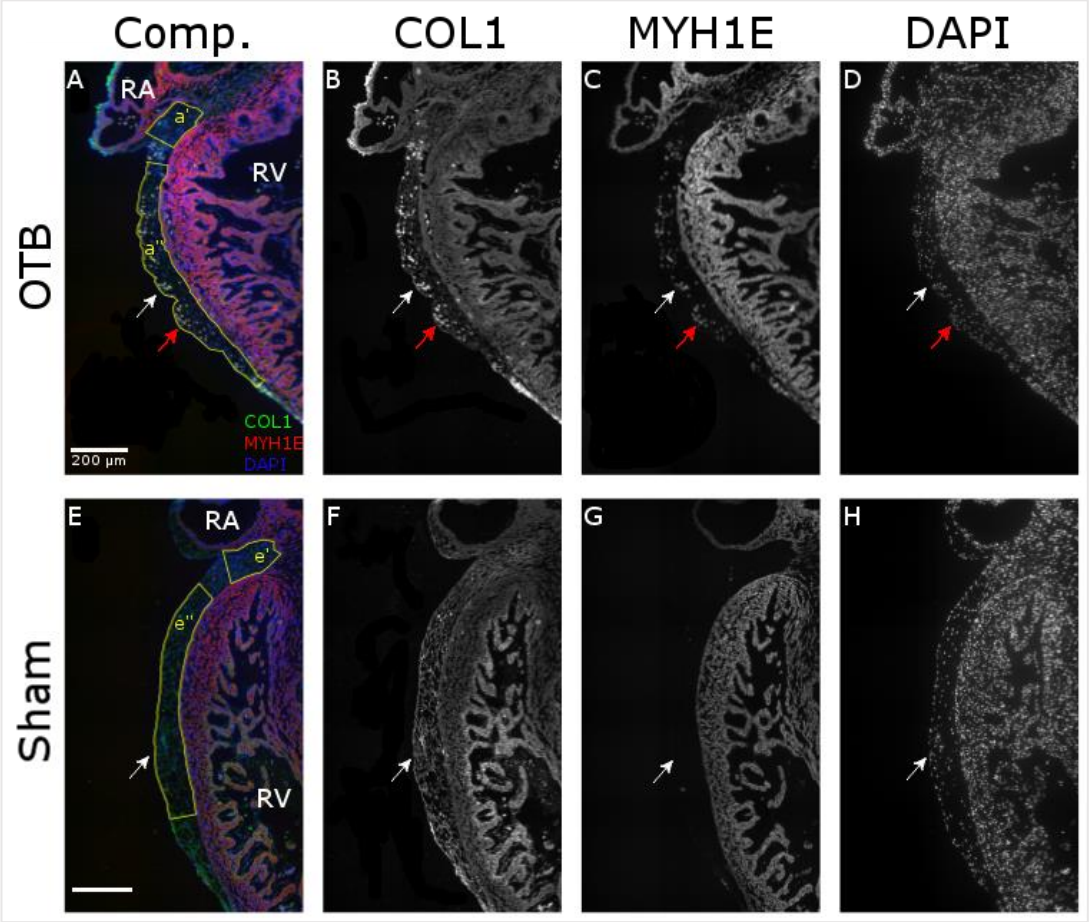

Figure 3.19: Immunostaining of HH29 heart sections with COL1, MYH1E and DAPI. Section of heart (A, E) stained showing the fixed area for the atrioventricular canal (a', e') and the epicardium covering the right ventricle (a'', e''). Each channel is also showed for collagen I (COL1; B, F), myocardium (MYH1E, sarcomeric myosin heavy chain; C, G) and DAPI (D, H). Blood cells fluoresce in all channels (red arrow). White arrow denotes the epicardium. Scale bar 200 µm for each group. RA; right atrium, RV; right ventricle. Comp., composite.

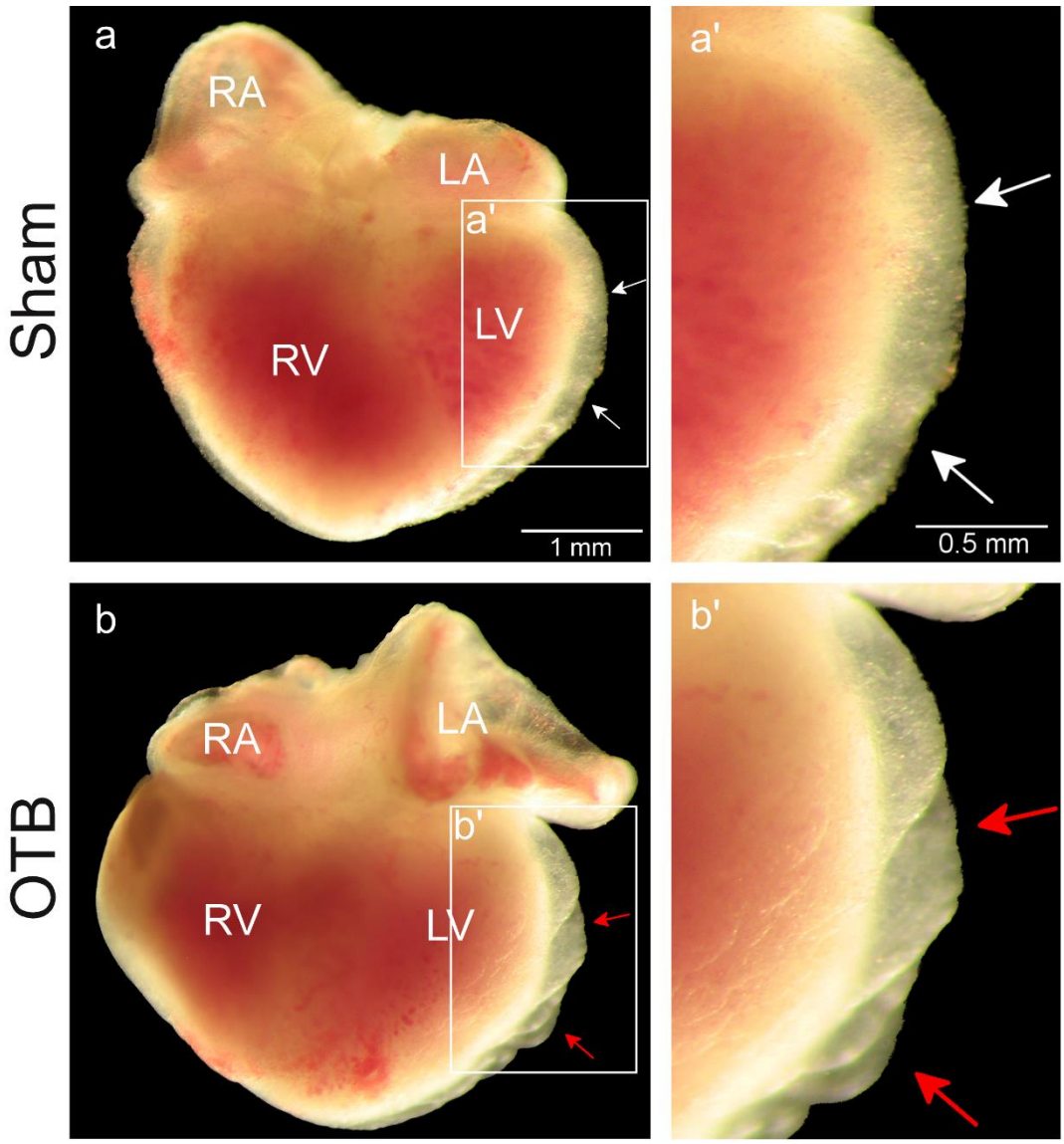

Figure 3.20: Epicardial morphology of HH29 hearts. Controls (a, a') displayed a normal external phenotype with an epicardium of normal size with no ruffles or blebbing (denoted by white arrow). The OTB hearts (b, b') exhibited an enlarged epicardium with ruffles on the epicardial surface and blebbing (red arrows). Scale bar 1 mm for a same for b and 0.5 mm for a' same for b'.

3.7.1 Collagen phenotype and the number of epicardial and blood cells

Four dependent variables were used for statistical analysis in each area; the number of epicardial cells, the number of blood cells, the number of all cells (epicardial cells and red blood cells) and the VAF (Fig. 3.21). In the epicardium

above the right ventricle, sham hearts had an average of 98.46 epicardial cells, 12.42 blood cells and a VAF of 0.548, whereas in the AV canal they had an average of 92.6 epicardial cells, 1.16 blood cells and a VAF of 0.285 (Fig. 3.21). In contrast, in the epicardium above the right ventricle, OTB hearts had an average of 84.15 epicardial cells, 48.38 blood cells and a VAF of 0.547, whereas in the AV canal they had an average of 77.56 epicardial cells, 1.75 blood cells and a VAF of 0.263 (Fig. 3.21). The multivariate, Hotelling's T^2 test was used for each area, since the areas had different sizes. The assumption of normality was tested using a Shapiro-Wilk normality test. The assumption of variance was also tested using a Levene's test for homogeneity of variance. There was also a variable number of blood cells present in the epicardium of OTB hearts, ranging from normal to approximately four times the number found in shams (Fig. 3.19; 3.21C).

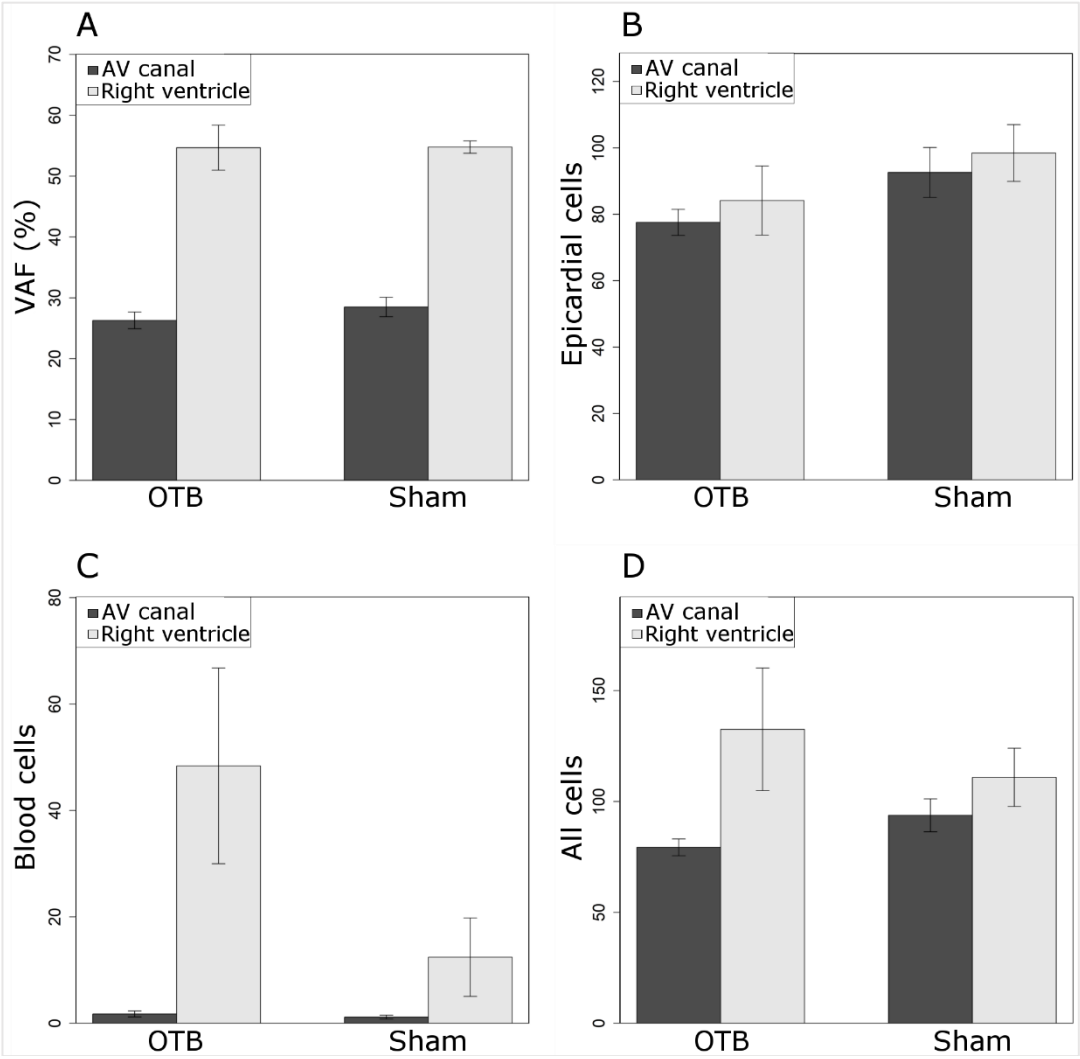

Figure 3.21: The void area fraction and average cell counts for each treatment group. The void area fraction (VAF; A), average number of epicardial cells (B), blood cells (C) and all cells (D) is shown. The measurements were taken from the epicardium in the atrioventricular (AV) canal and the epicardium covering the right ventricle (n=4 per group).

For the epicardial area above the right ventricle: All the dependent variables, number of epicardial cells (W=0.930, p=0.520), number of red blood cells (W=0.854, p=0.106), number of all cells (W=0.964, p=0.849) and VAF (W=0.954, p=0.753), were normally distributed. All the dependent variables, number of epicardial cells ($F_{(DF)}=0.118_{(1,6)}$, p=0.743), number of red blood cells ($F_{(DF)}=3.722_{(1,6)}$, p=0.102), number of all cells ($F_{(DF)}=1.458_{(1,6)}$, p=0.273) and VAF ($F_{(DF)}=4.185_{(1,6)}$, p=0.0868), had equal variances. The Hotelling's T^2 test showed no significant difference between the two treatment groups (T^2=2.191, F=2.921, d.f.=3, p=0.164).

For the epicardial area above the AV canal: All the dependent variables, number of epicardial cells (W=0.941, p=0.625), number of red blood cells (W=0.914, p=0.382), number of all cells (W=0.923, p=0.454) and VAF (W=0.961, p=0.823), were normally distributed. All the dependent variables, number of epicardial cells ($F_{(DF)}=0.285_{(1,6)}$, p=0.612), number of red blood cells ($F_{(DF)}=0.501_{(1,6)}$, p=0.506), number of all cells ($F_{(DF)}=0.350_{(1,6)}$, p=0.576) and VAF ($F_{(DF)}=0.498_{(1,6)}$, p=0.507), had equal variances. The Hotelling's T^2 test showed no significant difference between the two treatment groups (T^2=2.339, F=3.118, d.f.=3, p=0.150).

3.7.2 There was no difference in the axes ratio between sham and OTB hearts

Using the fixed area polygons (see section 3.7) an ellipse fit was carried out, where a major and minor axis was measured in the polygon. This allowed for an axes ratio measurement to be calculated using the major and minor axis (axes

ratio=major axis/ minor axis). Since the area had a fixed size of 0.06 mm^2 for the epicardium above the RV and 0.015 mm^2 for the epicardium in the AV canal any change in the major axis would be compensated by an opposite change on the minor axis (e.g. a 1 μm decrease in the major axis would result in a 1 μm increase in the minor axis). Therefore, the thickness but not the total area of the epicardium could be measured in the two different areas.

The assumption of normality was tested using a Shapiro-Wilk normality test. The assumption of variance was also tested using a Levene's test for homogeneity of variance. Followed by an independent samples t-test for each area. In the epicardial area above the right ventricle, the axes ratio had a normal distribution (W=0.936, p=0.673) and a homogeneous variance ($F_{(DF)}=0.600_{(1,6)}$, p=0.468). The OTB hearts had no significant difference (t=-0.176, d.f.=6, p=0.866), in comparison to shams (Fig. 3.22). In the epicardial area around the AV canal, the axes ratio had a normal distribution (W=0.893, p=0.249) but a significant difference in variance ($F_{(DF)}=8.687_{(1,6)}$, p=0.026). The OTB hearts had no significant difference (t=-1.261, d.f.=4.274, p=0.272), in comparison to shams (Fig. 3.22).

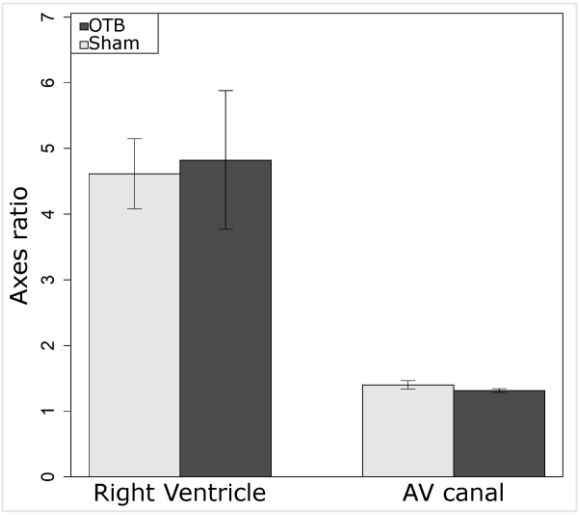

Figure 3.22: The axes ratio for each treatment group. The measurements were taken from the epicardium in the atrioventricular (AV) canal and the epicardium covering the right ventricle (n=4 per group).

3.7.3 Myocardilisation of the outflow tract

Further research was carried in the OFT of OTB hearts (n=4) due to the ectopic expression of *TBX18* and *TCF21* (section 3.2.4). Upon closer inspection of the OFT (Fig. 3.23) it was found that myocardilisation of the OFT in shams was under way but not extended along the OFT or entering into the epicardial area covering the OFT (Fig. 3.23a/a'). The semilunar valves (SLVs) were also undergoing maturation and they could be easily seen (Fig. 3.23a'). In contrast, the myocardilisation of the OFT in OTB hearts was extending further along the outflow region in comparison to controls (Fig. 3.23b/b'). The SLVs also showed gross malformations losing their valve like structure and looking more elongated along with the extended myocardium (Fig. 3.23b'). In addition, in both sham and OTB hearts the myocardium extended to the top of the SLVs, near or in the OFT region.

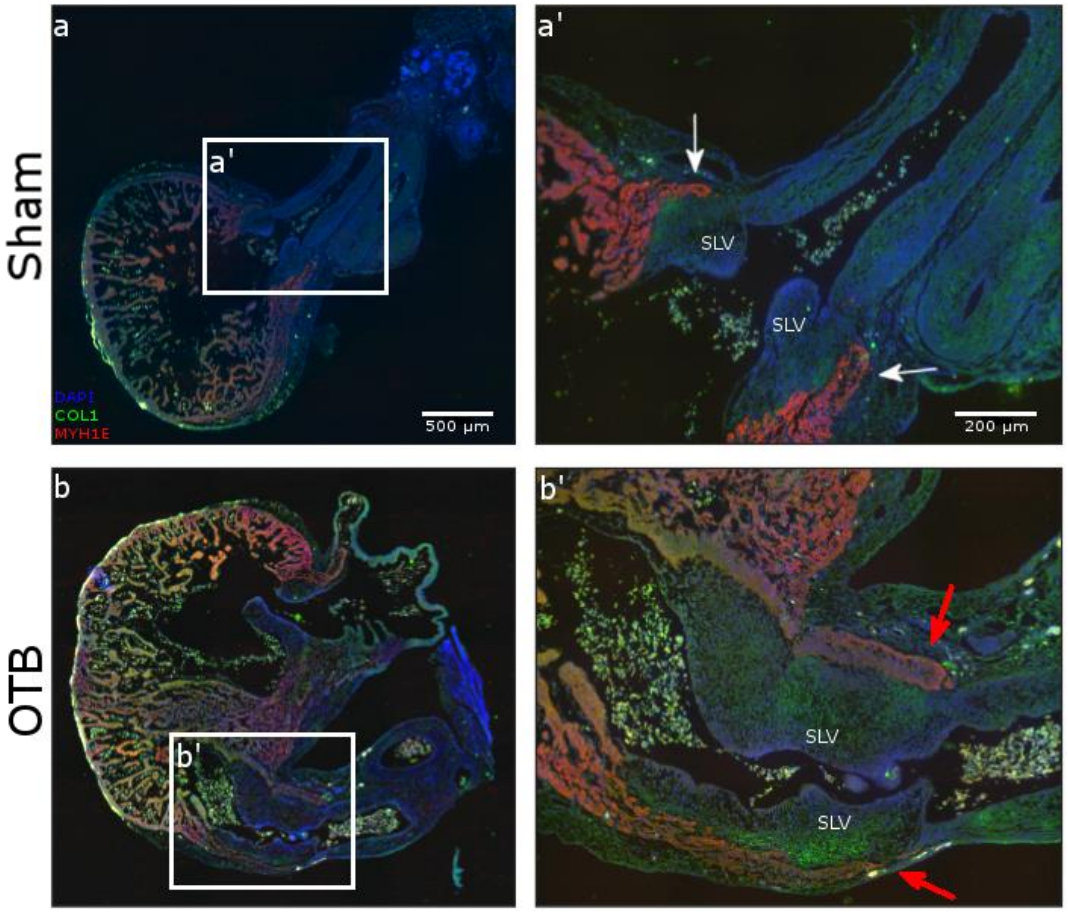

Figure 3.23: The myocardilisation of the outflow tract at HH29. Myocardium (red; MYH1E, sarcomeric myosin heavy chain), cell nuclei (blue),

and collagen I (green) were stained for sham (a) and OTB hearts (b). Shams exhibited normal myocardilisation of the OFT (a'; white arrows) but OTB hearts had an extended myocardilisation into the OFT (b'; red arrows). The semilunar valves (SLV) were found to be aberrant in OTB hearts. Scale 500 μm for a, b and 200 μm for a', b'.

3.8 Discussion

During cardiac development the proepicardial organ (PEO), which is formed near the sinus venosus (SV), migrates to the surface of the heart and envelops it (Lie-Venema et al., 2005). The migrating PEO attaches itself to the AV canal and inner curvature of the heart and migrates along the surface of the heart completely covering it. The epicardium covers the heart from dorsal to ventral (posterior to anterior) and from caudal to rostral (inferior to superior). However, there is a second epicardial population along the surface of the outflow tract (OFT), now termed the arterial epicardium (Gittenberger-de Groot et al., 2000; Pérez-Pomares et al., 2003).

The arterial epicardium, although it was discovered relatively recently (Gittenberger-de Groot et al., 2000; Pérez-Pomares et al., 2003), was found to be different from the venous epicardium on a molecular and morphological level (Pérez-Pomares et al., 2003). Arterial epicardial cells have a cuboidal morphology, whereas venous epicardial cells have a squamous phenotype. In addition, the arterial epicardium has a lower expression of RALDH2 and vimentin in comparison to the venous epicardium (Pérez-Pomares et al., 2003). The arterial epicardium starts to spread around the OFT at HH17, around the same time the venous epicardium spreads over the heart (Gittenberger-de Groot et al., 2012). Much is still unknown about the role of the arterial epicardium in development.

Inhibition or even late initiation of venous epicardial outgrowth can lead to hypoplasia of the compact myocardium (Gittenberger-de Groot et al., 2000). This can either be done mechanically, by physically blocking PEO migration (Gittenberger-de Groot et al., 2000), or by genetic manipulation of genes that affect epicardial migration and cell adhesion (Rhee et al., 2009; Takeichi et al., 2013). The relationship between epicardial outgrowth inhibition and a hypoplastic compact myocardium can be explained by two main cell processes; the addition of cells from the epicardium and myocardial proliferation. The epicardium sends a large number of EPDC in the myocardium, which will mainly adopt a fibroblast fate at HH29 (Wessels et al., 2012); these cells will increase the cells mass of the myocardium. The epicardium can also release mitogenic factors that promote myocardial proliferation (Li et al., 2011).

The epicardial and EPDC cells derived from it are maintained by cell division. The maintenance process is dependent on how the cell that is allowed to divide is oriented (Wu et al., 2010). This is affected by the orientation of the mitotic spindles apparatus, which is composed from microtubules and assist with chromosome segregation (Walczak and Heald, 2008). The cells can be oriented either parallel or perpendicular to the basement membrane of the epicardium (Wu et al., 2010). When cell division is perpendicular, one cell remains as an epicardial cell in the epithelium while the other cell migrates towards the subepicardial space. In contrast, a parallel cell division results in two epicardial cells staying in the epithelium (Wu et al., 2010). These findings suggest that cell division is not only essential for restoring the epicardial population, since part of it migrates away from the epithelium, but it appears to be important for epicardial EMT as well.

Since the epicardium is a highly heterogeneous population no epicardial specific genes have been discovered (Gittenberger-de Groot et al., 2012). Although WT1, TBX18 and TCF21 have been used as epicardial markers, not all epicardial cells express them and not all of them are expressed in one cell (Braitsch and Yutzey,

2013). In addition these three markers are not epicardium specific since TCF21 is also expressed in the allantois (Soulet et al., 2010), WT1 in the liver (Ishii et al., 2007) and TBX18 in the developing lower and upper limbs (Haenig and Kispert, 2004). These findings convey how difficult tracing of the whole epicardium is, since tracing every single cell is virtually impossible. When it comes to fibroblasts, the transcription factor (TF) TCF21 was found necessary for EPDC to differentiate into fibroblasts (Acharya et al., 2012). TCF21 is expressed in a wide range of epicardial cells at the start development, which can include future smooth muscle cells, but its expression gets more and more specific to future fibroblasts as development progresses (Acharya et al., 2012).

Although each of the main epicardial markers by itself is deemed inefficient for tracking all the epicardial cells, in this thesis we used all three of them at the same stages, using ISH, in order to get a clearer picture of epicardial migration. At HH24 all the markers showed some weak expression over the heart but strong expression on the tissue below the heart's apex and the distal part of the OFT. This staining can be due to the venous and arterial PEO since both of them are still around even after formation of their respective epicardial populations (Gittenberger-de Groot et al., 2012).

The ring of *WT1* expression seen in the HH26 OTB hearts, around the OFT, is associated with the arterial epicardium since the venous epicardium does not normally reach the distal part of the OFT (Pérez-Pomares et al., 2003). It is unlikely that this aberrant *WT1* expression seen in OTB hearts is caused directly by the position of the suture since the suture is located near the proximal end of the OFT. In addition, the arterial epicardium is known to express WT1, with no conclusive data showing specific expression of *TCF21* and *TBX18* (Vicente-Steijn et al., 2015). In this thesis using the ISH from HH28 it is confirmed that, normally, the arterial epicardium expresses *WT1*, as it was seen around the OFT. A low or absent expression of *TCF21* and *TBX18* was also seen in shams. However, OTB

hearts not only expressed *WT1* around the OFT but they also had a strong expression of *TCF21* and *TBX18*. The fact that *WT1* is expressed around the OFT by HH28 suggests that the ring of *WT1* expression at HH26 is not exactly ectopic but rather premature.

It is hard to say what role *TFC21* expression has on the OFT, since the function of the arterial epicardium is largely unknown. A recent study has suggested that OTB, and changes in haemodynamics generally, do result in aberrant collagen deposition (Rennie et al., 2017). If *TCF21* in the arterial epicardium is linked with fibroblast production, as it is to the venous epicardium (Acharya et al., 2012), changes in *TCF21* expression could be associated with fibroblasts function and collagen deposition on the OFT.

The increased expression of *TBX18* on the right side of the HH28 OTB heart has been confirmed in this thesis by qPCR (an increased *TBX18* expression at HH29). Although PE migration is asymmetric in chicken, coming only from the right side of the SV (Hiruma and Hirakow, 1989), at this stage it should have completely covered the heart. If this was a case of delayed migration the other two markers should also have had an asymmetric expression and *TBX18* underexpressed, rather than overexpressed. Although the notion that EPDC cells can give rise to cardiomyocytes is controversial, it has been demonstrated by some research groups (Cai et al., 2008; Zhou et al., 2008). Assuming that *TBX18* expressing cells are able to become cardiomyocytes (Cai et al., 2008), an increased *TBX18* expression would be protective against thinning of the compact myocardium. In this way, the increased expression of *TBX18* on the right heart side could be tied with the fact that the right side of OTB hearts had a normal morphological phenotype, in contrast with the left side, which was thinner and dilated, as shown in previous studies from our lab (Pang, 2016; section 1.14).

Semilunar valve (SLV) formation begins during HH29 with a pair of endocardial cushions forming in the OFT (Martinsen, 2005). Muscular tissue growth in the

proximal OFT, a process called myocardilisation, also muscularises the cushions. The increased expression of *TBX18* in the OFT of hearts at HH28 can be tied to the increased myocardilisation of the OFT at HH29, since Tbx18 expression was found indispensable for the myocardilisation of the SV (Christoffels, 2006; Wiese et al., 2009). It is possible that misexpression of TBX18 in the OFT could cause the same mechanism of myocardilisation to be active, causing an extended myocardium formation from the base of the OFT. The aberration found in the SLVs is novel and has not been previously described in literature before; another PhD student (Kawthar Alnahdi) will research it.

Although the RNA-sequencing study had great prospects, it did not show any clear results when it came to the epicardium. All the genes that were significantly down- or up-regulated had no clear ties with the epicardium. This could be due to a number of reasons. As the epicardium cannot be separated from the rest of the heart, genes expressed from the myocardium and endocardium with higher reads could have decreased the sensitivity of detecting epicardial related genes. Although RNA-sequencing has become the gold standard for whole transcriptome gene expression quantification (Anders and Huber, 2010; Mortazavi et al., 2008), when compared to qPCR the consistency reaches up to 85%, even for the best established reference samples (Everaert et al., 2017). Genes with inconsistent results when it comes to RNA-sequencing have a small size with fewer exons and low expression (Everaert et al., 2017).

The genes *SNAI1*, *SNAI2*, *TBX18*, *WT1*, *COL1A2*, *COL12A1*, *DDR2* and *SMAD2* were chosen for analysis by qPCR. TBX18 and WT1 are known for affecting migration of epicardial cells through the gene SNAI2 (Takeichi et al., 2013). SNAI1 promotes EMT together with SNAI2 (Medici, Hay and Olsen, 2008). COL1A2 (collagen I) is a major structural collagen, which primarily comes from epicardium derived cardiac fibroblasts (Acharya et al., 2012). COL12A1 (collagen XII) is a type of fibril associated collagen with interrupted triple helices. Collagen XII was found

to be expressed in the epicardium of zebrafishes (Marro et al., 2016) and binds to collagen I changing its biomechanical properties (Koch, 1995). COL12A1 expression also changes based on tensile stress (Flück et al., 2003), with the stress state leading to its upregulation. DDR2 is a membrane receptor found in a number of cells but in the heart it is exclusively expressed in cardiac fibroblasts (Morales et al., 2005). *DDR2* expression can impact collagen deposition and fibrillogenesis (Cowling et al., 2014). SMAD2 is one of the mediators of TGFβ signalling and is responsible for inducing gene transcription by mediating multiple signal pathways (Nakao, 1997). TGFβ is functionally important for the epicardium since it promotes the EPDCs to undergo EMT (Craig et al., 2010).

Of the nine genes tested by qPCR seven of them, *SNAI1*, *TBX18*, *WT1*, *COL1A2*, *COL12A1* and *SMAD2*, were in the RNA-sequencing dataset and two of them were absent, *SNAI2* and *DDR2*, because their cDNA sequence was labelled as "predicted" by NCBI. By DNA sequencing the gene fragments of *SNAI2* and *DDR2*, which were the targets of the qPCR primers, it was proven that NCBI's predicted sequence were correct for those parts of the sequence. Out of the five genes that were in the RNA-sequencing database two of them were found to be significantly different by qPCR but not RNA-sequencing. *COL12A1* was expressed at low levels, hence why inconsistent results were seen by RNA-sequencing, although both qPCR and RNA-sequencing $\log_2$ fold change values were similar (0.48 and 0.49 respectively). *TBX18* has none of the features that genes with inconsistent RNA-sequencing results tend to have. Since the qPCR results agree with the ISH results, on *TBX18*, it is safer to assume that not being significantly differentially expressed in the RNA-sequencing could be due to the DESeq algorithm used for fold change estimation (Love et al., 2014), since it can influence RNA-sequencing results (Everaert et al., 2017).

The adhesion proteins N- and E- cadherin are expressed in the cells of the epicardial epithelium (Martínez-Estrada et al., 2010; Wu et al., 2010). An

immunoblot was favoured over qPCR for the quantification of E- and N-cadherin. since cadherins are known to undergo cleavage and those cleavage products can be detected in an immunoblot (Ferber et al., 2008; Wheelock et al., 2008). In addition, TCF21 is the only TF in the epicardium with a very clearly defined role, specification of fibroblasts (Acharya et al., 2012), so measuring its protein expression levels would potentially be more valuable than RNA. Whole uncleaved N- and E- cadherin protein bands were easily visible in the immunoblot with no significant difference between sham and OTB hearts. TCF21 also showed a clear band with no significant difference between sham and OTB hearts.

Epicardial derived cells are a proliferative population during development, although quiescent after birth (Virágh et al., 1993). Proliferation was also found to be important for the replenishment of epicardial cell in the epithelium, since they undergo EMT (Wu et al., 2010). Not much is known about how apoptosis affects epicardial development. It has been shown that TBX18 null mice have decreased proliferation and increased apoptosis rates and this causes defects in the development of the future coronary vessel plexus (Wu et al., 2013). In this study there was no significant difference in the ratio of proliferating and apoptotic cells or the total cell number, although the total cells number was increased by 78.6% in OTB hearts, in the epicardium. Since this study was done on only one developmental stage, HH29, there might have been a different critical stage in development where the alteration of haemodynamics caused the aberrant apoptosis or proliferation ratio. In addition, any differences between the two groups might not have been significant due to the low number of biological repeats. Unfortunately, due to the amount of time, and other resources, it takes to manually count all the cells this study could not be repeated in other stages.

Although collagen I expression level was not found to be significantly different in HH29 OTB hearts, the collagen I phenotype was still examined since an aberrant expression of other ECM factors could cause a deformation of collagen I fibres.

OTB collagen I in the HH29 epicardium was found to have a normal patterning similar to shams and also the epicardial thickness was found to be similar, at least in the right side of the heart. The fact that the number of red blood cells was highly variable indicates that there is a malformation regarding the coronary vessels. At HH29 the coronary vasculature is still composed from endothelium layered vessels with no major contribution of smooth muscle cells (Poelmann et al., 1993), which means they have a thinner vessel wall in comparison to mature vessels. In addition, the OTB hearts are susceptible to an increase in blood pressure due to the banding procedure (Midgett et al., 2014), making the coronary vessels susceptible to bleeding. Leakage of red blood cells and plasma could be a possible explanation for an increase in epicardial volume.

In conclusion, although an abnormal epicardium can be seen at HH29 it is hard to pin point a single causative mechanism. Epicardial migration along the heart was found to be normal with *TBX18* being overexpressed at the right side of the heart. RNA-sequencing did not show a significant difference concerning any genes directly related to the epicardium, but qPCR showed overexpression of *COL12A1* and *TBX18*. N- and E-cadherin had a normal protein expression at HH29 as well as TCF21. The apoptosis and proliferation ratio as well as the total number of cells were also not significantly different between sham and OTB hearts at HH29. In addition, there were variable amounts of bleeding into the epicardium. This leaves the possibility that the deformation of the epicardium is caused by multiple factors together rather than a sole causative mechanism, requiring a multivariate analysis. For example, the increase in size could be partly due to an increase in cell proliferation coupled together with blood pooling in the epicardium and increased ECM deposition, since none of these factors alone were found to cause a significant difference. It is also possible that the major events causing the aberrant epicardium at HH29 took place on a previous developmental stage, requiring similar studies, outlined here for HH29, to be repeated on earlier developmental stages. Regarding the OFT, abnormal expression of *WT1* was

observed at HH26 and overexpression of *TCF21* and *TBX18* at HH28. At HH29, there was an increased myocardilisation of the OFT in OTB hearts together with newly described aberrations of the SLVs.

4 Coronary vessels development at HH35

4.1 Overview and aims

Coronary vessels (CVs) consist of two main cell populations, endothelial cells (ECs) and mural cells (Murakami and Simons, 2009). Mural cells can be either SMCs, which are found in arteries and veins, or pericytes, which are found around venules and capillaries (Olivey et al., 2004; Murakami and Simons, 2009). Vascular ECs form the inner lining of the vascular tube, with a single cell layer thickness, making the blood vessels. ECs have a plethora of important roles in blood vessels, including ultrafiltration, haemostasis and blood clotting (Udan et al., 2013). SMCs contain α-smooth muscle actin isoforms making them able to cause vasoconstriction or vasodilation, thus regulate blood flow and pressure, and provide structural stability to the blood vessels (Udan et al., 2013). Pericytes were found to be linked to ECs survival and proliferation but no conclusive evidence has demonstrated they are contractile (Udan et al., 2013), although it was found that a subset of them express α-smooth muscle actin in vivo (Ehler et al., 1995; Skalli et al., 1989).

In the chick, an early endothelial plexus is formed as early as HH29 (Bernanke and Velkey, 2002; Eralp, 2005). Although CVs reach a developmental milestone at HH33, with the right and left coronary artery formed and being attached to the aorta, these coronary arteries are not patent. Cells around the wall of the aorta, where the CVs are attached, need to undergo apoptosis in order to make the coronary ostia (Eralp, 2005). When the coronary arteries are patent, by HH35, blood can circulate in the CVs (Eralp, 2005; Bernanke and Velkey, 2002). EPDCs are able to differentiate into smooth muscle cell (SMC) precursors and most SMCs that make up the CVs come from the epicardium (Gittenberger-de Groot et al., 2000). Mechanical inhibition of epicardial outgrowth results in an absent coronary vasculature and delay of epicardial outgrowth results in CV malformations (Eralp, 2005). Whether or not EPDC cells can differentiate into ECs remains a controversial

subject, with evidence pointing both for and against (Katz et al., 2012; Lie-Venema et al., 2005).

In the heart ECs, SMCs and pericytes can be distinguished by specific marker genes. For example CSPG4 (NG2) is a marker of pericytes (Ozerdem et al., 2001). *NRP1* is expressed in the ECs of nascent arteries and *NRP2* is expressed in veins, which have low or no NRP1 expression (Herzog et al., 2001). Finally, SMCs have the actin isoform ACTA2 (α-SMA; alpha smooth muscle actin).

An extensive list of genes affect CV development, which includes genes that affect normal vessel development as well as epicardial genes. The epicardial markers WT1 and TBX18 were found to affect CV development. WT1 null mice have no CVs and TBX18 null mice have a decrease in CV branching and a smaller lumen diameter (Wagner, 2005; Wu et al., 2013). TCF21 is also an important epicardial marker in CV development since it prevents EPDCs from differentiating prematurely, by blocking SMCs differentiation (Braitsch and Yutzey, 2013; Nurnberg et al., 2015). Bves is also expressed in the epicardium as it is an early marker of SMCs; it is postulated to be important for cell adhesion and SMC differentiation (Reese et al., 1999; Wu et al., 2012). In addition, Connexin 43 (Cx43; GJA1) was found to be important for epicardial cell polarisation, during EMT, and in the development and pattering of the coronary vascular plexus (Li et al., 2002; Rhee et al., 2009).

During vessel maturation, a signalling cascade due to crosstalk between ECs and mural cells further stabilises the blood vessels. ECs can recruit and promote the proliferation of mural cells by secreting PDGFB and BDNF, which bind to their respective receptors PDGFRB and NTRK2 (TrkB), in mural cells (Donovan et al., 2000; Udan et al., 2013; Wagner, 2005). In addition, ECs have a TEK (TIE2) receptor, which binds to ANGPT1 (angiopoietin 1), secreted by the mural cells (Brindle, 2006; Udan, Culver and Dickinson, 2013).

Upon harvesting and external phenotypic analysis of HH35 OTB hearts external bleeding could be seen. Since HH35 is the point where coronary arteries are patent, and no bleeding was seen in previous stages, a set of experiments were designed to study the cause of this phenotype. Due to the fact that CVs have two different cell populations, ECs and mural cells, the reason of bleeding could be down to one or both cell populations being dysfunctional. SMCs ultimately come from the epicardium, suggesting that if there was an aberrant phenotype involving them it might be due to a differential expression in specific epicardial genes.

The specific experimental aims to address the phenotype of the CVs at HH35 were:

- Analyse the gene expression of epicardial and vascular genes that are tied to vessel maturation, angiogenesis and SMC/EPDC differentiation and migration in OTB hearts and compare it to shams.
- Morphologically and quantitatively, asses the coronary vasculature within different regions of OTB and shams hearts.
- Morphologically asses the major external coronary vessels of OTB and shams hearts.
- Analyse the ultrastructure of coronary vessels in OTB and sham hearts.

4.2 OTB hearts have external bleeding

Upon harvesting of hearts at HH35 (n=3 per treatment group) external bleeding could be seen on the anterior inferior aspect of the OTB hearts (Fig. 4.1 a, a') but not the posterior (Fig. 4.1 b, b'). HH35 sham hearts had no visible signs of bleeding (Fig. 4.1 c-d). The blood was trapped between the myocardium and the epicardium, in the subepicardial space. Further phenotypic analysis on all the hearts harvested at HH35, from different studies (n=12 per treatment group), showed various degrees of bleeding within the same region. From the 12 OTB hearts analysed 11 had visible external bleeding (91.67%), whereas from the 12 shams none did (0%). In contrast, no major bleeding was seen at HH29, in comparison to HH35, although there were signs of leakage (n=4, section 3.7).

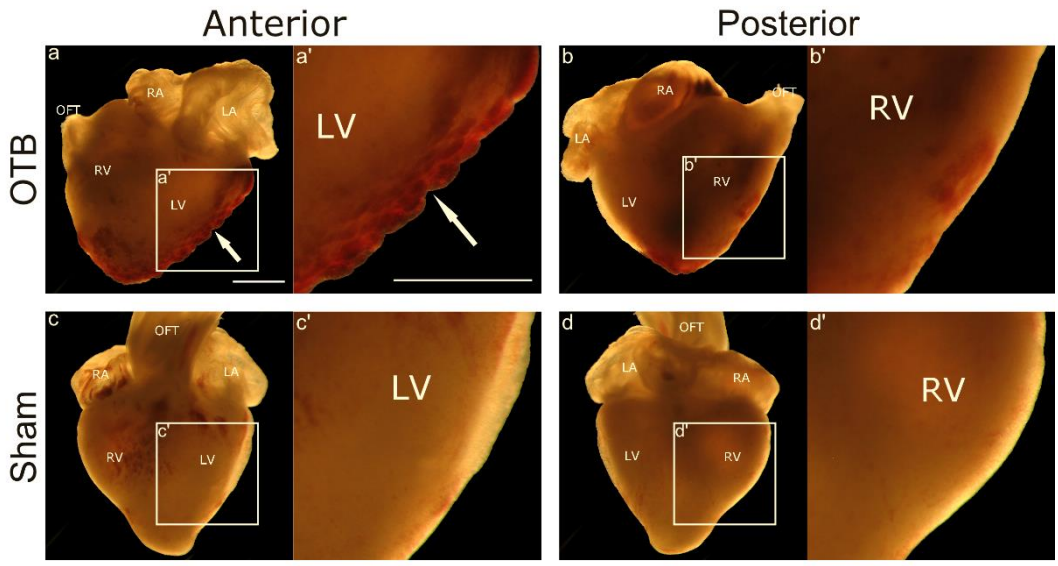

Figure 4.1: Bleeding in the subepicardium of HH35 OTB hearts. The bleeding (arrow) on an OTB heart could mainly be seen on the anterior aspect (a, a') but not the posterior (b, b'). Shams had no visible bleeding on either their anterior (c, c') or posterior (d, d') aspect. Key: OFT, outflow tract; RA, right atrium; LA, left atrium; RV, right ventricle; LV, left ventricle. Scale bar 1 mm for all panels.

4.3 Differential expression of genes involved with coronary vasculature development

In order to further investigate the cause of bleeding, six HH35 hearts (n=3 per treatment group) had their RNA isolated and converted to cDNA. The cDNA was used for qPCR. All the genes selected for qPCR were linked with angiogenesis, EPDCs migration or their differentiation into SMCs. The primer pair optimisation step was carried as previously mentioned (see section 3.4.1). The efficiency and r^2 for each primer pair can be found in Table 4.1. The genes GAPDH and TBP were used as reference genes for normalisation in order to measure the fold change (FC).

Primer pairs	Efficiency (%)	r^2
GAPDH*	99.6	1
TBP*	95.3	0.993
NRP1	110.0	0.999
NRP2	104.1	0.990
ANGPT1	106.7	0.998
NTRK2	110.0	0.992
BDNF	99.1	0.992
Bves	107.4	1
GJA1	104.8	0.999
CSPG4	93.8	0.992
PDGFRB	98.2	0.999
YAP1	105.3	0.998
TAZ	98.7	0.998
TBX18*	109.7	0.998

Table 4.1: The efficiency and r2 values of the primer pairs used for qPCR at vascular genes. The primer pairs were named after their target amplicon. *Primer pairs were optimised by Dr. Matt Parnall.

Twelve genes were analysed by qPCR, *NRP1*, *NRP2*, *ANGPT1*, *NTRK2*, *BDNF*, *Bves*, *GJA1*, *CSPG4*, *PDGFRB*, *YAP1*, *TAZ*, *TBX18*. Five of them were significantly downregulated, *NRP1* (FC=0.679; p=0.004), *ANGPT1* (FC=0.619; p=0.002), *NTRK2* (FC=0.334; p<0.001), *PDGFRB* (FC=0.491; p<0.001), *TBX18* (FC=0.464; p=0.01) and one of them was significantly upregulated, *BDNF* (FC= 2.747; p<0.001). However, six of them showed no change, *NRP2* (FC=0.932; p=0.441), *Bves (*FC=1.046; p=0.653), *GJA1* (FC=1.204; p=0.180), *CSPG4* (FC=1.101; p=0.463), *YAP1* (FC=0.876; p=0.397), *TAZ* (FC=0.978; p=0.886; Fig. 4.2). Statistics were carried out automatically by the REST software using a bootstrapped MANOVA. In conclusion, HH35 OTB hearts exhibited downregulation of the genes *NRP1*, *ANGPT1*, *NTRK2*, *PDGFRB*, *TBX18* but upregulation of *BDNF*, in comparison to shams.

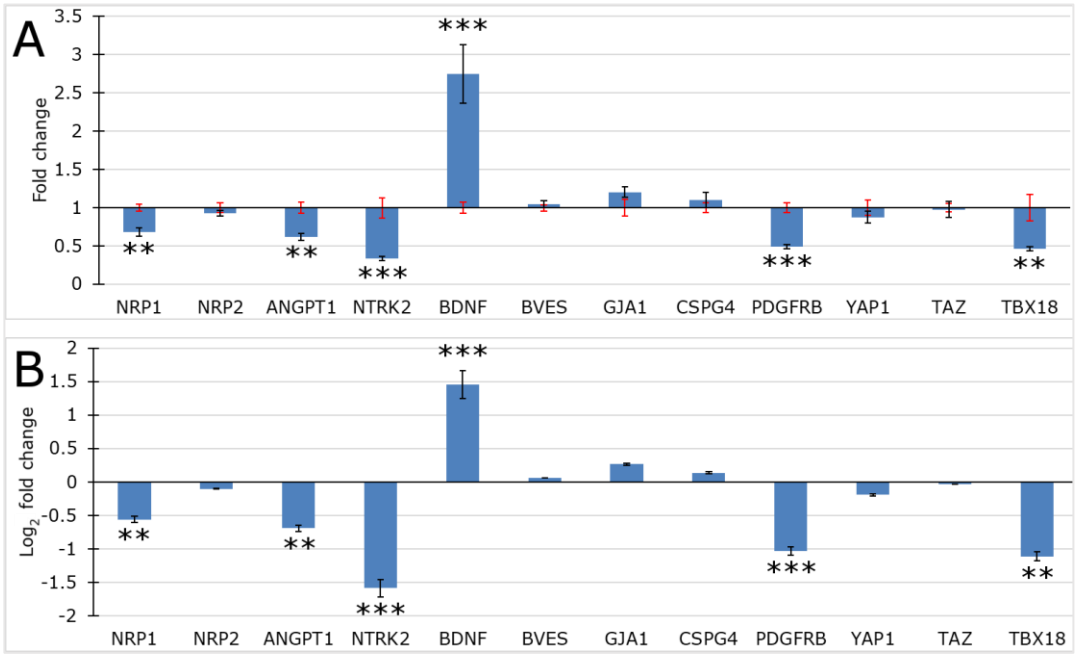

Figure 4.2: Relative expression differences between OTB and sham vascular genes at HH35. The fold change **(A)** and log_2 fold change **(B)** in OTB gene expression (bars) in comparison to shams (baseline). The error bars represent SEM (OTB, black; sham, red). Note that by definition shams have no error bars when log_2 transformed (n=3 per group). **p<0.01; ***p<0.001.

4.4 OTB hearts have aberrant coronary vasculature

An antibody against α-SMA was used to stain the actin of SMCs in order to visualise the vessels of hearts using fluorescent immunohistochemistry on sections (Fig. 4.3). Six HH35 hearts (n=3 per treatment group) were used in this experiment. The visualisation of CVs would allow further elucidation on any vessel abnormalities that could cause the bleeding in the OTB hearts. Vessels supported by SMCs were seen in the ventricular compact myocardium and in the epicardium around the ventricles in both sham and OTB hearts (Fig.4.3 c-f). Only one OTB heart (1/3) had SMC coated vessels in its interventricular septum (IVS; Fig.4.3 b) in contrast to shams (3/3; Fig.4.3 a). No vessels supported by SMCs were seen in the atria, of both treatment groups, so they were excluded from this study.

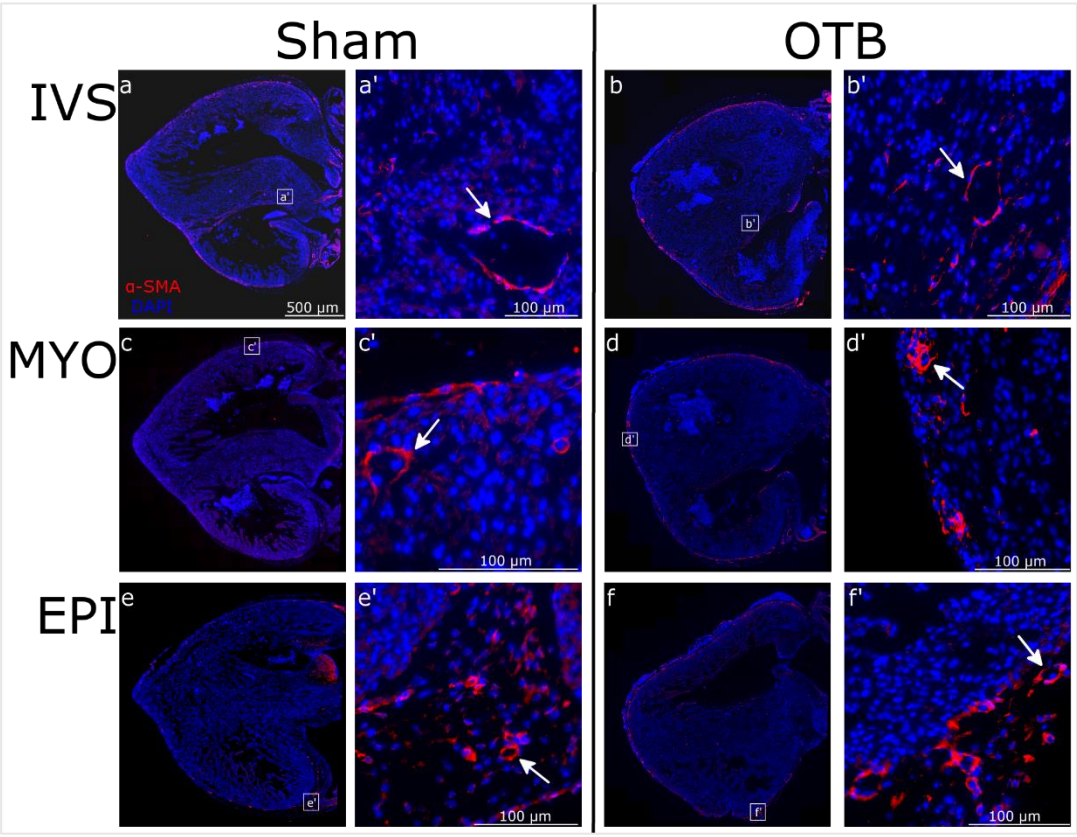

Figure 4.3: Fluorescent immunohistochemistry using DAPI and anti-α-SMA on sham and OTB hearts at HH35. Vessels supported by SMCs (arrows) were seen in the interventricular septum (IVS; a-b), the ventricular myocardium (MYO; c-d) and the epicardium (EPI; e-f) in sham and OTB hearts. The scale bar is the same from a-f.

In order to investigate the data further, three different readings were taken on all the vessels; number of vessels, lumen area and wall (SMCs) area. The number of vessels (Fig. 4.4A), the wall to lumen ratio (WLR; Fig.4.4B), calculated by dividing wall area by lumen area, and the vessel area (Fig. 4.4C), calculated by adding wall area with lumen area, were used as dependent variables, for initial statistical assessment. These readings were taken in three regions of each heart, the epicardium, myocardium and IVS.

The assumption of normality was tested in the residual of all dependent variables using a Shapiro-Wilk normality test. All dependent variables, vessel number (W=0.970, p=0.804), vessel area (W= 0.971, p=0.823) and WLR (W=0.957, p=0.534), were normally distributed. The assumption of variance was also tested, in all dependent variables and their interaction with the treatment and the different regions, using a Levene's test for homogeneity of variance. All dependent variables, vessel number ($F_{(DF)}=0.282_{(5,12)}$, p=0.914), vessel area ($F_{(DF)}=0.690_{(5,12)}$, p=0.616) and WLR ($F_{(DF)}=0.433_{(5,12)}$, p=0.818), had equal variances.

A multivariate analysis of variance (MANOVA) was first carried out to assess any potential statistical significance between the three dependent variables between all the regions. A MANOVA will test three different hypotheses; there is no difference between the treatment groups (H_1); there is no difference between the different regions (H_2); there is no interaction between the treatment and the different regions (H_3). There was no significant difference between the two treatments ($F_{(3,10)}=1.046$, p=0.414; H_1) but there was a significant difference between the three regions ($F_{(6,22)}=17.975$, $p<0.0001$; H_2) and the interaction between the treatment and regions ($F_{(6,22)}=5.374$, p=0.002; H_3). A post-hoc test was carried out to confirm where the differences occurred between the different factors. The Tukey's honest significance difference test (Tukey) was used as the chosen post-hoc test.

Only the relevant differences will be discussed in the results, since differences that occur normally between regions of the same treatment group are beyond the scope of this thesis (see appendix for all the p-values for each dependent variable between the different factor interactions; Table 8.2). The shams had a similar vessel area between their epicardium and IVS (p=0.972), whereas OTB hearts did not (p=0.049; Fig. 4.4A). Although the IVS is part of the ventricular myocardium, in OTB hearts there was significant difference in the vessel number (p=0.032; Fig.

4.4B) and WLR (p<0.0001; Fig. 4.4C), with the ventricular myocardium having a higher vessel number and WLR, in comparison to the IVS. On the other hand there was no difference in either the vessel number (p=0.999), nor WLR (p=0.852) in those regions. The ventricular myocardium of OTB hearts did not only have a significant WLR in comparison to the IVS but also in comparison to the epicardium covering it (p=0.001), whereas the shams did not (p=0.999; Fig. 4.4C). There was also a significant increase in the WLR of the OTB hearts, in comparison to shams, in the ventricular myocardium (p=0.009; Fig. 4.4C).

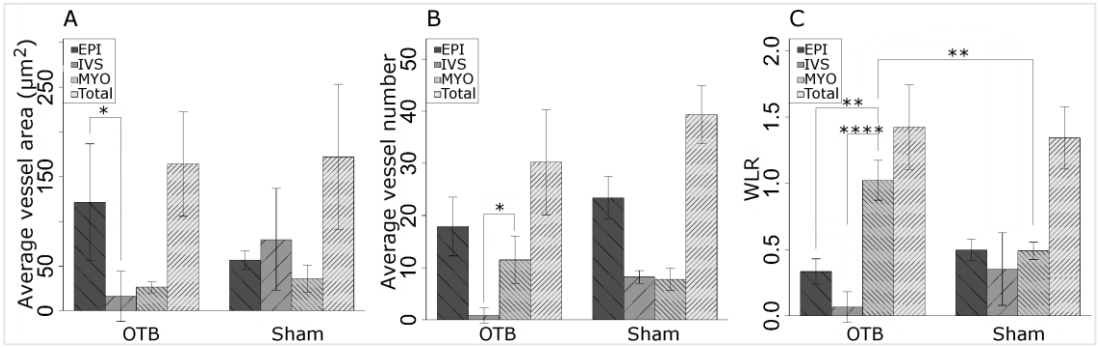

Figure 4.4: The three dependent variables measured for the coronary vasculature study. (A) The average vessel area of each region. **(B)** The average vessel number of each region. **(C)** The wall to lumen ratio (WLR) of each region. The error bars represent SEM (n=3 per group). Key: EPI, epicardium; IVS, interventricular septum; MYO, ventricular myocardium; *p<0.05; **p<0.01; ****p<0.0001

The average vessel area was highly variable in the epicardium of the OTB hearts, ranging from 73.6 to 195.8 μm^2, and the IVS for both treatment groups, ranging from 0 to 40.7 μm^2 for OTB hearts and from 13.8 to 109.7 μm^2 for shams. For the IVS it was to be expected since the average number of vessels was less than 10 in shams, where as in OTB only one heart had vessels with SMCs in its IVS. No identifiable vessels could be seen in the IVS of the other two OTB hearts. This

absence of identifiable vessels in the IVS also explains a part of the within-group differences seen in the OTB hearts, since the WLR of the IVS was significantly lower in the OTB group, in comparison to the epicardium ($p<0.01$) and the myocardium ($p<0.0001$). The average means of the lumen and wall area for the myocardium were closely examined (Fig.4.5). The wall area between the two treatment groups had a small difference (10.701%; Fig. 4.5A) but the difference concerning the lumen area was a lot higher (81.642%; Fig. 4.5B).

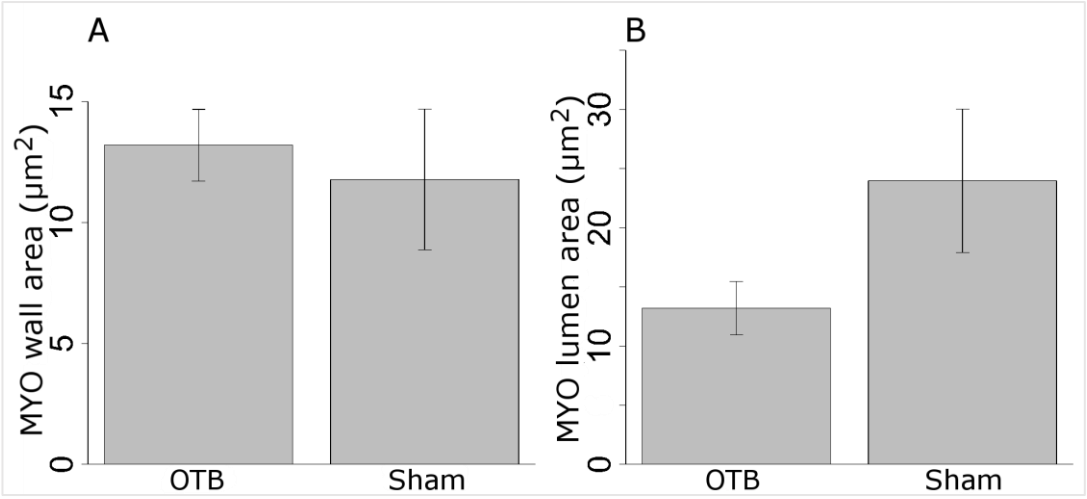

Figure 4.5: Wall and lumen area of the ventricular myocardial vessels between the two treatments. (A) The average wall area of the MYO vessels. **(B)** The average lumen area of the MYO vessels. The error bars represent SEM. Key: MYO, ventricular myocardium (n=3 per group).

In conclusion, the ventricular myocardium of OTB hearts at HH35 had vessels with a higher WLR, in comparison to shams. Upon further inspection the reason for the higher WLR in the ventricular myocardium was a decrease of the lumen area in OTB hearts. In addition, two of the three OTB hearts had no vessels covered by SMCs in their IVS.

4.5 Coronary vessels have aberrant wall architecture

In order to further investigate the structure of the CVs, TEM was used to examine the architecture of the coronary vessels. Eight HH35 hearts (n=4 per treatment group) were used in this experiment. The visualisation of CVs architecture would

allow an ultrastructural examination of vessel wall in order to pinpoint the main reason of bleeding in the heart myocardial wall. Five random vessels were examined in each sham and OTB hearts. In shams 80% (4/5) of the vessels had a continuous vessel wall (Fig. 4.6a) in contrast 40% (2/5) OTB hearts had a continuous vessel wall. Most vessels in OTB hearts (3/5) had an aberrant wall architecture with a discontinued coronary wall (Fig. 4.6b), with the endothelial cells not being in close contact to each other in contrast to shams. In addition, healthy coronary vessels had other cells adjacent to the vessel lining, whereas aberrant ones did not.

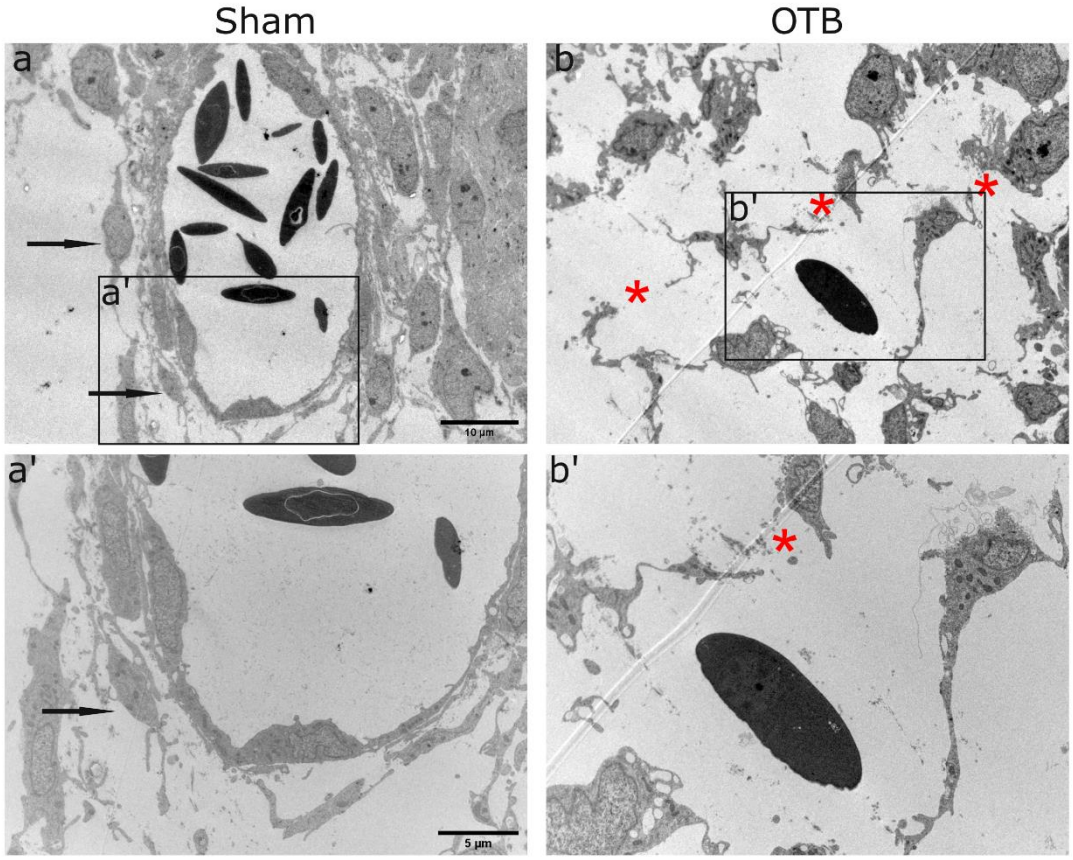

Figure 4.6: Coronary vessel architecture. Sham (a, a') and OTB (b, b') hearts were examine using TEM. OTB hearts had a discontinuous vessel wall (red asterisk). Shams had a number of cells adjacent to the vessel lining (black arrows) that were absent from OTB hearts. The scale bar is the same between a, b and a', b'.

4.6 Abnormalities in major coronary vessels

Whole HH35 hearts where injected with DiI, a water-soluble fluorophore which binds to cell membranes, and an antibody against α-SMA in order to visualise the vessels of hearts using a light sheet fluorescent microscope. Eight HH35 hearts (n=4 per treatment group) were used in this experiment. Examination of the major coronary vessels, which can be seen externally along the subepicardium, has showed abnormalities between OTB hearts and sham (Fig. 4.7).

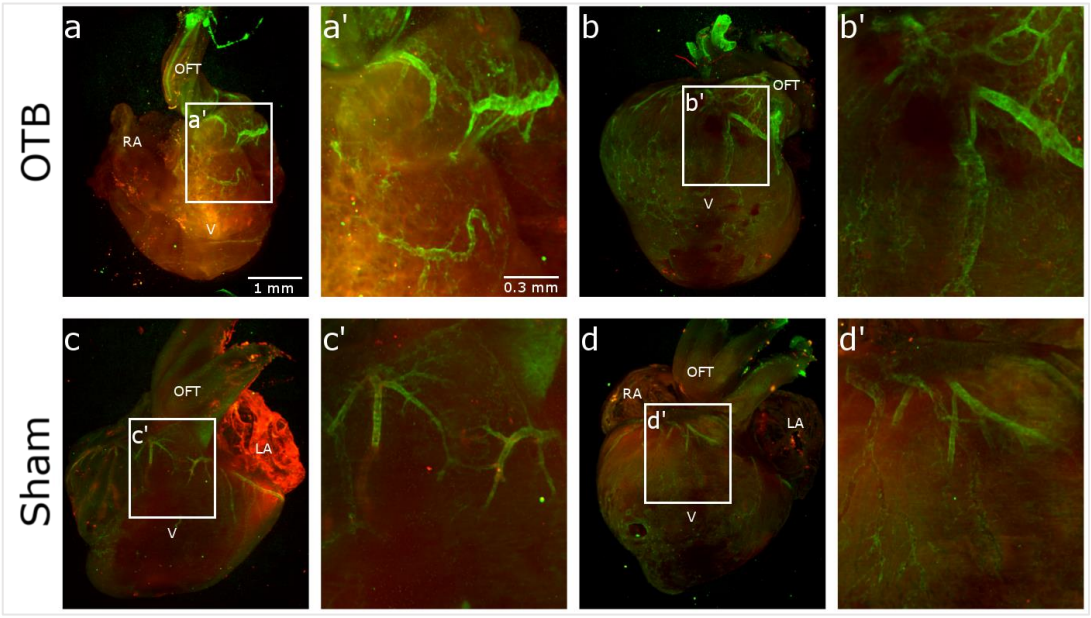

Figure 4.7: The major coronary vessels along the surface of the heart at HH35. OTB (a, a' b, b') and sham (c, c', d, d') hearts were stained with anti-α-SMA (green) and DiI (red). Key: OFT, outflow tract; RA, right atria; LA, left atria; V, ventricles. Scale bars the same between a-d and a'-d'.

OTB hearts had qualitatively bigger vessels (Fig. 4.7a, b) in comparison to shams (Fig. 4.7c, d). In addition, vessel patterning was different with vessels growing irregularly (Fig. 4.7a, b), whereas in shams vessels have a normal patterning of equal distances (Fig. 4.7c, d). Both sham and OTB hearts had a similar vessel orientation with vessels heading from the OFT towards the anterior and posterior regions of the heart. Moreover, the aberrant OFT phenotype seen at HH29 (section

3.7.3) in OTB hearts had further developed into a persistent truncus arteriosus (PTA) at HH35 (Fig. 4.8a, a'), with a non-septated OFT stemming from the heart. In contrast, controls at HH35 have a fully septated OFT with four stemming vessels, which is characteristic of the chicken (Fig. 4.8b, b'). In conclusion, the outer coronary vessels of HH35 OTB hearts appeared to be aberrant in comparison to shams.

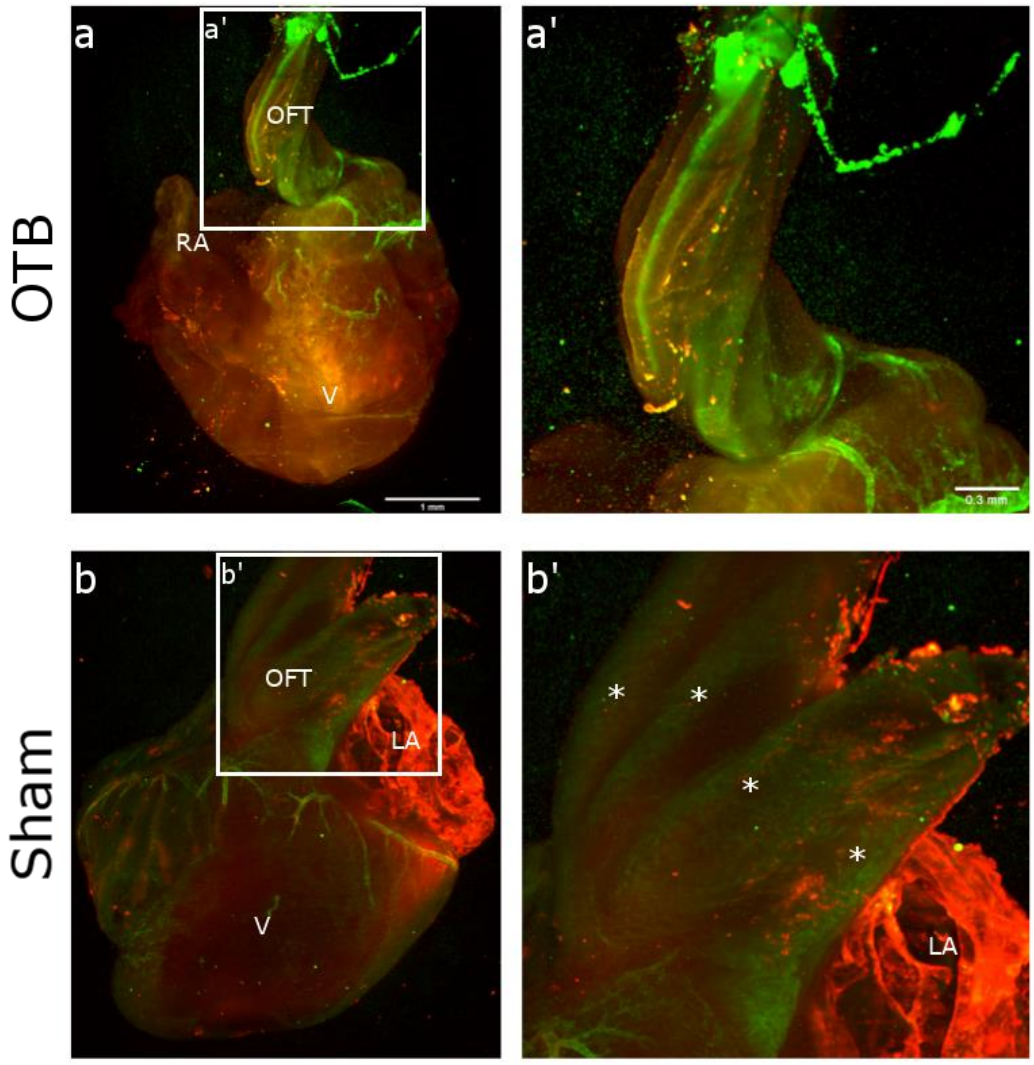

Figure 4.8: The OFT at HH35. OTB (a, a') and sham (b, b') hearts were stained with anti-α-SMA (green) and DiI (red). Shams OFT is septated into four stemming vessels (asterisks). In contrast, the OFT of OTB hearts remains unseptated. Key: OFT, outflow tract; RA, right atria; LA, left atria; V, ventricles. Scale bars 1 mm for a, b and 0.3 mm for a', b'.

4.7 Discussion

The coronary vasculature system is of the utmost importance to the heart, since as the myocardium develops, diffusion of nutrients and oxygen becomes less and less efficient (Olivey et al., 2004). The efficiency of diffusion decreases as the myocardium thickness increases. The coronary vasculature system overcomes the problem between myocardium and diffusion by providing a blood supply for it (Olivey et al., 2004). The coronary ostia of the arteries bind to the base of the aorta, just above the semilunar valves, and pass through the epicardium in order to get into the myocardium (Turner and Navaratnam, 1996). The cardiomyocytes and other cell populations found in the myocardium are dependent on coronary vessels for their survival and growth. In adults, ischaemia of the myocardium (e.g. from a myocardial infarction) causes severe problems and tissue necrosis in the myocardium (Buja, 2005).

The fact that most of the HH35 OTB hearts analysed in this study had bleeding in the subepicardial area strongly suggests that the coronary vasculature was aberrant. Upon further examination of various gene markers that have been associated with CV development, there was strong evidence showing that vessel maturation was stunted. Both neuropilins, NRP1 and NRP2, are expressed in ECs and neurons and both of them work as co-receptors for VEGF signalling (Fantin et al., 2009). VEGF is a well-studied angiogenesis factor and it has a pivotal role in vasculogenesis, angiogenesis and ECs survival and migration (Ferrara and Davis-Smyth, 1997). Mice with knock outs in both neuropilins die in utero, with an avascular yolk sac (Takashima et al., 2002). A knock out combination between the neuropilins, where one of the neuropilins is heterozygous while the other one is null, also results in embryonic lethality. In addition, these knock out combinations displayed vessels heterogeneous in size and large avascular regions in the embryo (Takashima et al., 2002). The qPCR results in this thesis showed downregulation of *NRP1* suggesting that VEGF signalling might be impaired and this could have a

potential impact to the function of ECs. Moreover, findings proposing that NRP1 is an early arterial marker can even suggest that the ECs in arteries are more impaired than the ones in veins (Herzog et al., 2001).

ANGPT1 (angiopoietin 1) was also found to be significantly downregulated in OTB hearts. ANGPT1, which is secreted by vein associated mural cells and the myocardium, binds to ECs' receptors promoting vessel maturation (Udan, Culver and Dickinson, 2013). The CVs of adult mice, with inhibited ANGPT1 signalling, have different sizes and patterning, compared to controls (Ward, Slyke and Dumont, 2004). PDGFB is also important for vessel maturation. PDGFB is secreted by ECs and binds to the PDGFRB on mural cells (Udan et al., 2013). PDGFB signalling is important for the migration and proliferation of SMCs during vessel maturation (Hellström et al., 1999). A large percentage of PDGFRB null mice exhibit hypoplasia of the compact myocardium and a VSD (Van den Akker et al., 2008). In addition, the mice had a number of coronary abnormalities, ranging from impaired arteriogenesis, enlargement of the vascular wall, to aberrant communication between ventricles and coronary arteries (Van den Akker et al., 2008). The downregulation of PDGFB shown in the results of this thesis strengthens the evidence of impaired CV maturation in the OTB model.

The ligand BDNF and its receptor NTRK2 (TrkB) were also found to be important for vascular development, although they were also found to be important in neuronal development (Donovan et al., 2000; Wagner, 2005). BDNF is also secreted by ECs and binds to NTRK2 in mural cells. NTRK2 null mice exhibited reduced pericytes and SMC numbers in CVs with increased vascular permeability and low vessel integrity (Anastasia et al., 2014). In addition, NTRK2 null mice die during late gestation, just before birth. Further, in vitro experiments suggest BDNF regulates the migration of mural cells in order to stabilize vessel development (Anastasia et al., 2014). Moreover, mice with a disrupted NTRK2 expression have fewer myocardial vessels (Wagner, 2005). BDNF null mice have deficient ECs

survival of the myocardial arteries and capillaries, early postnatal lethality and coronary vasculature haemorrhage (Donovan et al., 2000). The qPCR data in this thesis showed a significant downregulation of *NTRK2* and upregulation of *BDNF*. Assuming that the NTRK2 and BDNF protein levels reflect these gene expression differences, this could be a compensatory mechanism to overstimulate any remaining NTRK2 receptors.

A number of genes that are expressed in the epicardium, and not just in the cell populations directly taking part in vessel development, were found to play an important role in CV development. Bves is expressed in the PEO, epicardium, subepicardium and SMCs with a possible role in cell adhesion (Reese et al., 1999; Wada etal., 2001; Wu et al., 2012). In addition, evidence suggests that Bves takes part in tight junction (TJ) formation together with ZO1 (Wu et al., 2012). Connexins are gap junction protein channels that allow passage of molecule below 1.2 kDa (Gros and Jongsma, 1996). They are important for cell to cell interaction. Connexin 43 (Cx43; GJA1) was found to be expressed in the PEO and epicardium (Li et al., 2002; Rhee et al., 2009; Clauss et al., 2006). Cx43 null mice have abnormal coronary patterning and abnormal presence of fibroblasts in the epicardium (Li et al., 2002). Mice heterozygous for Cx43 also had abnormal coronary patterning (Clauss et al., 2006). In addition, although coronary patterning was abnormal, Cx43 null mice have normal SMCs differentiation (Li et al., 2002). YAP1 and TAZ are mediators of Hippo signalling, which mainly regulates cell proliferation, survival and apoptosis (Yu et al., 2015). YAP1 and TAZ were found important for epicardial EMT, epicardial cell proliferation and EPDCs differentiation into ECs (Singh et al., 2016). It is worth restating that EPDCs differentiation into ECs remains a controversial subject. The transcription factor TBX18 was found to not only be an epicardial marker but also important in CV development (Wu et al., 2013). Mice heterozygous for TBX18 have a smaller CV diameter in the epicardium and IVS and irregular CV patterning (Wu et al., 2013).

Taking in consideration the above results, the fact that *Bves*, *GJA1*, *YAP1* and *TAZ* expression was found in this thesis to not be significantly different, further strengthens the notion that although EPDC differentiation is normal vessel maturation is not. It is the first time that normal EPDC differentiation has been associated with abnormal vessel maturation, since it is not mentioned in previous literature work. The downregulation of *TBX18* partly agrees with previous *TBX18* null results, in mice, showing a smaller vessel lumen diameter and downregulation of *ANGPT1* (Wu et al., 2013); this is consistent with the data presented here. The fact that *CSPG4* (NG2), a pericyte marker (Ozerdem et al., 2001), showed no downregulation suggests that SMCs were more affected by OTB than pericytes. The downregulation of *PDGFRB*, *NTRK2* and *ANGPT1* further suggests that crosstalk between ECs and SMCs was aberrant.

The patterning of the major vessels on the surface of the heart showed abnormalities with bigger vessels in OTB hearts, in comparison to shams, that also seemed to have an irregular patterning with unequal distances between the vessels (Fig. 4.7). The high variability of the vessel area in the epicardium and the decreased lumen area in vessels of the myocardium can be explained by previous studies showing that downregulation of these genes causes CV patterning defects (Anastasia et al., 2014; Hellström et al., 1999; Ward et al., 2004; Wu et al., 2013). In addition, the fact that two OTB hearts had no CVs in the IVS, although it was not statistically significant, it is functionally significant since the absent vessels would be critical for not only supplying the myocardial cells with oxygen but also the bundle of His, an important part of the heart's conduction system (Frink and James, 1973). There is also the possibility that the IVS was just lacking mature, SMC covered vessels but instead had immature endothelial vessels. Vessels than are only supported by endothelial cells would be more susceptible in increases of shear pressure. The susceptibility of the vessels due to shear pressure could also explain their poor integrity, seen using TEM.

Previous studies have shown that OTB is associated with the emergence of a mature His-Purkinje system (HPS) in an earlier developmental stage, in comparison to controls (Reckova et al., 2003). In controls, hearts demonstrate a mature HPS starting from HH31 up to HH36, where all the hearts are expected to have a mature HPS phenotype. In the OTB model, hearts started exhibiting signs of a mature HPS at HH27 (Reckova et al., 2003). The lack of SMC covered vessels in the IVS found in OTB hearts, as described in this thesis, do not seem to be associated with the aberrant HPS phenotype previously described as HPS maturation starts when the CVs are no yet patent. As the original study (Reckova et al., 2003) did not cover any stages after HH31 the effects of the aberrant IVS vasculature on the HPS system needs to be researched more extensively.

In conclusion, OTB hearts at HH35 showed bleeding between the myocardium and the epicardium. This coincides with the developmental stage where the CVs are patent. Upon examination of gene expression there was downregulation of genes that are involved in vessel maturation, angiogenesis and CV patterning. The fact that gene expression of the pericyte marker *CSPG4* was normal and that the SMC area was not found to be significantly different between any of the regions in the two treatment groups suggests that EPDC differentiation was normal. In addition, previous research has shown that SMCs avoid migrating to vessels with high shear stress (Liu and Goldman, 2001; Sakamoto et al., 2006). In the OTB model a high shear stress is especially generated in the ventricles and the OFT (Midgett et al., 2014), which would logically lead to an increase in the shear stress of the CVs since the coronary ostia are located between the ligature and the ventricles. Moreover, a previous study that looked on CV development, in OTB hearts at HH36, also found impaired development of the main coronary arteries (Tomanek, 1999). EPDC migration appears normal since there is no significant difference in the number of cells in the epicardium, which could denote for any EPDC being held in the epicardial mesenchyme, and the migration markers *SNAI1* and *SNAI2* have a normal expression (section 5.2). The irregular patterning of the external major

coronary vessels also suggests problems with shear stress since abnormal patterning is more likely to be due to abnormal angiogenesis rather than abnormal SMC differentiation, denoted by the area of SMC not being significantly different between OTB and sham hearts, or EPDC migration. Moreover, the aberrant myocardilisation OFT phenotype seen at HH29 (section 3.7.3) seems to have matured into a PTA phenotype, which can have detrimental effects in the embryo due to the mixing of oxygenated and unoxygenated blood and can also lead to aberrant shear stress in the OFT and coronary ostia and vessels.

5 Changes in the ECM at HH35

5.1 Overview and aims

ECM proteins are secreted by specialised cells (e.g. fibroblasts) and provide structural and biochemical support to the surrounding tissue (Weber, 1989). Collagen III is expressed in the early embryonic heart and to some extent it is replaced by collagen I later in development (Liu et al., 1997). Collagen XII was also found to be expressed in the epicardium in the zebrafish (Marro et al., 2016). Changes in fibrillogenesis, the development of collagen fibres, and collagen crosslinking can all result in changes in the tensile strength of tissues and also changes to the myocardial architecture (Weber, 1989).

In the heart ECM is predominately, but not exclusively, produced by cardiac fibroblasts, which in turn derive from the epicardium (Acharya et al., 2012). The transcription factor TCF21 can be used as a marker of cardiac fibroblasts in later stages of development (Acharya et al., 2012). Although fibroblasts can be found coupled with cardiomyocytes, they cannot generate an action potential like the cardiomyocytes. However, mechanical forces (e.g. stretch and compression) can change their membrane potential (Abramochkin et al., 2014). This crosstalk between fibroblasts and cardiomyocytes happens via connexins (Camelliti, 2004). Connexin 40 (Cx40) and 45 (Cx45) are both expressed in fibroblasts. Cx40 is preferably expressed in gap junctions between fibroblasts, but fibroblast-cardiomyocyte junctions use Cx45 (Camelliti, 2004). The fact that fibroblasts are mechanosensitive, taken together with the fact that they have a cellular connection with cardiomyocytes, could mean that they are able to change cardiomyocyte function based on mechanical stresses.

Although the ECM is comprised of a number of structural proteins the most well-known ones are the collagens. Three major collagen changes have been previously described, that can affect heart remodelling; changes in collagen content, changes

in collagen crosslinking and changes in collagen concentration (Badenhorst, 2003). There are a number of cell membrane receptors that bind to ECM proteins and are able to initiate a signalling cascade within the cell, altering its transcriptome. DDR2 is found almost exclusively in cardiac fibroblasts in the heart, although it can be found in a range of different cells in other tissues (Camelliti et al., 2005). DDR2 was found to be able to bind to collagen I and changes in DDR2 expression in the heart can impact collagen deposition and fibrillogenesis (Agarwal et al., 2002; Cowling et al., 2014). Integrins are also important cell membrane receptors that bind to a number of ECM proteins with RGD motifs (e.g. fibronectin) and can affect proliferation, migration and differentiation (Giancotti, 1999).

The specific experimental aims to address cell migration, ECM composition and architecture and fibroblasts numbers were:

- Taking in to account changes in DDR2 and collagen XII, seen by qPCR in HH29 OTB hearts, these genes will be reassessed at HH35 in OTB and sham hearts.
- Since ECM changes are linked to migration, expression of migratory markers will be evaluated by qPCR.
- The number of TCF21+ cells and the structure of collagen I will be assessed through immunohistochemistry.
- The ability of TCF21+ cells to promote collagen I expression will also be indirectly assessed by measuring the amount of TCF21+ cells in relation to collagen I coverage in the tissue.
- The morphology of the epicardium will be assessed at HH35.

5.2 Differential expression of genes expressed in fibroblasts

All the genes selected for qPCR were linked with the ECM and fibroblasts, *COL1A2*, *COL12A1*, *DDR2*; migration, *SNAI1*, *SNAI2*, *SMAD2*, *WT1*; and cell junction integrity, *TJP1* (see section 3.4). A subset of genes that were evaluated at HH29 by qPCR were revaluated at HH35. Six hearts (n=3 per treatment group) had their RNA isolated and converted to cDNA. The cDNA was used for qPCR. The primer

pair optimisation step was carried out the same way as previously mentioned (see section 3.4.1). The efficiency and r^2 for each primer pair can be found in Table 5.1. The genes GAPDH and TBP were selected as reference genes for normalisation in order to measure the fold change (FC).

Primer pairs	Efficiency (%)	r^2
GAPDH*	99.6	1
TBP*	95.3	0.993
SNAI1	90.4	0.999
SNAI2	103.5	0.998
DDR2	93.3	0.999
TJP1	102.6	0.998
COL1A2	95.3	0.999
COL12A1	93.2	0.999
WT1	100.1	0.999
SMAD2	108.1	0.998

Table 5.1: The efficiency and r2 values of the primer pairs used for qPCR at ECM and migratory genes. The primer pairs were named after their target amplicon. *Primer pairs were optimised by Dr. Matt Parnall.

From the eight genes analysed by qPCR one of them was significantly downregulated, two of them were upregulated and five of them showed no change (Fig. 5.1). Namely, *SNAI1* (FC=1.035; p=0.815), *SNAI2* (FC=0.739; p=0.060), *TJP1* (FC=1.301; p=0.066), *WT1* (FC=1.040; p=0.771) and *SMAD2* (FC=0.947; p=0.675) showed no significant differential expression. *DDR2* (FC=1.749; p<0.001) and *COL12A1* (FC=2.274; p<0.001) were significantly upregulated and *COL1A2* (FC=0.641; p=0.007) was downregulated. Statistics were carried out automatically by the REST software using bootstrapped MANOVA.

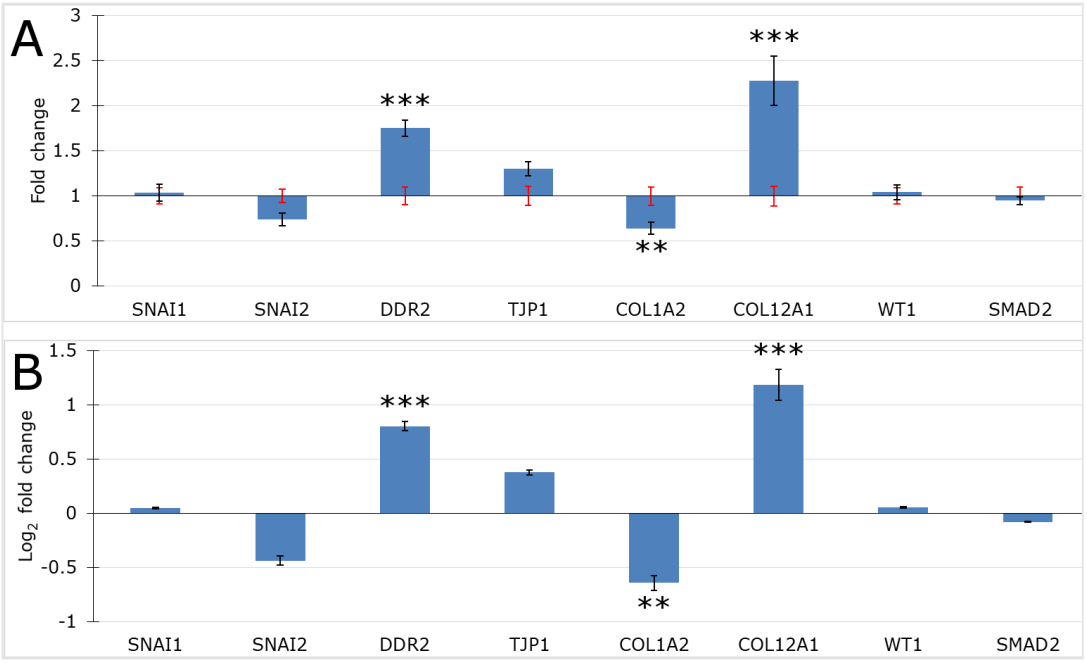

Figure 5.1: Relative expression differences between OTB and sham ECM and migratory genes at HH35. The fold change (A) and $\log_2$ fold change (B) in OTB gene expression (bars) in comparison to shams (baseline). The error bars represent SEM (OTB, black; sham, red). Note that by definition shams have no error bars when $\log_2$ transformed (n=3 per group). **p<0.01; ***p<0.001.

5.3 Immunoblot on cell adhesion molecules and TCF21 at HH35

Immunoblot analysis was used to quantify expression of proteins that could potentially give a more useful insight on the OTB model on the protein expression level, rather than the gene expression level. Protein for immunoblots from 12 HH35 hearts (n=6 per treatment group) was isolated. GAPDH expression was used for normalisation. The relative protein expression levels of N-cadherin, E-cadherin and TCF21 were measured (Fig. 5.2A; three dependent variables). In comparison to shams, whose protein expression was assumed to be 100%, OTB hearts had an expression 100.792% for N-cadherin, 100.413% for E-cadherin and 65.146% for TCF21 (Fig. 5.2B).

The assumption of normality was tested in all dependent variables using a Shapiro-Wilk normality test. N-cadherin (W=0.920, p=0.289), TCF21 (W=0.930, p=0.381) and E-cadherin (W= 0.981, p=0.987) were normally distributed. The assumption of variance was tested using a Levene's test for homogeneity of variance. N-cadherin ($F_{(DF)}=0.001_{(1,10)}$, p=0.975), E-cadherin ($F_{(DF)}=0.004_{(1,10)}$, p=0.953) and TCF21 ($F_{(DF)}=4.271_{(1,10)}$, p=0.066) had equal variances. An independent samples t-test was used to assess statistical significance between the two treatment groups. The cell adhesion molecules N-cadherin (t=0.161, d.f.=10, p=0.875) and E-cadherin (t=0.043, d.f.=10, p=0.966) showed no significant difference (Fig. 5.2B). However, the transcription factor and epicardial/fibroblast marker TCF21 (t=-6.374, d.f.=10, p<0.0001) showed a significant difference (Fig. 5.2B).

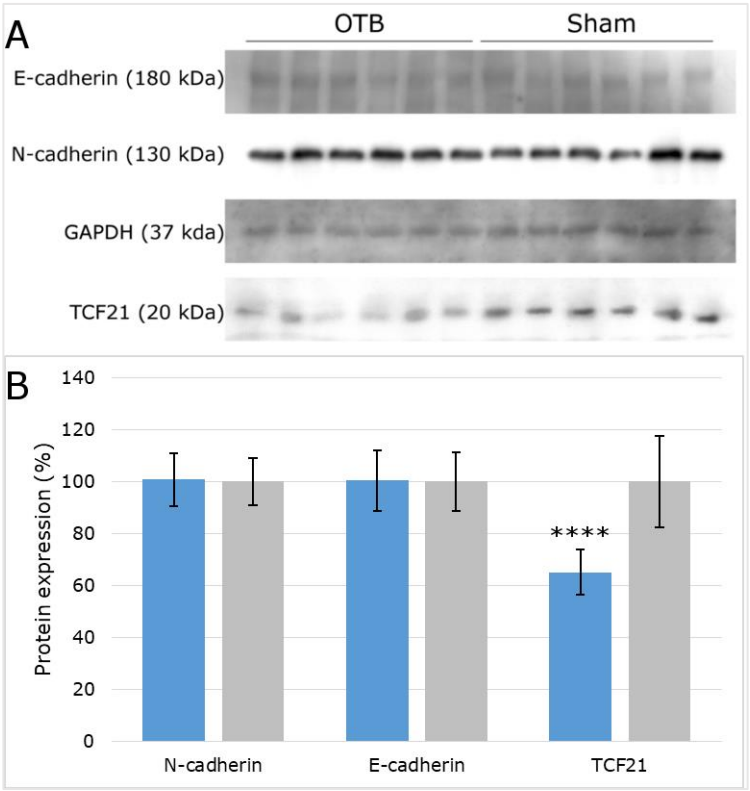

Figure 5.2: HH35 immunoblot. (A) The immunoblot showing the protein band for each protein used. (B) The protein expression of OTB (blue) proteins in comparison to shams (grey). Error bars represent SEM (n=6 per group). **** p<0.0001

5.4 Analysis of TCF21+ cell number and collagen I distribution

5.4.1 TCF21+ cell numbers in the heart

The low protein expression of TCF21 together with the differential expression of collagens by qPCR led to a further investigation of the phenotype. Six HH35 hearts (n=3 per treatment group) were used for fluorescent immunohistochemistry using anti-TCF21 and anti-collagen I antibodies, and counterstaining with DAPI (Fig. 5.3). The average number of TCF21+ cells (one dependent variable) was counted in four regions; AV canal, epicardium, ventricles and atria (Fig. 5.4). An average of 38 sections were analysed per heart. The average number of TCF21+ cells for shams was; 472.86 in the epicardium, 365.22 in the myocardium, 134.68 in the atria and 201.09 for the AV canal giving 1173.85 cells. Similarly, the average number of TCF21+ cells for OTB hearts was; 494.53 in the epicardium, 312.81 in the myocardium, 178.54 in the atria and 217.25 for the AV canal giving 1203.12 cells (Fig. 5.4). Red blood cells in the tissue were fluorescing in all channels (Fig. 5.3d,d',h,h').

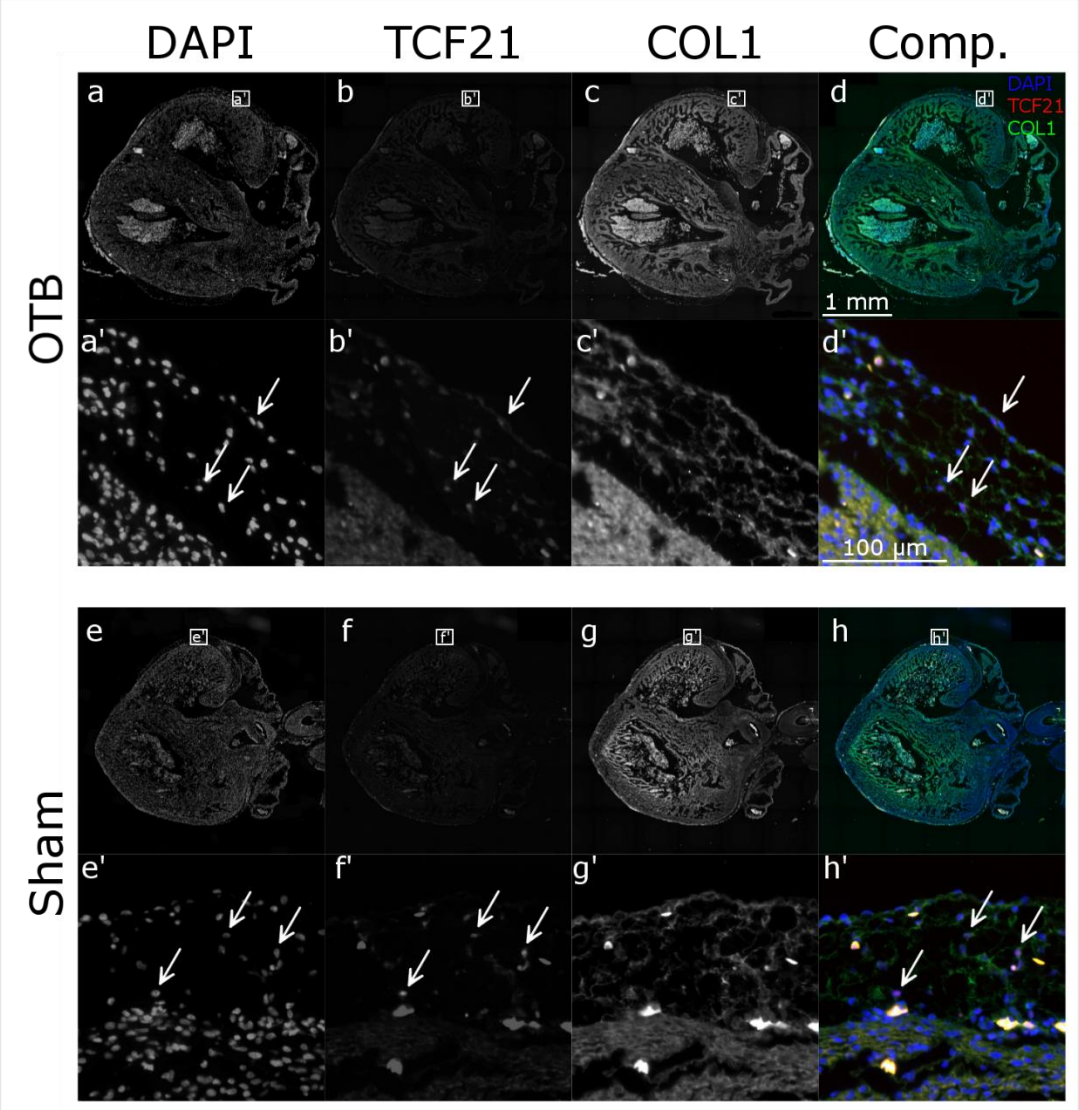

Figure 5.3: Fluorescent immunohistochemistry using anti-TCF21, anti-Col1 and DAPI at HH35. a'-h' are high magnifications of boxed areas denoted in a-h panels. TCF21 is found in the nucleus and colocalises with DAPI (arrows). Scale bar 1 mm for a-h and 100 µm for a'-h'. Blood cells fluoresced in all channels.

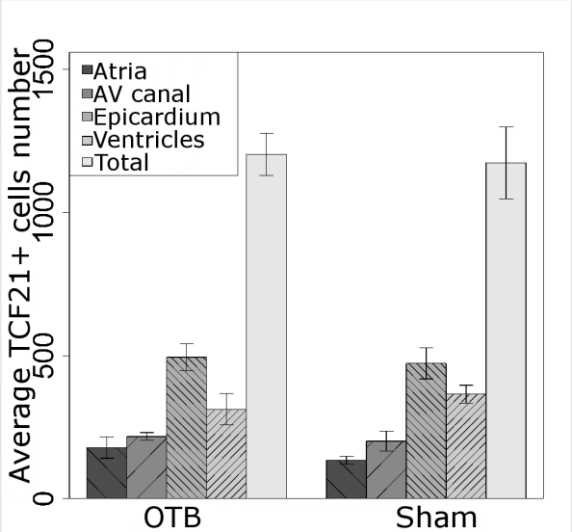

Figure 5.4: The average number of TCF21+ cells in the different heart regions. The error bars represent SEM (n=3 per group). Key: AV, atrioventricular.

The assumption of normality was tested in the residual of the dependent variable using a Shapiro-Wilk normality test. The average number of TCF21+ cells (W=0.949, p=0.252), was normally distributed. The assumption of variance was also tested, in the interaction of the dependent variable with the treatment and the different regions, using a Levene's test for homogeneity of variance. The average number of TCF21+ cells ($F_{(DF)}=0.538_{(7,16)}$, p=0.794) had an equal variance. A two-way ANOVA was carried out to assess any potential statistical significance between the two treatment groups and all the regions, concerning the dependent variable. A two-way ANOVA will test three different hypotheses, concerning the dependent variable; there is no difference between the treatment groups (H_1); there is no difference between the different regions (H_2); there is no interaction between the treatment and the different regions (H_3). There was no significant difference between the two treatments ($F_{(1,16)}=0.071$, p=0.794; H_1) and the interaction between the treatment and the different regions ($F_{(3,16)}=0.571$, p=0.642; H_3) but there was a significant difference between the four regions ($F_{(3,16)}=28.239$, $p<0.0001$; H_2).

A post-hoc test was carried out to confirm where the differences occurred between the different regions. The Tukey test was used as the chosen post-hoc test. The

differences between regions were not of interest since it is expected for different regions to have different amount of TCF21+ cells. The reason is due to differences in the size of the region and the permissiveness of epicardial migration. The epicardium had significantly more TCF21+ cells in comparison to the atria ($p<0.0001$), AV canal ($p<0.0001$) and ventricles ($p=0.009$). The ventricles was the only other region to have significantly more TCF21+ cells and this was in comparison to the atria ($p=0.001$).

5.4.2 TCF21 and collagen I measurements taken in a fixed size area

Since the OTB hearts had bleeding in the anterior inferior aspect (see section 4.2) counting the average number of TCF21- cells in the epicardium was impossible due to the fact that red blood cells in the chick are nucleated, thus appearing as DAPI positive cells in the epicardium. In order to overcome this problem a fixed area of 0.06 mm^2 for the epicardium on top of the right ventricle (Fig. 5.5 area a and c), and 0.015 mm^2 for the epicardium in the AV canal, was defined (Figure 5.5 area b and d). The area was free of any major bleeding so the number of TCF21+ and TCF21- cells could be measured as well as the void area fraction (VAF=empty space/total area) of the collagen I channel. Upon closer inspection of collagen I in the epicardium above the ventricles a thicker, more prominent expression of collagen I could be seen above the right ventricle (Fig. 5.5).

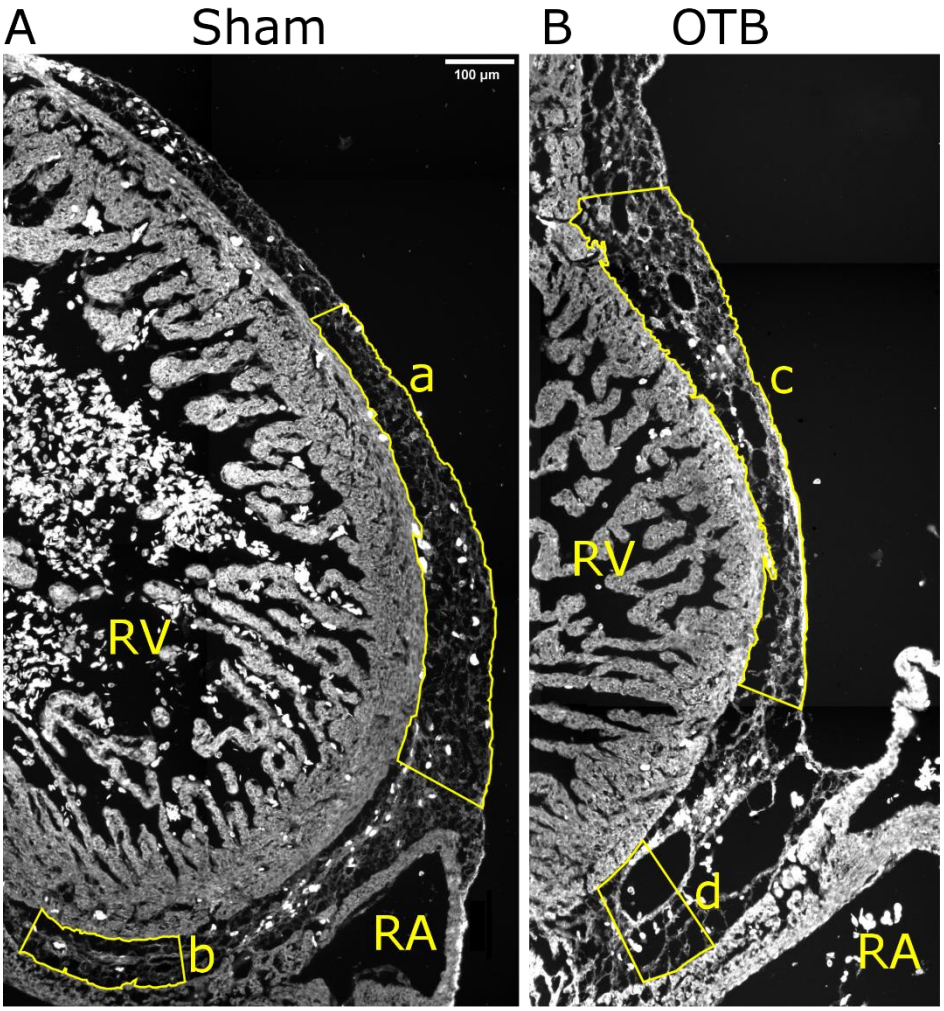

Figure 5.5: The defined area of the epicardium above the right ventricle and at the AV canal. The area was 0.06 mm^2, for the epicardium on top of the right ventricle (a, c), and 0.015 mm^2, for the epicardium at the AV canal (b, d). Key: RV, right ventricle; RA, right atria. Scale bar same for A and B. The hearts are stained for collagen I.

Four dependent variables were used for statistical analysis in each area, the number of TCF21+ cells, the number of TCF21- cells, the TCF21+ cells density (=TCF21+ cells/total cells) and the VAF (Fig. 5.6). In the epicardium above the right ventricle, sham hearts had an average of 78.03 TCF21+ cells, 45.88 TCF21- cells, a TCF21+ cell density of 0.63 and a VAF of 0.58, whereas in the AV canal they had an average of 27.03 TCF21+ cells, 29.58 TCF21- cells, a TCF21+ cell

density of 0.48 and a VAF of 0.48 (Fig. 5.6). In contrast, in the epicardium above the right ventricle, OTB hearts had an average of 134.08 TCF21+ cells, 59.47 TCF21- cells, a TCF21+ cell density of 0.69 and a VAF of 0.47, whereas in the AV canal they had an average of 29.11 TCF21+ cells, 19.17 TCF21- cells, a TCF21+ cell density of 0.63 and a VAF of 0.56 (Fig. 5.6). The multivariate, Hotelling's T^2 test was used for each area, since the areas had different sizes. The assumption of normality was tested using a Shapiro-Wilk normality test. The assumption of variance was also tested using a Levene's test for homogeneity of variance.

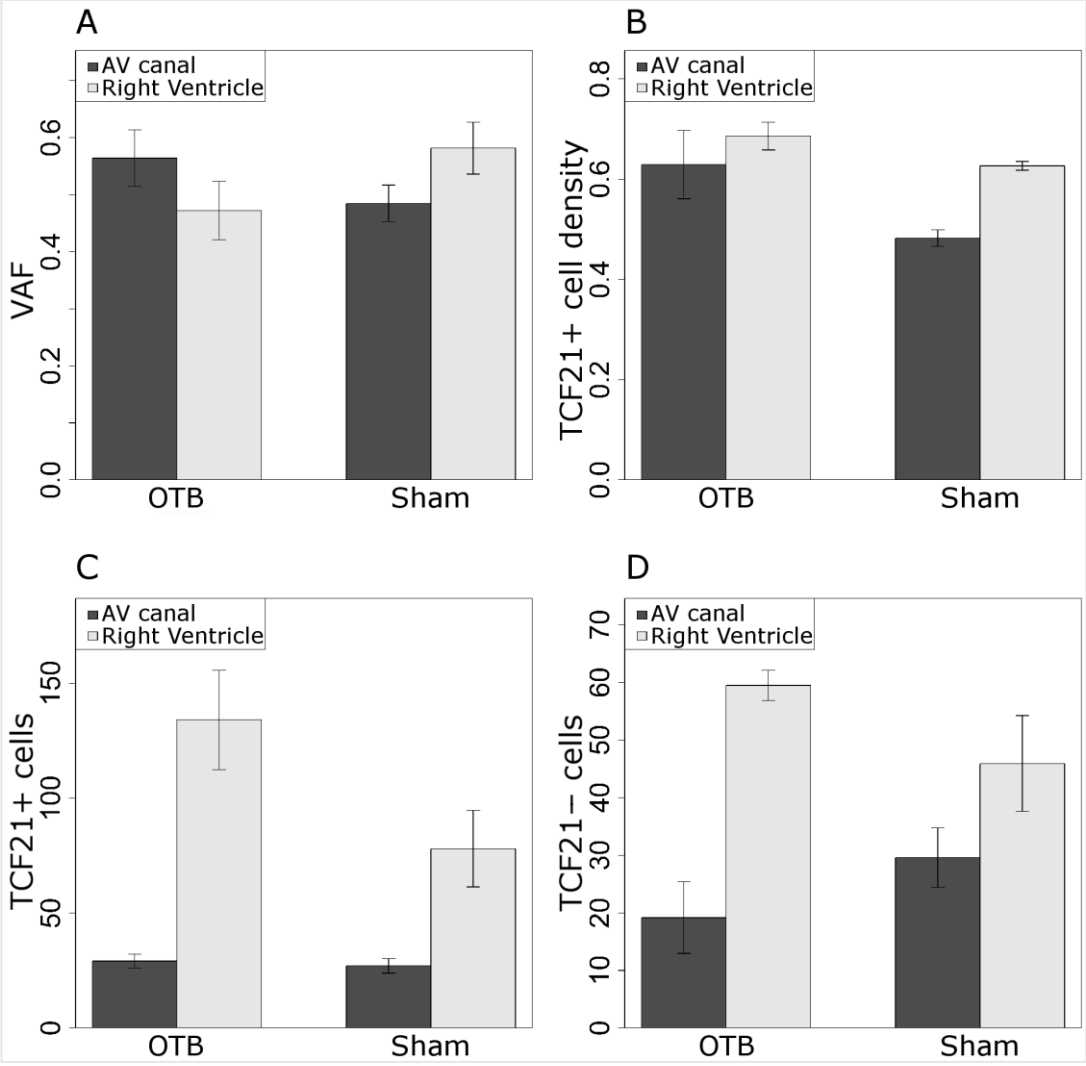

Figure 5.6: The measurements taken from the fixed area of the epicardium above the right ventricle and the AV canal. (A) The void area fraction (VAF) measurements. (B) The TCF21+ cell density measurements. (C)

The average TCF21+ cell number measurements. (D) The average TCF21+ cell number measurements. The error bars represent SEM (n=3 per group). Key: AV canal, the epicardium area covering the atrioventricular (AV) canal; epicardium, the epicardium above the right ventricle.

For the epicardial region above the right ventricle, all the dependent variables, number of TCF21+ cells (W=0.986, p=0.977), number of TCF21- cells (W=0.847, p=0.149), TCF21+ cell density (W=0.858, p=0.181) and VAF (W=0.925, p=0.539), were normally distributed. All the dependent variables, number of TCF21+ cells ($F_{(DF)}=0.128_{(1,4)}$, p=0.739), number of TCF21- cells ($F_{(DF)}=1.221_{(1,4)}$, p=0.331), TCF21+ cell density ($F_{(DF)}=0.995_{(1,4)}$, p=0.375) and VAF ($F_{(DF)}<0.001_{(1,4)}$, p=0.991), had equal variances. The Hotelling's T^2 test showed no significant difference between the two treatment groups ($T^2=6.075$, F=1.519, d.f.=4, p=0.537).

For the epicardial region in the AV canal: All the dependent variables, number of TCF21+ cells (W=0.848, p=0.152), number of TCF21- cells (W=0.967, p=0.864), TCF21+ cell density (W=0.848, p=0.152) and VAF (W=0.986, p=0.978), were normally distributed. All the dependent variables, number of TCF21+ cells ($F_{(DF)}=0.008_{(1,4)}$, p=0.932), number of TCF21- cells ($F_{(DF)}=0.046_{(1,4)}$, p=0.840), TCF21+ cell density ($F_{(DF)}=1.144_{(1,4)}$, p=0.345) and VAF ($F_{(DF)}<0.328_{(1,4)}$, p=0.597), had equal variances. The Hotelling's T^2 test showed no significant difference between the two treatment groups ($T^2=111.751$, F=27.938, d.f.=4, p=0.141). In conclusion, two regions of interest were measured in the epicardium; one in the epicardium covering the right ventricle and one covering the AV canal. There was no difference in the VAF, TCF21+ cell density and number of TCF21+ and TCF21- cells between OTB and sham hearts at HH35.

5.4.3 The number of TCF21+ cells significantly correlates with a decrease in the void area of collagen I

To further test the notion that TCF21+ cells are responsible for the production of collagen the amount TCF21+ cells, measured in every section (n=12 per biological repeat; n=36 per treatment group) was plotted against the VAF (Fig. 5.7), in the fixed area polygons. If the TCF21+ cells are mature enough to be fibroblast at HH35 and produce collagen I, the VAF should decrease as the number of TCF21+ cells increase. A correlation and a regression test were deemed as the appropriate statistical tests. The measurements were carried using the data acquired by the fixed areas (see section 5.4.2). The assumption of normality was tested using a Shapiro-Wilk normality test.

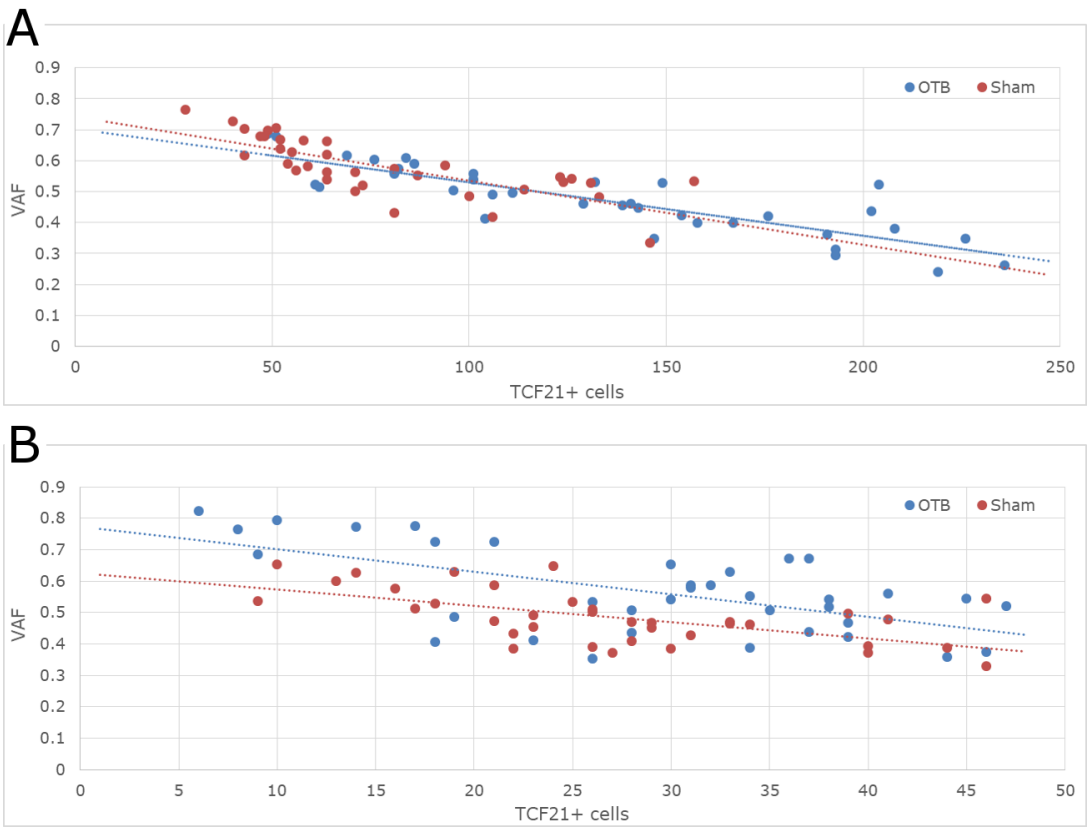

Figure 5.7: The linear relationship between VAF and TCF21+ cells. As the number of TCF21+ cells increases the void area of collagen I decreases. (A) The linear regression in the OTB and sham hearts in the epicardial region above the right ventricle. (B) The linear regression in the OTB and sham hearts in the

epicardial region of the AV canal (n=3 per group). Key: VAF, void area fraction (area devoid of collagen I/total area).

For the epicardial region above the right ventricle, the OTB hearts had a normally distributed TCF21+ cell number (W=0.954, p=0.141) and a normally distributed VAF (W=0.987, p=0.943). A Pearson's correlation was used to assess correlation between the two variables. There was a strong significant correlation between the two variables (r=-0.847, d.f.=34, p<0.0001). A regression was also carried out with significant results ($F_{(1,34)}$=86.64, p<0.0001; r^2=0.710). The sham hearts had an abnormally distributed TCF21+ cell number (W=0.904, p=0.004) and a normally distributed VAF (W=0.980, p=0.761). A Spearman's correlation was used to assess correlation between the two variables. There was a strong significant correlation between the two variables (ρ=-0.856, p<0.0001). A regression was also carried out with significant results ($F_{(1,34)}$=44.09, p<0.0001; r^2=0.552).

For the epicardial region in the AV canal: The OTB hearts had a normally distributed TCF21+ cell number (W=0.955, p=0.151) and a normally distributed VAF (W=0.957, p=0.168). A Pearson's correlation was used to assess correlation between the two variables. There was a significant correlation between the two variables (r=-0.601, d.f.=34, p=0.0001). A regression was also carried out with significant results ($F_{(1,34)}$=19.28, p=0.0001; r^2=0.343). The sham hearts had a normally distributed TCF21+ cell number (W=0.972, p=0.487) and a normally distributed VAF (W=0.965, p=0.303). A Pearson's correlation was used to assess correlation between the two variables. There was a significant correlation between the two variables (r=-0.601, d.f.=34, p=0.0001). A regression was also carried out with significant results ($F_{(1,34)}$=19.23, p=0.0001; r^2=0.342). In conclusion, the number of TCF21+ cells was found to be inversely proportional to the VAF in both areas of the epicardium for both OTB and sham hearts at HH35.

5.4.4 The epicardium of OTB hearts is thinner above the ventricles

Using the fixed area polygons (see section 5.4.2) an ellipse fit was carried out, where a major and minor axis was measured in the polygon. This allowed for an axes ratio measurement to be calculated using the major and minor axis (axes ratio=major axis/ minor axis). Since the area had a fixed size of 0.06 mm^2 for the epicardium above the RV and 0.015 mm^2 for the epicardium in the AV canal any change in the major axis would be compensated by an opposite change on the minor axis (e.g. a 1 μm decrease in the major axis would result in a 1 μm increase in the minor axis). In this way the thickness, but not the total area, of the epicardium could be measured in the two different regions. The epicardium above the right ventricle of sham hearts had an average major axis of 603.98 μm and a minor axis of 132.04 μm, whereas in the AV canal they had an average major axis of 246.60 μm and a minor axis of 82.88 μm (Fig. 5.8). In contrast, the epicardium above the right ventricle of OTB hearts had an average major axis of 727.17 μm and a minor axis of 108.55 μm, whereas in the AV canal they had an average major axis of 223.62 μm and a minor axis of 94.44 μm (Fig. 5.8).

The assumption of normality was tested using a Shapiro-Wilk normality test. The assumption of variance was also tested using a Levene's test for homogeneity of variance. Followed by an independent samples t-test for each region. In the epicardial region above the right ventricle, the axes ratio had a normal distribution ($W=0.972$, $p=0.487$) and homogenous variance ($F_{(DF)}=0.046_{(1,4)}$, $p=0.840$). The OTB hearts had a significantly higher axes ratio ($t=3.528$, $d.f.=4$, $p=0.024$), in comparison to shams, denoting a thinner and wider epicardial area (Fig 5.8A). In the epicardial region around the AV canal, the axes ratio had a normal distribution ($W=0.972$, $p=0.487$) and homogenous variance ($F_{(DF)}=0.046_{(1,4)}$, $p=0.840$). The OTB hearts had no significant difference ($t=-0.807$, $d.f.=4$, $p=0.465$), in comparison to shams (Fig. 5.8A).

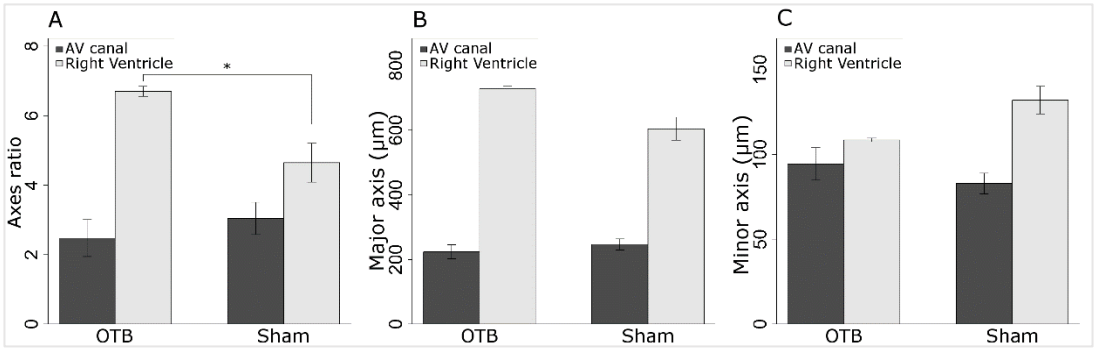

Figure 5.8: The axes measurement for the epicardium polygons. (A) The axes ratio of the two polygons in shams and OTB. (B) The major axis of the two polygons in shams and OTB. (C) The minor axis of the two polygons in shams and OTB. The error bars represent SEM (n=3 per group). Key: AV canal, the epicardium region covering the atrioventricular (AV) canal; epicardium, the epicardium above the right ventricle.

Upon closer inspection of the major and minor axis, it can be seen that the area in the epicardium above the right ventricle has a longer major axis (Fig. 5.8B) but a shorter minor axis (Fig. 5.8C) in OTB hearts. Although this is to be expected since the axes ratio were significantly different and the area of the polygon has a fixed size, the fact the relationship of the two axis was not linear denotes changes in curvature as well (Fig. 5.9). The changes in the morphology of the area did not follow any kind of direction on the z plane (e.g. getting smaller or bigger) and were variable through the different sections of the same biological repeat.

In conclusion, HH35 OTB hearts had a higher axes ratio in the polygon covering the right ventricle, in comparison to shams. The area of the epicardium covering the right ventricle in OTB hearts had a longer major axis, in comparison to shams. No significant difference was seen in the polygon covering the AV canal between the two treatment groups.

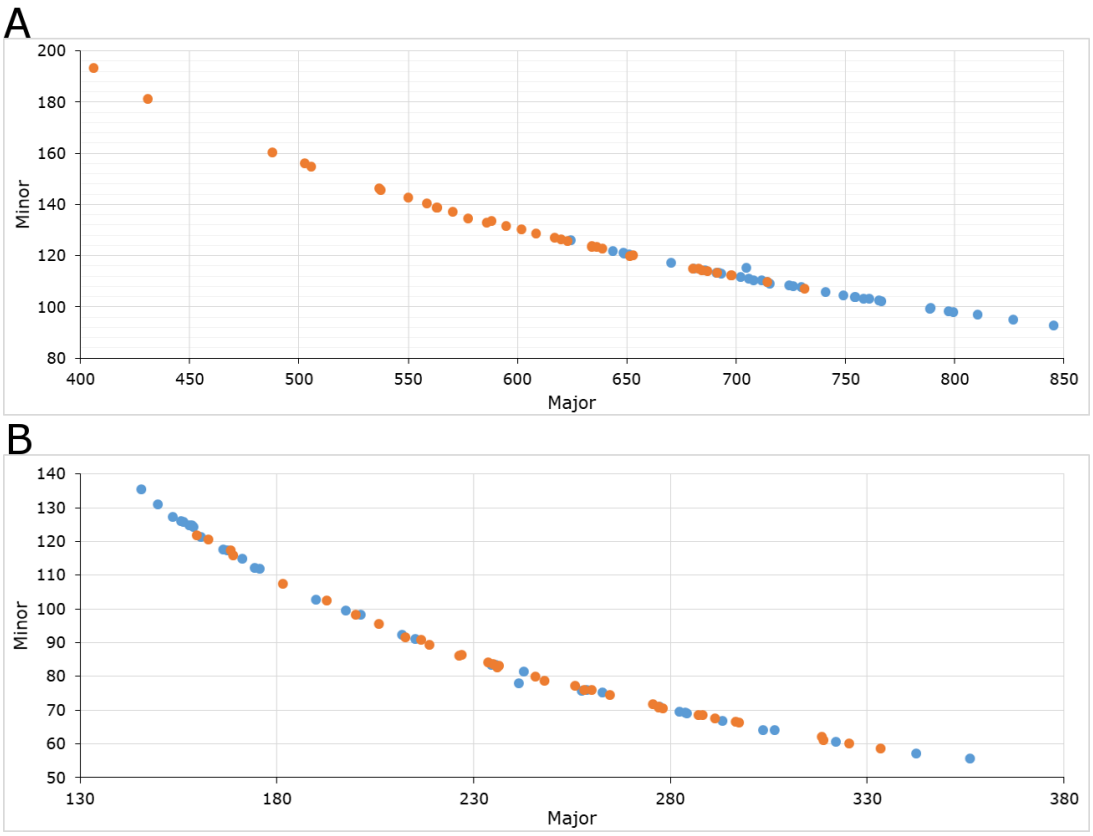

Figure 5.9: The relationship between the major and minor axes in the fixed polygons. An increase in the major axis will result in a decrease in the minor axis and vice versa. (A) The major and minor axes relationship in the OTB (blue) and sham (orange) hearts in the epicardial region above the right ventricle. (B) The major and minor axes relationship in the OTB (blue) and sham (orange) hearts in the epicardial region of the AV canal (n=3 per group).

5.4.5 The ECM fibres of the ventricular epicardium show signs of stress

Transmission electron microscopy (TEM) was used to further examine the epicardial ECM above the ventricles. Eight HH35 hearts (n=4 per group) were appropriately stained and sectioned to reveal the architecture of the ECM (Fig. 5.10). Sham hearts had loose ECM fibres whereas OTB hearts' ECM fibres showed clear signs of stretch along the anterior to posterior axis, in parallel to the

myocardium (Fig. 5.10). In addition, ECM fibres appeared closer together suggesting an increase in local fibre density.

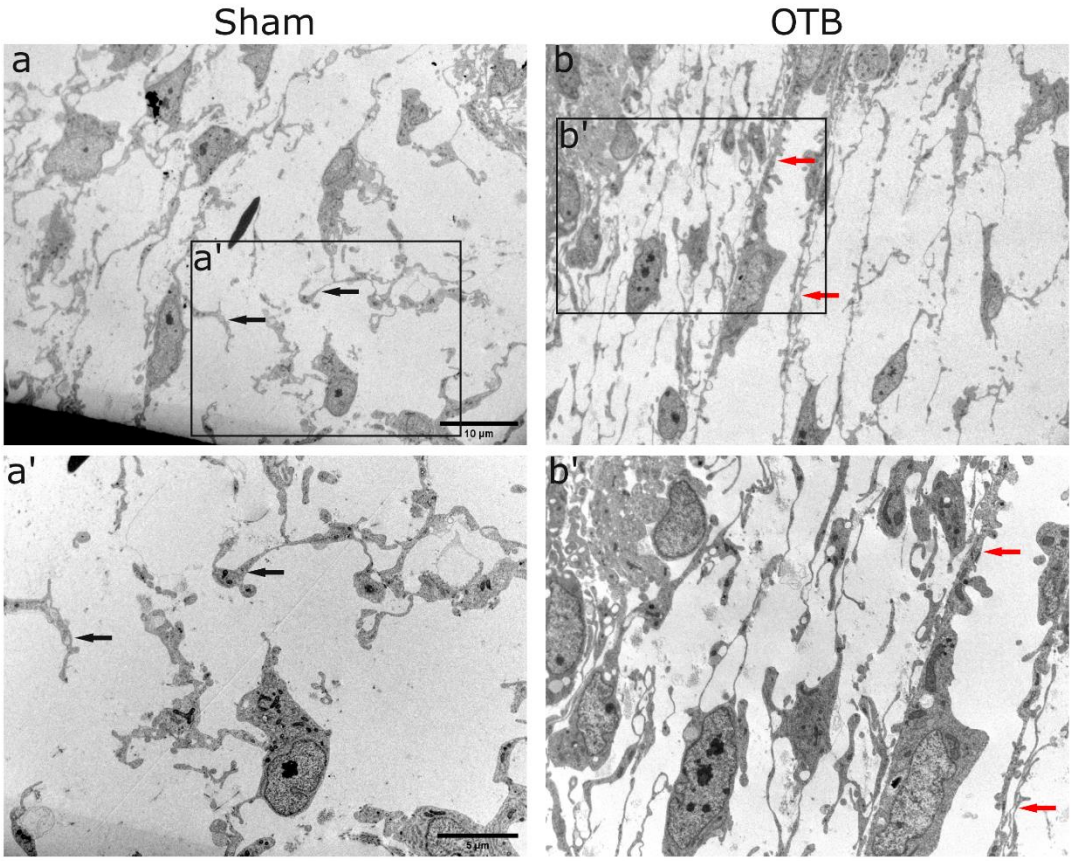

Figure 5.10: Transmission electron microscopy images of the ventricular epicardium. The ECM fibres of shams (a and a'; black arrows) and OTB (b and b'; red arrows) hearts have two very different kinds of patterns. OTB hearts' ECM fibres were stretched along the myocardium. a' and b' are higher magnifications of the boxes in panels a and b. Scale bar 10 µm fir a and b; 5 µm for a' and b'.

5.5 Discussion

The increased expression of *COL12A1* and *DDR2* from the qPCR data suggests a change in the ECM composition and tissue remodelling under stress. As previously mentioned, collagen XII expression changes based on tensile stress (Flück et al., 2003) and *DDR2* expression can impact collagen deposition and fibrillogenesis

(Cowling et al., 2014). The downregulation of *COL1A2* also suggests ECM remodelling. The downregulation of *COL1A2* together with the downregulation of TCF21, as was seen in the immunoblot, are in agreement with the literature (Acharya et al., 2012). Although DDR2 and TCF21 are both fibroblast markers, qPCR results showed that *DDR2* expression was higher in OTB hearts whereas immunoblotting results revealed a decrease in TCF21. This discrepancy can be due to the fact that DDR2 expression changes in response to changes in the ECM and mainly collagen I (Cowling et al., 2014), since the expression of collagen I and XII were aberrant in OTB hearts.

The question to be answered after the qPCR and immunoblot findings was if the downregulation of TCF21 and *COL1A2* is enough to cause a phenotypic change. The average number of TCF21+ cells was the same between OTB and sham hearts, which suggests that the downregulation of TCF21 did not affect the number of TCF21+ cells, but instead TCF21 has a lower expression in each cell. The number of TCF21+ cells on the epicardium covering the left ventricle in OTB hearts, was technically difficult to measure since the bleeding in the subepicardial space (see section 4.2) resulted in a number of autofluorescing red blood cells covering part of the tissue. The results on the number of TCF21+ cells in the epicardium were reconfirmed, on a smaller scale, by measuring the number of TCF21+ cells in a fixed area of tissue.

The *COL1A2* downregulation was technically more challenging to address, since measuring the total amount of collagen was nearly impossible, partly due to the bleeding in the OTB hearts and the absence of an assay that would measure only collagen I in the epicardium, instead of the whole heart. The fixed area was used to measure the void to area fraction (VAF) of collagen I by measuring the total area where collagen I was absent, in the fixed area, and then dividing it by the fixed area. Conversely the Collagen I to area fraction could be easily calculated by subtracting the VAF from 1. The fact that there was no significant difference in the

VAF between shams and OTB hearts suggest that the amount of collagen I was not significantly impacted. Upon closer examination, a phenotypic difference could be seen in the arrangement of collagen I fibres in the epicardium, above the RV. The collagen I fibres appeared thicker and the whole morphology resembled that of a squished sponge. In addition, TEM has showed that the ECM fibres in OTB hearts show clear signs of stretch in parallel to the ventricular myocardium.

In order to further elucidate the collagen I phenotype the morphology of the polygons, that were used to define the affixed area, were characterised using an ellipse fit. The ellipse fit measurements give minor and major axis. The minor axis is always the shortest one and the major is always the longest one, in length. Using the axes ratio it is possible to measure by what approximation the shape resembles a perfect square, or circle. A perfect square is expected to have an axes ratio of 1; any deviation from 1 suggests that the shape is more elongated in one axis more than the other, resulting in an elongated rectangle. The fact that OTB hearts had a higher axes ratio, in comparison to shams, means that they are more elongated along the surface of the heart and are less thick. A caveat in this type of study is that the total area of the epicardium is not measured so a higher axes ratio does not necessarily mean a smaller or larger epicardial area. The total area of the epicardium was also technically challenging to accurately measure due to the low tissue integrity at the bleeding regions, more commonly found above the LV. The change in the axes ratio explains the collagen I phenotype since the same amount of collagen possibly exists in both treatments but in the epicardium it is pressed together giving it a thicker appearance.

Although no previous studies can be found relating ECM orientation in the heart under strain and fibroblasts, previous studies using cultured fibroblasts in bioreactors under static and cyclic strain have been performed (Gauvin et al., 2011). Cultured fibroblasts and the surrounding ECM are oriented parallel to the axis of the induced strain (Gauvin et al., 2011); this phenotype is similar to the

one seen in this thesis, with all the epicardial ECM fibres adopting a similar axis. Moreover, there is a general upregulation of ECM protein production under strain (Gauvin et al., 2011), which can also be seen in the case of collagen XII. Although collagen I also tends to be upregulated with an increase in tissue strain, the in vivo model presented here has a number of factors affecting fibroblast transcription, which could result in collagen I downregulation, with *TCF21* levels being a prime example.

In conclusion, the ECM and fibroblasts continue to show significant changes, shown by the altered transcription levels of *DDR2*, *COL1A2* and *COL12A1*. In addition, TCF21 was underexpressed although the number of TCF21+ cells have been found to be not significantly different between OTB and sham hearts. By looking further at the VAF and the number of TCF21+ cells a significant negative correlation exists, suggesting that TCF21+ cells at HH35 have a fibroblast phenotype and are responsible for the production of collagen I in the epicardium. The epicardium was found to be thinner and the ECM matrix had an anterior to posterior alignment in OTB hearts instead of a random one. These results suggest general changes in the architecture of the ECM in the epicardium and further point towards the generation of a strain in OTB hearts, possibly generated by the haemodynamic alterations.

6 General discussion

Alterations of haemodynamics during development is believed to be one of the causes of CHDs. In humans 0.9% of all the born infants have a congenital heart disease (CHD; van der Linde et al., 2011). Prenatal fatal CHDs have been reported to be even higher, reaching 5-10% (Hoffman, 1995). The relevance of the epicardium in these diseases is hard to elucidate in the new-born, since the epicardium is part of the pericardium at that stage and quiescent, its function being a serous protective layer (Rodriguez and Tan, 2017). During development the epicardium is of the utmost importance since inhibition of epicardial growth is embryonically lethal (Gittenberger-de Groot et al., 2000). Knockdown of genes expressed in the epicardium can cause a range of malformations not only in the epicardium but also in the valves and the myocardium (Braitsch et al., 2012; Pang et al., 2017; Takeichi et al., 2013; Wu et al., 2012).

In this thesis, we have mainly looked at two chick developmental stages. At HH29 the heart has four complete chambers, i.e. the interventricular and interatrial septum are fully formed (Wittig and Münsterberg, 2016). The OFT has just started to septate into the future aorta and pulmonary artery, at the distal end of the heart (Anderson, 2003). The proepicardium has migrated over the surface of the myocardium and the epicardium has formed to cover the heart (Nahirney, Mikawa and Fischman, 2003). The EPDC have already started migrating and can be found in the ventricles, atria and AV cushions (Männer, 1999). The coronary vasculature is an endothelial plexus, which is only patent to the sinus venosus with no attachments to the OFT (Poelmann et al., 1993).

In shams, at HH35 OFT septation is complete and the semilunar valves have formed (Anderson, 2003). The epicardium continues to send EPDC to the myocardium and they can now be seen in the developing AV valves (Gittenberger-de Groot et al., 1998). The EPDC also differentiate into fibroblasts and smooth muscle cells (Braitsch et al., 2012; Braitsch and Yutzey, 2013). The coronary

vasculature is now supported by SMCs with the coronary arteries being attached to the aorta and patent (Poelmann et al., 1993). Experiments with different n numbers were used throughout this thesis in order to balance between time and cost.

6.1 Epicardial architecture in OTB hearts

6.1.1 Gross morphology

It was previously noted that the total area of the epicardium had an increase of 60.1% in HH29 OTB hearts (see section 1.14; Pang, 2016), although the thickness of the epicardium in OTB hearts was not found to be significantly different from shams in the data described in this thesis. This discrepancy is possibly due to the method used in the study in this thesis (see section 3.7). The thickness was only measured on two points of the epicardium, covering the right ventricle and right AV canal, instead of the whole epicardium. The method used by Pang (2016) also measured the extension of the epicardium along the surface of the myocardium. If an OTB heart epicardium with the same average thickness as the shams was covering a larger portion of the myocardium it would be impossible to be picked up by the method used in this thesis. HH35 OTB hearts were found to have a thinner epicardium in comparison to shams.

The epicardium of HH29 OTB hearts in this study was confirmed to have an abnormal morphology with ruffles on its surface, as previously noted (Pang, 2016). The reason for the formation of these ruffles is not fully understood. The number of epicardial cells was not signicantly different between sham and OTB hearts, suggesting that this is not due to a hindrance in migration and further accumulation of cells in the subepicardial space. In addition, proliferation and apoptosis were also found to be normal in HH29 OTB hearts.

6.1.2 ECM architecture

Collagen XII was found to be expressed in the epicardium of zebrafishes (Marro et al., 2016). In addition, collagen XII binds to collagen I changing its biomechanical properties (Koch, 1995), for example stiffness. COL12A1 expression increases when the tissue is under tensile stress (Flück et al., 2003). DDR2 is a membrane receptor found in cardiac fibroblasts (Morales et al., 2005). DDR2 is mainly activated by binding to collagen I and III, both of which are major heart collagens (Vogel at al., 1997). *DDR2* knockout hearts have decreased collagen deposition, resulting in reduced collagen density, (Cowling et al., 2014) but DDR2 overexpression was found to increase cell invasion and migration (Xu et al., 2014).

In HH29 OTB hearts, there was upregulation of COL12A1 suggesting that the heart is under tensile stress, possibly due to the increased blood pressure in the ventricles. In addition, the upregulation of DDR2 at HH29 can signal the start of altered collagen deposition in the OTB hearts and points to a signalling cascade where DDR2 will bind to the altered collagen and further change the molecular signalling within the fibroblasts. COL12A1 (collagen XII) is a type of fibril associated collagen with interrupted triple helices. Collagen I density in the OTB hearts was normal as well as *COL1A2* expression.

In HH35 OTB hearts, the further increase in expression of COL12A1 and DDR2, as seen by qPCR, suggests a change in ECM composition and tissue remodelling under stress. The downregulation of COL1A2, at HH35, also suggests ECM remodelling. It is possible for the increased expression of COL12 to be a response to the increase of stress due to the expansion of the underlying myocardium, due to dilation (see section 1.14; Pang, 2016), causing the epicardium to stretch around it. It is not yet known how DDR2 overexpression affects collagen deposition. Collagen I density in the OTB hearts was normal suggesting that it was not affected by DDR2 overexpression.

In HH29 and HH35 OTB hearts, the VAF of collagen I was comparable between OTB and sham hearts, which suggests that the amount of collagen I was not significantly impacted. However, upon closer examination of HH35 OTB hearts, a phenotypic difference could be seen in the arrangement of collagen I fibres in the epicardium. The collagen I fibres appeared thicker and the whole morphology resembled that of a squished sponge. Further proof that the collagen I phenotype is due to the collagen fibres coming close together can also be seen in the measurements of epicardial thickness, which show that the OTB hearts epicardium is actually thinner. In addition, HH35 OTB TEM results revealed that the ECM fibres were stretched anterior to posterior, in parallel to the ventricular myocardium; in comparison, shams had relaxed ECM fibres. This morphology is reminiscent of a balloon being pumped, when the internal pressure rises the balloon walls respond by generating an opposite force due to surface tension making the balloon walls to stretch thinner. All these factors further suggest an increase in stress due to the expansion of the underlying myocardium causing the epicardium to stretch around it.

In HH29 OTB hearts, the protein expression of TCF21, which is a fibroblast marker in later stages of development (Acharya et al., 2012), had no significant difference in comparison to shams. On the other hand, in HH35 OTB hearts, TCF21 was found to be downregulated. The average number of TCF21+ cells was the same between HH35 OTB and sham hearts, which suggests that the downregulation of TCF21 did not affect the number of TCF21+ cells but most probably, TCF21 has a lower expression in each cell. Moreover, since the numbers of TCF21+ cells was comparable between sham and OTB hearts in the myocardium it can also be said that EPDC migration was normal, at least for TCF21+ cells.

6.2 Epicardial migration in OTB hearts

In HH29 and HH35 OTB hearts, the epicardial migration is normal and the epicardium covered the heart. The expression of N- and E- cadherin was also

normal suggesting a healthy epithelium, although cadherins are also expressed in the myocardium (Ferreira-Cornwell et al., 2002). The expression of cadherins in the myocardium hinders the sensitivity of the western analysis, since any small change in the epicardium will be concealed by the high expression of cadherins in the myocardium. The number of epicardial cells is also normal, which shows that migration was not altered in the subepicardial space.

In HH29 OTB hearts, *TBX18* was upregulated, most notably on the right side of the heart, in comparison to shams. Although, the function of TBX18 has not fully be elucidated in the epicardium, knockdown of TBX18 was found to affect migration (Takeichi et al., 2013) but no data is available for TBX18 overexpression. It is known that knock down of TBX18 inhibits EMT by downregulating *SNAI2* expression (Takeichi et al., 2013); however SNAI2 was found to be normally expressed in HH29 OTB hearts. It could be that *TBX18* overexpression does not have any severe effect in the epicardium, at least in the amount it was expressed at HH29 OTB hearts, since EMT is also regulated by WT1 (Takeichi et al., 2013), which also had a normal expression. HH35 OTB hearts had a downregulation of *TBX18* but also normal expression of *SNAI2* and *WT1*.

6.3 The outflow tract

The arterial epicardium, covering the OFT, is known for expressing WT1 but no data has been shown that analyses *TCF21* and *TBX18* expression (Vicente-Steijn et al., 2015). This thesis confirms that the arterial epicardium at HH28 normally expresses *WT1*, covering the whole of the OFT, with low or absent expression of *TCF21* and *TBX18*. However, HH28 OTB hearts not only expressed *WT1* but they also had a strong expression of *TCF21* and *TBX18*. It is hard to say what role *TBX18* and *TFC21* expression has on the OFT, since the function of the arterial epicardium is largely unknown. Previous research suggests that changes in haemodynamics cause aberrant collagen deposition in the OFT, making the OFT stiffer (Rennie et al., 2017). If *TCF21* in the arterial epicardium is linked with

fibroblasts, as it is to the venous epicardium, changes in *TCF21* expression could be associated OFT stiffness. TBX18 was found to be responsible for the myocardialisation of the sinus venosus and its stemming veins (Christoffels, 2006). The missexpression of TBX18 in the OFT might be able to enhance the myocardialisation of the OFT. This theory is supported by an increased in the extent of myocardialisation that was found in the OFT of OTB hearts together with aberrant semilunar valves. At HH35 OTB hearts, the OFT showed a phenotype strongly reminiscent of persistent truncus arteriosus, with a common large arterial trunk at the base of the OFT, which is septated to the aorta and pulmonary artery.

6.4 The coronary vasculature

A possible reason for the ruffles in HH29 OTB hearts is the breakage of the early CV causing blood to enter the epicardium. Although the number of blood cells was not found to be significanly higher, due to the high variability of the numbers, this does not exclude this explanation since plasma trapped in the epicardium can also stretch the tissue. The bleeding was possibly caused due to the breakage of the fragile endothelial plexus by the high blood pressure, due to the OFT banding. The increased numbers of red blood cells suggest vessel breakage, which can be responsible for plasma leaking in the epicardium creating an oedema in the epicardium. Since tissue morphology techniques using sectioning mainly rely in the dehydration of the tissue, detecting plasma leakage in the epicardium is impossible with these techniques.

HH35 OTB hearts had major bleeding in the subepicardial area, which seems to be a continuation of the phenotype seen at HH29. The downregulation of the vascular markers *NRP1*, *ANGPT1*, *PDGFRB* and *NTRK2* suggests that vessels maturation is aberrant; this could lead to problems to either/both the endothelial structural integrity and to the SMCs. The qPCR data in this thesis showed a significant downregulation of NTRK2 and upregulation of BDNF, which can suggest a compensatory mechanism to overstimulate any remaining NTRK2 receptors. The

transcription factor TBX18 was found to be not only an important epicardial marker but also important in CV development (Wu et al., 2013). Mice heterozygous for TBX18 have a smaller CV diameter in the epicardium and IVS and irregular CV patterning. In addition, *ANGPT1* expression was found to be lower when *TBX18* was knocked down (Wu et al., 2013).

In HH35 OTB hearts, the average vessel area in the epicardium was highly variable and the vessels of the myocardium had a smaller lumen area. These findings can be explained by previous studies showing that downregulation of the genes examined in this thesis causes CV patterning defects (Anastasia et al., 2014; Hellström et al., 1999; Ward et al., 2004; Wu et al., 2013). The patterning of the major vessels on the surface of the heart also showed abnormalities with bigger vessels in OTB hearts, with unequal distances between the vessels, again pointing towards patterning abnormalities. Moreover, HH35 TEM results showed that the endothelial cells in OTB hearts are not as tightly connected allowing blood leakage in the subepicardial space.

6.5 Conclusion

The epicardium has received little attention when it comes to CHDs. Hence, this thesis highlights the need of further research into the role of the epicardium during development and its role in CHDs. In this study, we showed that alteration of haemodynamics via OFT banding resulted in an aberrant epicardial morphology and coronary vasculature with the phenotype getting progressively more severe during development. A number of genes associated the ECM and vasculature were significantly altered in expression. The epicardium showed signs of blood leakage at HH29, where the early endothelial plexus stems from the SV; by HH35 the epicardium had severe bleeding and a morphology pointing towards increase in tensile stress. In addition, the tensile stress at HH35 OTB hearts was evident by the ECM architecture by a further increase of collagen XII expression, from HH29 to HH35, and by the ECM fibres showing clear signs of stretch parallel to the

myocardium. Overall, H0 is rejected in this thesis. Hence, there was a functional effect on the epicardium itself, in relation to the ECM and its cell lineages, SMCs and fibroblasts. The results clearly show that alteration of haemodynamics can be embryonically lethal due to breakage of the CVs and also significantly alter tissue architecture due to an increase in mechanical stress in the heart.

Although, TBX18 in this study was shown to be upregulated in HH29 OTB hearts and then downregulated at HH35, not much is known about the role of TBX18 in the epicardium. Especially since there are no studies where TBX18 in the epicardium is overexpressed. Studies with TBX18 overexpression could shed new light in its role in epicardial development. In addition, more research is needed in the role of collagen XII in the heart. Since the heart has to continually contract and relax in order to pump blood around the body mechanical stress will be applied to the myocardium and the surrounding tissues on a daily basis. Not much is known about the role of collagen XII in the chick heart, including its spatiotemporal expression during development and its role in cases where mechanical stress changes. Studies with increased or reduced cardiac load, resulting to more or less mechanical stress respectively, together with analysis of collagen XII accumulation and expression would shed new light in its function. Furthermore, more analysis should be done on the effects of altered haemodynamics in the CVs. This study has looked at the CVs under an increased haemodynamic load, but more research can be done in the development of the main coronary arteries and their patterning. Moreover, a model with decreased haemodynamic load could be used to assess how the coronary vasculature development changes in comparison to a normal haemodynamic load and an increased one.

7 References

Abramochkin, D. V., Lozinsky, I.T. and Kamkin, A., 2014. Influence of mechanical stress on fibroblast–myocyte interactions in mammalian heart. *Journal of Molecular and Cellular Cardiology*, [online] 70, pp.27–36.

Acharya, A., Baek, S.T., Huang, G., Eskiocak, B., Goetsch, S., Sung, C.Y., Banfi, S., Sauer, M.F., Olsen, G.S., Duffield, J.S., Olson, E.N. and Tallquist, M.D., 2012. The bHLH transcription factor Tcf21 is required for lineage-specific EMT of cardiac fibroblast progenitors. *Development*, [online] 139(12), pp.2139–2149.

Adachi, I., Seale, A., Uemura, H., McCarthy, K.P., Kimberley, P. and Ho, S.Y., 2009. Morphologic spectrum of truncal valvar origin relative to the ventricular septum: Correlation with the size of ventricular septal defect. *The Journal of Thoracic and Cardiovascular Surgery*, [online] 138(6), pp.1283–1289.

Agarwal, G., Kovac, L., Radziejewski, C. and Samuelsson, S.J., 2002. Binding of Discoidin Domain Receptor 2 to Collagen I: An Atomic Force Microscopy Investigation. *Biochemistry*, [online] 41(37), pp.11091–11098.

Van den Akker, N.M.S.M.S., Winkel, L.C.J.C.J., Nisancioglu, M.H.H., Maas, S., Wisse, L.J.J., Armulik, A., Poelmann, R.E.E., Lie-Venema, H., Betsholtz, C. and Gittenberger-de Groot, A.C.C., 2008. PDGF-B signaling is important for murine cardiac development: Its role in developing atrioventricular valves, coronaries, and cardiac innervation. *Developmental Dynamics*, [online] 237(2), pp.494–503.

Anastasia, A., Deinhardt, K., Wang, S., Martin, L., Nichol, D., Irmady, K., Trinh, J., Parada, L., Rafii, S., Hempstead, B.L.L. and Kermani, P., 2014. Trkb Signaling in Pericytes Is Required for Cardiac Microvessel Stabilization. *PLoS ONE*, [online] 9(1), p.e87406.

Anders, S. and Huber, W., 2010. Differential expression analysis for sequence count data. *Genome Biology*, [online] 11(10), p.R106.

Anderson, R.H., 2002. Development and structure of the atrial septum. *Heart*, [online] 88(1), pp.104–110.

Anderson, R.H., 2003. Development of the heart: (2) Septation of the atriums and ventricles. *Heart*, [online] 89(8), pp.949–958.

Anderson, R.H., Webb, S., Brown, N.A., Lamers, W. and Moorman, A., 2003. Development of the heart: (3) Formation of the ventricular outflow tracts, arterial valves, and intrapericardial arterial trunks. *Heart*, [online] 89(9), pp.1110–1118.

Andrés-Delgado, L. and Mercader, N., 2016. Interplay between cardiac function

and heart development. *Biochimica et Biophysica Acta (BBA) - Molecular Cell Research*, [online] 1863(7), pp.1707–1716.

Badenhorst, D., 2003. Cross-linking influences the impact of quantitative changes in myocardial collagen on cardiac stiffness and remodelling in hypertension in rats. *Cardiovascular Research*, [online] 57(3), pp.632–641.

Bakkers, J., 2011. Zebrafish as a model to study cardiac development and human cardiac disease. *Cardiovascular Research*, [online] 91(2), pp.279–288.

Barnes, R.M., Firulli, B.A., VanDusen, N.J., Morikawa, Y., Conway, S.J., Cserjesi, P., Vincentz, J.W. and Firulli, A.B., 2011. Hand2 Loss-of-Function in Hand1-Expressing Cells Reveals Distinct Roles in Epicardial and Coronary Vessel Development. *Circulation Research*, [online] 108(8), pp.940–949.

Bartman, T., Walsh, E.C., Wen, K.-K., McKane, M., Ren, J., Alexander, J., Rubenstein, P.A. and Stainier, D.Y.R., 2004. Early Myocardial Function Affects Endocardial Cushion Development in Zebrafish. *PLoS Biology*, 2(5), p.e129.

Ben-Shachar, G., Arcilla, R.A., Lucas, R. V. and Manasek, F.J., 1985. Ventricular trabeculations in the chick embryo heart and their contribution to ventricular and muscular septal development. *Circulation Research*, [online] 57(5), pp.759–766.

Benesh, E.C., Miller, P.M., Pfaltzgraff, E.R., Grega-Larson, N.E., Hager, H.A., Sung, B.H., Qu, X., Baldwin, H.S., Weaver, A.M. and Bader, D.M., 2013. Bves and NDRG4 regulate directional epicardial cell migration through autocrine extracellular matrix deposition. *Molecular Biology of the Cell*, [online] 24(22), pp.3496–3510.

van den Berg, G. and Moorman, A.F.M., 2011. Development of the Pulmonary Vein and the Systemic Venous Sinus: An Interactive 3D Overview. *PLoS ONE*, [online] 6(7), p.e22055.

Bernanke, D.H. and Velkey, J.M., 2002. Development of the coronary blood supply: Changing concepts and current ideas. *The Anatomical Record*, [online] 269(4), pp.198–208.

Braitsch, C. and Yutzey, K., 2013. Transcriptional Control of Cell Lineage Development in Epicardium-Derived Cells. *Journal of Developmental Biology*, [online] 1(2), pp.92–111.

Braitsch, C.M., Combs, M.D., Quaggin, S.E. and Yutzey, K.E., 2012. Pod1/Tcf21 is regulated by retinoic acid signaling and inhibits differentiation of epicardium-derived cells into smooth muscle in the developing heart. *Developmental Biology*, [online] 368(2), pp.345–357.

Braitsch, C.M., Kanisicak, O., van Berlo, J.H., Molkentin, J.D. and Yutzey, K.E.,

2013. Differential expression of embryonic epicardial progenitor markers and localization of cardiac fibrosis in adult ischemic injury and hypertensive heart disease. *Journal of Molecular and Cellular Cardiology*, [online] 65, pp.108–119.

Brand, T., 2003. Heart development: molecular insights into cardiac specification and early morphogenesis. *Developmental Biology*, [online] 258(1), pp.1–19.

Brindle, N.P.J., 2006. Signaling and Functions of Angiopoietin-1 in Vascular Protection. *Circulation Research*, [online] 98(8), pp.1014–1023.

Brown, W.R.A., Hubbard, S.J., Tickle, C. and Wilson, S.A., 2003. The chicken as a model for large-scale analysis of vertebrate gene function. *Nature Reviews Genetics*, [online] 4(2), pp.87–98.

Buja, L.M., 2005. Myocardial ischemia and reperfusion injury. *Cardiovascular Pathology*, [online] 14(4), pp.170–175.

Burggren, W.W., Warburton, S.J. and Slivkoff, M.D., 2000. Interruption of cardiac output does not affect short-term growth and metabolic rate in day 3 and 4 chick embryos. *The Journal of experimental biology*, [online] 203(Pt 24), pp.3831–8.

Cai, C.-L., Martin, J.C., Sun, Y., Cui, L., Wang, L., Ouyang, K., Yang, L., Bu, L., Liang, X., Zhang, X., Stallcup, W.B., Denton, C.P., McCulloch, A., Chen, J. and Evans, S.M., 2008. A myocardial lineage derives from Tbx18 epicardial cells. *Nature*, [online] 454(7200), pp.104–108.

Camelliti, P., 2004. Fibroblast Network in Rabbit Sinoatrial Node: Structural and Functional Identification of Homogeneous and Heterogeneous Cell Coupling. *Circulation Research*, [online] 94(6), pp.828–835.

Camelliti, P., Borg, T. and Kohl, P., 2005. Structural and functional characterisation of cardiac fibroblasts. *Cardiovascular Research*, [online] 65(1), pp.40–51.

Cano, E., Carmona, R., Ruiz-Villalba, A., Rojas, A., Chau, Y.-Y., Wagner, K.D., Wagner, N., Hastie, N.D., Muñoz-Chápuli, R. and Pérez-Pomares, J.M., 2016. Extracardiac septum transversum/proepicardial endothelial cells pattern embryonic coronary arterio–venous connections. *Proceedings of the National Academy of Sciences*, [online] 113(3), pp.656–661.

Cao, J., Wang, J., Jackman, C.P., Cox, A.H., Trembley, M.A., Balowski, J.J., Cox, B.D., De Simone, A., Dickson, A.L., Di Talia, S., Small, E.M., Kiehart, D.P., Bursac, N., and Poss, K.D., 2017. Tension Creates an Endoreplication Wavefront that Leads Regeneration of Epicardial Tissue. *Developmental Cell*, [online] 42(6), pp.600-615.e4.

Çengel, Y.A. and Cimbala, J.M., 2006. *Fluid mechanics: fundamentals and applications*. 1st ed. Boston: McGraw-HillHigher Education.

Chang, C., 1931. The formation of the interatrial septum in chick embryos. *The Anatomical Record*, [online] 50(1), pp.9–22.

Cherry, E.M. and Eaton, J.K., 2013. Shear thinning effects on blood flow in straight and curved tubes. *Physics of Fluids*, [online] 25(7), p.073104.

Ching, Y.-H., Ghosh, T.K., Cross, S.J., Packham, E.A., Honeyman, L., Loughna, S., Robinson, T.E., Dearlove, A.M., Ribas, G., Bonser, A.J., Thomas, N.R., Scotter, A.J., Caves, L.S.D., Tyrrell, G.P., Newbury-Ecob, R.A., Munnich, A., Bonnet, D. and Brook, J.D., 2005. Mutation in myosin heavy chain 6 causes atrial septal defect. *Nature Genetics*, [online] 37(4), pp.423–428.

Chiquet, M., Birk, D.E., Bönnemann, C.G. and Koch, M., 2014. Collagen XII: Protecting bone and muscle integrity by organizing collagen fibrils. *The International Journal of Biochemistry & Cell Biology*, [online] 53, pp.51–54.

Christoffels, V.M., 2006. Formation of the Venous Pole of the Heart From an Nkx2-5-Negative Precursor Population Requires Tbx18. *Circulation Research*, [online] 98(12), pp.1555–1563.

Cirotto, C. and Arangi, I., 1989. How do avian embryos breathe? oxygen transport in the blood of early chick embryos. *Comparative Biochemistry and Physiology Part A: Physiology*, [online] 94(4), pp.607–613.

Clauss, S.B., Walker, D.L., Kirby, M.L., Schimel, D. and Lo, C.W., 2006. Patterning of coronary arteries in wildtype and connexin43 knockout mice. *Developmental Dynamics*, [online] 235(10), pp.2786–2794.

Cowling, R.T., Yeo, S.J., Kim, I.J., Park, J.I., Gu, Y., Dalton, N.D., Peterson, K.L. and Greenberg, B.H., 2014. Discoidin domain receptor 2 germline gene deletion leads to altered heart structure and function in the mouse. *AJP: Heart and Circulatory Physiology*, [online] 307(5), pp.H773–H781.

Craig, E.A., Austin, A.F., Vaillancourt, R.R., Barnett, J. V. and Camenisch, T.D., 2010. TGFβ2-mediated production of hyaluronan is important for the induction of epicardial cell differentiation and invasion. *Experimental Cell Research*, [online] 316(20), pp.3397–3405.

Culver, J.C. and Dickinson, M.E., 2010. The Effects of Hemodynamic Force on Embryonic Development. *Microcirculation*, [online] 17(3), pp.164–178.

Dai, W., Dong, Q., Chen, M., Zhao, L., Chen, A., Li, Z. and Liu, S., 2016. Changes in cardiac structure and function in a modified rat model of myocardial

hypertrophy. *Cardiovascular Journal of Africa*, [online] 27(3), pp.134–142.

Dal-Bianco, J.P. and Levine, R.A., 2013. Anatomy of the Mitral Valve Apparatus. *Cardiology Clinics*, [online] 31(2), pp.151–164.

deAlmeida, A.C., van Oort, R.J. and Wehrens, X.H.T., 2010. Transverse Aortic Constriction in Mice. *Journal of Visualized Experiments*, [online] (38).

Donovan, M.J., Lin, M.I., Wiegn, P., Ringstedt, T., Kraemer, R., Hahn, R., Wang, S., Ibañez, C.F., Rafii, S. and Hempstead, B.L., 2000. Brain derived neurotrophic factor is an endothelial cell survival factor required for intramyocardial vessel stabilization. *Development (Cambridge, England)*, [online] 127(21), pp.4531–40.

Ehler, E., Jat, P.S., Noble, M.D., Citi, S., and Draeger, A., 1995. Vascular smooth muscle cells of H-2Kb-tsA58 transgenic mice. Characterization of cell lines with distinct properties. *Circulation*, [online] 92(11), pp.3289–3296.

Eralp, I., 2005. Coronary Artery and Orifice Development Is Associated With Proper Timing of Epicardial Outgrowth and Correlated Fas Ligand Associated Apoptosis Patterns. *Circulation Research*, [online] 96(5), pp.526–534.

Everaert, C., Luypaert, M., Maag, J.L. V., Cheng, Q.X., Dinger, M.E., Hellemans, J. and Mestdagh, P., 2017. Benchmarking of RNA-sequencing analysis workflows using whole-transcriptome RT-qPCR expression data. *Scientific Reports*, [online] 7(1), p.1559.

Fantin, A., Herzog, B., Mahmoud, M., Yamaji, M., Plein, A., Denti, L., Ruhrberg, C. and Zachary, I., 2014. Neuropilin 1 (NRP1) hypomorphism combined with defective VEGF-A binding reveals novel roles for NRP1 in developmental and pathological angiogenesis. *Development*, [online] 141(3), pp.556–562.

Fantin, A., Maden, C.H.H. and Ruhrberg, C., 2009. Neuropilin ligands in vascular and neuronal patterning. *Biochemical Society Transactions*, [online] 37(6), pp.1228–1232.

Ferber, E.C., Kajita, M., Wadlow, A., Tobiansky, L., Niessen, C., Ariga, H., Daniel, J. and Fujita, Y., 2008. A Role for the Cleaved Cytoplasmic Domain of E-cadherin in the Nucleus. *Journal of Biological Chemistry*, [online] 283(19), pp.12691–12700.

Ferrara, N. and Davis-Smyth, T., 1997. The Biology of Vascular Endothelial Growth Factor. *Endocrine Reviews*, [online] 18(1), pp.4–25.

Ferreira-Cornwell, M.C., Luo, Y., Narula, N., Lenox, J.M., Lieberman, M. and Radice, G.L., 2002. Remodeling the intercalated disc leads to cardiomyopathy in mice misexpressing cadherins in the heart. *Journal of Cell Science*, 115(8),

pp.1623–1634.

Flück, M., Giraud, M.-N., Tunç, V. and Chiquet, M., 2003. Tensile stress-dependent collagen XII and fibronectin production by fibroblasts requires separate pathways. *Biochimica et Biophysica Acta (BBA) - Molecular Cell Research*, [online] 1593(2–3), pp.239–248.

Fox, J., 2005. The R Commander: A Basic-Statistics Graphical User Interface to R. *Journal of Statistical Software*, [online] 14(9), pp.1–41.

Frink, R.J. and James, T.N., 1973. Normal Blood Supply to the Human His Bundle and Proximal Bundle Branches. *Circulation*, [online] 47(1), pp.8–18.

Gauvin, R., Parenteau-Bareil, R., Larouche, D., Marcoux, H., Bisson, F., Bonnet, A., Auger, F.A., Bolduc, S. and Germain, L., 2011. Dynamic mechanical stimulations induce anisotropy and improve the tensile properties of engineered tissues produced without exogenous scaffolding. *Acta Biomaterialia*, 7(9), pp.3294–3301.

Giancotti, F.G., 1999. Integrin Signaling. *Science*, [online] 285(5430), pp.1028–1033.

Giannopoulos, A.A., Chepelev, L., Sheikh, A., Wang, A., Dang, W., Akyuz, E., Hong, C., Wake, N., Pietila, T., Dydynski, P.B., Mitsouras, D. and Rybicki, F.J., 2015. 3D printed ventricular septal defect patch: a primer for the 2015 Radiological Society of North America (RSNA) hands-on course in 3D printing. *3D Printing in Medicine*, [online] 1(1), p.3.

von Gise, A., Zhou, B., Honor, L.B., Ma, Q., Petryk, A. and Pu, W.T., 2011. WT1 regulates epicardial epithelial to mesenchymal transition through β-catenin and retinoic acid signaling pathways. *Developmental Biology*, [online] 356(2), pp.421–431.

Gittenberger-de Groot, A.C., Vrancken Peeters, M.-P.F.M., Bergwerff, M., Mentink, M.M.T. and Poelmann, R.E., 2000. Epicardial Outgrowth Inhibition Leads to Compensatory Mesothelial Outflow Tract Collar and Abnormal Cardiac Septation and Coronary Formation. *Circulation Research*, [online] 87(11), pp.969–971.

Gittenberger-de Groot, A.C., Vrancken Peeters, M.-P.F.M.P., Mentink, M.M.T., Gourdie, R.G. and Poelmann, R.E., 1998. Epicardium-derived cells contribute a novel population to the myocardial wall and the atrioventricular cushions. *Circulation Research*, [online] 82(10), pp.1043–1052.

Gittenberger-de Groot, A.C., Winter, E.M., Bartelings, M.M., Jose Goumans, M., DeRuiter, M.C. and Poelmann, R.E., 2012. The arterial and cardiac epicardium in

development, disease and repair. *Differentiation*, [online] 84(1), pp.41–53.

Go, A.S., Mozaffarian, D., Roger, V.L., Benjamin, E.J., Berry, J.D., Blaha, M.J., Dai, S., Ford, E.S., Fox, C.S., Franco, S., Fullerton, H.J., Gillespie, C., Hailpern, S.M., Heit, J.A., Howard, V.J., Huffman, M.D., Judd, S.E., Kissela, B.M., Kittner, S.J., Lackland, D.T., Lichtman, J.H., Lisabeth, L.D., Mackey, R.H., Magid, D.J., Marcus, G.M., Marelli, A., Matchar, D.B., McGuire, D.K., Mohler, E.R., Moy, C.S., Mussolino, M.E., Neumar, R.W., Nichol, G., Pandey, D.K., Paynter, N.P., Reeves, M.J., Sorlie, P.D., Stein, J., Towfighi, A., Turan, T.N., Virani, S.S., Wong, N.D., Woo, D. and Turner, M.B., 2014. Heart Disease and Stroke Statistics--2014 Update: A Report From the American Heart Association. *Circulation*, [online] 129(3), pp.e28–e292.

Goldsmith, E.C., Hoffman, A., Morales, M.O., Potts, J.D., Price, R.L., McFadden, A., Rice, M. and Borg, T.K., 2004. Organization of fibroblasts in the heart. *Developmental Dynamics*, [online] 230(4), pp.787–794.

Graham, A., 2001. The development and evolution of the pharyngeal arches. *Journal of Anatomy*, [online] 199(1), pp.133–141.

Gray, H. and Clemente, C.D., 1985. *Anatomy of the human body*. 30th ed. Philadelphia: Lea & Febiger.

Gros, D.B. and Jongsma, H.J., 1996. Connexins in mammalian heart function. *BioEssays*, [online] 18(9), pp.719–730.

Gs, A.K., Raj, B., Santhosh, K.S., Sanjay, G. and Kartha, C.C., 2014. Ascending aortic constriction in rats for creation of pressure overload cardiac hypertrophy model. *Journal of visualized experiments : JoVE*, [online] (88), p.e50983.

Gupta, S.K., Bamforth, S.D. and Anderson, R.H., 2015. How frequent is the fifth arch artery? *Cardiology in the Young*, [online] 25(04), pp.628–646.

Hachicha, Z., Dumesnil, J.G., Bogaty, P. and Pibarot, P., 2007. Paradoxical Low-Flow, Low-Gradient Severe Aortic Stenosis Despite Preserved Ejection Fraction Is Associated With Higher Afterload and Reduced Survival. *Circulation*, [online] 115(22), pp.2856–2864.

Haenig, B.B. and Kispert, A., 2004. Analysis of TBX18 expression in chick embryos. *Development Genes and Evolution*, [online] 214(8), pp.407–11.

Hamburger, V. and Hamilton, H.L., 1992. A series of normal stages in the development of the chick embryo. *Developmental Dynamics*, [online] 195(4), pp.231–272.

Hellström, M., Kalén, M., Lindahl, P., Abramsson, A. and Betsholtz, C., 1999. Role

of PDGF-B and PDGFR-beta in recruitment of vascular smooth muscle cells and pericytes during embryonic blood vessel formation in the mouse. *Development (Cambridge, England)*, [online] 126(14), pp.3047–55.

Hervé, M., 2011. GrapheR: a multiplatform GUI for drawing customizable graphs in R. *The R Journal*, 3(2), pp.45–53.

Herzog, Y., Kalcheim, C., Kahane, N., Reshef, R. and Neufeld, G., 2001. Differential expression of neuropilin-1 and neuropilin-2 in arteries and veins. *Mechanisms of development*, [online] 109(1), pp.115–119.

Hiruma, T. and Hirakow, R., 1989. Epicardial formation in embryonic chick heart: Computer-aided reconstruction, scanning, and transmission electron microscopic studies. *American Journal of Anatomy*, [online] 184(2), pp.129–138.

Hiruma, T., Nakajima, Y. and Nakamura, H., 2002. Development of pharyngeal arch arteries in early mouse embryo. *Journal of Anatomy*, [online] 201(1), pp.15–29.

Hoffman, J.I., 1995. Incidence of congenital heart disease: II. Prenatal incidence. *Pediatric Cardiology*, [online] 16(4), pp.155–65.

Hoffman, J.I.. and Kaplan, S., 2002. The incidence of congenital heart disease. *Journal of the American College of Cardiology*, [online] 39(12), pp.1890–1900.

Hogers, B., DeRuiter, M.C., Baasten, A.M.J., Gittenberger-de Groot, A.C. and Poelmann, R.E., 1995. Intracardiac Blood Flow Patterns Related to the Yolk Sac Circulation of the Chick Embryo. *Circulation Research*, [online] 76(5), pp.871–877.

Hogers, B., DeRuiter, M.C., Gittenberger-de Groot, A.C. and Poelmann, R.E., 1999. Extraembryonic venous obstructions lead to cardiovascular malformations and can be embryolethal. *Cardiovascular research*, [online] 41(1), pp.87–99.

Hörl, D., Rojas Rusak, F., Preusser, F., Tillberg, P., Randel, N., Chhetri, R.K., Cardona, A., Keller, P.J., Harz, H., Leonhardt, H., Treier, M. and Preibisch, S., 2018. BigStitcher: Reconstructing high-resolution image datasets of cleared and expanded samples. *bioRxiv*.

Huang, C., Sheikh, F., Hollander, M., Cai, C., Becker, D., Chu, P.-H., Evans, S. and Chen, J., 2003. Embryonic atrial function is essential for mouse embryogenesis, cardiac morphogenesis and angiogenesis. *Development (Cambridge, England)*, 130(24), pp.6111–6119.

Illi, B., 2003. Shear Stress-Mediated Chromatin Remodeling Provides Molecular Basis for Flow-Dependent Regulation of Gene Expression. *Circulation Research*, [online] 93(2), pp.155–161.

Ishii, Y., Garriock, R.J., Navetta, A.M., Coughlin, L.E. and Mikawa, T., 2010. BMP Signals Promote Proepicardial Protrusion Necessary for Recruitment of Coronary Vessel and Epicardial Progenitors to the Heart. *Developmental Cell*, [online] 19(2), pp.307–316.

Ishii, Y., Langberg, J.D., Hurtado, R., Lee, S. and Mikawa, T., 2007. Induction of proepicardial marker gene expression by the liver bud. *Development*, [online] 134(20), pp.3627–3637.

Jain, R., Rentschler, S. and Epstein, J.A., 2010. Notch and cardiac outflow tract development. *Annals of the New York Academy of Sciences*, [online] 1188(1), pp.184–190.

Jankowska-Steifer, E., Madej, M., Niderla-Bielińska, J., Ruminski, S., Flaht-Zabost, A., Czarnowska, E., Gula, G., Radomska-Leśniewska, D.M. and Ratajska, A., 2015. Vasculogenic and hematopoietic cellular progenitors are scattered within the prenatal mouse heart. *Histochemistry and Cell Biology*, [online] 143(2), pp.153–169.

Jaworska-Wilczynska, M., Trzaskoma, P., Szczepankiewicz, A.A. and Hryniewiecki, T., 2016. Pericardium: structure and function in health and disease. *Folia Histochemica et Cytobiologica*, [online] 54(3), pp.121–125.

Jenkins, K.J., Correa, A., Feinstein, J.A., Botto, L., Britt, A.E., Daniels, S.R., Elixson, M., Warnes, C.A. and Webb, C.L., 2007. Noninherited Risk Factors and Congenital Cardiovascular Defects: Current Knowledge. *Circulation*, 115(23), pp.2995–3014.

Katz, T.C., Singh, M.K., Degenhardt, K., Rivera-Feliciano, J., Johnson, R.L., Epstein, J.A. and Tabin, C.J., 2012. Distinct Compartments of the Proepicardial Organ Give Rise to Coronary Vascular Endothelial Cells. *Developmental Cell*, [online] 22(3), pp.639–650.

Kimball, T.R., Daniels, S.R., Loggie, J.M.H., Khoury, P. and Meyer, R.A., 1993. Relation of left ventricular mass, preload, afterload and contractility in pediatric patients with essential hypertension. *Journal of the American College of Cardiology*, [online] 21(4), pp.997–1001.

Kirby, M.L. and Sahn, D.J., 2010. Mouse Models of Congenital Heart Defects: What's Missing? *Circulation: Cardiovascular Imaging*, [online] 3(3), pp.228–230.

Kleinman, C.S., Tabibian, M., Starc, T.J., Hsu, D.T. and Gersony, W.M., 2007. Spontaneous Regression of Left Ventricular Dilation in Children with Restrictive Ventricular Septal Defects. *The Journal of Pediatrics*, [online] 150(6), pp.583–586.

Koch, M., 1995. Large and small splice variants of collagen XII: differential expression and ligand binding. *The Journal of Cell Biology*, [online] 130(4), pp.1005–1014.

Kolk, M.V. V, Meyberg, D., Deuse, T., Tang-Quan, K.R., Robbins, R.C., Reichenspurner, H. and Schrepfer, S., 2009. LAD-ligation: a murine model of myocardial infarction. *Journal of visualized experiments : JoVE*, [online] (32).

Komiyama, M., Ito, K. and Shimada, Y., 1987. Origin and development of the epicardium in the mouse embryo. *Anatomy and Embryology*, [online] 176(2), pp.183–189.

de Lange, F.J., 2004. Lineage and Morphogenetic Analysis of the Cardiac Valves. *Circulation Research*, [online] 95(6), pp.645–654.

Lavine, K.J., Yu, K., White, A.C., Zhang, X., Smith, C., Partanen, J. and Ornitz, D.M., 2005. Endocardial and epicardial derived FGF signals regulate myocardial proliferation and differentiation in vivo. *Developmental Cell*, [online] 8(1), pp.85–95.

Li, P., Cavallero, S., Gu, Y., Chen, T.H.P., Hughes, J., Hassan, A.B., Bruning, J.C., Pashmforoush, M. and Sucov, H.M., 2011. IGF signaling directs ventricular cardiomyocyte proliferation during embryonic heart development. *Development*, [online] 138(9), pp.1795–1805.

Li, W.E.I., Waldo, K., Linask, K.L., Chen, T., Wessels, A., Parmacek, M.S., Kirby, M.L. and Lo, C.W., 2002. An essential role for connexin43 gap junctions in mouse coronary artery development. *Development (Cambridge, England)*, [online] 129(8), pp.2031–2042.

Lie-Venema, H., Eralp, I., Maas, S., Gittenberger-De Groot, A.C., Poelmann, R.E. and Deruiter, M.C., 2005. Myocardial heterogeneity in permissiveness for epicardium-derived cells and endothelial precursor cells along the developing heart tube at the onset of coronary vascularization. *The Anatomical Record Part A: Discoveries in Molecular, Cellular, and Evolutionary Biology*, [online] 282A(2), pp.120–129.

Lin, C.-J., Lin, C.-Y., Chen, C.-H., Zhou, B. and Chang, C.-P., 2012. Partitioning the heart: mechanisms of cardiac septation and valve development. *Development*, [online] 139(18), pp.3277–3299.

van der Linde, D., Konings, E.E.M., Slager, M.A., Witsenburg, M., Helbing, W.A., Takkenberg, J.J.M. and Roos-Hesselink, J.W., 2011. Birth Prevalence of Congenital Heart Disease Worldwide. *Journal of the American College of Cardiology*, [online]

58(21), pp.2241–2247.

Liu, S.Q. and Goldman, J., 2001. Role of blood shear stress in the regulation of vascular smooth muscle cell migration. *IEEE Transactions on Biomedical Engineering*, [online] 48(4), pp.474–483.

Liu, X., Wu, H., Byrne, M., Krane, S. and Jaenisch, R., 1997. Type III collagen is crucial for collagen I fibrillogenesis and for normal cardiovascular development. *Proceedings of the National Academy of Sciences of the United States of America*, [online] 94(5), pp.1852–1856.

Lluri, G., Huang, V., Touma, M., Liu, X., Harmon, A.W. and Nakano, A., 2015. Hematopoietic progenitors are required for proper development of coronary vasculature. *Journal of Molecular and Cellular Cardiology*, [online] 86, pp.199–207.

Love, M.I., Huber, W. and Anders, S., 2014. Moderated estimation of fold change and dispersion for RNA-seq data with DESeq2. *Genome Biology*, [online] 15(12), p.550.

Maître, J.-L. and Heisenberg, C.-P., 2013. Three Functions of Cadherins in Cell Adhesion. *Current Biology*, [online] 23(14), pp.R626–R633.

Männer, J., 1999. Does the subepicardial mesenchyme contribute myocardioblasts to the myocardium of the chick embryo heart? A quail-chick chimera study tracing the fate of the epicardial primordium. *The Anatomical record*, [online] 255(2), pp.212–226.

Markl, M., Kilner, P.J. and Ebbers, T., 2011. Comprehensive 4D velocity mapping of the heart and great vessels by cardiovascular magnetic resonance. *Journal of Cardiovascular Magnetic Resonance*, [online] 13(1), p.7.

Marro, J., Pfefferli, C., de Preux Charles, A.-S., Bise, T. and Jaźwińska, A., 2016. Collagen XII Contributes to Epicardial and Connective Tissues in the Zebrafish Heart during Ontogenesis and Regeneration. *PLOS ONE*, [online] 11(10), p.e0165497.

Martínez-Estrada, O.M., Lettice, L.A., Essafi, A., Guadix, J.A., Slight, J., Velecela, V., Hall, E., Reichmann, J., Devenney, P.S., Hohenstein, P., Hosen, N., Hill, R.E., Muñoz-Chapuli, R. and Hastie, N.D., 2010. Wt1 is required for cardiovascular progenitor cell formation through transcriptional control of Snail and E-cadherin. *Nature Genetics*, [online] 42(1), pp.89–93.

Martinsen, B.J., 2005. Reference guide to the stages of chick heart embryology. *Developmental Dynamics*, [online] 233(4), pp.1217–1237.

Medici, D., Hay, E.D. and Olsen, B.R., 2008. Snail and Slug Promote Epithelial-Mesenchymal Transition through -Catenin-T-Cell Factor-4-dependent Expression of Transforming Growth Factor- 3. *Molecular Biology of the Cell*, [online] 19(11), pp.4875–4887.

Midgett, M., Goenezen, S. and Rugonyi, S., 2014. Blood flow dynamics reflect degree of outflow tract banding in Hamburger-Hamilton stage 18 chicken embryos. *Journal of The Royal Society Interface*, [online] 11(100), pp.20140643–20140643.

Midgett, M. and Rugonyi, S., 2014. Congenital heart malformations induced by hemodynamic altering surgical interventions. *Frontiers in Physiology*, [online] 5.

Moerkamp, A.T., Lodder, K., van Herwaarden, T., Dronkers, E., Dingenouts, C.K.E., Tengström, F.C., van Brakel, T.J., Goumans, M.-J. and Smits, A.M., 2016. Human fetal and adult epicardial-derived cells: a novel model to study their activation. *Stem Cell Research & Therapy*, [online] 7(1), p.174.

del Monte, G., Casanova, J.C., Guadix, J.A., MacGrogan, D., Burch, J.B.E., Perez-Pomares, J.M. and de la Pompa, J.L., 2011. Differential Notch Signaling in the Epicardium Is Required for Cardiac Inflow Development and Coronary Vessel Morphogenesis. *Circulation Research*, [online] 108(7), pp.824–836.

Moore-Morris, T., Guimarães-Camboa, N., Banerjee, I., Zambon, A.C., Kisseleva, T., Velayoudon, A., Stallcup, W.B., Gu, Y., Dalton, N.D., Cedenilla, M., Gomez-Amaro, R., Zhou, B., Brenner, D.A., Peterson, K.L., Chen, J. and Evans, S.M., 2014. Resident fibroblast lineages mediate pressure overload–induced cardiac fibrosis. *Journal of Clinical Investigation*, [online] 124(7), pp.2921–2934.

Morales, M.O., Price, R.L. and Goldsmith, E.C., 2005. Expression of Discoidin Domain Receptor 2 (DDR2) in the Developing Heart. *Microscopy and Microanalysis*, [online] 11(03), pp.260–267.

Mortazavi, A., Williams, B.A., McCue, K., Schaeffer, L. and Wold, B., 2008. Mapping and quantifying mammalian transcriptomes by RNA-Seq. *Nature Methods*, [online] 5(7), pp.621–628.

Murakami, M. and Simons, M., 2009. Regulation of vascular integrity. *Journal of Molecular Medicine*, [online] 87(6), pp.571–582.

Nahirney, P.C., Mikawa, T. and Fischman, D.A., 2003. Evidence for an extracellular matrix bridge guiding proepicardial cell migration to the myocardium of chick embryos. *Developmental Dynamics*, [online] 227(4), pp.511–523.

Nakao, A., 1997. TGF-beta receptor-mediated signalling through Smad2, Smad3 and Smad4. *The EMBO Journal*, [online] 16(17), pp.5353–5362.

Neeb, Z., Lajiness, J.D., Bolanis, E. and Conway, S.J., 2013. Cardiac outflow tract anomalies. *Wiley Interdisciplinary Reviews: Developmental Biology*, [online] 2(4), pp.499–530.

Norton, J.M., 2001. TOWARD CONSISTENT DEFINITIONS FOR PRELOAD AND AFTERLOAD. *Advances in Physiology Education*, [online] 25(1), pp.53–61.

Nurnberg, S.T., Cheng, K., Raiesdana, A., Kundu, R., Miller, C.L., Kim, J.B., Arora, K., Carcamo-Oribe, I., Xiong, Y., Tellakula, N., Nanda, V., Murthy, N., Boisvert, W.A., Hedin, U., Perisic, L., Aldi, S., Maegdefessel, L., Pjanic, M., Owens, G.K., Tallquist, M.D. and Quertermous, T., 2015. Coronary Artery Disease Associated Transcription Factor TCF21 Regulates Smooth Muscle Precursor Cells That Contribute to the Fibrous Cap. *PLOS Genetics*, [online] 11(5), p.e1005155.

Obi, S., Yamamoto, K., Shimizu, N., Kumagaya, S., Masumura, T., Sokabe, T., Asahara, T. and Ando, J., 2008. Fluid shear stress induces arterial differentiation of endothelial progenitor cells. *Journal of Applied Physiology*, [online] 106(1), pp.203–211.

Olivey, H.E., Compton, L.A. and Barnett, J. V., 2004. Coronary Vessel Development. *Trends in Cardiovascular Medicine*, [online] 14(6), pp.247–251.

Olivey, H.E., Mundell, N.A., Austin, A.F. and Barnett, J. V, 2006. Transforming growth factor-β stimulates epithelial–mesenchymal transformation in the proepicardium. *Developmental Dynamics*, [online] 235(1), pp.50–59.

Ottaviani, G. and Buja, L.M., 2016. Congenital Heart Disease. In: *Cardiovascular Pathology*. [online] Elsevier, pp.611–647.

Oyen, N., Poulsen, G., Boyd, H.A., Wohlfahrt, J., Jensen, P.K.A. and Melbye, M., 2009. Recurrence of Congenital Heart Defects in Families. *Circulation*, [online] 120(4), pp.295–301.

Ozerdem, U., Grako, K.A., Dahlin-Huppe, K., Monosov, E. and Stallcup, W.B., 2001. NG2 proteoglycan is expressed exclusively by mural cells during vascular morphogenesis. *Developmental Dynamics*, [online] 222(2), pp.218–227.

Pang, K.L., 2016. The role of abnormal haemodynamics and cardiac troponin T in cardiogenesis. The University of Nottingham.

Pang, K. L., Parnall, M., and Loughna, S., 2017. Effect of altered haemodynamics on the developing mitral valve in chick embryonic heart. *Journal of Molecular and Cellular Cardiology*, [online] 108, pp.114–126.

Parnall, M., 2017. *The role of structural myosin proteins and heamodynamics on the cardiac conduction system, with optimisation of RNA-seq in altered*

haemodynamics model. The University of Nottingham.

Penny, D.J. and Vick, G.W., 2011. Ventricular septal defect. *The Lancet*, [online] 377(9771), pp.1103–1112.

Pérez-Pomares, J.M., Phelps, A., Muñoz-chápuli, R. and Wessels, A., 2001. The contribution of the proepicardium to avian. *International Journal for Developmental Biology*, 45(S1), pp.155–156.

Pérez-Pomares, J.M., Phelps, A., Sedmerova, M. and Wessels, A., 2003. Epicardial-like cells on the distal arterial end of the cardiac outflow tract do not derive from the proepicardium but are derivatives of the cephalic pericardium. *Developmental Dynamics*, [online] 227(1), pp.56–68.

Pfaffl, M.W., 2001. A new mathematical model for relative quantification in real-time RT-PCR. *Nucleic Acids Research*, [online] 29(9), p.45e–45.

Pfaffl, M.W., 2002. Relative expression software tool (REST(C)) for group-wise comparison and statistical analysis of relative expression results in real-time PCR. *Nucleic Acids Research*, [online] 30(9), p.36e–36.

Plavicki, J.S., Hofsteen, P., Yue, M.S., Lanham, K.A., Peterson, R.E. and Heideman, W., 2014. Multiple modes of proepicardial cell migration require heartbeat. *BMC Developmental Biology*, [online] 14(1), p.18.

Poelmann, R.E., Gittenberger-de Groot, A.C., Mentink, M.M., Bökenkamp, R. and Hogers, B., 1993. Development of the cardiac coronary vascular endothelium, studied with antiendothelial antibodies, in chicken-quail chimeras. *Circulation Research*, [online] 73(3), p.559 LP-568.

Preibisch, S., Saalfeld, S. and Tomancak, P., 2009. Globally optimal stitching of tiled 3D microscopic image acquisitions. *Bioinformatics*, [online] 25(11), pp.1463–1465.

Rana, M.S., Sizarov, A., Christoffels, V.M. and Moorman, A.F.M., 2014. Development of the human aortic arch system captured in an interactive three-dimensional reference model. *American Journal of Medical Genetics Part A*, [online] 164(6), pp.1372–1383.

Reckova, M., Rosengarten, C., DeAlmeida, A., Stanley, C.P., Wessels, A., Gourdie, R.G., Thompson, R.P. and Sedmera, D., 2003. Hemodynamics Is a Key Epigenetic Factor in Development of the Cardiac Conduction System. *Circulation Research*, 93(1), pp.77–85.

Reese, D.E., Zavaljevski, M., Streiff, N.L. and Bader, D., 1999. bves:A Novel Gene Expressed during Coronary Blood Vessel Development. *Developmental Biology*,

[online] 209(1), pp.159–171.

Rennie, M., Stovall, S., Carson, J., Danilchik, M., Thornburg, K. and Rugonyi, S., 2017. Hemodynamics Modify Collagen Deposition in the Early Embryonic Chicken Heart Outflow Tract. *Journal of Cardiovascular Development and Disease*, [online] 4(4), p.24.

Rhee, D.Y., Zhao, X.-Q., Francis, R.J.B., Huang, G.Y., Mably, J.D. and Lo, C.W., 2009. Connexin 43 regulates epicardial cell polarity and migration in coronary vascular development. *Development*, [online] 136(18), pp.3185–3193.

Risebro, C.A., Vieira, J.M., Klotz, L. and Riley, P.R., 2015. Characterisation of the human embryonic and foetal epicardium during heart development. *Development*, [online] 142(21), pp.3630–3636.

Rodgers, L.S., Lalani, S., Runyan, R.B. and Camenisch, T.D., 2008. Differential growth and multicellular villi direct proepicardial translocation to the developing mouse heart. *Developmental Dynamics*, [online] 237(1), pp.145–152.

Rodriguez, E.R. and Tan, C.D., 2017. Structure and Anatomy of the Human Pericardium. *Progress in Cardiovascular Diseases*, [online] 59(4), pp.327–340.

Rothe, C., 2003. Toward consistent definitions for preload and afterload—revisited. *Advances in Physiology Education*, [online] 27(1), pp.44–45.

Rudman, M., Blackburn, H.M., Graham, L.J.W. and Pullum, L., 2004. Turbulent pipe flow of shear-thinning fluids. *Journal of Non-Newtonian Fluid Mechanics*, [online] 118(1), pp.33–48.

Ruijtenbeek, K., De Mey, J.G.R. and Blanco, C.E., 2002. The Chicken Embryo in Developmental Physiology of the Cardiovascular System: A Traditional Model with New Possibilities. *American Journal of Physiology - Regulatory, Integrative and Comparative Physiology*, [online] 283(2), pp.R549–R551.

Rutland, C., Warner, L., Thorpe, A., Alibhai, A., Robinson, T., Shaw, B., Layfield, R., Brook, J.D. and Loughna, S., 2009. Knockdown of alpha myosin heavy chain disrupts the cytoskeleton and leads to multiple defects during chick cardiogenesis. *Journal of Anatomy*, [online] 214(6), pp.905–915.

Sadler, T.W., 2006. *Langman's medical embryology*. 10th ed. Philadelphia: Lippincott Williams & Wilkins.

Sakamoto, N., Ohashi, T. and Sato, M., 2006. Effect of Fluid Shear Stress on Migration of Vascular Smooth Muscle Cells in Cocultured Model. *Annals of Biomedical Engineering*, [online] 34(3), pp.408–415.

Sanada, H., Shimizu, M., Shimizu, K., Kita, Y., Sugihara, N. and Takeda, R., 1991. Left atrial afterload mismatch in hypertrophic cardiomyopathy. *The American Journal of Cardiology*, [online] 68(10), pp.1049–1054.

Schaefer, K.S., Doughman, Y.Q., Fisher, S.A. and Watanabe, M., 2004. Dynamic patterns of apoptosis in the developing chicken heart. *Developmental Dynamics*, [online] 229(3), pp.489–499.

Schindelin, J., Arganda-Carreras, I., Frise, E., Kaynig, V., Longair, M., Pietzsch, T., Preibisch, S., Rueden, C., Saalfeld, S., Schmid, B., Tinevez, J.-Y., White, D.J., Hartenstein, V., Eliceiri, K., Tomancak, P. and Cardona, A., 2012. Fiji: an open-source platform for biological-image analysis. *Nature Methods*, [online] 9(7), pp.676–682.

Schlueter, J. and Brand, T., 2013. Subpopulation of Proepicardial Cells Is Derived From the Somatic Mesoderm in the Chick Embryo. *Circulation Research*, [online] 113(10), pp.1128–1137.

Sedmera, D., Pexieder, T., Rychterova, V., Hu, N. and Clark, E.B., 1999. Remodeling of chick embryonic ventricular myoarchitecture under experimentally changed loading conditions. *The Anatomical Record*, [online] 254(2), pp.238–252.

Segura, A.M., Frazier, O.H. and Buja, L.M., 2014. Fibrosis and heart failure. *Heart Failure Reviews*, [online] 19(2), pp.173–185.

Sheng, W., Qian, Y., Wang, H., Ma, X., Zhang, P., Diao, L., An, Q., Chen, L., Ma, D. and Huang, G., 2013. DNA methylation status of NKX2-5, GATA4 and HAND1in patients with tetralogy of fallot. *BMC Medical Genomics*, 6(1), p.46.

Shi, L., Goenezen, S., Haller, S., Hinds, M.T., Thornburg, K.L. and Rugonyi, S., 2013. Alterations in pulse wave propagation reflect the degree of outflow tract banding in HH18 chicken embryos. *AJP: Heart and Circulatory Physiology*, [online] 305(3), pp.H386–H396.

Singh, A., Ramesh, S., Cibi, D.M., Yun, L.S., Li, J., Li, L., Manderfield, L.J., Olson, E.N., Epstein, J.A. and Singh, M.K., 2016. Hippo Signaling Mediators Yap and Taz Are Required in the Epicardium for Coronary Vasculature Development. *Cell* Reports, [online] 15(7), pp.1384–1393.

Skalli, O., Pelte, M.F., Peclet, M.C., Gabbiani, G., Gugliotta, P., Bussolati, G., Ravazzola, M., and Orci, L., 1989. Alpha-smooth muscle actin, a differentiation marker of smooth muscle cells, is present in microfilamentous bundles of pericytes. *Journal of Histochemistry & Cytochemistry*, [online] 37(3), pp.315–321.

Smith, M.C., 1966. Effects of Turbulence on Laminar Skin Friction and Heat

Transfer. *Physics of Fluids*, [online] 9(12), p.2337.

Soulet, F., Kilarski, W.W., Antczak, P., Herbert, J., Bicknell, R., Falciani, F. and Bikfalvi, A., 2010. Gene signatures in wound tissue as evidenced by molecular profiling in the chick embryo model. *BMC Genomics*, [online] 11(1), p.495.

Stovall, S., Midgett, M., Thornburg, K. and Rugonyi, S., 2016. Changes in dynamic embryonic heart wall motion in response to outflow tract banding measured using video densitometry. *Journal of Biomedical Optics*, [online] 21(11), p.116003.

Takashima, S., Kitakaze, M., Asakura, M., Asanuma, H., Sanada, S., Tashiro, F., Niwa, H., Miyazaki, J., Hirota, S., Kitamura, Y., Kitsukawa, T., Fujisawa, H., Klagsbrun, M. and Hori, M., 2002. Targeting of both mouse neuropilin-1 and neuropilin-2 genes severely impairs developmental yolk sac and embryonic angiogenesis. *Proceedings of the National Academy of Sciences*, [online] 99(6), pp.3657–3662.

Takeichi, M., Nimura, K., Mori, M., Nakagami, H. and Kaneda, Y., 2013. The Transcription Factors Tbx18 and Wt1 Control the Epicardial Epithelial-Mesenchymal Transition through Bi-Directional Regulation of Slug in Murine Primary Epicardial Cells. *PLoS ONE*, [online] 8(2), p.e57829.

Tandon, P., Miteva, Y. V., Kuchenbrod, L.M., Cristea, I.M. and Conlon, F.L., 2013. Tcf21 regulates the specification and maturation of proepicardial cells. *Development*, [online] 140(11), pp.2409–2421.

Tevosian, S.G., Deconinck, A.E., Tanaka, M., Schinke, M., Litovsky, S.H., Izumo, S., Fujiwara, Y. and Orkin, S.H., 2000. FOG-2, a Cofactor for GATA Transcription Factors, Is Essential for Heart Morphogenesis and Development of Coronary Vessels from Epicardium. *Cell*, [online] 101(7), pp.729–739.

Thiene, G. and Frescura, C., 2010. Anatomical and pathophysiological classification of congenital heart disease. *Cardiovascular Pathology*, [online] 19(5), pp.259–274.

Tobita, K. and Keller, B.B., 2000. Right and left ventricular wall deformation patterns in normal and left heart hypoplasia chick embryos. *American Journal of Physiology-Heart and Circulatory Physiology*, [online] 279(3), pp.H959–H969.

Tobita, K., Schroder, E.A., Tinney, J.P., Garrison, J.B. and Keller, B.B., 2002. Regional passive ventricular stress-strain relations during development of altered loads in chick embryo. *American Journal of Physiology - Heart and Circulatory Physiology*, [online] 282(6), pp.H2386–H2396.

Tomanek, R., 1999. Rate of coronary vascularization during embryonic chicken

development is influenced by the rate of myocardial growth. *Cardiovascular Research*, [online] 41(3), pp.663–671.

Trembley, M.A., Velasquez, L.S., de Mesy Bentley, K.L. and Small, E.M., 2015. Myocardin-related transcription factors control the motility of epicardium-derived cells and the maturation of coronary vessels. *Development*, [online] 142(1), pp.21–30.

Turner, K. and Navaratnam, V., 1996. The positions of coronary arterial ostia. *Clinical Anatomy*, [online] 9(6), pp.376–380.

Tuzcu, E.M., Moodie, D.S., Chambers, J.L., Keyser, P. and Hobbs, R.E., 1990. Congenital heart diseases associated with coronary artery anomalies. *Cleveland Clinic journal of medicine*, [online] 57(2), pp.147–152.

Udan, R.S., Culver, J.C. and Dickinson, M.E., 2013. Understanding vascular development. *Wiley Interdisciplinary Reviews: Developmental Biology*, [online] 2(3), pp.327–346.

Vicente-Steijn, R., Scherptong, R.W.C., Kruithof, B.P.T., Duim, S.N., Goumans, M.J.T.H., Wisse, L.J., Zhou, B., Pu, W.T., Poelmann, R.E., Schalij, M.J., Tallquist, M.D., Gittenberger-de Groot, A.C. and Jongbloed, M.R., 2015. Regional differences in WT-1 and Tcf21 expression during ventricular development: implications for myocardial compaction. *PLOS ONE*, [online] 10(9), p.e0136025.

Virágh, S., Gittenberger-de Groot, A.C., Poelmann, R.E. and Kálmán, F., 1993. Early development of quail heart epicardium and associated vascular and glandular structures. *Anatomy and Embryology*, [online] 188(4), pp.381–93.

Vogel, W., Gish, G.D., Alves, F. and Pawson, T., 1997. The Discoidin Domain Receptor Tyrosine Kinases Are Activated by Collagen. *Molecular Cell*, [online] 1(1), pp.13–23.

Vrancken Peeters, M.-P.F.M., Gittenberger-de Groot, A.C., Mentink, M.M.T. and Poelmann, R.E., 1999. Smooth muscle cells and fibroblasts of the coronary arteries derive from epithelial-mesenchymal transformation of the epicardium. *Anatomy and Embryology*, [online] 199(4), pp.367–378.

Wada, A.M., Reese, D.E. and Bader, D.M., 2001. Bves: prototype of a new class of cell adhesion molecules expressed during coronary artery development. *Development (Cambridge, England)*, [online] 128(11), pp.2085–2093.

Wagner, N., 2005. Coronary vessel development requires activation of the TrkB neurotrophin receptor by the Wilms' tumor transcription factor Wt1. *Genes & Development*, [online] 19(21), pp.2631–2642.

Walczak, C.E. and Heald, R., 2008. Mechanisms of mitotic spindle assembly and function. *International review of cytology*, [online] 265, pp.111–158.

Waller, B.F., Orr, C.M., Slack, J.D., Pinkerton, C.A., Van Tassel, J. and Peters, T., 1992. Anatomy, histology, and pathology of coronary arteries: a review relevant to new interventional and imaging techniques--Part I. *Clinical cardiology*, 15(6), pp.451–457.

Ward, N.L., Van Slyke, P., Sturk, C., Cruz, M. and Dumont, D.J., 2004. Angiopoietin 1 expression levels in the myocardium direct coronary vessel development. *Developmental Dynamics*, [online] 229(3), pp.500–509.

Ward, N.L.L., Slyke, P.V. Van and Dumont, D.J.J., 2004. Functional inhibition of secreted angiopoietin: a novel role for angiopoietin 1 in coronary vessel patterning. *Biochemical and Biophysical Research Communications*, [online] 323(3), pp.937–946.

Weber, K.T., 1989. Cardiac interstitium in health and disease: The fibrillar collagen network. *Journal of the American College of Cardiology*, [online] 13(7), pp.1637–1652.

Wenink, A.C.G., 1981. Embryology of the ventricular septum. *Virchows Archiv A Pathological Anatomy and Histology*, [online] 390(1), pp.71–79.

Wessels, A., van den Hoff, M.J.B., Adamo, R.F., Phelps, A.L., Lockhart, M.M., Sauls, K., Briggs, L.E., Norris, R.A., van Wijk, B., Perez-Pomares, J.M., Dettman, R.W. and Burch, J.B.E., 2012. Epicardially derived fibroblasts preferentially contribute to the parietal leaflets of the atrioventricular valves in the murine heart. *Developmental Biology*, [online] 366(2), pp.111–124.

Wheelock, M.J., Shintani, Y., Maeda, M., Fukumoto, Y. and Johnson, K.R., 2008. Cadherin switching. *Journal of Cell Science*, [online] 121(6), pp.727–735.

Wiese, C., Grieskamp, T., Airik, R., Mommersteeg, M.T.M., Gardiwal, A., de Gier-de Vries, C., Schuster-Gossler, K., Moorman, A.F.M., Kispert, A. and Christoffels, V.M., 2009. Formation of the Sinus Node Head and Differentiation of Sinus Node Myocardium Are Independently Regulated by Tbx18 and Tbx3. *Circulation Research*, [online] 104(3), pp.388–397.

van Wijk, B., van den Berg, G., Abu-Issa, R., Barnett, P., van der Velden, S., Schmidt, M., Ruijter, J.M., Kirby, M.L., Moorman, A.F.M. and van den Hoff, M.J.B., 2009. Epicardium and Myocardium Separate From a Common Precursor Pool by Crosstalk Between Bone Morphogenetic Protein- and Fibroblast Growth Factor-Signaling Pathways. *Circulation Research*, [online] 105(5), pp.431–441.

Wittig, J. and Münsterberg, A., 2016. The Early Stages of Heart Development: Insights from Chicken Embryos. *Journal of Cardiovascular Development and Disease*, [online] 3(2), p.12.

Wren, C., Birrell, G. and Hawthorne, G., 2003. Cardiovascular malformations in infants of diabetic mothers. *Heart (British Cardiac Society)*, 89(10), pp.1217–1220.

Wu, M., Smith, C.L., Hall, J.A., Lee, I., Luby-Phelps, K. and Tallquist, M.D., 2010. Epicardial Spindle Orientation Controls Cell Entry into the Myocardium. *Developmental Cell*, [online] 19(1), pp.114–125.

Wu, S.-P., Dong, X.-R., Regan, J.N., Su, C. and Majesky, M.W., 2013. Tbx18 regulates development of the epicardium and coronary vessels. *Developmental Biology*, [online] 383(2), pp.307–320.

Wu, Y.-C., Liu, C.-Y., Chen, Y.-H., Chen, R.-F., Huang, C.-J. and Wang, I.-J., 2012. Blood Vessel Epicardial Substance (Bves) Regulates Epidermal Tight Junction Integrity through Atypical Protein Kinase C. *Journal of Biological Chemistry*, [online] 287(47), pp.39887–39897.

Xu, J., Lu, W., Zhang, S., Zhu, C., Ren, T., Zhu, T., Zhao, H., Liu, Y. and Su, J., 2014. Overexpression of DDR2 contributes to cell invasion and migration in head and neck squamous cell carcinoma. *Cancer Biology & Therapy*, [online] 15(5), pp.612–622.

Ye, J., Coulouris, G., Zaretskaya, I., Cutcutache, I., Rozen, S. and Madden, T.L., 2012. Primer-BLAST: A tool to design target-specific primers for polymerase chain reaction. *BMC Bioinformatics*, [online] 13(1), p.134.

Yu, F.-X., Zhao, B. and Guan, K.-L., 2015. Hippo Pathway in Organ Size Control, Tissue Homeostasis, and Cancer. *Cell*, [online] 163(4), pp.811–828.

Yu, F., Lu, B., Gao, Y., Hou, Z., Schoepf, U.J., Spearman, J. V., Cao, H., Sun, M. and Jiang, S., 2013. Congenital anomalies of coronary arteries in complex congenital heart disease: Diagnosis and analysis with dual-source CT. *Journal of Cardiovascular Computed Tomography*, 7(6), pp.383–390.

Yuan, S., Zaidi, S. and Brueckner, M., 2013. Congenital heart disease: emerging themes linking genetics and development. *Current Opinion in Genetics & Development*, [online] 23(3), pp.352–359.

Yue, M.S., Plavicki, J.S., Li, X.-Y., Peterson, R.E. and Heideman, W., 2015. A co-culture assay of embryonic zebrafish hearts to assess migration of epicardial cells in vitro. *BMC Developmental Biology*, [online] 15(1), p.50.

Zhou, B., Honor, L.B., He, H., Ma, Q., Oh, J.-H., Butterfield, C., Lin, R.-Z., Melero-Martin, J.M., Dolmatova, E., Duffy, H.S., Gise, A. von, Zhou, P., Hu, Y.W., Wang, G., Zhang, B., Wang, L., Hall, J.L., Moses, M.A., McGowan, F.X. and Pu, W.T., 2011. Adult mouse epicardium modulates myocardial injury by secreting paracrine factors. *Journal of Clinical Investigation*, [online] 121(5), pp.1894–1904.

Zhou, B., Ma, Q., Rajagopal, S., Wu, S.M., Domian, I., Rivera-Feliciano, J., Jiang, D., von Gise, A., Ikeda, S., Chien, K.R. and Pu, W.T., 2008. Epicardial progenitors contribute to the cardiomyocyte lineage in the developing heart. *Nature*, [online] 454(7200), pp.109–113.

8 Appendix

Genes	cDNA size (bp)	gDNA size (bp)
***WT1* (ISH)**	455	14931
***TCF21* (ISH)**	769	1792
***COL1A2* (qPCR)**	215	1466
***COL12A1* (qPCR)**	106	1203
***CSPG4* (qPCR)**	142	687
***DDR2* (qPCR)**	169	493
***EEF1A1* (qPCR)**	209	596
***NRP1* (qPCR)**	139	3159
***NRP2* (qPCR)**	137	14300
***ANGPT1* (qPCR)**	207	26007
***BDNF* (qPCR)**	163	163
***NTRK2* (qPCR)**	169	4670
***Bves* (qPCR)**	211	6097
***GJA1* (qPCR)**	159	6100
***GAPDH* (qPCR)**	188	317
***PDGFRB* (qPCR)**	124	1170
***SMAD2* (qPCR)**	225	18274
***SNAI1* (qPCR)**	200	955
***SNAI2* (qPCR)**	146	561
***TAZ* (qPCR)**	173	173
***TBP* (qPCR)**	221	1522
***TJP1* (qPCR)**	102	3264
***WT1* (qPCR)**	170	6658
***YAP1* (qPCR)**	138	20964

Table 8.1: The gene fragment's sizes used for ISH and qPCR. The cDNA and gDNA sizes of the amplicons are shown.

Variable	Region:Treatment comparison	Difference	Adjusted p-values
Vessel Area (μm^2)	IVS:OTB-EPI:OTB	-105.020252	0.0488043*
	MYO:OTB-EPI:OTB	-94.903317	0.0836709
	EPI:Sham-EPI:OTB	-64.697526	0.3582222
	IVS:Sham-EPI:OTB	-41.640642	0.7603605
	MYO:Sham-EPI:OTB	-85.538411	0.1357068
	MYO:OTB-IVS:OTB	10.116934	0.9993801
	EPI:Sham-IVS:OTB	40.322726	0.7823547
	IVS:Sham-IVS:OTB	63.37961	0.3781272
	MYO:Sham-IVS:OTB	19.48184	0.9867522
	EPI:Sham-MYO:OTB	30.205792	0.9189247
	IVS:Sham-MYO:OTB	53.262675	0.5499882
	MYO:Sham-MYO:OTB	9.364906	0.9995738
	IVS:Sham-EPI:Sham	23.056884	0.9725184
	MYO:Sham-EPI:Sham	-20.840886	0.9821857
	MYO:Sham-IVS:Sham	-43.897769	0.721208
Vessel Number	IVS:OTB-EPI:OTB	-17.062376	0.0009086***
	MYO:OTB-EPI:OTB	-6.413633	0.3115808
	EPI:Sham-EPI:OTB	5.508836	0.4591214
	IVS:Sham-EPI:OTB	-9.695709	0.0550584
	MYO:Sham-EPI:OTB	-10.151362	0.042452*
	MYO:OTB-IVS:OTB	10.648742	0.0319102*
	EPI:Sham-IVS:OTB	22.571212	0.0000647****
	IVS:Sham-IVS:OTB	7.366667	0.196034
	MYO:Sham-IVS:OTB	6.911014	0.2461001
	EPI:Sham-MYO:OTB	11.92247	0.0153376*
	IVS:Sham-MYO:OTB	-3.282076	0.8651302

	MYO:Sham-MYO:OTB	-3.737729	0.7937639
	IVS:Sham-EPI:Sham	-15.204545	0.0024354**
	MYO:Sham-EPI:Sham	-15.660198	0.0019041**
	MYO:Sham-IVS:Sham	-0.455653	0.9999836
Wall to Lumen Ratio	IVS:OTB-EPI:OTB	-0.267981407	0.2954339
	MYO:OTB-EPI:OTB	0.688274209	0.0010591**
	EPI:Sham-EPI:OTB	0.16471572	0.7450312
	IVS:Sham-EPI:OTB	0.017983983	0.9999865
	MYO:Sham-EPI:OTB	0.156547655	0.7806456
	MYO:OTB-IVS:OTB	0.956255616	0.0000471****
	EPI:Sham-IVS:OTB	0.432697127	0.0339436
	IVS:Sham-IVS:OTB	0.285965389	0.2394914
	MYO:Sham-IVS:OTB	0.424529061	0.0380519*
	EPI:Sham-MYO:OTB	-0.523558489	0.009531**
	IVS:Sham-MYO:OTB	-0.670290227	0.0013331**
	MYO:Sham-MYO:OTB	-0.531726555	0.0085123**
	IVS:Sham-EPI:Sham	-0.146731738	0.8208227
	MYO:Sham-EPI:Sham	-0.008168066	0.9999997
	MYO:Sham-IVS:Sham	0.138563672	0.8515993

Table 8.2: The results from the Tuckey post-hoc test for the coronary vasculature fluorescent immunohistochemistry. The post-hoc results between the region:treatment comparisons and their difference, as well as the adjusted p-values. Keys: interventricular septum, IVS; myocardium, MYO; epicardium, EPI; *p<0.05; **p<0.01; ***p<0.001; ****p<0.0001

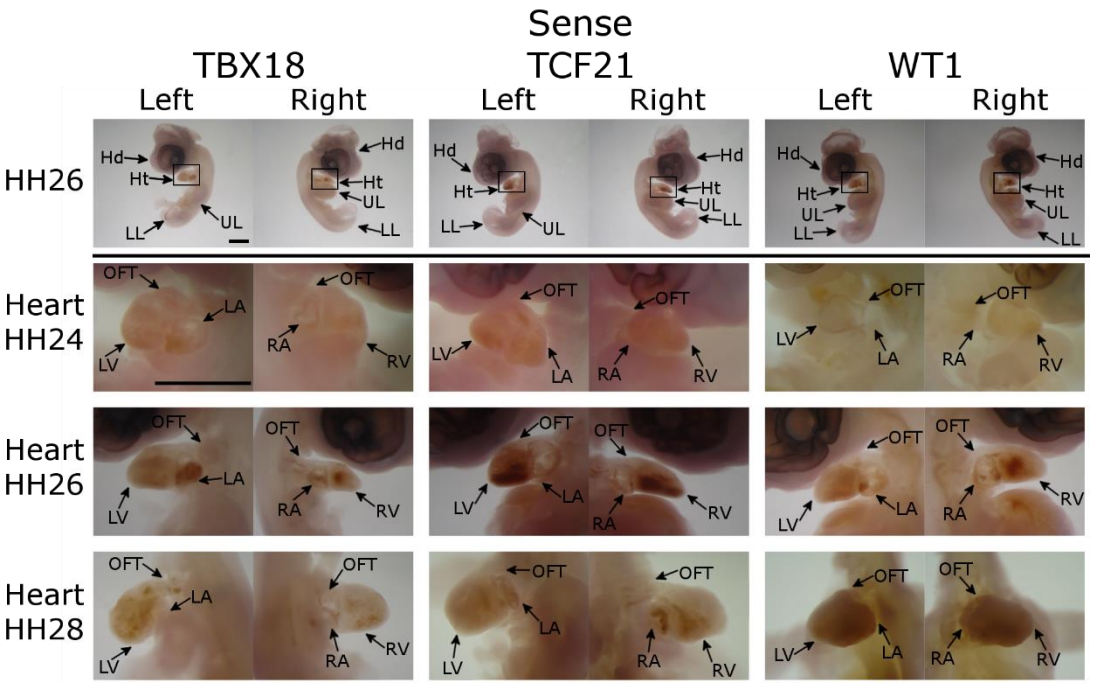

Figure 8.1: Sense results from the ISH experiments. The same embryo is shown on its left and right sides. Each heart is a 4X magnification of the HH26 representative whole embryo on top. Scale bar: 2 mm. The scale bar is the same for each magnification. Keys: Hd, head; Ht, heart; UL, upper limb; LL, lower limb; OFT, outflow tract; LA, left atria; RA, right atria; LV, left ventricle; RV, right ventricle; A, atria.

COL1A2

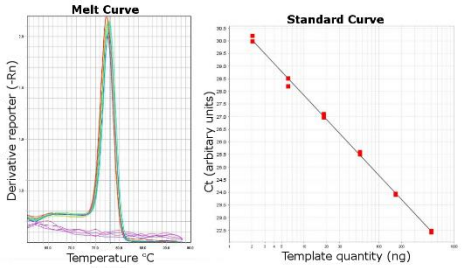

GJA1

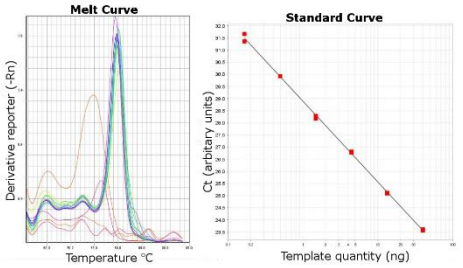

COL12A1

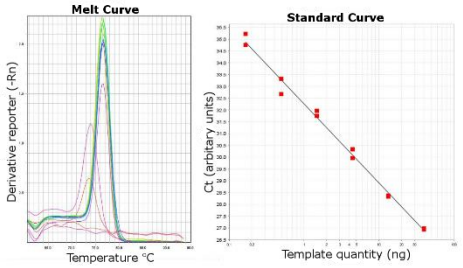

GAPDH

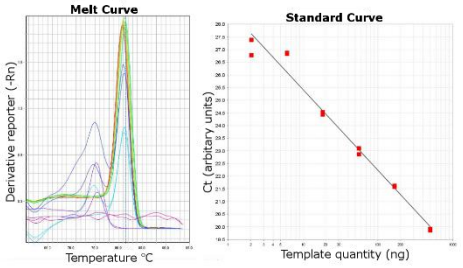

CSPG4

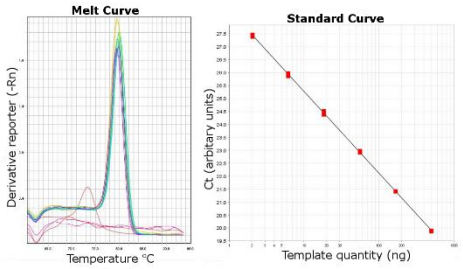

PDGFRB

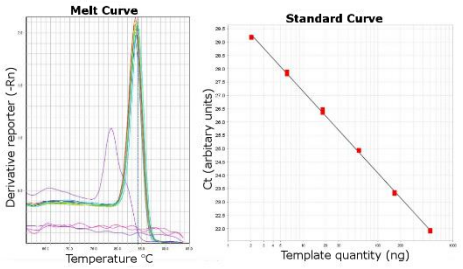

DDR2

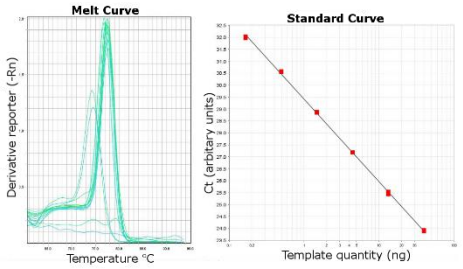

SMAD2

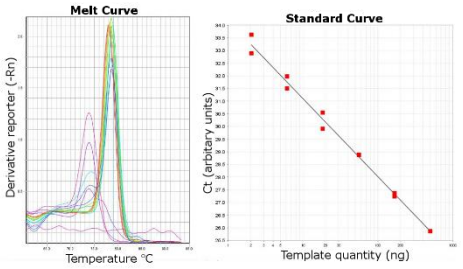

EEF1A1

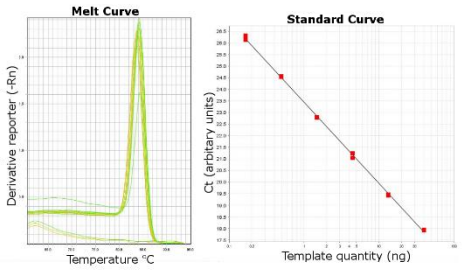

SNAI1

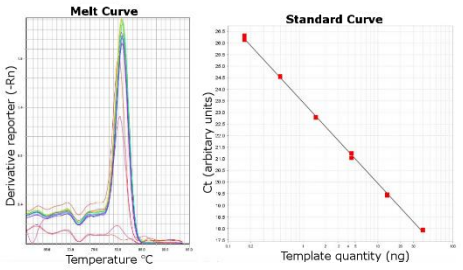

NRP1

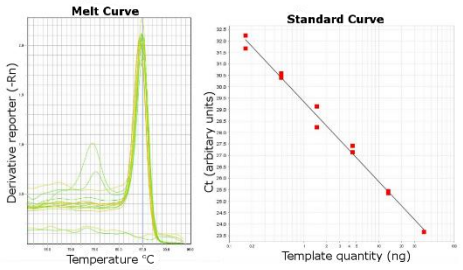

SNAI2

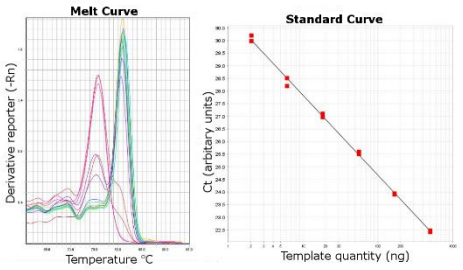

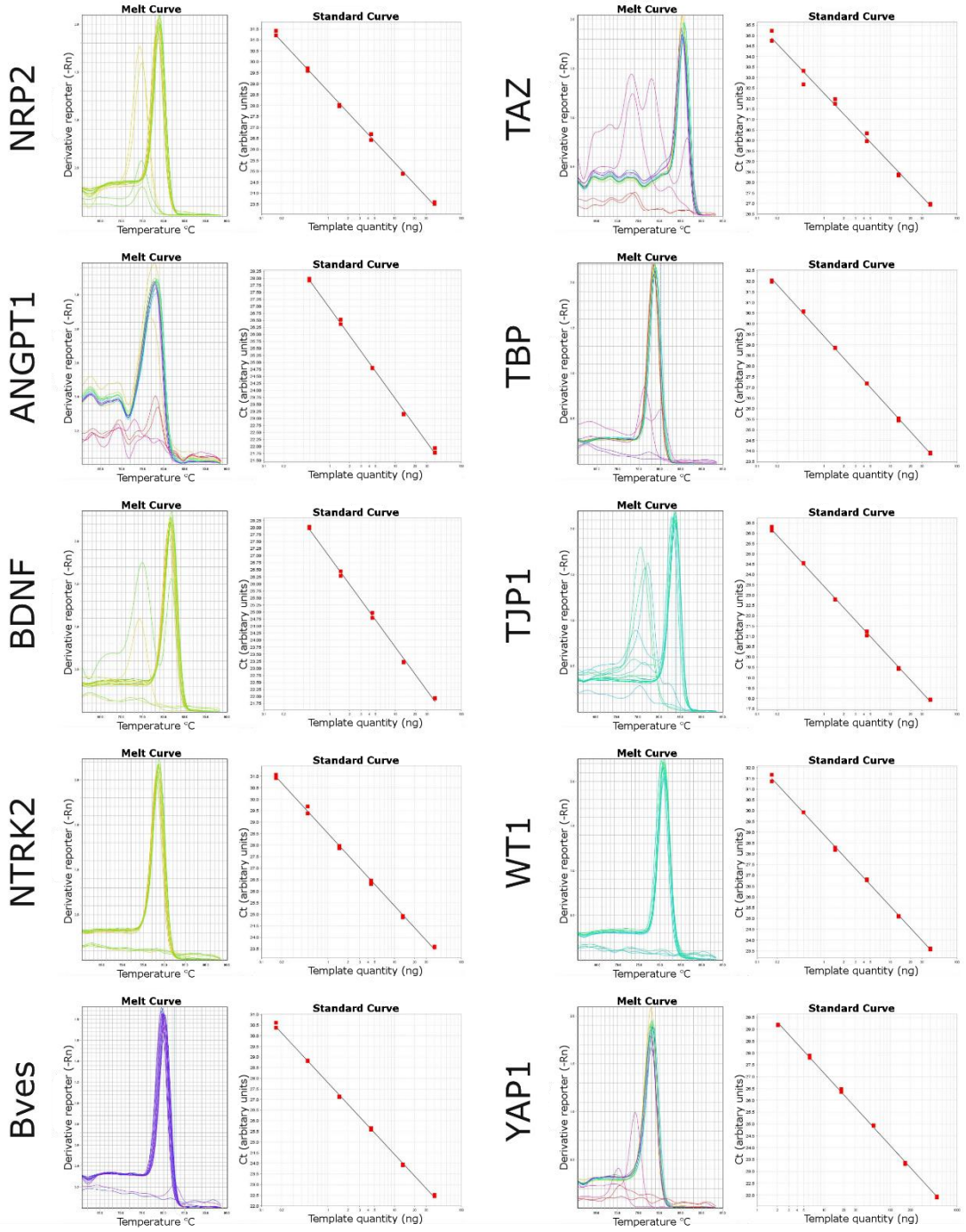

Figure 8.2: qPCR primer optimisation. On the melting curve graph, the derivative reporter (negative derivative of the function of fluorescent intensity vs. melting temperature) is plotted against the melting temperature. On the standard curve graph, the threshold cycle (C_t) is plotted against the total amount of cDNA template for each dilution. Note that the standard curve is generated only by readings taken from the cDNA template. cDNA samples had a single,

almost overlapping peak whereas RNA and water controls had a few or no peak. Peaks in lower temperatures, in relation to the major, denote primer dimers.

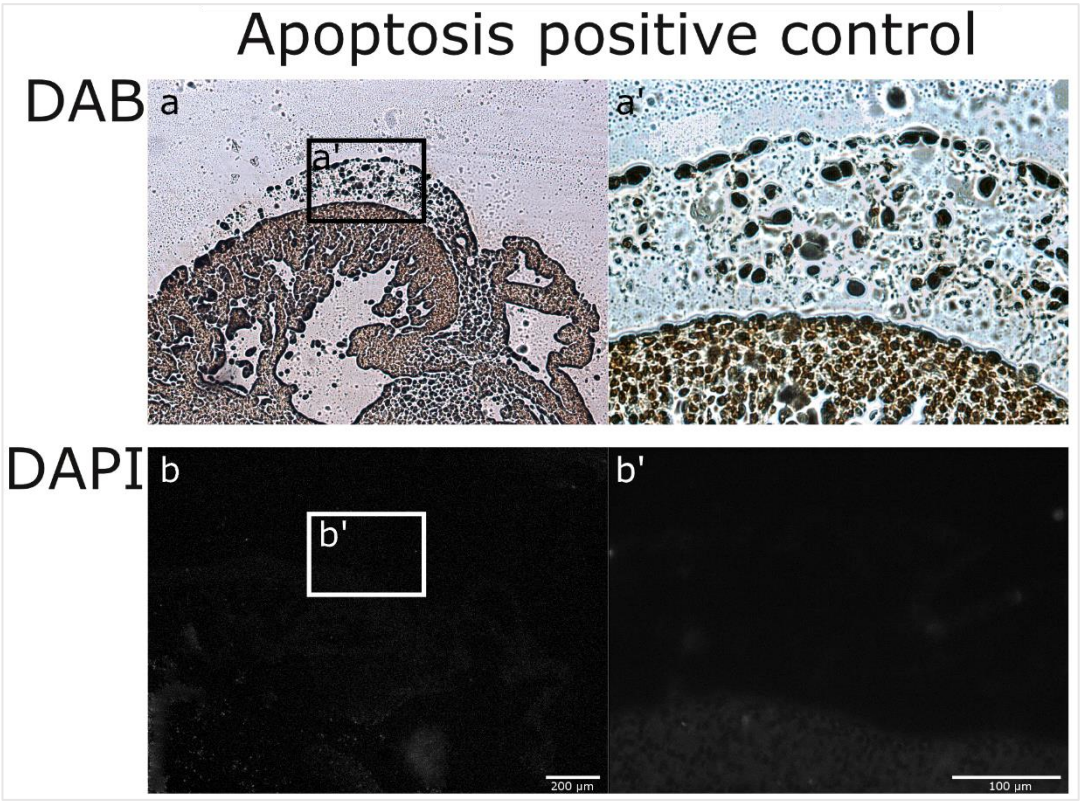

Figure 8.3: Apoptosis positive control. Immunostaining was achieved using TdT enzyme and anti-digoxigenin conjugated antibody. The addition of DAB chromogen resulted in the cells being stained black-brown (a). DAPI was used to counterstain all the other cells (b). DAB positive cells were DAPI negative. Boxed areas in a-b are shown in a'-b'. The scale bar is the same for all panels.